THE UNIVERSITY *of* EDINBURGH

Exploring the Multifunctionality of a Giant Commercial Microgel

David Crosby

Doctor of Philosophy
The University of Edinburgh
April 2021

Abstract

Microgels are soft colloidal particles composed of networks of cross-linked polymers used in a variety of industrial products such as pharmaceuticals, cosmetics and personal care items. The attraction of using microgels is their ability to tune the rheology of suspensions by reversibly swelling, often triggered in response to stimuli such as pH or temperature. However, recently the research is focussed on their emulsifying capabilities which is a result of their polymer building blocks. Much of the literature is focussed on 'model' microgel systems synthesised for research but there are no reports on the commercial microgel considered here used in many personal care products. In this thesis, a commercial microgel system composed of a block co-polymer called Sepimax Zen (SZ) was analysed to understand its rheology modifying and emulsifying capabilities and the results were discussed in the context of existing literature on model microgel systems. In addition to bridging the gap between model and commercial systems, we aim to understand how the polymer-colloid duality of microgels determines the intrinsic functions of microgel particles.

The rheological profile of the SZ microgels was tested using a combination of steady shear and oscillatory rheology. Steady state measurements revealed that at sufficiently dilute concentrations the suspensions behave as Newtonian liquids, however, once a critical concentration (0.03 wt%) has been reached they reveal shear thinning behaviour. At higher concentrations (0.08 wt%) a yield stress develops indicating the formation of a network structure. Oscillatory measurements revealed the nature of these networks with strain measurements indicating that microgels form networks by interpenetrating their polymeric chains, similar to polymers. The resultant networks were found to be 'soft' set gels when compared to other microgel systems with a cross link density of 1500 monomers per crosslink.

In order to understand the dynamics and to determine the size of the SZ microgels

Differential Dynamic Microscopy (DDM) was used. DDM measures the dynamics of a population of colloids via image analysis, allowing the mobility and the size of individual colloids to be characterised. From these measurements SZ microgels were found to be 2.7 μm in radius at low concentrations < 0.03 wt%, above which their mobility is greatly reduced, coinciding with the onset of shear thinning. The reduced mobility is likely due to the attractive interactions between SZ microgels where surface chains entangle, since similar results are predicted for adhesive spheres. The response to salt was also investigated by exposing the microgel to a range in concentrations of NaCl from 0.001 mM to 2000 mM. Unexpectedly, the microgel is considerably tolerant of salt, only reducing in size at a high critical concentration of 200 mM NaCl at which it reduces in size by a factor of 2; an important observation when considering them in commercial formulations. In order to simulate the effect crowding has on this microgel a non-excluding polymer called Ficoll-400 was used to tune the osmotic pressure of suspensions. At the highest Ficoll-400 concentration SZ microgel particles were found to deswell from 2.7 μm down to 0.52 μm, a much larger decrease than observed with other microgel systems. As one of the first studies to analyse microgel particles using DDM these results demonstrate how valuable DDM is to provide insight into the rheology of these soft particle systems.

Using a combination of pendant drop tensiometry and cryo-SEM measurements the stabilisation of a n-dodecane-water interface by SZ microgels was determined. SZ microgels were found to significantly reduce the interfacial tension by building up layers of microgels on the surface of the interface. These SZ-stabilised interfaces are highly elastic, $E' > 20$ mN/m, $E'' < 1$ mN/m, similar to colloid-laden interfaces. The interfacial elasticity was dependent on size of the microgel, as deswollen microgels resulted in more effectively packed interfaces resulting in more elastic interfaces, E' increases to almost 30 mN/m. A surprising observation was that SZ-stabilised interfaces appeared to be immune to buckling, a phenomenon observed when particle-laden interfaces are destabilised. We conclude this effect is due to SZ microgel particles associative behaviour and solubility. When significantly disturbed by an interface SZ microgel particles detach in order to associate with other microgel particles in the bulk. This phenomenon has been seen in a few microgel systems, however, this work is the first to investigate it in detail. These findings could have a profound effect on how microgels are made given their multifunctional properties

In the final chapter the effect SZ has on emulsion stability and rheology is

analysed. SZ-stabilised oil-in-water emulsions were found to make emulsion-filled gels. The oil drops initially behave as passive fillers and then appear to behave as active fillers at $\phi \approx 20\,\%$, increasing the elasticity of the emulsion gels. Furthermore, SZ-stabilised emulsions are stable only up to 30 wt%, considerably lower than for other emulsion systems. We conclude that this is a result of the large microgel particles associating only lightly at the interface and therefore the emulsion becomes active when microgel-laden emulsion droplets are in contact (at $\phi \approx 20\,\%$) and is unstable when emulsion droplets are closer than one microgel particle apart. The stability of emulsions were tested by combining the results of centrifugation and drying experiments. The centrifugation experiments determined the critical disjoining pressure, the pressure at which the oil is dispelled from the matrix, which was found to be similar to traditional surfactant systems. The drying experiments revealed that emulsions dried down to a partially coalesced emulsion film, separated by a thin polymeric film which is similar to studies on surfactant-stabilised systems.

This thesis explores the properties of a commercial microgel system and contrasts the results to model microgel systems. The SZ microgels were found to be highly unusual giant microgels, much larger than previously studied microgel systems, exhibiting both colloidal and polymeric behaviour. Through combining the rheological and DDM measurements, this thesis provides a standard for studying microgels and other soft matter systems. The results of this thesis form a strong basis for developing a framework for designing microgels with dual functionality, preventing emulsion coalescence and creaming, as required for industrial applications. Future work could focus on understanding the adsorption of microgels at the interfaces of different oils i.e. more polar oils.

Declaration

I declare that this thesis was composed by myself, that the work contained herein is my own except where explicitly stated otherwise in the text, and that this work has not been submitted for any other degree or professional qualification except as specified.

(*David Crosby, April 2021*)

Acknowledgements

First and foremost I'd like to thank Dr. Tiffany Wood for being an exemplary supervisor. Without her continual encouragement, patience, understanding and guidance I would not have been able to complete this thesis.

I also must thank Prof. Alex Lips and Prof. Wilson Poon for spending many hours discussing the work in this thesis. Despite their hectic schedules they always had time to engage with me and and discuss my findings which was extremely helpful.

The differential dynamic microscopy experiments would not have been possible without the knowledge and expertise of Dr. Vincent Martinez. I am greatly appreciative for his proof reading and helpful suggestions concerning that chapter.

I need to thank Dr. Thomas Glen for assisting me with the cryo-SEM experiments. Furthermore, I would also like to thank Dr. Hamid Kellay of the University of Bordeaux for hosting me while I conducted thin film experiments presented in this thesis.

Many thanks my industrial supervisors, Dr. David Moore and Dr. Michael Thompson at GSK. From engaging with me in discussions and arranging visits to GSK laboratories in Weybridge, they really went above and beyond to support me during the PhD.

A large thank you must go to SOFI CDT management teams of all three sites. The training and networking events provided throughout my PhD have been some of the key highlights. Furthermore, the support during the project selection, resultant relocation and thesis submission was very much appreciated.

I would like to say thank you to all my fellow PhD students, from both Edinburgh University and the SOFI CDT. You have made it an incredibly enjoyable and edifying experience, and I feel like I have made friends for life. I'd also like to extend that thank you to all my closest friends, made both before and during my PhD experience, for your continual support throughout.

I of course need to thank my family in particular my dad Ian, and my aunt Fiona, for their unwavering support over the years. Their constant encouragement and guidance helped spur me on to finally achieve this long held goal.

Contents

Abstract i

Declaration iv

Acknowledgements v

Contents vi

List of Figures x

List of Tables xx

1 Introduction 1

1.1 What is microgel? 1

1.1.1 Defining a Microgel 1

1.1.2 Synthesis of Microgels 2

1.1.3 Composition and Structure 5

1.2 Microgels as Rheology Modifiers 13

1.2.1 Rheology of Dispersions 13

1.2.2 Flow Behaviour of Microgel Suspensions 20

1.2.3 Effect of Phase Volume and Concentration 21

1.2.4 Viscoelascity of Microgel Suspensions 24

1.3 Microgels as Emulsifiers 26
1.3.1 Traditional Emulsifiers 26
1.3.2 Microgels at Interfaces 30
1.4 Emulsions 35
1.4.1 Thin Film Formation of Emulsions 39
1.5 Outline of Thesis 41

2 Materials and Methods 42

2.1 Materials 42
2.1.1 Microgel Stock Preparation 43
2.1.2 Model Emulsion Preparation 44
2.2 Rheology 44
2.2.1 Steady Shear Rheology 44
2.2.2 Oscillatory Rheology 47
2.2.3 Experimental Protocol 49
2.2.4 Rheological Measurements 49
2.3 Differential Dynamic Microscopy 50
2.3.1 Background of Differential Dynamic Microscopy 50
2.3.2 Experimental Protocol 52
2.3.3 Sample Preparation 52
2.3.4 Imaging Setup 53
2.4 Pendent Drop Tensiometry 54
2.4.1 Background of Pendant Drop Tensiometry 54
2.4.2 Oscillatory Tensiometry 56

2.5 Experimental Protocol 58
2.5.1 Material Preparation 58
2.5.2 Imaging Set Up 59
2.6 Cryo-SEM 60
2.6.1 Experimental Protocol 61
2.7 Confocal Microscopy 61
2.7.1 Experimental Protocol 62
2.7.2 Confocal Microscopy Set-Up 62
2.7.3 Bordeaux Set-Up 63
2.7.4 Stability Measurements 64
2.8 Experimental Protocol 64

3 Rheology of SZ Microgels 66

3.1 Steady-Shear Rheology 66
3.1.1 Flow Behaviour 66
3.1.2 Dilute Regime 67
3.1.3 Concentrated Regime 71
3.2 Oscillatory Rheology 74
3.2.1 Large Amplitude Rheology 74
3.2.2 Shear Elasticity of the Microgel Network 77
3.3 Linking the Shear and Oscillatory Rheology 78
3.4 Summary 80

4 Dynamics of SZ Microgels 82

4.1 SZ Microgels Diffusivity in Water 83

4.2 Effect of Salt on SZ microgels 87

4.3 Effect of Osmotic Pressure on SZ Microgels..... 94

4.4 Summary 97

5 SZ Microgels at the Oil-Water Interface 100

5.1 Effect on Interfacial Tension 101

5.1.1 Variations of IFT with different SZ Concentrations..... 101

5.2 Effect on Interfacial Elasticity 109

5.2.1 Variations of Elasticity with SZ Concentration 109

5.2.2 Variations of Elasticity and Surface Pressure with Time 111

5.2.3 Variations of Elasticity with Surface Pressure..... 113

5.3 Absence of Interfacial Buckling 118

5.4 Cryo-SEM Measurements of SZ-stabilised Interfaces..... 121

5.5 Summary 126

6 SZ Microgels in Emulsions 128

6.1 Rheology of SZ-stabilised emulsions..... 128

6.2 Centrifugation of SZ-stabilised emulsions..... 134

6.3 Analysis of Thin-films of SZ-stabilised emulsions 136

6.4 Summary 142

7 Conclusions and Outlook 144

Bibliography 147

List of Figures

1.1 Schematic of microgel formation by surfactant-free emulsion polymerization. Initially, unstable precursor particles aggregate to form new primary particles. At the end of nucleation stage, all new precursor particles are captured by existing stable particles. Taken from [2]. 4

1.2 Schematic of microgel formation by emulsification. Taken from [2]. 5

1.3 Schematic of a generic microgel particle showing how they can swell and deswell reversibly. Taken from [10]. 5

1.4 Left: Schematic of a polyelectrolyte microgel in its swollen state. The solid dots represent the cross-links while the unfilled dots are counter-ions and the outer shell is where electro-neutrality is not satisfied. Taken from [13]. Right: Schematic of a core-shell microgel with a highly cross-linked core (Red) and a light cross-linked corona (Blue). Taken from [14]. 7

1.5 Schematic diagram of phases of block copolymers. LAM-lamellar, CYL- cylindrical, SPH-spheres, GYR-gyroid, PL-perforated lamellar and OBDD-ordered continuous double diamond. Taken from [17]. 12

1.6 Schematic showing the variations of how stress (σ) varies as a function of shear rate ($\dot{\gamma}$). The curves show the profiles of Newtonian (1), shear thinning (2), shear thickening and yield stress materials (4 and 5). Taken from [21]. 13

1.7 A log-log representation of how the viscosity (η) of xanthan gum gels depends on the concentration of xanthan gum, with the critical concentrations marked. Taken from [22]. 17

1.8 Schematic of the hard sphere dispersion phase diagram showing fluid-crystal phase transition, glass transition, random-close packing and crystalline maximum packing limits. Taken from [21] . . 19

1.9 Comparison of how the Kreiger Dougherty equation, $\eta_{rel} = \left(1 - \frac{\phi}{\phi_m}\right)^{[\eta]\phi_m}$, varies for different suspensions. Taken from [2]. . . 20

1.10 Schematic of increasing microgel crowding which illustrates how the swelling factor k changes as the centre-to-centre distance between particles decreases. Taken from [29]. 23

1.11 Variations in the storage modulus (G') calculated as a function of concentration Sephadex G1005, at 0.25 Hz. Taken from [33]. . . . 26

1.12 Schematic of a surfactant molecule with a hydrophilic head group and hydrophobic tail group stabilising an oil droplet in water. . . 28

1.13 Schematic of particles wetting an interface at various contact angles, θ. Taken from [47]. 29

1.14 Schematic of a particle adsorbing to an interface showing the energy barrier of adsorption (ΔE_{ads}) which increases as more particles adsorb to the interface (increasing by $\Delta E_{barrier}$). Taken from [58] 31

1.15 Left: (Top) Cryo-SEM images of dodecane drops covered by PNIPAM microgels: (a) large view of a drop (scale bar is 5 μm), (bottom) (b) hexagonal organisation of microgels at the interface (scale bar is 1 μm), the microgels appear flattened. Right: Cryo-SEM image of the interface of a heptane-in-water emulsion drop covered by PNIPAM microgels with a schematic of the particle structure and arrangement at the interface. Taken from [71] . . . 33

1.16 Cryo-SEM images of microgels at the water/n-heptane interfaces imaged from the oil side with a schematic demonstrating the protrusion of microgels at the oil-water interface. Taken from [79] 35

1.17 Schematic diagrams of systems of emulsion droplets and gels: emulsion-filled gel (Left) and emulsion gel (Right). 37

1.18 Schematic of the deposition of an emulsion on a substrate. A depicts the initial stage of deposition where B shows a schematic of drying-front induced coalescence occurring and C shows how emulsion coalesces from the nucleation mode. 40

2.1 Schematic of the Sepimax Zen polymer 42

2.2 Optical microscopy image of a dried down microgel suspension. . . 43

2.3 Schematic diagram of shear flow being generated between sliding layers of fluid. Equations show how shear rate $\dot{\gamma}$ and shear stress σ are quantified. 45

2.4 Schematic diagram of a rotational rheometer with a fluid in between the plates. The top plate rotates with rotational velocity V and torsional force F leading to the flow being initiated. A number of geometries used on with rotational rheometers are also shown: (a) parallel plate, (b) cone and plate and (c) cross-hatched. 46

2.5 Illustration of a amplitude sweep where the storage modulus (G') and loss modulus (G'') are measured as a function of stress. LVR stands for the linear viscoelastic regime where the the initial structure has not been compromised. 2 is the stress at where the material starts to lose solid-character and 1 is where G' and G'' cross and is referred to as the yield point. Taken from [97]. 49

2.6 Schematic of the image processing to obtain the DICFs, $g(\vec{q}, \tau)$. Left image depicts how the intensity is tracked as images are collected to form videos, middle image is a non-averaged image collected from an experiment, $\langle |F_{D_i}(\vec{q}, t)| \rangle^2$ and (right) averaged image, $g(\vec{q}, \tau)$. Taken from [98]. 51

2.7 Schematic of a pendant drop with labelled a co-ordinate systems (described in the text) which describes how the Young-Laplace equation is fitted to the drop profile. Taken from [101]. 55

2.8 Schematic of Krüss DSA100 drop tensiometer. 1. Computer-controlled piezoelectic pump for volume oscillations, 2. CCD camera and prism to reflect drop image into camera, 3. Moveable z-stage, 4. Diffuse light source, 5. Straight needle, 6. J-needle and 7. Cuvette. 59

2.9 Schematic demonstrating the basic principle of SEM. 61

2.10 Schematic diagram of the principle of confocal microscopy. 62

2.11 Left: Schematic of the aluminium block with a 20 μm gap etched on the side and the resultant coverslip with the emulsion spread on it, the red parts are the dispersed oil phase. Right: Schematic of the of the coverslip being imaged with a 20 μm film deposited. . 63

2.12 Schematic of the microscopy set-up used while in Bordeaux. Taken from [92]. 63

3.1 Variations in shear stress σ plotted as a function of applied shear rate $\dot{\gamma}$ for various suspensions at different SZ concentrations. . . . 67

3.2 Variations in relative viscosity η_{rel} plotted as a function of SZ concentration measured at specific shear rates. The dotted line highlight critical SZ concentrations: 0.025 wt% and 0.1 wt%. . . . 67

3.3 Variations of the relative viscosity η_{rel} plotted as a function of SZ concentration. The dashed line represents the fit to the modified Einstein relation $\eta_{rel} = 1 + 2.5kC + 5.9(kC)^2$). 68

3.4 Variations of the inverse viscosity η^{-1} as a function of shear stress σ for different concentrations of SZ. 70

3.5 Variations of the flow index n plotted as function of SZ concentration. n was determined by fitting stress-shear rate data to the power-law fluid equation, $\sigma = k\dot{\gamma}^n$. The dotted line at 0.03 wt% represents when the microgel suspensions go from Newtonian ($n = 1$) materials to shear thinning ($n < 1$). 70

3.6 Variations in the shear stress σ plotted as a function of applied shear rate $\dot{\gamma}$. Dashed lines are the fits of the data to $\sigma = \sigma_y(1 + (\tau\dot{\gamma}^\beta)) = \sigma_y + k\dot{\gamma}^\beta$. 71

3.7 Variations of the yield stress σ_y plotted as a function of concentration of SZ for the concentrated microgel suspensions. Inset shows how the shear thinning exponent β changes with concentration of SZ. 72

3.8 Variations of the time constant τ plotted as a function of concentration of SZ for the concentrated microgel suspensions. 73

3.9 Variations of the critical strain γ_{crit} plotted as a function SZ concentration. γ_{crit} is the strain where G' crosses G'' in the oscillatory rheology plots shown in Figure 3.10. 75

3.10 Variations in the storage and the loss moduli plotted as a function of strain of the SZ microgel suspensions at various concentrations. Filled symbols represent the storage modulus and unfilled is the loss modulus. 76

3.11 Variations of the plateau modulus G_0 plotted as a function SZ concentration. G_0 is determined by averaging G' is the LVR. . . 77

3.12 Variations in the shear stress σ, which has been rescaled by the yield stress σ_y, plotted as a function of the shear rate $\dot{\gamma}$, which is rescaled by the solvent viscosity η_s by the plateau modulus G_0. . 79

3.13 Variations in the yield stress σ_{yield} plotted as a function of SZ concentration, triangles represent σ_{yield} extracted from the oscillatory rheology in Figure 3.10 and circles represent the σ_{yield} obtained by fitting the to steady state shear rheology $\sigma = \sigma_y(1 + (\tau\dot{\gamma}^\beta)) = \sigma_y + k\dot{\gamma}^\beta$. 80

3.14 Phase diagram of the SZ microgels, showing the key features uncovered from the rheological measurements detailed throughout this chapter. 81

4.1 Variation of the differential image correlation function g plotted as a function of the delay time τ, at fixed q value of $1.66\,\mu\mathrm{m}^{-1}$, for a variety of SZ concentrations. 83

4.2 Variation of the differential image corrlation function g plotted as a function of the delay time τ, for a fixed concentration of SZ of $0.01\,\mathrm{wt}\%$, at a variety of q values. 83

4.3 Variation of the relaxation time τ_R plotted as a function of the wave vector magnitude q. τ_R was determined from the fits shown in Figure 4.1. Inset graph shows how the exponent n depends on the SZ concentration (C). 86

4.4 Variation of the average stretch exponent β plotted as a function of the SZ concentration. β was determined from the fits shown in Figure 4.1. 86

4.5 Variation of the average diffusion coefficient D plotted as a function of the SZ concentration. D was determined from the fits shown in Figure 4.1. The dotted black indicates where the dilute regime ends ($0.005\,\mathrm{wt}\%$) and the green line represents the average D for dilute regime while the red lines represents the standard deviation. 87

4.6 Variation of the average diffusion coefficient D plotted as a function of the NaCl concentration, at a fixed SZ concentration of $0.000\,25\,\mathrm{wt}\%$. The dotted black indicates where the shrinkage occurs ($200\,\mathrm{mM}$) and the green line represents the average D for dilute regime while the red lines represents the standard deviation. 88

4.7 Variation of the differential image corrlation function g plotted as a function of the delay time τ, at fixed q value of $1.5\,\mu\mathrm{m}^{-1}$, for a variety of SZ concentrations with $200\,\mathrm{mM}$ NaCl added. 89

4.8 Variation of the relaxation time τ_R plotted as a function of the wave vector magnitude q concentration for a variety of SZ concentrations with $200\,\mathrm{mM}$ NaCl added. β was determined from the fits shown in Figure 4.7, where the data was fitted to equation 4.1 90

4.9 Variation of the average stretch exponent β plotted as a function of the SZ concentration at a fixed salt concentration of $200\,\mathrm{mM}$. β was determined from the fits shown in Figure 4.1, where the data was fitted to equation 4.1. 91

4.10 Variation of the average diffusion coefficient D plotted as a function of the SZ concentration, at a fixed salt concentration of $200\,\mathrm{mM}$. D was determined from the fits shown in Figure 4.7, where the data was fitted to equation 4.1. 92

4.11 Variation of the rescaled diffusivity D/D_0 plotted as a function of the SZ concentration for both swollen and deswollen microgels. Red points represent the swollen microgels and blue points represent the deswollen case. 92

4.12 Variation of the rescaled diffusivity plotted D/D_0 as a function of the volume fraction of microgels ϕ. Inset: ϕ plotted as a function of the SZ concentration. Red points represent the swollen microgels and blue points represent the deswollen case. 93

4.13 Variation of the average diffusion coefficient D plotted as a function of the osmotic pressure Π_{osmo}, at a fixed concentration of SZ 0.0025 wt%. 96

4.14 Variations in osmotic pressure Π_{osmo} as a function of Ficoll-400 concentration, taken from work done in [100]. Inset: Variations of the relative viscosity η_{rel} as a function of Ficoll 400 concentration, taken from work done in [99]. 96

4.15 Variation of the rescaled hydrodynamic radius R/R_0 plotted as a function of the osmotic pressure Π_{osmo}, exerted by Ficoll-400, for a fixed concentration of SZ 0.0025 wt%. 97

4.16 Phase diagram of the SZ microgels, showing the key features uncovered from the DDM and rheology measurements detailed in Chapter 3 and Chapter 4. 98

4.17 Schematics diagrams showing how SZ microgels act in response to increasing salt concentration (top) and increasing osmotic pressure (bottom). 99

5.1 Variations of interfacial tension IFT as a function of drop age of a dodecane drop in an aqueous background with various concentrations of SZ microgels present. SZ concentrations are as follows: 0.000 25 wt% (red), 0.005 wt% (blue), 0.01 wt% (green), 0.05 wt% (yellow) and 0.08 wt% (purple). The inset shows the same data but the the natural logarithm of x-axis has been taken. 101

5.2 Typical interfacial tension dynamics of protein adsorption at the oil-water interface showing methods of quantifying each regime. Induction time of Regime I determined by extrapolating slope from Regime II to zero surface pressure. Slopes of Regimes II and III show logarithmic dependence of tension on time. Taken from [149]. 103

5.3 Schematic of protein adsorption at the oil-water interface in the early stages of adsorption, named Regime I . Regime I where the interface is filled with protein molecules which relax into less compact structures causing declines in IFT at the oil-water interface. Taken from [149]. 103

5.4 Schematic of protein adsorption at the oil-water interface in the mid stages of adsorption, named Regime II . Regime II where an incubation phase where proteins diffuse to the interface and initiate confirmation changes in order to adsorb to the oil-water interface. Taken from [149]. 104

5.5 Schematic of protein adsorption at the oil-water interface in the late stages of adsorption, named Regime III. Regime III where continued conformational changes of initial adsorbed layers and aggregation promote slow declines in tension over extended periods of time. Taken from [149]. 104

5.6 (a) Short-time and (b) long-time adsorption curves fitted with equations 5.1 and 5.2 respectively. SZ concentrations are as follows: 0.000 25 wt% (red), 0.005 wt% (blue), 0.01 wt% (green), 0.05 wt% (yellow) and 0.08 wt% (purple) along with respective dashed fit lines. 106

5.7 Variations in dilational storage modulus E', plotted as a function applied frequency f, of the microgel laden dodecane-water interface. SZ concentrations are as follows: 0.000 25 wt% (red), 0.005 wt% (blue), 0.01 wt% (green), 0.05 wt% (yellow) and 0.08 wt% (purple). 110

5.8 Variations in dilational loss modulus E'', plotted as a function applied frequency f, of the microgel laden dodecane-water interface. SZ concentrations are as follows: 0.000 25 wt% (red), 0.005 wt% (blue), 0.01 wt% (green), 0.05 wt% (yellow) and 0.08 wt% (purple). 111

5.9 Variations of the dilational storage E', dots and loss moduli E'', squares plotted as a function of time as SZ microgels adsorb to a n-dodecane/water interface. The red curve denotes swollen microgels sized at 2.7 μm and the blue curve denotes the deswollen case, with 200 mM of NaCl was added to osmotically shrink the microgels to 1.3 μm. 112

5.10 Variations of the surface pressure Π and plotted as a function of time as SZ microgels adsorb to a n-dodecane/water interface. The red curve denotes swollen microgels sized at 2.7 μm and the blue curve denotes the deswollen case, were 200 mM of NaCl was added to osmotically shrink the microgels to 1.3 μm. 113

5.11 Variations of the dilational storage modulus E' plotted as a function of surface pressure Π as SZ microgels adsorb to a n-dodecane/water interface. 0.000 25 wt% of SZ was used and microgels had a radius of 2.7 μm. 114

5.12 Variations of the dilational storage modulus E' plotted as a function of surface pressure Π as SZ microgels adsorb to a n-dodecane/water interface. 0.000 25 wt% of SZ was used with 200 mM salt, in order to shrink the microgels, giving an average radius of 1.3 μm. 115

5.13 Variations of the dilational storage modulus E' plotted as a function of surface pressure Π as SZ microgels adsorb to a n-dodecane/water interface. 0.000 25 wt% of SZ was used and microgels had a radius of 2.7 μm. The black line is the linear fit to the data and the solid red line marks where the interface has been saturated with microgels. 116

5.14 Variations of the dilational storage modulus E' plotted as a function of surface pressure Π as SZ microgels adsorb to a n-dodecane/water interface. 0.000 25 wt% of SZ was used with 200 mM salt, in order to shrink the microgels, giving an average radius of 1.3 μm. The black line is the linear fit to the data and the solid blue line marks where the interface has been saturated with microgels. 117

5.15 Top: A SZ-stabilised dodecane drop undergoing a compression-expansion (30 μL compressed to 5 μL and expanded back to 30 μL) cycle in an aqueous background, the droplet has been shrunk with no buckling occurring on the surface. Bottom: A particle-stabilised water drop in oil buckling during a compression-expansion cycle, taken from [177]. 118

5.16 Variations of interfacial tension γ as a function of drop age of a dodecane drop in an aqueous background with 0.000 25 wt% SZ microgels present. The red curve represents swollen SZ microgels ($R = 2.7\,\mu$m), the blue curve is for deswollen microgels ($R = 1.3\,\mu$m) adsorbing to an oscillating drop. The black curve is for swollen microgels ($R = 2.7\,\mu$m) adsorbing to a static drop. 120

5.17 A Cryo-SEM image of an caprylic/capric triglyceride oil drop stabilised by a highly compressed layer of microgels. This image was taken of an oil-in-water emulsion stabilised by 0.5 wt% which has been sublimed for 30 minutes to remove any ice crystals on the surface. 121

5.18 A cryo-SEM image of an caprylic/capric triglyceride oil drop stabilised by a highly compressed layer of microgels. This image was taken of an oil-in-water emulsion stabilised by 0.5 wt% which had not been sublimed. 123

5.19 A cryo-SEM image of an caprylic/capric triglyceride oil drop stabilised by a highly compressed layer of microgels. This image was taken of an oil-in-water emulsion stabilised by 0.01 wt% which has not been sublimed. 124

5.20 A cryo-SEM image of the surface of a partially stabilised caprylic/-capric triglyceride oil drop, showing the imprints of microgels on the surface. This image was taken of an oil-in-water emulsion stabilised by 0.01 wt% which has not been sublimed. 124

5.21 Schematic of the geometry used to measure the protrusion depth of the SZ microgel. In the diagram $D_{hydrodynamic}$ is the hydrodynamic diameter of the microgel,$R_{hydrodynamic}$ is the hydrodynamic radius of the microgel, $D_{contact}$ is the diameter of the microgel in contact with the interface, R_c is the radius of the microgel in contact with the interface and S is the distance from the center of the microgel to the $D_{contact}$. The bottom image shows how the microgel is attached at the interface. The microgel on the bottom left is indicative of SZ with an approximate contact angle of 20° whereas on the right is particle with contact angle of 90°. 125

5.22 Schematic of the SZ adsorption mechanism showing the comparison to a spherical particle (right) and microgel (left). For the microgel the blue represents the hydrophilic sections and the red being the hydrophobic chains which mediate adsorption to the interface. 126

6.1 Variations in shear stress σ plotted as a function of applied shear rate $\dot{\gamma}$ for the a range of SZ-stabilised emulsions. The SZ concentrations is 0.5 wt% is each case. Solid lines indicate the fits to the Hershel-Bulkley equation. 129

6.2 Variations in viscosity η plotted as a function of applied shear rate $\dot{\gamma}$ for the a range of SZ-stabilised emulsions. The SZ concentrations is 0.5 wt% is each case. 130

6.3 Variations in the storage modulus G' of SZ-stabilised emulsions, with a fixed SZ concentration of 0.5 wt%, as a function of oil content. 131

6.4 Effects of oil content on the elasticity of SZ-stabilised emulsions. The logarithm of G'_E/G'_M, where G'_E is the storage modulus of the emulsion gel and G'_M is the storage modulus of the gel matrix, is plotted against the oil content. 132

6.5 Schematic of emulsion drops coming together without a microgel layer (top) and with a microgel layer (bottom). D represents the diameter of the emulsion drop, r is the separation between the emulsion centres and r_{mod} is the separation with a microgel layer added. 133

6.6 Vortexed emulsions each containing 10 wt% of oil with various concentrations of SZ: left to right 2.5×10^{-3} wt%, 0.01 wt%, 0.04 wt% and 0.08 wt%. (a) Emulsions after vortexing, (b) Vortexed emulsions after 24 hours and (c) Centrifuged emulsions. 134

6.7 Confocal microscopy images of drying model emulsions containing 20 wt% of CCT and 0.5 wt% of SZ. The CCT has been dyed with Nile red while the dark areas represent the gel matrix. Each panel is taken at different time points of the the drying process. 136

6.8 (a) Variations of the area of aqueous phase A, at different heights of the SZ-stabilised emulsion film, plotted as a function of time. (b) Variations of the normalised area of aqueous phase A_{norm}, at different heights of the SZ-stabilised emulsion film, plotted as a function of time. 137

6.9 Variations of the normalised area of aqueous phase averaged over all depths of the film $< A_{norm} >$ plotted as a function of time. . . 138

6.10 Variations of the predicted SZ concentration $C_{predicted}(wt\%)$ plotted as a function of time. 139

6.11 Image of the base of a dried sheared thin film of a SZ-stabilised (0.5 wt%) emulsion with 20 wt% of Caprylic/Capric Triglyceride. The film had been dried, in the open atmosphere, for approximately 30 minutes. The resulting structure shows partially coalesced droplets of oil separated by thin polymer films resulting in web-like structure. 140

6.12 Image of the base of a dried sheared thin film of a SZ-stabilised (0.5 wt%) emulsion with 20 wt% of Caprylic/Capric Triglyceride. The film had been dried, in the open atmosphere, for approximately 30 minutes. The resulting structure shows partial coalescenced pools of oil separated by thin polymer films resulting in web-like structure.Images show base of thin films of a SZ-stabilised (0.5 wt%) emulsion with 20 wt% of Caprylic/Capric Triglyceride, where the aqueous phase has been dyed with fluorescein, darker regions indicate where the Caprylic/Capric Triglyceride oil is. . . 141

6.13 Images show base of thin films of a SZ-stabilised (0.5 wt%) emulsion with 20 wt% of Caprylic/Capric Triglyceride, where the aqueous phase has been dyed with fluorescein, darker regions indicate where the Caprylic/Capric Triglyceride oil is.. 142

List of Tables

3.1 Values of experimental parameters determined from fitting the rheology experiments of concentrated microgel suspensions (data shown in Figure 3.6) in the concentrated regime with $\sigma = \sigma_y(1 + (\tau\dot{\gamma}^{\beta})) = \sigma_y + k\dot{\gamma}^{\beta}$. 74

5.1 Bulk concentration of microgels, in wt% C and mol/m^3 C_0, and the Stokes-Einstein Diffusion Coefficient D. D values were taken from previous DDM results in Chapter 4. 106

5.2 Slopes and R^2 of the linear fits to the short and long time IFT data. 107

5.3 Values of γ_0, γ_∞ and ΔE determined from fitting the short and long time IFT data using 5.1 and 5.2. 107

5.4 Average values of the dilational storage E' and loss E'' moduli for aged ($>$ 11 hours) n-dodecane drop surrounded by microgel suspensions at multiple concentrations. 110

5.5 Gradients obtained for the linear fits in Figures 5.13 and 5.14. . . 116

5.6 γ_∞ values for each of the curves displayed in Figure 5.16. 120

6.1 Values of experimental parameters determined from fitting the rheology data of SZ-stabilised emulsions with the Herschel-Bulkley relation. 130

6.2 Values of the critical g-value critical g_{kcrit} and critical osmotic pressure P_{OSM}^{CR} for the various emulsions. Each emulsion contained 10 wt% of oil with various concentrations of SZ. 135

Chapter 1

Introduction

1.1 What is microgel?

1.1.1 Defining a Microgel

Baker *et al.* was the first to use the term 'microgel', which was used to describe cross-linked polybutadiene latex particles [1]. The term 'micro' referred to the size of the particle, $\approx 1\,\mu$m, whereas 'gel' referred to their ability to swell in certain solvents. Swelling occurs when the microgels take in solvent causing an increase in size. Baker *et al.* emphasised that microgels consist of very high molecular weight polymer networks and, in this case, each latex particle was an individual polymer molecule. Baker defined microgels as colloidal particles (0.1 nm-1 μm) which form stable dispersions and can swell in the presence of the correct solvent. However, this definition encompasses colloidal entities which are not considered microgels [2]. Both surfactant and polymeric micelles also fit these criteria but they are not referrred to as microgels, due to their stability. Surfactant micelles have a finite lifetime with rapidly exchanging surfactant monomers whereas microgels have a static composition. At the other extreme, aqueous block copolymer micelles based on long hydrophobic blocks can be long-lived; however, the hydrophobic cores tend not to swell very much with water [2]. This leads to the final criteria a material must show to be defined as a microgel: microgels must have stable structures which is achieved by cross-linking occurring between the individual polymer molecules. The cross-linking can be either chemical or physical and, like any colloidal dispersion, microgel particles can aggregate, flocculate or coagulate.

This gives the definition of a microgel that is known today:

A microgel is a soft colloidal particle composed of a cross-linked network of polymers. The cross-linking can be chemically induced through a reaction or physically by association of polymers.

Microgels are used in a broad range of industrial applications and consumer products including coatings, paints, inks, oil recovery, controlled drug delivery, cosmetics, personal care, home care, food, and pharmaceuticals. An essential feature in many of these applications is the rheology of the microgel suspension during processing, storage, and transport of products. The microgel's ability to swell increases the viscosity of suspensions resulting in a gel-like consistency. Over the years microgels have been formulated to react to stimuli such as temperature or pH, leading to an increased interest both academically and commercially. The academic microgel literature tends to study homemade instead of commercial microgels. Most of the literature on microgels is focussed on microgel particles called PNIPAM, which is readily polymerized into linear water-soluble polymers, microgels, or macrogels [3]. PNIPAM derivatives have received much attention because the microgels are very uniform and the swelling properties are temperature-sensitive [3]. However, there has been little work trying to link the findings of academic microgels to commercial products. Two commercial microgel systems which have been widely studied are Carbopol and β-lactoglobulin. Carbopol is widely used as a rheology modifier in a variety of formulations such as personal care products and coatings, whereas β-lactoglobulin is a protein-based microgel made from denaturing whey proteins, extracted during milk production. β-lactoglobulin microgels are used in food products, such as yoghurt, and act to thicken and stabilise the components of the mixture [4] [5]. This study aims to characterise a new commercial microgel and compare the results to 'model' microgel systems.

1.1.2 Synthesis of Microgels

When synthesizing microgels there are a number of factors which must be considered including controlling the particle size distribution, the colloidal stability, and the distribution of specific functional groups such as crosslinkers. Given the diversity of microgel preparation strategies it is useful to distinguish

them based on the microgel formation mechanism such as those formed by homogeneous nucleation or those formed by emulsification.

In homogeneous nucleation, a solution of monomers, and a cross-linking agent, is fed into the system and microgel particles form over the course of polymerization. A key requirement for discrete microgel particle formation is that the resultant polymer must be insoluble under the polymerization conditions, as monomers giving soluble polymers under the polymerization conditions will form a macrogel. For example, PNIPAM microgels readily form when the monomer is polymerized in water at $70°C$ because PNIPAM is water insoluble at high temperature [6]. In contrast, acrylamide, a common monomer with a similar chemical structure to PNIPAM, gives a water-soluble polymer at all temperatures, so polyacrylamide microgels cannot be prepared by homogeneous polymerization in water. Polymerization of aqueous acrylamide solutions gives a macrogel [6]. Microgel preparations involving homogeneous nucleation include the following types of polymerizations: emulsion polymerization and surfactant-free emulsion polymerization [7]. In emulsion polymerisation the monomers are dispersed in oil using surfactants which surrounded by an aqueous phase such as water. A water-soluble free radical initiator, which promotes polymerisation, is added and the monomers leave the droplets to polymerise. The dispersed oil drops then act as reservoirs until depleted leaving a suspension of cross-linked particles. However, this process can be undertaken without the need of a surfactant hence, surfactant free polymerisation. In this method the continuous phase must have a high dielectric constant and ionic initiators are used [7] [2]. The resultant charged polymer chains formed during polymerisation act as surfactant molecules and stabilise the growing particles. Both methods have shown to yield very small microgel particles ($\approx 150\,\text{nm}$), however, surfactant free polymerisation is preferred as it eliminates the difficulty of removing excess surfactant molecules [7].

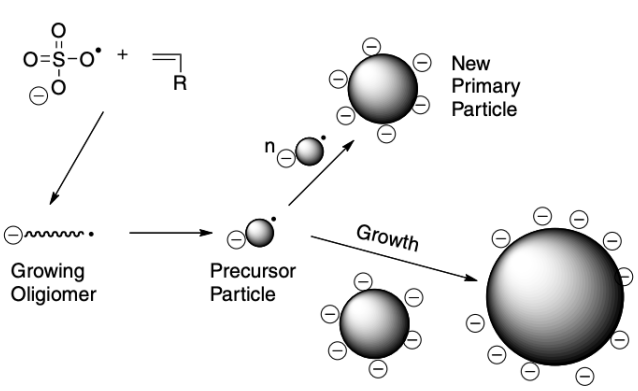

Figure 1.1: *Schematic of microgel formation by surfactant-free emulsion polymerization. Initially, unstable precursor particles aggregate to form new primary particles. At the end of nucleation stage, all new precursor particles are captured by existing stable particles. Taken from [2].*

Microgels generated by emulsification begin with an aqueous pregel solution which is suspended in an oil or brine phase to give a water-in-oil emulsion. The pregel can be either a monomer or polymer solution. When the polymerisation initiates the emulsion droplets undergo a chemical reaction to gel each emulsion droplet. This type of polymerization is often called inverse emulsion polymerization or miniemulsion polymerization [8] [9]. A distinction between these two types of polymerizations is for miniemulsion polymerisation include a solute for the dispersed phase with ultra-low solubility in the continuous phase to prevent Oswald ripening. Whereas for oil-in-water emulsions, the solute is a hydrophobic long-chain alkane, whereas for water-in-oil emulsions, salts provide this function. Figure 1.2 shows the schamtaics of the two distinct gelation mechanisms [2]. The second case illustrated in Figure 1.2 occurs when reaction of the pregel causes new particles to nucleate within the emulsion droplet.

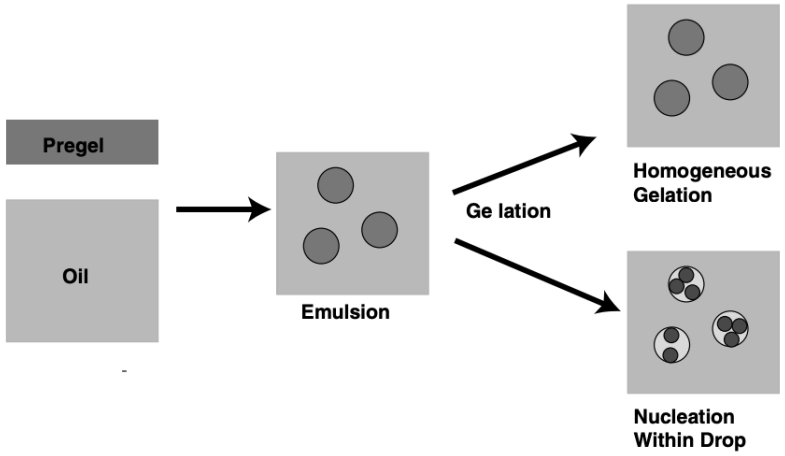

Figure 1.2: *Schematic of microgel formation by emulsification. Taken from [2].*

1.1.3 Composition and Structure

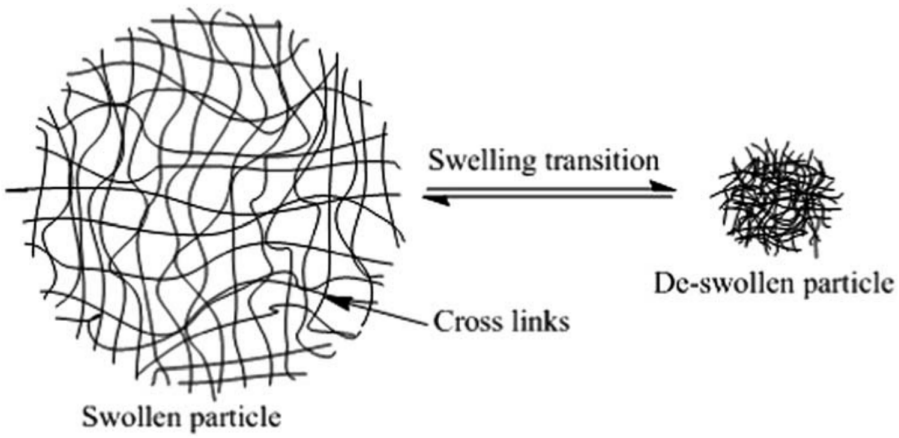

Figure 1.3: *Schematic of a generic microgel particle showing how they can swell and deswell reversibly. Taken from [10].*

Figure 1.3 shows a schematic representation of a generic microgel. Microgels, like other colloids, undergo Brownian motion in suspensions. Highly swollen microgel suspensions are transparent, whereas slightly swollen gel suspensions are milky white like a conventional latex dispersion [2]. Highly swollen particles have a refractive index close to that of water. Thus, swollen microgels scatter little light compared to dispersions of unswollen organic polymers, such as polystyrene. Microgels are very resistant to aggregation as their surfaces often

bear electrical charges and dangling surface chains. High colloidal stability is further illustrated by the ability of freeze-dried or precipitated (ultracentrifuged) microgels to spontaneously redisperse in water [2]. In general, microgels tend to be more colloidally stable in the swollen form where van der Waals attraction is diminished and surface hairs can sterically stabilise the microgel particles

Typical water contents for microgels vary from 10 - 90 wt% depending upon the chemistry of the microgel dispersion. Measuring a microgel's molecular weight is challenging as it is difficult to measure the average dry mass of polymer per particle. Microgel molecular weight can be estimated from a variety of ways including the measurement of the size of the microgels or calculating the effective particle volume fraction from viscosity measurements [11]. As mentioned earlier, microgels typically have short polymer chains extending from the particles' surface. The presence of these chains was postulated in the first PNIPAM microgel publication in order to explain the exceptionally high colloidal stability in concentrated electrolyte. Furthermore, surface chains would provide steric stabilisation [3]. In general, the surface topology of microgels has been poorly described in the literature. In most cases, neither the length distributions nor the density of surface chains is known, however, certain synthesis techniques, such as a living radical reaction, have resulted in uniform chain densities [12]. An example of this involved using living radical polymerisation to grow PNIPAM hairs on a core particle [12]. Virtually all microgels are electrically charged as it is difficult to prepare a nonionic aqueous microgel. The main sources of the electrically charged groups are ionic free radical initiators and/or ionic monomers copolymerised into the polymer network. Two of the popular and well studied microgel systems are the polyelectrolyte and core-shell microgels.

Polyelectrolyte microgels consist of cross-linked copolymer chains bearing ionisable groups which are swollen by water. In polyelectrolyte microgels, it is the osmotic pressure associated with the high translational entropy of the small ions which determines the softness of the individual particles [13]. Research has shown that softness controls most of the flow properties of microgel dispersions and that it is possible to get a desired macroscopic behaviour by tuning the microscopic structure of the individual particle, which is key to many industrial applications. Core-shell microgels are characterised by their distinct heavily cross-linked core which is surrounded by a 'soft', not as cross-linked, corona. The architecture of core-shell microgels has made them plausible candidates for drug delivery vehicles i.e. delivering drugs under certain conditions, such as pH or

by swelling/deswelling [7]. However, in order to understand the behaviour of the microgel system, the behaviour of the polymer building blocks must be considered.

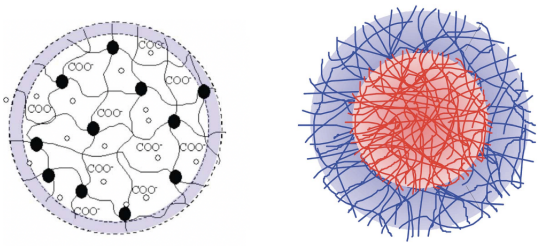

Figure 1.4: *Left: Schematic of a polyelectrolyte microgel in its swollen state. The solid dots represent the cross-links while the unfilled dots are counter-ions and the outer shell is where electro-neutrality is not satisfied. Taken from [13]. Right: Schematic of a core-shell microgel with a highly cross-linked core (Red) and a light cross-linked corona (Blue). Taken from [14].*

Polymers

Polymers are long chain-like molecules made up of repeating sub-units joined together by covalent chemical bonds. The repeating units, which join together to make up a polymer, are known as monomers. Naturally occurring polymers play an essential role in biology such as DNA, which is a polymer composed of monomer units called nucleotides. Other examples include proteins and polysaccharides, which are abundant in everyday life and essential for many biological processes. Since the mid-19th century scientists have been synthesising polymers with a range of applications, resulting in polymeric materials being abundant in everyday life.

One important parameter of polymer chains is their physical size which is partially dictated by the composition. Given the many different configurations polymers can potentially have there are numerous different classifications. Primarily there are two main categories: homopolymers and copolymers. Homopolymers are polymers made up of identical monomers whereas copolymers are made up of at least two different monomers, the latter will be discussed in more detail later. Depending on their composition and the environment, polymer chains can either be stretched-out and rod-like, or tightly packed collapsed bundles. General measures of polymer chains are required in order to classify them. One measure is the contour length (R_c), which is simply the length of the chain measured along its contour. The contour length, however, gives no information on the spatial

arrangement, for this the mean-squared end-to-end distance ($\langle R^2 \rangle$) is required. Mathematically both R_c and $\langle R^2 \rangle$ are represented by the following equations [15],

$$R_c = Na, \tag{1.1}$$

$$\vec{R_N} = \sum_{i=1}^{N} \vec{a_i}, \tag{1.2}$$

$$\langle R^2 \rangle = \langle \vec{R_N} \cdot \vec{R_N} \rangle, \tag{1.3}$$

where N is the number of monomers in the polymer chain, a is the length of one of the monomer units, $\vec{R_N}$ is the vector which connects the ends of the chain and $\vec{a_i}$ is the vector of the i^{th} monomer unit in the chain. The angular brackets indicate that this is an average over an ensemble of possible configurations the polymer has taken.

One of simplest models used for understanding polymer chains is known as the ideal chain model. In this model, long range interactions between monomer units are ignored. Therefore, the $\langle R^2 \rangle$ of an ideal chain is given by,

$$\langle R^2 \rangle = \langle \vec{R_N} \cdot \vec{R_N} \rangle = \left(\sum_{i=1}^{N} \vec{a_i} \cdot \sum_{j=1}^{N} \vec{a_j} \right). \tag{1.4}$$

Assuming all the bond vectors are the same, then $\vec{a_i} \cdot \vec{a_j} = a^2 \cos\theta_{ij}$, where θ_{ij} is the bond angle between i^{th} and j^{th} monomers. Therefore, equation 1.4 can be simplified to,

$$\langle R^2 \rangle = a^2 \sum_{i=1}^{N} \sum_{j=1}^{N} \langle \cos(\theta_{ij}) \rangle, \tag{1.5}$$

where again the angular brackets indicate that the bond angle is being averaged over a number of configurations. A simpler alternative is the freely joined chain model where it is assumed that monomers cannot interact with each other and can rotate freely. If the monomers cannot interact, the polymer configuration is a 3D random walk, there are no correlations between bond angles meaning if $i = j$

the angular term is zero. Therefore, for this model $\langle R^2 \rangle$ is,

$$\langle R^2 \rangle = Na^2. \tag{1.6}$$

However, in practice real polymers cannot rotate freely as monomers can interact influencing the conformations of the molecule. Equation 1.6 can be rewritten to take into account short range interactions by introducing a term known as the characteristic ratio. The characteristic ratio, C_∞, represents the level of interaction between different monomer units of a polymer chain. Each polymer chain has its own distinct C_∞, which is calculated by considering the number of interactions monomers have with their neighbours, but assumes that these reduce on moving along the chain. Therefore, to account for these short correlations equation 1.6 is amended to,

$$\langle R^2 \rangle = Nb^2 = NC_\infty a^2. \tag{1.7}$$

The key result that can be extracted from these models is that the mean end-to-end distance is proportional to the square root of the number of monomers. The results of these models have allowed key parameters of polymers to be quantified and from these results, the spatial distribution of polymers was inferred.

In order to understand how a polymer arranges itself spatially one must look at the Helmholtz free energy of the system. The change in free energy ΔF of an ideal freely jointed polymer chain is,

$$\Delta F = \frac{3k_bTR^2}{2Na} \tag{1.8}$$

where k_b is Boltzmann's constant and T is the temperature. Equation 1.8 reveals that ΔF increases as R, meaning as the polymer is stretched the free energy increases as well as the end-to-end distance. The laws of thermodynamics state that systems will arrange themselves to minimize their free energy. Assuming there are no interactions between monomers, the internal energy of this system is zero meaning that its energy is entirely entropic. Therefore, if the chain is stretched there will be an entropic force which will act to restore the chain back to its ideal size, the restoring force $\frac{dF}{dR}$ is proportional to R. This finding is analogous to the classical spring, however, the difference being that the restoring

force in a spring is energetically driven while for polymers this force is entropically driven. This simple yet powerful result has provided a solid basis for development of other polymer theories, however, it should be noted that these models make numerous assumptions which are not applicable to real polymers.

The first assumption being that these models assume that the conformation of the polymer is completely random. However, for a polymer in a solvent the conformation will be affected by excluded-volume interactions. Excluded-volume interactions occur as one monomer cannot occupy the space of another, therefore, in practice polymers undergo a self-avoiding walk. In order to account for this effect Paul Flory modelled polymers as if the monomers were hard spheres which could move freely like a gas confined in a volume of R^3, where R is the end-to-end distance [15]. This restriction translates to a reduction in entropy of the system, as the amount of configurations are limited. In Flory's approximation,

$$R = N^{3/5} v^{1/5} b^{2/5}, \tag{1.9}$$

where v is the excluded volume per monomer. Comparing to the ideal chain where $\langle R^2 \rangle \propto N^{1/2}$, introducing excluded volume causes chains to swell which becomes significant for large polymer chains. These results have also been confirmed experimentally and with simulations showing that $\langle R^2 \rangle$ is related to the molecular weight of the polymer M_w. $\langle R^2 \rangle$ and M_w are related in the following way:

$$\langle R^2 \rangle = M_w^N. \tag{1.10}$$

N has been found to range from approximately 0.56-0.59, however, $\langle R^2 \rangle$ has been shown to be dependent on the environment the polymer is exposed to [16]. The choice of solvent is crucial when conducting studies of polymers as the interactions between the solvent and monomer units influence the configuration of the molecule. Solvents are classified into three categories: good solvents in which polymer and solvent interactions are favourable causing swelling ($\langle R^2 \rangle \propto N^{3/5}$), poor solvents where polymer-polymer interactions are favoured causing polymer to coil up and theta solvents which are solvents where excluded volume interactions and polymer-polymer interactions balance each other causing chains to follow a random walk ($\langle R^2 \rangle \propto N^{1/2}$). Often studies are carried in theta conditions as polymer chains follow the ideal chain model meaning they are fully extended, poor solvents can even be tuned to act as theta solvents. By varying

the temperature of poor solvents one can cause it to act as a theta solvent, this temperature is known as the theta temperature

Block Copolymers

As mentioned in the previous section, copolymers are polymers which are composed of more than one type of monomer unit. Block copolymers are copolymers in which monomer units are arranged in blocks along the chain. This results in the polymer chain being composed of distinct blocks of monomers which repeat along the molecule. An interesting feature of block copolymers is their ability to separate, under certain conditions, leading to the formation of domains with different microstructures. The self-assembly of block copolymers can be tuned by varying parameters such as the types of blocks, the size of the blocks or their volume fractions. The tendency for different blocks to separate is quantified by Flory's interaction parameter, χ [15]. When considering a mix of polymers and polymer-solvents, χ accounts for the interactions between different polymers or polymer-solvent interactions and has general form of,

$$\chi = \frac{A}{T} + B, \tag{1.11}$$

where T is the temperature and A and B are material-dependent constants [15]. Generally, when mixing two polymer chains, the interaction energy is $\chi k_b T$ per monomer, in block copolymers these chains are attached, meaning that likelihood of two chain separating is proportional to χN, where N is the degree of polymerisation.

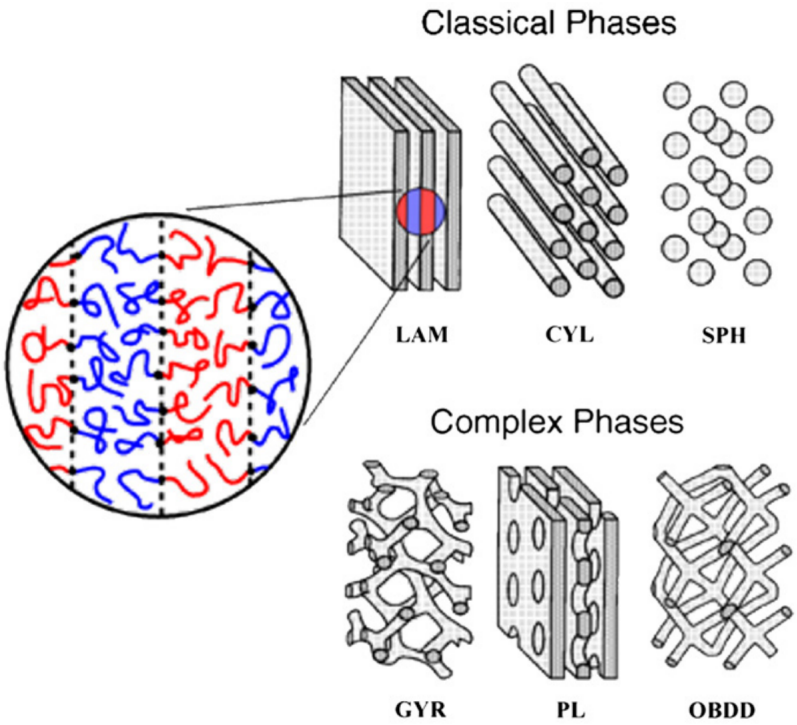

Figure 1.5: *Schematic diagram of phases of block copolymers. LAM-lamellar, CYL- cylindrical, SPH-spheres, GYR-gyroid, PL-perforated lamellar and OBDD-ordered continuous double diamond. Taken from [17].*

Given the variety of structures which block copolymers can assemble into their uses are just as varied. Typical applications involve implementing them into systems which go through compositional or environmental change, leading to the system reorientating. This allows materials to be tuned so they respond to specific stimuli. An example of such materials would be stimuli responsive pharmaceuticals, by using block copolymers pharmaceuticals can be tailored to respond differently in different conditions such as temperature and pH [18]. The responses could include the release of materials which were embedded in the system, similar to how emulsions could release materials [19] [20].

1.2 Microgels as Rheology Modifiers

1.2.1 Rheology of Dispersions

Basics of Rheology

The rheological profiles of colloidal dispersions has been widely studied for many years due to their relevance to many industrial products. Food, pharmaceuticals and cosmetics are a few of the many examples of products which rely on the knowledge of colloidal rheology. The rheology of suspensions is governed by the type of dispersant, such as polymer molecules or hard particles. Furthermore, the interactions between the colloids are fundamental to understanding the bulk properties of materials.

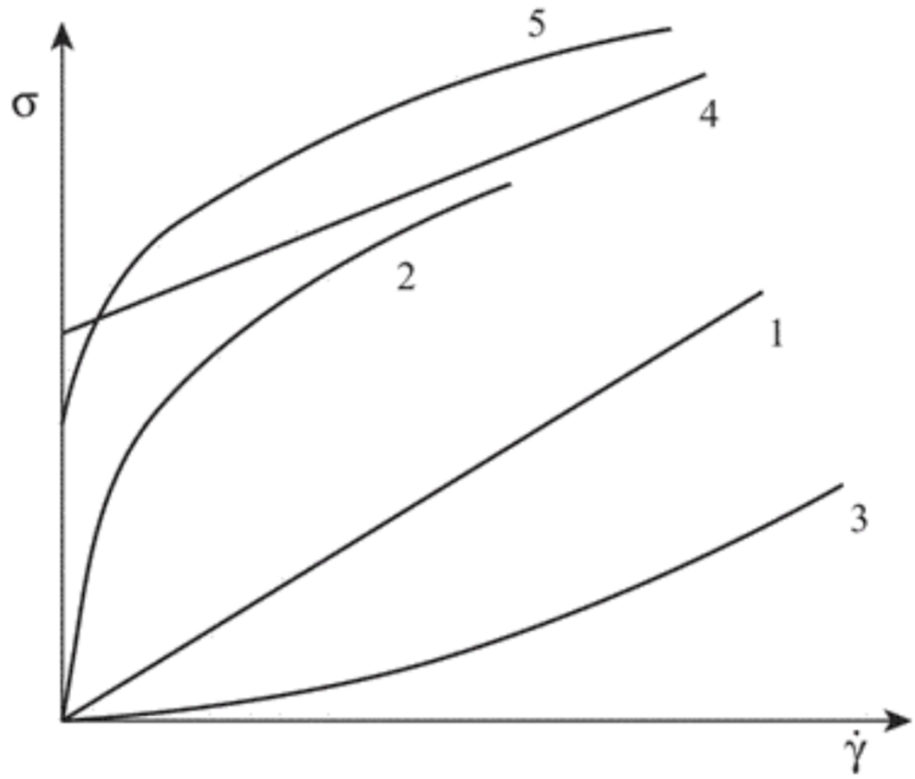

Figure 1.6: *Schematic showing the variations of how stress (σ) varies as a function of shear rate ($\dot{\gamma}$). The curves show the profiles of Newtonian (1), shear thinning (2), shear thickening and yield stress materials (4 and 5). Taken from [21].*

For most suspensions, the shear stress in simple shear flow is not proportional to the shear rate. Such systems are non-Newtonian whereas for Newtonian materials the shear stress is proportional to the shear rate. Non-linear relations between shear stress and shear rate, as represented by curves 2 and 3, in Figure 1.6 often result in linear plots in a log-log representation. This means that the relation between shear stress and shear rate can be described by a power law,

$$\sigma = k\dot{\gamma}^n, \tag{1.12}$$

where n, the power law index, which is the slope of this relation in a logarithmic plot, and k is the consistency index. Such materials that follow this relation are known as the power-law fluids. If the flow index is $n < 1$ the material is known as shear thinning, while $n > 1$ describes shear thickening materials.

For suspensions that can be described by the power-law fluid relation the shear stress decreases to zero as the shear rate tends to zero. This condition defines a fluid, which by definition cannot be in equilibrium under a non-zero shear stress. However, for many materials the stress tends to a finite value when the shear rate is systematically decreased (curves 4 and 5 in Figure 1.6). The high shear limit can still exhibit a Newtonian behaviour. Curve 4 describes a Bingham body:

$$\sigma = \sigma_y + \eta_{pl}\dot{\gamma}, \tag{1.13}$$

where the σ_y is the yield stress and η_{pl} is the plastic viscosity. When the high shear limit is a power law rather than Newtonian, the Herschel-Bulkley model is often deployed:

$$\sigma = \sigma_y + k\dot{\gamma}^n. \tag{1.14}$$

A third model is occasionally applied to suspensions with a yield stress:

$$\sigma^n = \sigma_y^n + k\dot{\gamma}^n \tag{1.15}$$

For $n = 1/2$ this becomes the Casson equation, which is often used to model the flow of blood, a biological suspension [21]. The power law in these relations can be expressed as $(k\dot{\gamma})^n$ or $k\dot{\gamma}^n$. The form $(k\dot{\gamma})^n$ is often preferred as k then has

dimensions of inverse time while for the case $k\dot{\gamma}^n$ the dimensions of k depend on the value of n. In addition to a yield stress, some suspensions display further complexity, such as a viscosity which is not a function of just the instantaneous shear rate. Shaking or shearing the sample causes a gradual decrease in viscosity, which recovers when the material is at rest. A reversible, time-dependent viscosity defines thixotropy. It is encountered in some common products such as tomato ketchup and latex paint [21].

Materials described by the equations 1.12-1.15 are referred to as viscoelastic materials. A viscoelastic material combine properties of elastic solids with those of viscous fluids. The stresses in an elastic body depend on how far the actual shape of the material deviates from the non-deformed equilibrium state, irrespective of the time scale of the deformation. Whenever stresses have been applied viscoelastic material always returns to the non-deformed state when the stresses are released. Therefore, ideal elastic materials can be considered as having a perfect memory for their non-deformed reference configuration. However, a liquid has no memory at all, so that when the shear stress is released it remains in its last position. Energetically, the work done in an elastic deformation is stored in the material as potential energy and can be totally recovered when the material returns to its non-deformed state. A suitable procedure for testing the nature of a material is to suddenly, or very rapidly, apply a shear deformation which is then held constant. For a perfectly elastic solid, the resulting stress would remain constant indefinitely. In a liquid the stress would be very high when a deformation is applied rapidly, because the shear rate would be extremely large. After the rapid deformation stops, there would be no flow anymore and the stress would immediately drop to zero. In a viscoelastic material the stress would gradually decay in time, a phenomenon called stress relaxation. If the viscoelastic material is a solid, the stress would relax only partially and would level off at a finite value. A typical probe of the elastic character and viscous character is to impose a small oscillatory strain. In this test, materials can be described by a kind of generalization of Hooke's law, using a constant shear modulus G^* which does not assume stress and strain to be in phase:

$$\sigma = G^*\gamma \tag{1.16}$$

G^* can be decomposed into two components: the in-phase compnent G' which describes the elastic component of the stress known as the storage modulus and

the out-of-phase component G'' represents the viscous energy which is called the loss modulus,

$$\sigma = (G' + iG'')\gamma. \tag{1.17}$$

This proportionality between stress and strain only applies in the linear region i.e. at sufficiently low strains. The names of the components refer to what happens with the corresponding mechanical energy. In a purely elastic deformation, no energy is lost. It is completely stored as potential energy during the deformation and is totally recovered when the deformation is reduced to zero. This will be explored in more detail in Chapter 2.

Polymer Suspensions

For polymer solutions, the rheology is primarily dictated by the conformation of the individual polymer chains, however, as the concentration increases polymer-polymer interactions become more important. The conformation of polymer molecules is determined by the type of solvent they are subjected to. When concentrated enough polymers form gels. Gelation is defined as the conversion of a liquid to a highly disordered solid by forming percolating networks between molecules or particles in the liquid. These networks can form through one of two mechanisms: physical cross-linking or chemical cross-linking. Physical cross-linking occurs due to particles or molecules interacting without permanently bonding to each other, such interactions could include electrostatic attractions. Chemical cross-linking occurs when the particle or molecules permanently covalently bond to one another.

In order for cross-linking to occur, the polymer chains need to be in close proximity to one another, which occurs once a critical concentration is reached. The critical concentration and is defined as the concentration at which the polymers start to interact with one another (overlap). One way to identify this concentration is to look at how the viscosity of the material changes as a function of concentration. As the viscosity is a measure of resistance to flow, a change is expected as you reach the overlap concentration; the polymers will interact changing the viscosity. Typically, the creation of polymer networks leads to an increase in viscosity as the network strengthens the gel.

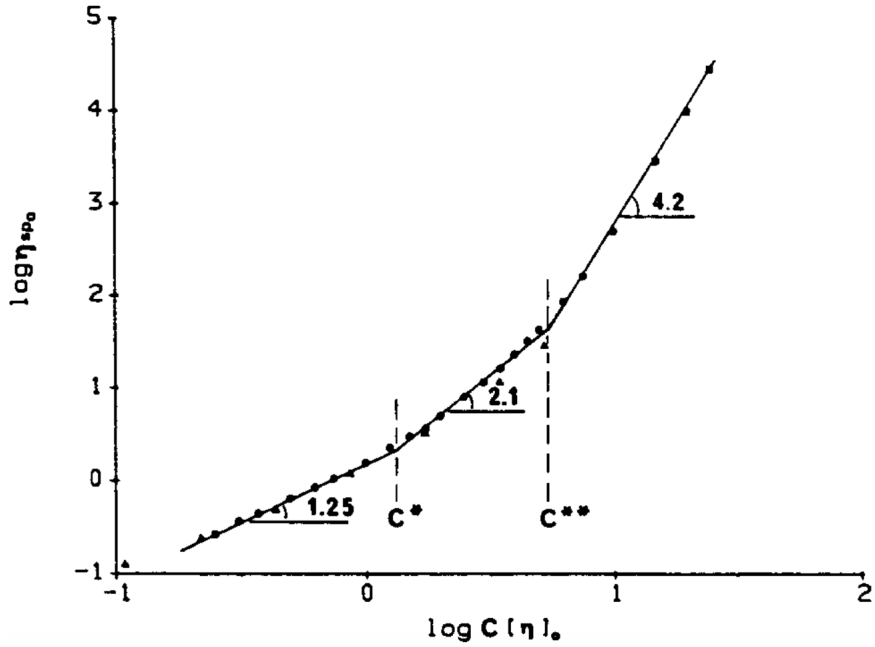

Figure 1.7: *A log-log representation of how the viscosity (η) of xanthan gum gels depends on the concentration of xanthan gum, with the critical concentrations marked. Taken from [22].*

Figure 1.7 shows the the relation between viscosity and concentration for xanthan gum, a physical cross-linking polymer. Xanthan gum is a naturally occurring polymer obtained from bacteria commonly added to food products to thicken them or prevent the separation of ingredients [22]. The critical concentration $C_* = 3 \times 10^{-4}\,\mathrm{g/ml}$ has been marked on the graph and is identified by the change in gradient observed. Cuvelier *et al.* results also indicate that a second critical concentration $C_{**} = 1 \times 10^{-3}\,\mathrm{g/ml}$ exists with further analysis suggesting a restructuring of the network. For example, at C_* the polymers are starting to interact sufficiently enough to increase the viscosity, however, at C_{**} secondary interactions such as restructuring or entanglements of multiple chains are occurring [22]. These findings indicate that when formulating products it is crucial to consider the characteristic properties of polymers, such as flexibility and size, as these will influence how the polymers interact. There are primarily three main structures which physical-crosslinks can take: helical, microcrystallite and nodular. Helical structures arise when polymer chains wind around each other forming structures which resemble helices, this is observed in gelatin another naturally occurring polymer thickener [23] [24]. Microcrystallites are structures where polymers form locally organised domains which display semi-crystalline structures [25]. Nodal structures or domains form as a result of mixing polymers

with distinct blocks, therefore, when brought together the polymer's structure is determined via similar domains interacting i.e. hydrophobic blocks interacting with other hydrophobic blocks [26].

Colloidal Suspensions

Similar to polymer solutions the rheology of colloidal particle suspensions is governed by the interactions between individual particles. For freely diffusing spherical particles the mean square displacement $\langle(\Delta r(t))^2\rangle$, where $r(t)$ is the distance a particle has diffused, by the time t is given by,

$$\langle(\Delta r(t))^2\rangle = 6Dt. \tag{1.18}$$

The coefficient D is the Einstein-Smoluchowski diffusivity, which for a spherical colloid is,

$$D = \frac{k_b T}{6\pi\eta R}, \tag{1.19}$$

where k_b is Boltzmanns constant, T is the temperature of the system, η is the viscosity of the fluid and R is the colloid's radius [21]. Upon increasing the concentration the particle-particle interactions become more prominent and D decreases. As the concentration of colloids increases the effective phase volume of n colloids $\phi = 4\pi n R^3/3$ also increases and this in turn determines the rheology of the suspension. For dilute suspensions ($\phi < 0.2$) the relative viscosity η_{rel} (the relative viscosity is given as $\eta_{rel} = \eta/\eta_s$, where η and η_s are the viscosities of the suspension and solvent respectively) can be expressed as,

$$\eta_{rel} = 1 + 2.5\phi + 5.9\phi^2 + ... \tag{1.20}$$

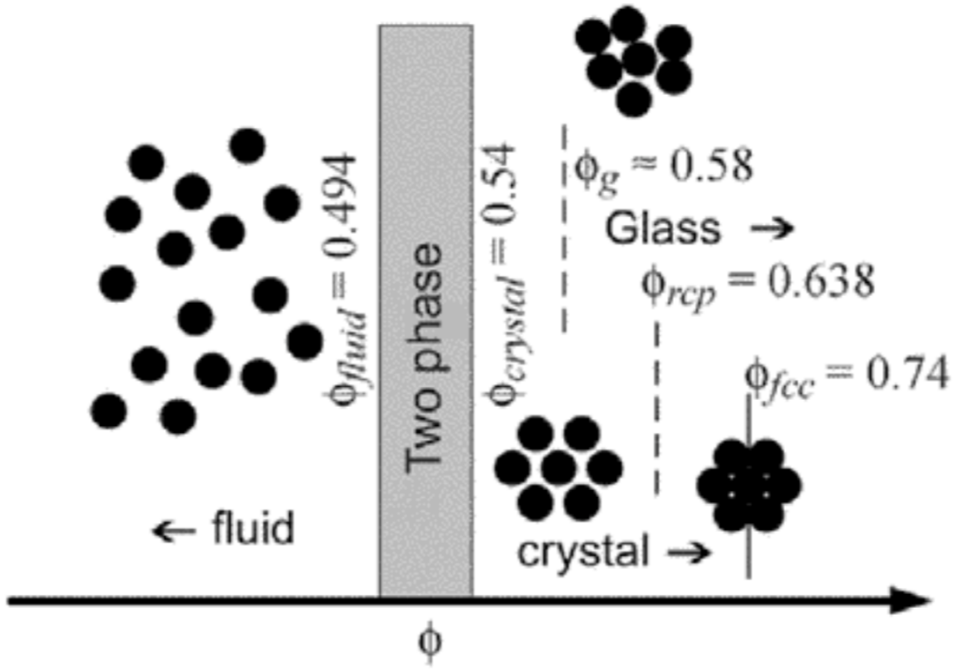

Figure 1.8: *Schematic of the hard sphere dispersion phase diagram showing fluid-crystal phase transition, glass transition, random-close packing and crystalline maximum packing limits. Taken from [21]*

As stated this Einstein approximation is accurate up to $\phi_{eff} = 0.2$, beyond this particle interactions become more dominant. For $\phi_{eff} > 0.2$, multi-particle collisions increase in frequency and hence higher order terms become more important. Krieger and Dougherty proposed a semi-empirical correlation for effective viscosity of solid-liquid suspensions which is valid for full range of particle volume fraction as follows [27]:

$$\eta_{rel} = \left(1 - \frac{\phi}{\phi_m}\right)^{[\eta]\phi_m}, \tag{1.21}$$

where ϕ_m is the maximum particle volume fraction at which flow can occur and $[\eta]$ is the intrinsic viscosity and varies according to the shape of the particles, which is 2.5 for spheres. ϕ_m varies substantially for different systems e.g. for hard spheres $\phi_m = 0.635$ whereas for emulsions $\phi_m = 0.71$. Figure 1.9 shows qualitatively how η_{rel} behaves as a function of ϕ_{eff} for different suspensions.

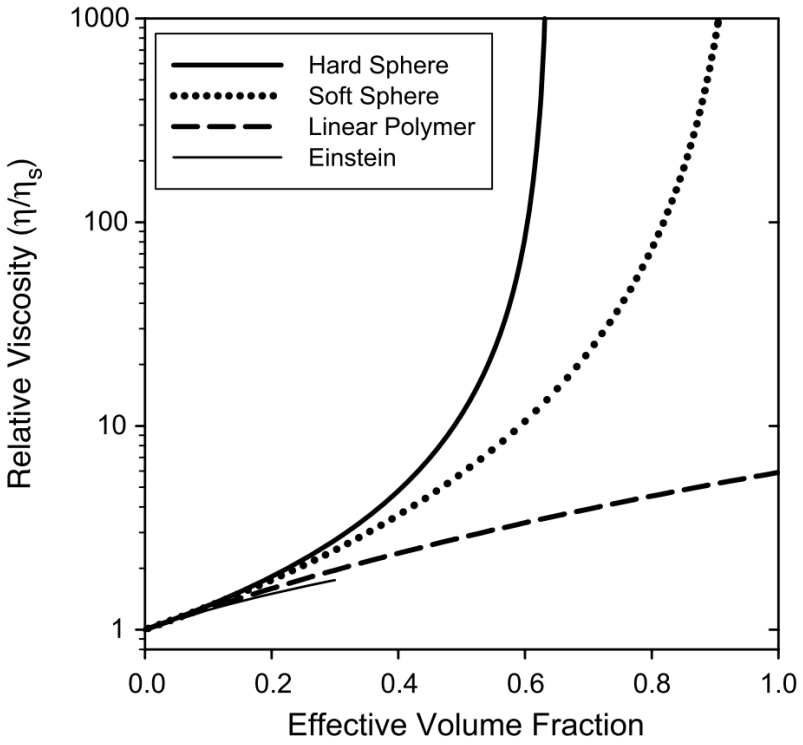

Figure 1.9: *Comparison of how the Kreiger Dougherty equation,* $\eta_{rel} = \left(1 - \frac{\phi}{\phi_m}\right)^{[\eta]\phi_m}$*, varies for different suspensions. Taken from [2].*

1.2.2 Flow Behaviour of Microgel Suspensions

Given that microgels are soft particles composed of cross-linked polymer networks their rheological profile has similarities to both hard particles and single polymers [11]. Unlike polymer solutions, microgels suspensions do not have the non-linear elastic and extensional properties, however, they do show an increase in viscosity of suspensions by forming shear thinning networks at relatively low solids content.

The combination of properties result in a unique flow behavior and textural response displayed by microgel suspensions, frequently leading to favorable consumer responses to products [2]. At high phase volumes where particles are in contact and they are confined giving longer relaxation times. Concentrated microgel suspensions typically behave as a soft glass with a response that depends on the particle properties, while at lower concentrations they flocculate to form a soft gel where the properties are dependent on the colloidal forces between

particles [28]. Furthermore, microgels have the potential to incorporate solvent into their structure as they do not have a well-defined boundaries since the degree of cross-linking can vary through an individual particles. Microgel suspensions exhibit strong shear-thinning behaviour, whether they are in the form of a soft glass or a soft gel. They possess a viscosity at high shear rates that is typically lower than that found for a polymeric system with similar low-shear viscosity.

1.2.3 Effect of Phase Volume and Concentration

For dilute suspensions ($\phi < 0.2$) by using the Einstein relation and measuring the variations of relative viscosity, the volume fraction of colloids can be determined. However, as microgels have properties of both hard colloids and polymers, estimating their ϕ is more difficult. This is mainly due to the swelling ability of microgels, since they incorporate solvent into their structure. Just as the η of polymer fluids is related to the molecular weight and to the conformation of the molecules, η for microgels is related to how swollen they are in the suspension. The Batchelor equation for the contribution of hard spheres (to second order) to the viscosity is given by,

$$\eta_{rel} = 1 + 2.5\phi + 5.9\phi^2. \tag{1.22}$$

In order to account for the swelling ability of the microgels ϕ_{eff} can be expressed as $\phi_{eff} = kc$, where c is the concentration of microgel and k is the swelling factor [29]. This approach allows the determination of the volume fraction at any particular weight concentration provided k is independent of concentration. k can also be used to evaluate the effects of external stimuli such as solvent quality, pH or temperature on the swellability of the microgels. The Batchelor equation becomes,

$$\eta_{rel} = 1 + 2.5kc + 5.9(kc)^2, \tag{1.23}$$

this approach has been found to be a reasonable prediction of the viscosity of microgel suspensions for $\phi_{eff} \approx 0.2$ [30]. At higher concentrations ($\phi_{eff} > 0.2$), the influence of multi-body interactions and crowding effects must also be accounted for. For hard spheres, the Krieger–Dougherty model, $\eta_{rel} = (1 - \phi/\phi_{cp})^{-\eta\phi_{cp}}$ has been widely used to describe the rheology of microgels at

high phase volumes. However, ϕ_{cp} is difficult to define for microgels given their ability to swell and deform, whereas for hard particles ($\phi_{cp} \approx 0.635$) and emulsion drops ($\phi_{cp} \approx 0.71$) it is well defined. The viscosity can deviate from these rheological models at high phase volumes ($\phi_{eff} > 0.5$) if the specific volume is not constant with concentration. This occurs due to microgel-microgel interactions and interparticle forces become more prominent. In this situation, effects such as particle deformation, compression, solvent loss due to osmotic deswelling, interpenetration between microgels, and steric confinement where swelling is limited by the amount of available solvent can lead to the the specific volume of the microgels decreasing with increasing concentration. This will in turn lead to a deviation of the rheological response from that predicted by the models discussed above, and alter the effective phase volume of the microgels, $\phi_{eff} = kc$. Senffet *et al.* calculated master curves, with k fixed constant, by analysing dilute suspensions of temperature-sensitive PNIPAM and core-shell latex particles using rheology and light scattering [31]. Deviation from the hard sphere behavior was found for effective phase volumes above about $\phi_{eff} \approx 0.5$, which resulted in a lower viscosities than predicted for hard spheres. This effect is attributed to the fact that at high volume fractions deformation/compression of the neutral PNIPAM microgels start to have an effect. Similar observations on the influence of particle compression at high concentrations have been made for other colloidal microgels and core–shell or sterically stabilized particle suspensions [11] [32]. For microgel systems with a highly cross-linked core and a less dense outer corona, the viscosity was found to be considerably lower than for hard spheres and interpenetration between microgels allowed the effective volume fraction to exceed unity (i.e., $\phi_{eff} > 1$). The polymer architecture of such systems closely resembles that of star polymers, with low arm density, and as such they are referred to as 'star-like' microgels.

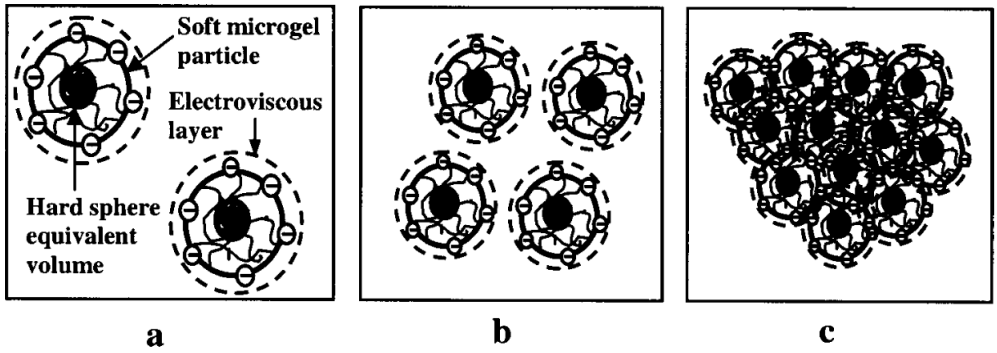

Figure 1.10: *Schematic of increasing microgel crowding which illustrates how the swelling factor k changes as the centre-to-centre distance between particles decreases. Taken from [29].*

Studies have also investigated the rheology of microgel suspensions with k not fixed i.e. so the size of the microgels is not constant throughout the experiment due to swelling/deswelling [29]. As concentration of microgels increases, as $\phi_{eff} \rightarrow 1$, the interparticle distance decreases between the microgels, causing the deviations from the hard colloid rheological models. Tan *et al.* investigated the rheology of a series of aqueous suspensions containing acrylate-based charged colloidal microgels (e.g., methacrylic acid-ethyl acrylate (MAA-EA) cross-linked with diallyl phthalate) in different conditions such as pH and salt [29]. Tan *et al.* found that for a critical particle concentration, the concentration of free counter-ions in the solution can be large enough to induce osmotic de-swelling of soft particles, resulting in the shrinkage of the particles. Figure 1.10 shows a representation of the changes in k, where k should decrease with increasing microgel concentration. As microgel particles are filled with large amounts of solvent they are soft and porous. In the dilute solutions, interparticle interaction is absent and k remains constant. With increasing concentration, the interparticle distance between microgel particles is reduced and the concentration of free counteions in the solution can be large enough to induce an osmotic deswelling of soft particles. Increasing interparticle interactions causes the microgel to shrink, resulting in a corresponding decrease in k, until it approaches the hard sphere limit described by the black core (see Figure 1.10). This consideration of the changing k value results in in the maximum packing limit, which for hard particles is 0.635, can increase to 1.5 for some soft sphere systems. The influence of osmotic deswelling was calculated and quantified for microgel suspensions by Cloitre *et al.*, and following this approach Tan *et al.* utilised an ion specific electrode to show that the free counterions increased with increasing microgel concentration

[13] [29]. This resulted in stronger osmotic deswelling and confirmed that the specific volume k decreases with increasing concentration. In addition, osmotic pressure exerted by counterions in the solvent within these microgels helps to maintain particle conformation [13].

1.2.4 Viscoelascity of Microgel Suspensions

When microgels are very concentrated, and in close proximity ($\phi_{eff} > 0.5$), the linear viscoelastic response depends strongly on the individual particle modulus, the interparticle distance between neighbouring particles and on the microstructure. Microgel deformation gives rise to strong repulsive interactions [33], and a general expression can be formulated for the high frequency plateau modulus of monodisperse spherical particles as a function of the interaction potential and pair correlation function using statistical mechanics [33]:

$$G = Nk_bT + \left(\frac{2\pi N^2}{15}\right)\int_0^\infty g(r)\frac{d}{dr}\left[r^4\left(\frac{dV(r)}{dr}\right)\right]dr, \tag{1.24}$$

where k_b is the Boltzmann constant, N is the microgel number density, $g(r)$ is the radial distribution function, $V(r)$ is the pair interaction potential and $dV(r)/dr$ is the force that particles exert on one another as a function of their center-center separation, r. $g(r)$ is approximated as a delta function centred at the nearest neighbour, which was approximated from studies of electrostatically-stabilized concentrated polystyrene system, which results in a lattice-like microstructure [34]. For this case, equation 1.24 can be simplified to,

$$G \propto \frac{1}{r}\left(\frac{\partial^2 V}{\partial r^2}\right). \tag{1.25}$$

Assuming that the interparticle distance d is related to the closest packed volume fraction ($r^3 = d^3(\phi_{cp}/\phi_{eff})$, and the interparticle potential is of the form $V \propto 1/r^n$, then equation 1.25 becomes $G \propto \phi_{eff}^m$. The power law exponent is given by $m = (n/3) + 1$ and although this approach neglects hydrodynamic interactions and an osmotic term, it has been found to adequately describe experimental data for a range of different concentrated microgel suspensions [35] [36].

The Hertz Model, which states that the deformations are related to the particle elasticity, is often applied to understand the deformation forces in concentrated

microgels [37]. The Hertzian pair potential given as a function of the shear elastic modulus inside the particles (G_p), the Poisson ratio (v) and the radius of the particle (R_0) is as follows,

$$V(r) = \left(\frac{32}{15}\right) R_0^{1/2} \left(R_0 - \frac{r}{2}^{5/2}\right) \frac{G_p}{1-v}. \tag{1.26}$$

Now assuming that non-central forces such as friction and adhesion are negligible in the case of highly swollen microgels, due to the particles soft nature meaning only nearest neighbours interactions are relevent, G of the suspension can be expressed as a function of G_p [33]. Starting with equation 1.24 and taking $g(r)$ to be a delta function and taking the thermal contribution, Nk_bT to be negligible results in,

$$G = \frac{\phi_c z G_p}{5\pi(1-v)} \left[(\phi_r^{2/3} - \phi_r^{1/3})^{(1/2)} - (\phi_r - \phi_r^{2/3})^{3/2}\right], \tag{1.27}$$

where z is the number of nearest neighbors and the reduced packing fraction is given by $\phi_r = \phi_{eff}/\phi_c$. This model was found to predict essential features of a number of microgel systems, including Sephadex, with the result shown in Figure 1.11 [33]. Such features include the prediction of a rapid increase in the shear modulus at a critical concentration followed by a levelling off at higher concentrations, as well as an overall dependence on particle modulus. After this levelling out of G, the gradient beyond ϕ_c can be used to extract more details of the concentrated microgel network. For a macroscopic, continuous gel, which is approximately the case for highly concentrated microgel networks, theory of rubber elasticity predicts $G \approx G' \approx (c_p/N)k_bT$, where c_p is the critical concentration of microgels and N is the number of monomers per crosslink which is a measure of the microgels stiffness [38].

At extremely high concentrations, where $\phi_{eff} > 1$, microgels continue to deswell and the elasticity of the suspension scales with the elasticity of the intraparticulate material. Under such conditions, it is anticipated that the microgel suspension behaves like a macroscopic gel in terms of its elasticity. However, it is not necessarily a universal response since microgels do not behave as bulk macroscopic gels; they can retain their identity as single particles even at very high effective phase volumes.

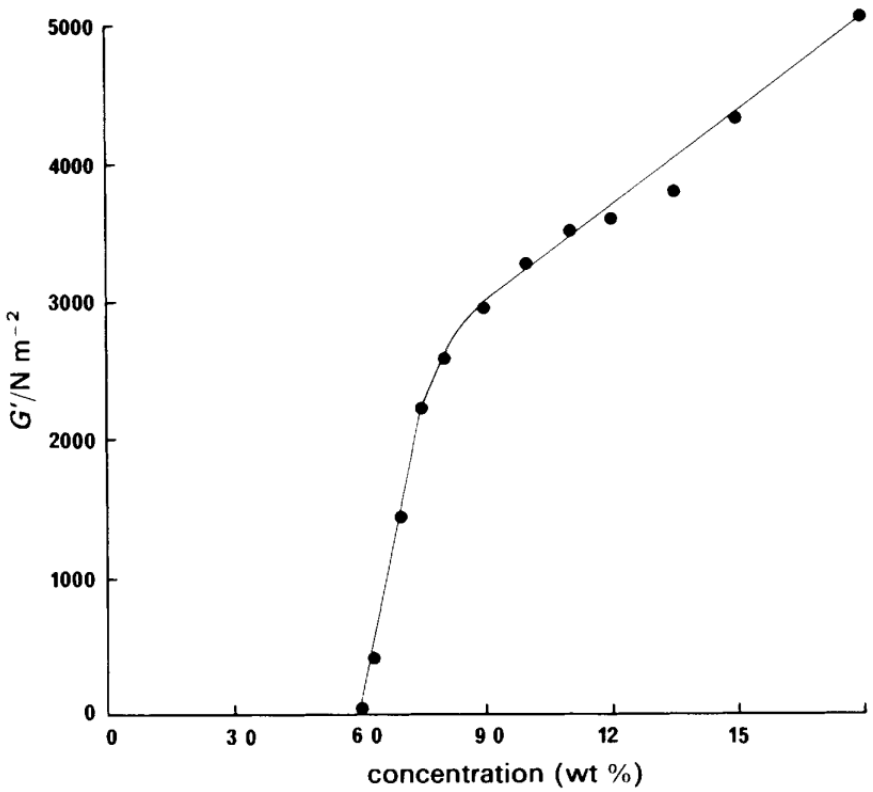

Fig. 3. Dependence of storage modulus G' on concentration of Sephadex G100S at 0.25 Hz.

Figure 1.11: *Variations in the storage modulus (G') calculated as a function of concentration Sephadex G1005, at* 0.25 Hz. *Taken from [33].*

1.3 Microgels as Emulsifiers

1.3.1 Traditional Emulsifiers

Surfactants

A surface active agent or surfactant is a molecule which has one part which is hydrophilic (water soluble) and one part which is hydrophobic (oil soluble). Surfactants act to stabilise emulsions due to their amphiphilic nature, as they localise on the interface between phases. By gathering on the interface between the two components, this results in a decrease in interfacial tension. As

the interfacial tension decreases, the energy cost to form a spherical droplet $\Delta E_{interface}$ of radius R which is given by,

$$\Delta E_{interface} = 4\pi R^2 \gamma, \tag{1.28}$$

where γ is the interfacial tension between the two phases, in turn decreases. Surfactant-stabilised emulsions are commonly included in systems to introduce hydrophobic species, which are to be released when the systems are perturbed or subject to enviromental changes [39]. Perturbations such as shearing or mixing can disrupt and destabilise emulsions, leading to phase inversion and delivery of encapsulated material [40] [41]. The dynamic nature of surfactants is due to the adhesion energy of surfactant to an interface ΔE_{adh} being low. The ΔE_{adh} of a spherical particle to an interface can be expressed as,

$$\Delta E_{adh} = 4\pi\gamma R_h^2 (1 \pm \cos\theta)^2, \tag{1.29}$$

where R_h^2 is the hydrodynamic radius of the particle and θ is the contact angle between the particle and the interface. The sign inside the brackets is positive or negative depending on whether the particle is being desorbed into bulk $(-)$ or into the droplet phase $(+)$ phase. Wheras surfactant adsorption is a dynamic equilibrium, meaning the free energy gain is comparable to the entropy change of the system. Therefore, changes in temperature or in composition can cause surfactants in systems to reassemble into different structures or destablise [42] [43] [44].

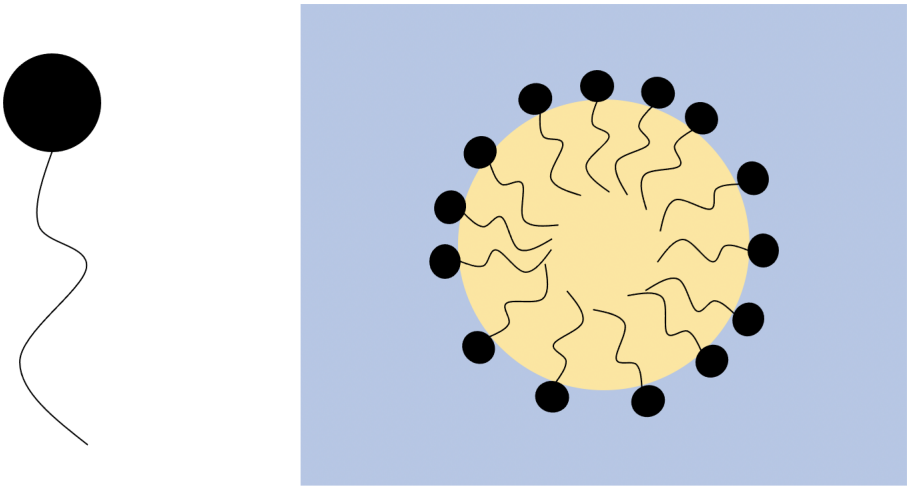

Figure 1.12: *Schematic of a surfactant molecule with a hydrophilic head group and hydrophobic tail group stabilising an oil droplet in water.*

Particles

Particle-stabilised or Pickering emulsions are widely used alternatives to surfactant stablised emulsions [45]. For particles with a size of a few tens of nanometres, this energy takes values of the order of $1000\,k_bT$ for contact angles that are not close to 0° or 180° [46].

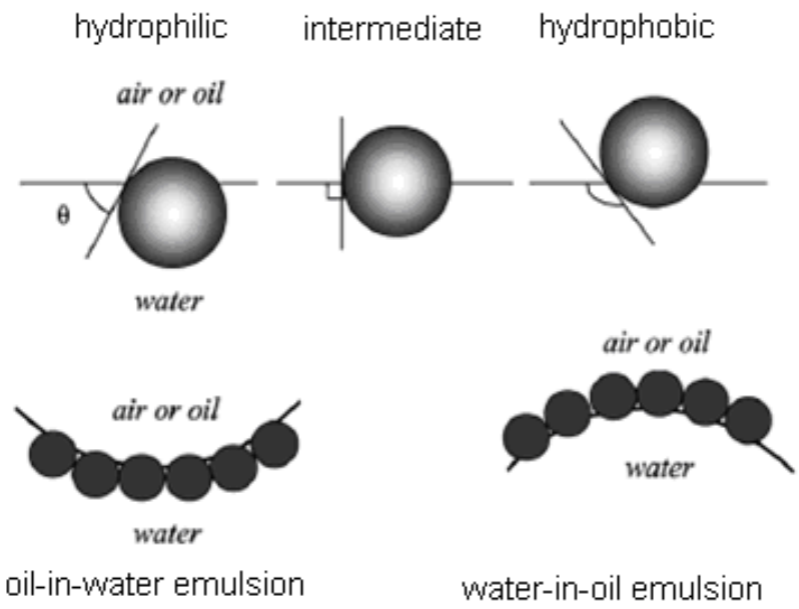

Figure 1.13: *Schematic of particles wetting an interface at various contact angles, θ. Taken from [47].*

For bigger colloids, this energy becomes even larger and hence the adsorption can be considered as irreversible. This situation is in strong contrast to that of surfactant molecules which, due to their small desorption energies of the order of $1 - 10k_bT$, can desorb on a relatively short timescale and hence cannot always completely preclude instability events. Particle-stabilised interfaces are also much more rigid than surfactant-stabilised ones due to the dense packing of adsorbed particles. Such rigidity may confer applicable benefits, e.g., enhancing the mouth feel of low-fat foods [48]. However, this rigidity also leads to buckling under stress which is undesirable as it may lead to the leakage of emulsion drops [49] [50] [51] [52] [53]. The buckling phenomena is characterised by of the wrinkling of the surface of a particle-stabilised drop whose volume has decreased [54] [55]. This buckling can be a limiting factor for the application of Pickering emulsions. Furthermore, particle-stabilised emulsions have also been shown to be destabilised under shear, this again being the result of the stiff particle-laden interfaces being unable to rearrange as an emulsion deforms under flow [56] [57].

1.3.2 Microgels at Interfaces

The polymer-colloid duality of microgel particles makes them interesting: the fact that they are particles makes them adsorb very strongly to the interface, however, their polymeric charcter means they can tuned to interact. This combination of properties makes microgel particles ideal candidates for preparing emulsions with tunable stability [58]. Owing to these attractive properties, in particular PNIPAM (based) particles at fluid interfaces have been extensively studied in recent years. Several studies were performed and the suitability of PNIPAM as an emulsifier has been demonstrated [58]. The subsequent particle-laden interfaces are elastic similar to particle-laden interfaces. However, the kinetics of adsorption and thermodynamics of the interactions between microgel particles differ due to the difference in rigidity and their intrinsic swelling ability [59].

Adsorption Kinetics of Microgels

Several experimental studies into particles adsorbing at fluid–fluid interfaces have been performed, most of them with stiff colloids and a few with soft microgel particles. It is experimentally established that an air–water or oil–water interface is negatively charged [60] . Therefore, depending on the ionic strength, negative particles adsorb either very slowly or not at all, whereas positively charged particles adsorb readily [61]. In physical modelling of the adsorption kinetics of microgels, a distinction is usually made between diffusion controlled transport where the interface is bare, which occurs in the initial stages of adsorption, and adsorption to microgel-laden interfaces, which occurs during the latter stages of adsorption. This approach is similar to that of adsorbing surfactants, as presented for example by Ward and Tordai [62]. Briefly, in the absence of external flow fields, the transport of particles is governed by Fickian diffusion. The mass transport rate can be expressed as,

$$\frac{\partial c}{\partial t} = D\frac{\partial^2 c}{\partial x^2}, \tag{1.30}$$

where c is the bulk concentration, D is the Stokes-Einstein diffusion coefficient of the microgels and x is the distance to the interface. Assuming initially the interface is bare, $\Gamma(0) = 0$ where $\Gamma(t)$ is the time dependent surface concentration, and a uniform concentration $c(x, 0) = c_\infty$ in the bulk liquid, the boundary

condition can be expressed as,

$$\frac{\partial \Gamma}{\partial t} = D \left[\frac{\partial c}{\partial x} \right]_{x=0}. \tag{1.31}$$

Assuming the absence of an adsorption barrier and an interfacial area that is so small that even the maximum adsorption would not significantly deplete particles from the liquid, i.e. $c(\infty, t) = c_\infty$, Equations 1.31 and 1.32 result in the well known expression of Ward and Tordai [62]. In case of irreversible adsorption, $\Gamma(t)$ can be expressed as,

$$\Gamma(t) = 2c_\infty \sqrt{\frac{Dt}{\pi}}. \tag{1.32}$$

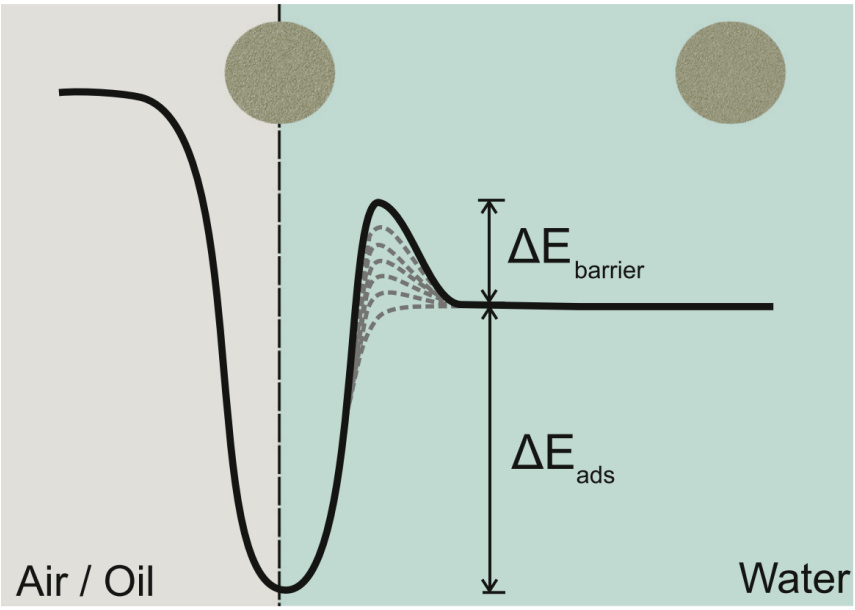

Figure 1.14: *Schematic of a particle adsorbing to an interface showing the energy barrier of adsorption (ΔE_{ads}) which increases as more particles adsorb to the interface (increasing by $\Delta E_{barrier}$). Taken from [58]*

Until now it has been assumed that the particles do not have to cross an adsorption barrier, the description has to be extended to account for this. Figure 1.14 is a schematic of the energy landscape associated with the adsorption process considering the influence of the adsorption barrier. Electrostatic interactions of particles are incorporated in an exponential term, while the effect of an area that is

occupied by already adsorbed particles is taken into account by a linear term [63]. This approach is similar to that of Adamczyk and co-workers who study the role of electrostatic interactions in the adsorption of particles on solid–liquid interfaces [64] [65]. Several of the mentioned studies into interfacial particle adsorption are performed by measuring the dynamic interfacial tension using axisymmetric drop shape analysis [66] [67]. From such measurements there have been initial decay in γ that is proportional to $t^{1/2}$, however as adsorption progresses of γ becomes proportional to $t^{1/2}$; this is consistent from Ward's work which infers that $\Gamma(t)$ rises quickly initially, and then gradually saturates as the interface becomes more crowded. This has been reinforced with work done by Deshmukh *et al.* who investigated the spread of PNIPAM microgels at the air-water interfaces under compression. They reported that the adsorption process can be clearly separated into two regimes. At short times, the adsorption process is controlled by the diffusion of the particles from bulk to the interface. At long times, the interface gets filled with particles leading to a slower decrease of Γ at longer times.

Interactions of Microgels at the Interface

Microgel particles at a fluid–fluid interface exhibit a behaviour that is intermediate to that of hard particles and polymers. The thermodynamics and interactions at an interface can be expected to be different from those of hard particles due to their swelling ability. The interactions that are dominant for hard particles could be very weak for microgel particles. As microgels can deform in bulk and at an interface meaning there are more degrees of freedom available to the system [36] [68] [69] . The interaction potential between PNIPAM microgels in bulk has been found to differ from hard particles particularly at higher concentrations. For swollen microgels with $\phi_{eff} < 0.3$ effective volume the interactions observed are similar to that of hard sphere systems. However, as the ϕ_{eff} increases beyond 0.3 the particles starts to deform, the softness suddenly becomes apparent. This has been described with an effective potential $u(r)$ of the form,

$$u(r) = \epsilon \left(\frac{\sigma}{r}\right)^n, \tag{1.33}$$

where r is the separation between the centres of two particles, σ is a nominal particle diameter, ϵ establishes the energy scale and exponent n controls the stiffness of the potential [70]. However, when microgels adsorb onto an interface,

they will deform in a different manner. Studies have been found particles are stretched out when the surface coverage is low, due to the free energy gain (i.e. reduction) of covering a bigger interfacial area is high as compared to the energy cost that is related to the elastic deformation of the particle [71]. Furthermore, PNIPAM has been found to protrude into the oil phase with the majority of the particle remaining in the aqueous phase [72]. This protrusion effect highlights another degree of freedom that needs to be considered when considering the interactions of microgels at the interface.

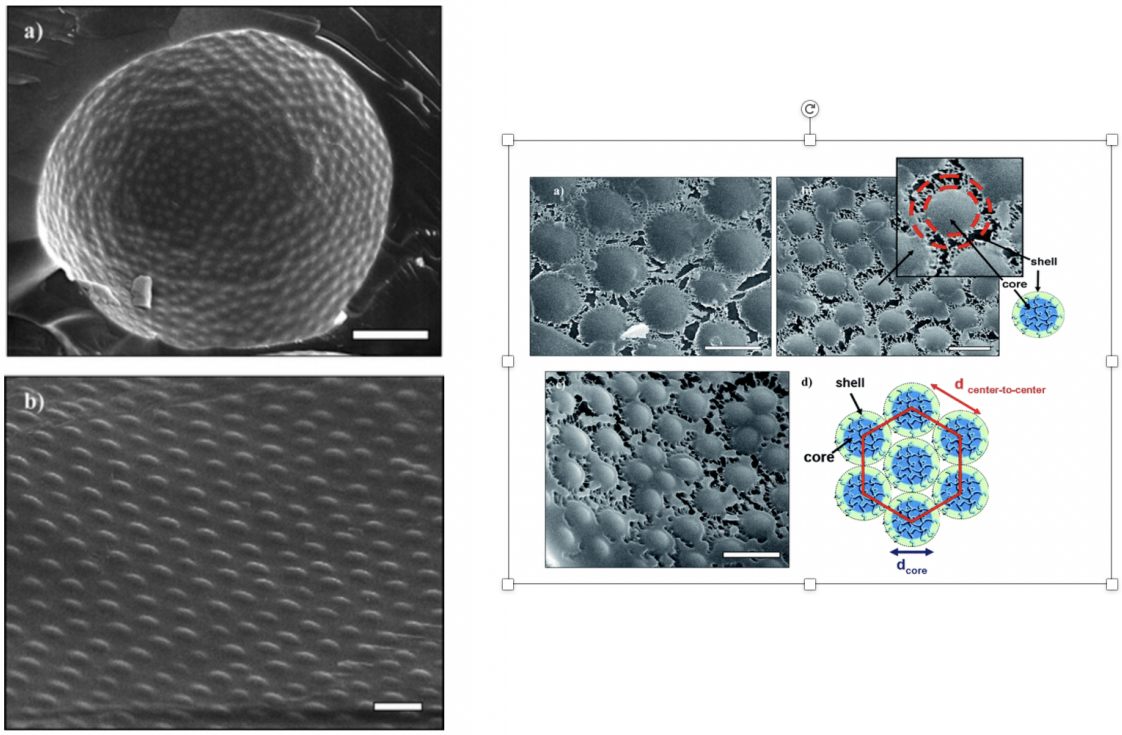

Figure 1.15: *Left: (Top) Cryo-SEM images of dodecane drops covered by PNIPAM microgels: (a) large view of a drop (scale bar is* $5\,\mu$m*), (bottom) (b) hexagonal organisation of microgels at the interface (scale bar is* $1\,\mu$m*), the microgels appear flattened. Right: Cryo-SEM image of the interface of a heptane-in-water emulsion drop covered by PNIPAM microgels with a schematic of the particle structure and arrangement at the interface. Taken from [71]*

Dilational Rheology of Microgels at the Interface

Given the stabilising ability of microgels, they have often been investigated with the aim of using them as emulsifiers [58]. In order to compare to other emulsifiers,

surfactants or Pickering stabilisers, the dilational rheology of microgel-laden interfaces is tested. Dilational rheology allows the elasticity of interfaces to be quantified and many studies have found that particle-laden and microgel-laden interfaces are both highly elastic. However, given that microgels can respond to different stimuli such as temperature or pH, there are significant differences. Brugger *et al.* studied layers of PNIPAM-co-MAA microgel particles at a heptane–water interface and found that both pH and temperature had an effect on the elasticity [73]. At low temperature and high pH, the interface was found to be predominantly elastic, when the microgels are at their most swollen. Increasing the temperature above the volume temperature transition, where PNIPAM microgels shrink, caused a dramatic increase in the viscous character of the interface. The effect of the pH on the interfacial rheological properties was substantiated by the cryo-SEM images of the interfacial layer taken at different pH. At high pH where the particles are charged, the interface exhibited a soft gel-like structure that gave rise to an elastic response to mechanical deformation [73]. However, at low pH where the charge on the particles is lower, the resultant layer was more compact and more prone to breaking easily upon deformation. Furthermore, particle tracking studies have looked at the interfacial dynamics of microgels, the motion of particles at the interface was arrested at low bulk concentrations of PNIPAM particles [74]. Given these findings, the stimuli responsive nature of these particles results in a rich behaviour with morphological transformations that can have interesting consequences for the interfacial rheology.

Microgel particles differ fundamentally from hard particles, regarding their interfacial assembly. They are inherently surface active and they readily adsorb to the interface. As a consequence, dense layers are formed very easily. This was first noticed by Ngai *et al.* in their freeze-fracture SEM images of PNIPAM-co-MAA stabilised toluene–water emulsions [75]. Schmidt *et al.* showed that it was not electrostatic interactions but the deformable nature of the microgels is responsible for the stability of emulsions [76]. Subsequent studies found that PNIPAM microgels formed hexagonally packed ordered layers at the interface, with the core protruding up from the interface surrounded by a flat shell composed of the corona [77] [78]. This arrangement is often described as the 'fried egg-like' morphology and is due to the uneven distribution of crosslinker within the microgels. Furthermore, inverse emulsions were found to be stabilised by multilayers of undeformed microgels located inside the aqueous phase [78]. Further studies showed that microgels are substantially flattened with an internal core that

protruded slightly into the oil phase and protrusion height was independent of pH [79]. In summary, the microgels structure at interface is an important factor that governs the stability of emulsions. Both in case of hard and soft particles, the resistance to coalescence arises due to the presence of a continuous elastic layer of closely packed particles at the interface. For microgel particles, the deformation of these particles at the interface gives rise to interesting mesostructures that ultimately help in stabilising these emulsions.

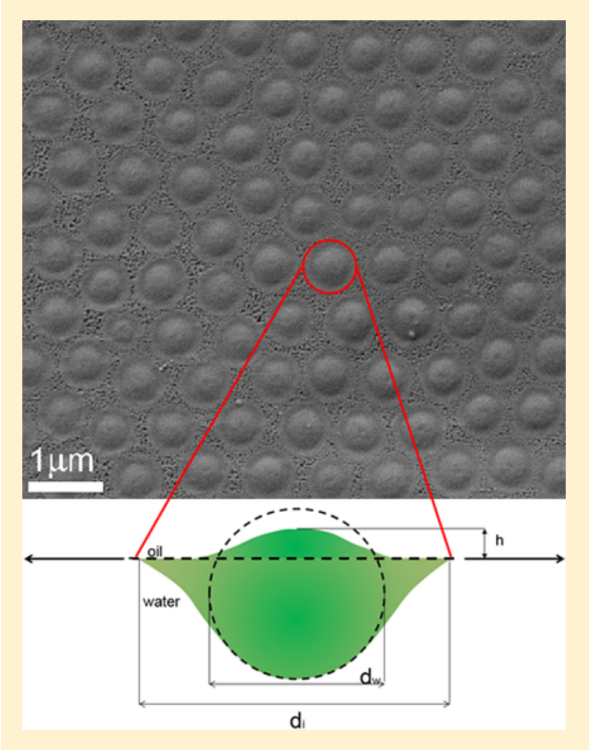

Figure 1.16: *Cryo-SEM images of microgels at the water/n-heptane interfaces imaged from the oil side with a schematic demonstrating the protrusion of microgels at the oil-water interface. Taken from [79]*

1.4 Emulsions

Given that microgels have the abilty to both thicken suspensions and stabilise interfaces, there has been a growing interest in using them as emulsifiers. An emulsion is a system formed by the mixing of two immiscible liquids, where one liquid is typically dispersed in stabilised droplets within a continuous phase of the second liquid. However, in order to be fully stabilised, the addition of surfactants and particles is needed to reduce the high energy cost needed to maintain

an interface between the two components. The simplest method for making emulsions is to shear the two immiscible liquids, resulting in the fragmentation of one phase into the other. The most common and reliable appliances used to produce emulsions being rotor-stators and high-pressure homogenisers [80]. Emulsions are ubiquitous in everyday life as well as industry, particularly in food and cosmetics.

Structuring of Emulsions

Further components are required to stabilise emulsions, as over time droplets tend to coalesce in order to minimise the interfacial area and by extension the interfacial energy. Emulsions can break down by two distinct mechanisms: Ostwald ripening and coalescence [81]. Coalescence occurs when the surfaces of two droplets, in close proximity, are damaged resulting in the droplets combining. Ostwald ripening is the transfer of material from smaller droplets to bigger ones due to differences in Laplace pressure [81]. Eventually each of these leads to loss of the dispersed system and the two immiscible liquids form completely separate domains. In order to suppress these processes surface active agents are commonly introduced to stabilise the dispersed system.

The interaction between the dispersed phase and the emulsifier can also affect the structuring of emulsion-based systems. An example demonstrating this is an emulsion-filled gels. An emulsion-filled gel is a colloidal material which is composed of dispersed emulsions embedded in a gel matrix. When emulsions are incorporated into a gel matrix, there are generally two distinct structures which form: an emulsion-filled gel or an emulsion gel. An emulsion-filled gel is where the emulsion droplets act as a replacement to some of the solvent in the gel matrix. Whereas, an emulsion gel is a particular gel in which the aggregation of the emulsion droplets forms a network which determines the bulk properties of the material. Although these two structures are distinct in practice, emulsion-filled gels can be formed with a mixture of separate and partially aggregated droplets [82].

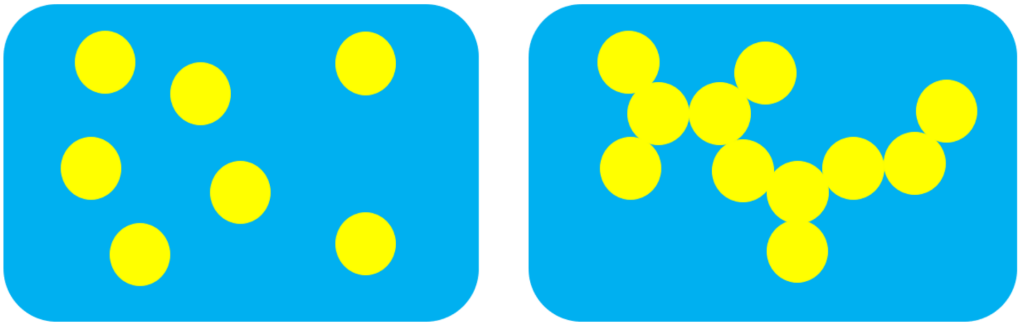

Figure 1.17: *Schematic diagrams of systems of emulsion droplets and gels: emulsion-filled gel (Left) and emulsion gel (Right).*

The bulk properties of emulsion-filled gels depend upon both the physical and chemical characteristics of the embedded emulsion droplets and the background gel matrix. Properties such as the volume fraction and spatial distribution of droplets as well as droplet-gel interactions all influence the bulk characteristics of the material. The surface chemistry of the emulsion drops determines whether they interact with the continuous gel phase. The nature of these interactions determines whether the drops are bound or unbound to the background gel network. If droplets are bound, they are referred to as an active filler and if not, they are known as inactive fillers [82]. Active fillers act to enhance or reduce the strength of the gel, this is as a result of the surfaces of droplets interaction with the molecules which make up the gel. Inactive fillers do not bond to the background gel and always reduce the mechanical strength of the gel. Emulsion-filled gels have been studied extensively due to their applications in industry. By incorporating active fillers into systems you can tune the mechanical strength and the sensory profile of the materials which is used in both the food and cosmetics industries.

Dickinson *et al.* used oscillatory rheology to compare the rheological properties of emulsion-filled gels with droplets stabilised by a surfactant (Tween 20) and droplets stabilised by a protein (whey protein isolate) [83]. Dickinson *et al.* found that surfactant-stabilised droplets weakened the gel strength (inactive filler) while protein-stabilised droplets strengthened the gel (active filler). Other work conducted by Chen and Dickinson comparing emulsion-filled gels to protein gels uncovered that the stabilisation procedure was key [84]. Droplets which were stabilized with the protein were found to be chemically connected into the gel matrix thereby strengthening the gel. Droplets stabilised by surfactants were

found not to be chemically connected to the matrix. Surfactants were shown to change the chemical affinity of the droplets surface and unless matched to the gelling protein, incorporating into the network does not occur. It was also found that the more inactive the filler the weaker the gel became, which was attributed to the slippery interface between the droplets and the gel matrix [84]. More recent work done by Weir *et al.* investigated the rheological properties of a basic caramel mix composed of water, sugar, protein and fat [85]. Using time-temperature super- position, Weir *et al.* managed to construct a frequency master curve which spanned 12 decades of frequency. The results indicates that fat droplets acted as active fillers stabilised by proteins suspended in the sugar-protein gel matrix. Additionally the rheology indicated that the protein gel was composed of a branched network held together by bond percolation [15]. Using oscillatory rheology a detailed phase diagram of caramel was constructed and given the simplicity of the caramel system this research provides a solid benchmark needed for tuning other similarly structured systems.

Measuring Instabilities of Emulsions

In order to predict this critical instability in emulsions, centrifugation can be employed to accelerate the process. Typically this is done using a centrifuge, a device that uses centrifugal force to separate out the components of mixtures such as emulsions. Centrifuges achieve this by spinning samples at high speeds in order to generate high centrifugal forces. The relative centrifugal force RCF is determined by rotational radius r of the centrifuge, the angular velocity ω and g the gravitational acceleration of Earth, $RCF = r\omega^2/g$ [86].

A widely accepted measure of instability in emulsions is the critical disjoining pressure P_{osm}^{CR}. P_{osm}^{CR} is defined as the pressure required to release the dispersed phase from the emulsion network to form a coalesced layer [87] [86]. P_{osm}^{CR} is defined mathematically below,

$$P_{osm}^{CR} = \Delta\rho g_k (V_{OIL} - V_{REL})/A_{TT}, \tag{1.34}$$

where $\Delta\rho$ is the difference in mass densities of the oil and water phases, g_k is the centrifugal acceleration, V_{OIL} is the the total volume of oil in the emulsion, V_{REL} is the volume of oil released on top of the cream and A_{TT} is the cross sectional area of the vial [87]. From this expression, it can be seen that by varying the RCF, and

g_k, one can accurately determine the stability of emulsions. This technique has been used in many studies to determine how stable to sedimentation emulsions can be a key metric for when formulating emulsion based products [87][86] [88].

1.4.1 Thin Film Formation of Emulsions

The understanding of mechanism by which emulsions form thin films has been widely studied as it crucial to the formulation of paints, coatings and adhesives [89] [88]. Typically films are generated by shearing the emulsion on a substrate, and over time the emulsion will dry down and the microstructure will change as the aqueous component evaporates. A key understanding of this process is crucial in the formulation of products where a thin emulsion film is the end step. For example, sunscreen products are sheared down onto the surface of the skin in order to protect the consumer from harmful effects [90]. Ideally this is done by the sunscreen drying down to a microscopic film where the light-absorbing substance is distributed evenly over the skin [90]. Events such as Ostwald ripening and coalescence will affect the efficacy of such products, as the resulting film will be heterogeneous i.e. the sunscreen will not be evenly distributed. Therefore, the understanding of how to avoid heterogeneous films is crucial for the development of sunscreen formulations as well as other emulsion based systems like paints and coatings [89] [91].

The generally accepted mechanism consists of three stages. During the initial stages of drying, the aqueous phase evaporates, leading to the dispersed phase increasing in concentration, with droplets gradually coming into contact, eventually becoming jammed. Further evaporation of water can lead to capillary pressures being generated between droplets, which causes deformations as they squeeze together. Finally when the pressure between drops is sufficiently high, coalescence and phase inversion take place.

There have been numerous studies that have attempted to visualise and construct a framework to understand the final stages of the drying phenomenon. These studies typically generate a thin film, usually by shearing, and then using high-resolution microscopy, individual events can be imaged and tracked as a function of time. In such experiments, coalescence occurs either through a nucleation-and-growth mechanism, where coalesced pockets form and grow randomly throughout the sample, or through a coalescence front that propagates into the sample from the drying end. This drying-induced coalescence is a result from the pressure

gradient generated drying front into the bulk of the sample, established by limited water transport through the Plateau borders [88]. A schematic of these processes is shown in Figure 1.18.

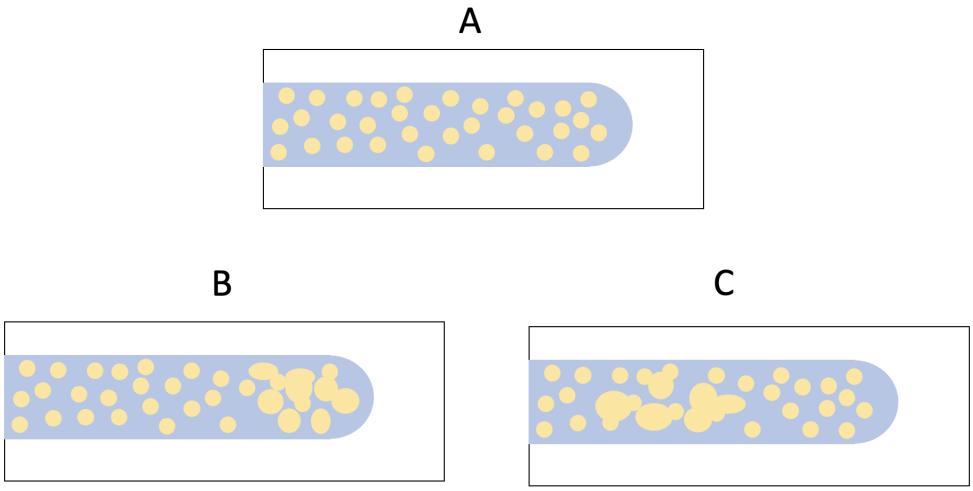

Figure 1.18: *Schematic of the deposition of an emulsion on a substrate. A depicts the initial stage of deposition where B shows a schematic of drying-front induced coalescence occurring and C shows how emulsion coalesces from the nucleation mode.*

Feng *et al.* studied the coalescence of surfactant-stabilised oil-in-water emulsions by measuring the P_{osm}^{CR} between individual droplets [88]. Feng *et al.* determined that the dominating process is determined by a balance between the established pressure profile, generated at the boundary of the drying front, and the P_{osm}^{CR} in the emulsion. The P_{osm}^{CR} can be calculating the curvature between droplets, as the drying process progressed, using high precision microscopy. Very stable emulsions, with high P_{osm}^{CR}, tend to develop steep pressure profiles, which favour front-dominated coalescence, while unstable emulsions with low P_{osm}^{CR} develop shallower pressure gradients, leading to nucleation-and-growth being the dominating coalescence mode [88]. These results offer new insights into the microscopic mechanisms governing the complex and poorly understood macroscopic phenomena during phase inversion of drying emulsions. This study reinforces why the P_{osm}^{CR} is a key metric when assessing emulsion stability.

Similar studies have been conducted which test how the deposition of the emulsions affects the coalescence behaviour observed in thin films [92][93]. Deblais *et al.* sheared oil-in-water emulsions down onto glass substrates using a rigid blade attached to a motor, allowing the deposition speed to be controlled [92]. They

found that complete coverage of the substrate was only achieved if a threshold velocity was exceeded, which is dependent on the deposition height, the distance between the end of the blade and the substrate. However, Deblais *et al.* found the drying and coalescence behaviour was found to be determined by the differences in wetting properties of the dispersed phase. This was tested by using two different emulsion systems, one in which the dispersed phase favoured wetting the substrate and a second system where the continuous phase was favoured [92]. For the system where the dispersed phase wets the interface destabilisation occurs mainly by nucleation whereas for the second system coalescence occurred at the film's front. This study further demonstrates that the thin film formation of emulsions is a rich and complex problem which is determined by the unique properties of each emulsion system.

1.5 Outline of Thesis

This overview of the rich literature on microgels, focussing on their rheological and emulsifying properties, provided the basis for investigating the subject of this thesis, a commercial amphiphilic microgel system called Sepimax Zen. This thesis aims to address the following questions:

- How does the rheology of SZ compare to simpler, more widely studied microgel systems?
- How does SZ act to stablise oil-water interfaces?
- How does the polymer-colloid duality determine the influence the properties of SZ microgels?
- How does SZ dual functionality act when used in emulsions?

  This thesis answers these questions by using a variety of experimental techniques which will be explained in the following chapter. The results are then presented in subsequent chapters.

Chapter 2

Materials and Methods

2.1 Materials

SZ is a crosslinked water-soluble comb polymer which was obtained from Seppic and used as purchased. SZ is composed of 4 monomer units ammonium acryloyl dimethyl taurate, dimethyl acrylamide, lauryl methacrylate and laureth 4 methacrylate, resulting in the formation of a high molecular weight polymer [94]. Mass spectrometry returned a molecular weight of $\approx 10^5$Da. A schematic of the polymer unit is shown in Figure 2.1, the backbone is largely hydrophilic while the side chains are hydrophobic. SZ comes as a pre-neutralised powder which when dispersed in water forms microgel particles.

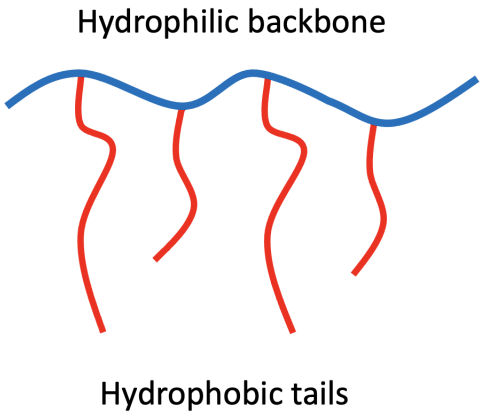

Figure 2.1: *Schematic of the Sepimax Zen polymer*

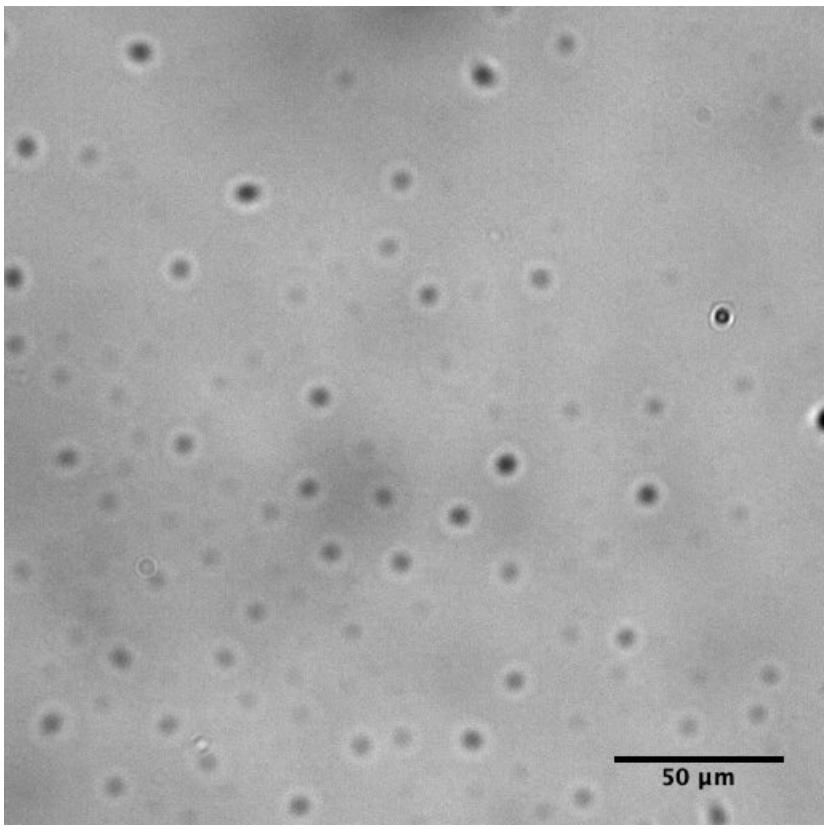

Figure 2.2: *Optical microscopy image of a dried down microgel suspension.*

Figure 2.2 shows an optical microscopy image of a dried down microgel suspension showing microgels with an average hydrodynamic diameter of $\approx 6\,\mu$m. However, as SZ dispersions were transparent a more advanced optical technique was used to analyse them in water.

2.1.1 Microgel Stock Preparation

Microgel suspensions were made by making a stock solution and diluting to various concentrations. To make the stock SZ was weighed out and Milli-Q water was added until the stock concentration was reached. The suspension was then mixed using a Fisons WhirliMixer at 30 000 RPM for 1 minute. After resting the suspension overnight the stock was centrifuged for 1 minute at 1200g, using a Thermo Scientific Sorvall ST40, to remove any air bubbles and impurities. Once this has been done the stock was diluted down using Milli-Q water to the desired concentrations. The SZ concentrations ranged from 0.01 wt% - 2 wt% in samples.

2.1.2 Model Emulsion Preparation

A model emulsion system was formulated following consultation of the industrial partner associated with the project. The model is a three-component system containing Sepimax Zen, Caprylic/Capric Triglyceride (Myritol 312, BASF) a commonly used cosmetic oil and Milli-Q water. Emulsions are prepared by adding the Sepimax Zen (SZ) to the Caprylic/Capric Triglyceride (CCT) first and then adding the Milli-Q water. This protocol was suggested by Seppic and resulted in more stable emulsions. If SZ is added to the aqueous phase first resultant emulsions would have a fraction oil which could not be incorporated. Once weighed out emulsions were mixed, using a IKA T10 Ultra-Turrax rotor stator, for 2 minutes at 30 000 RPM.

2.2 Rheology

Rheology is the study of the flow of matter: primarily liquids but also 'soft solids' or materials which under certain conditions will flow rather than stretch elastically. Rheology deals with the deformation of solid-like materials as well as the flow of liquid-like substances, with a focus on viscoelastic materials. A viscoelastic material is a material which exhibits both solid-like and liquid-like properties in response to force, deformation or time. The most common flow behaviour, and the one that is most easily measured on a rotational rheometer or viscometer, is shear flow.

2.2.1 Steady Shear Rheology

Shear flow can be depicted as layers of fluid sliding over one another, with each layer moving faster than the one beneath it [95]. The top layer of the fluid having the highest velocity and the bottom layer being stationary. In order for shear flow to occur the system must be subjected to an external force. Shear stress is defined as the force F applied over a unit area A, as shown in Figure 2.3. In response to this force the uppermost layer moves a distance x, while the bottom layer remains stationary. This generates a displacement gradient across the sample x/h which is known is the shear strain γ. For a fluid where the constituents can move relative to one another, the shear strain will continue to increase for as long the stress is

applied. This creates a velocity gradient which is termed the shear rate which is the rate of change of strain with time $d\gamma/dt$. However, for a solid, where the constituents can not move relative to each other, the strain will be finite for an applied stress meaning flow does not occur [95].

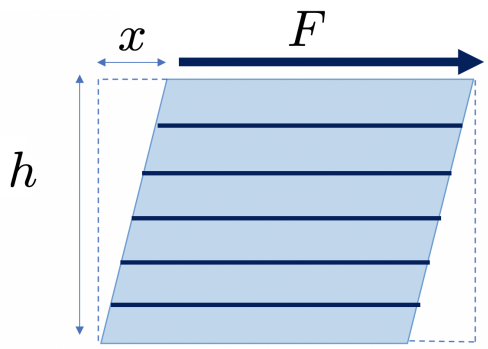

$$\sigma = \frac{F}{A} \qquad \gamma = \frac{x}{h}$$

$$\dot{\gamma} = \frac{d\gamma}{dt}$$

Figure 2.3: *Schematic diagram of shear flow being generated between sliding layers of fluid. Equations show how shear rate $\dot{\gamma}$ and shear stress σ are quantified.*

As a shear stress is applied to a fluid momentum is transferred as the substance flows. Momentum is transferred through the layers of fluid by collisions and interactions between components, leading to a reduction in fluid velocity. The coefficient of proportionality between the shear stress and shear rate is defined as the shear viscosity or dynamic viscosity.

$$\sigma = \eta\dot{\gamma} \tag{2.1}$$

The shear viscosity is a quantitative measure how the fluid resists the relative motion of the top and bottom plates. A common way to measure the rheological behaviour of materials is to use a rotational rheometer, a schematic is shown in Figure 2.4. Rotational rheometers can either be stress or strain controlled: stress-controlled rheometers work by imposing a torsional force F and then the rotational speed V is measured whereas for a strain-controlled, V is applied and F is measured [96]. In a strain-controlled rheometer (the type used in this thesis) the material is placed between two plates. The bottom plate moves at a fixed rotational speed and the torsional force produced on the top plate is measured. The shear rate V/h is calculated by knowing the gap height, h, and the rotational speed of the bottom plate which is fixed by $V = R\omega$, where R is the radius of

the plates and ω is the angular velocity. The top plate then rotates at the V and the F needed to maintain this is measured.

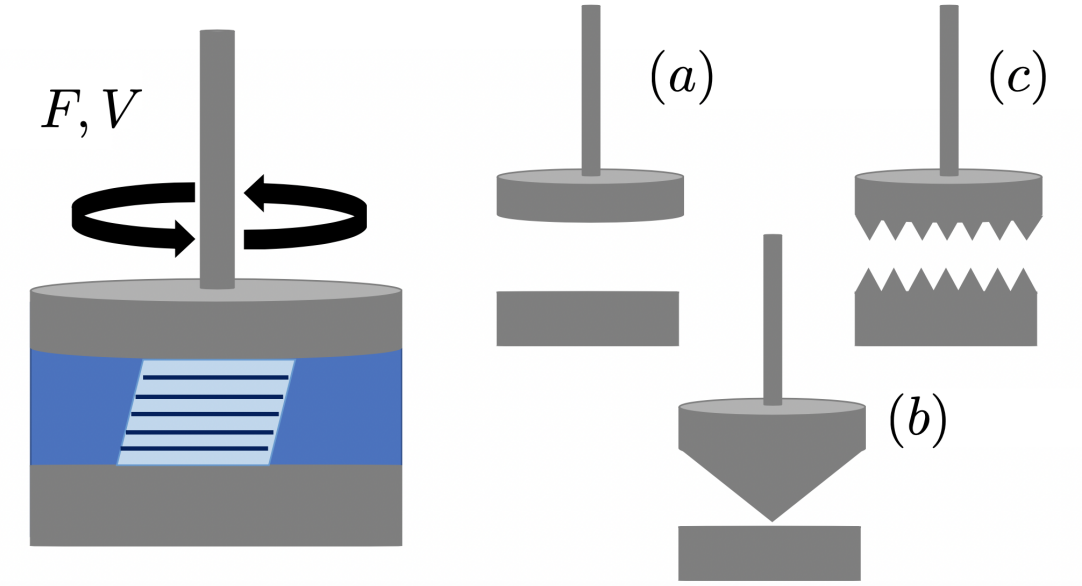

Figure 2.4: *Schematic diagram of a rotational rheometer with a fluid in between the plates. The top plate rotates with rotational velocity V and torsional force F leading to the flow being initiated. A number of geometries used on with rotational rheometers are also shown: (a) parallel plate, (b) cone and plate and (c) cross-hatched.*

Several geometries are available for rheometers including parallel plate, cone and plate and cross-hatched. The cone and plate geometry is the most precise rheologically as the angled cone gives an even shear field across the whole sample [96]. The shear rate $\dot{\gamma}$ of a cone and plate geometry is given by,

$$\dot{\gamma} \approx \omega/\alpha \tag{2.2}$$

where ω is the rotation speed and α is the cone angle, this approximation holds for sufficiently small cone angle [21]. The equation shows that the shear rate, for a cone and plate is the same throughout the sample as its independent of radius. Whereas parallel plate is the shear rate is given by,

$$\dot{\gamma} = \frac{\omega R}{h} \tag{2.3}$$

where r is the radius of the plates [21]. In this case γ varies linearly starting from zero in the center of the plate and reaching a maximum at the edge. An advantage of the parallel plate geometry is that the height of the gap can easily be changed, even without reloading the sample. As the gap height can be easily changed it means it is particularly advantageous when measuring viscous samples. Wall slip occurs when the material, near the surface of the plates, experiences large velocity gradients leading to the measured viscosity being significantly lower [96]. By performing a series of experiments at different gap heights one can determine and account for any wall slip that occurs by comparing the flow behaviour at the various heights. Another way to avoid wall slip is to roughen the surface of plates by either sandblasting them, resulting in a roughened surface. An alternative to sandblasted plates are cross-hatched plates, which are parallel plates where the surfaces have distinct 'teeth' to prevent slip of material at the wall. Typically cross-hatched and sandblasted plates are used to investigate concentrated suspensions where wall slip can occur. For the rheology measurements both cross-hatched parallel plate (emulsions and concentrated microgel dispersions) and cone and plate (dilute microgel dispersions) geometries were used. The microgel rheology can be found in Chapter 3 and the emulsion rheology in Chapter 6.

2.2.2 Oscillatory Rheology

Oscillatory rheology is commonly employed to investigate the dynamic and structural behaviour of complex fluids. Typically this done by imposing a sinusoidal shear rate $\dot{\gamma}$ of the form,

$$\dot{\gamma} = \gamma_0 sin\omega t \tag{2.4}$$

where γ_0 is the strain amplitude, ω is the frequency of the oscillation and t is time. If γ_0 is small enough that the fluid structure is not disturbed significantly, the stress measured represents the random rearrangements which occur in the equilibrium state for Newtonian fluids. For viscoelastic materials these tests can reveal intricate details of the structure such as the degree of cross-linking in a gel. The shear stress $\sigma(t)$ produced as a response is sinusoidal and has a general

form of,

$$\sigma(t) = \gamma_0[G'(\omega)sin\omega t + G''(\omega)cos\omega t] \tag{2.5}$$

The storage modulus $G'(\omega)$ represents the elastic energy stored in the material and the loss modulus $G''(\omega)$ represents the viscous dissipation of this energy. Small amplitude oscillatory tests are divided into strain, stress, frequency and temperature sweeps. In strain and stress sweeps the amplitude is varied while keeping the frequency and temperature constant. These tests find the linear viscoelastic regime of the material, which is the limit within which the structure has not yet been compromised. In this regime the rheological properties are independent of frequency and all further small amplitude tests are performed within this regime.

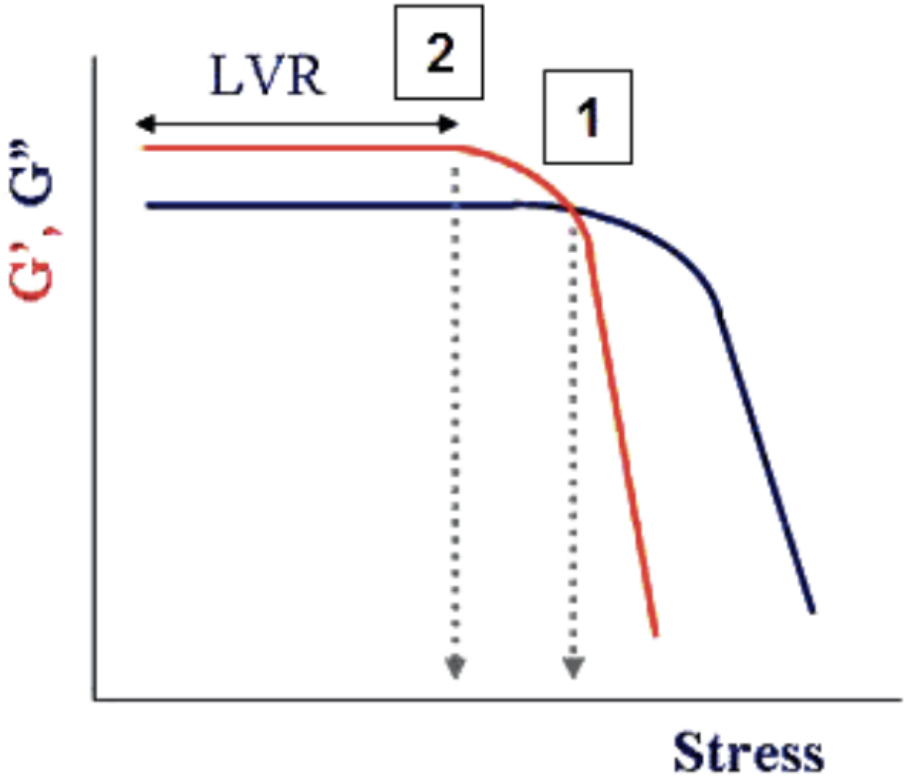

Figure 2.5: *Illustration of a amplitude sweep where the storage modulus (G') and loss modulus (G'') are measured as a function of stress. LVR stands for the linear viscoelastic regime where the the initial structure has not been compromised. 2 is the stress at where the material starts to lose solid-character and 1 is where G' and G'' cross and is referred to as the yield point. Taken from [97].*

2.2.3 Experimental Protocol

2.2.4 Rheological Measurements

Microgel Suspensions

All rheological measurements were done using a strain-controlled Ares G2 rheometer. Two geometries were used to characterise the the SZ dispersions: a 40 mm cone and plate geometry (gap = 0.0022 mm) and a 40 mm cross-hatched geometry (gap = 1 mm) with roughness $\approx$ 1 mm. Two geometries were

necessary due to the suspensions becoming more gel-like as the SZ concentration is increased, ($> 0.3\,\mathrm{wt}\%$), therefore, the geometry was switched to cross-hatched to account for any wall slip. Each sample was loaded then trimmed and left for 1 minute before each measurement. A solvent trap was then fitted with wetted paper towel on the interior to ensure minimal evaporation during tests. Flow sweeps were conducted at shear rates $0.1\,\mathrm{s}^{-1}$ to $100\,\mathrm{s}^{-1}$, with 5 points measured per decade. Before each measurement the substance was allowed to equilibrate for 20 s and a measurement time of 20 s with the final value being averaged over this window. Amplitude sweep tests were conducted at a frequency of 0.1 Hz with the strain being varied from 0.1 % to 200 %. Samples were again rested for approximately 1 minute before the measurement. For the most dilute samples of SZ the equilibration time was extended to 100 s, to account for experimental noise. Each sample was tested to 2 or 3 times to assess reproducibility.

2.3 Differential Dynamic Microscopy

2.3.1 Background of Differential Dynamic Microscopy

Differential Dynamic Microscopy (DDM) is an optical technique which can measure the mobility of colloids such as particles. DDM works by tracking the dynamics of the local density of colloids via image analysis, allowing the mobility and the size of individual colloids to be characterised.

DDM uses time-lapse images of colloids, described by the intensity $I(\vec{r}, t)$, where $\vec{r}$ is pixel position and t is time. As the particles move, $I(\vec{r}, t)$ fluctuates with time [98]. Therefore, the intensity difference $D(\vec{r}, \tau)$ between pairs of images at different delay times, τ can be expressed as,

$$D(\vec{r}, \tau) = I(\vec{r}, t + \tau) - I(\vec{r}, t) = \Delta I(\vec{r}, \tau) - \Delta I(\vec{r}, 0), \tag{2.6}$$

where $\Delta I(\vec{r}, t) = I(\vec{r}, t) - \langle I \rangle$ denotes the intensity fluctuations and $\langle I \rangle$ is the average intensity across the images. Fourier transforming $D(\vec{r}, \tau)$ gives,

$$F_D(\vec{q}, \tau) = \int D(\vec{r}, \tau) e^{i\vec{q}\cdot\vec{r}} d\vec{r}, \tag{2.7}$$

For stationary, isotropic processes, $F_D(\vec{q},\tau)$ is averaged over the start time t and azimuthally in q-space to calculate the basic output of DDM, which is called the 'differential intensity correlation function' (DICF), $\langle|F_D(q,\tau)|^2\rangle$ where q is the magnitude of the wave vector $\vec{q}$ [99]. The DICF is the square modulus of the difference of two images separated by time τ and can be expressed mathematically as,

$$g(\vec{q},\tau) = \langle|I(\vec{q},t+\tau) - I(\vec{q},t)|\rangle, \tag{2.8}$$

in equation 2.8, $\langle ...\rangle$ means the average over the initial time t, and $I(\vec{q},t)$ is the Fourier transform of $I(\vec{r},t)$, which picks out the component in the image $I(\vec{r},t)$ that varies sinusoidally with wavelength $2\pi/q$ in the direction $\vec{q}$.

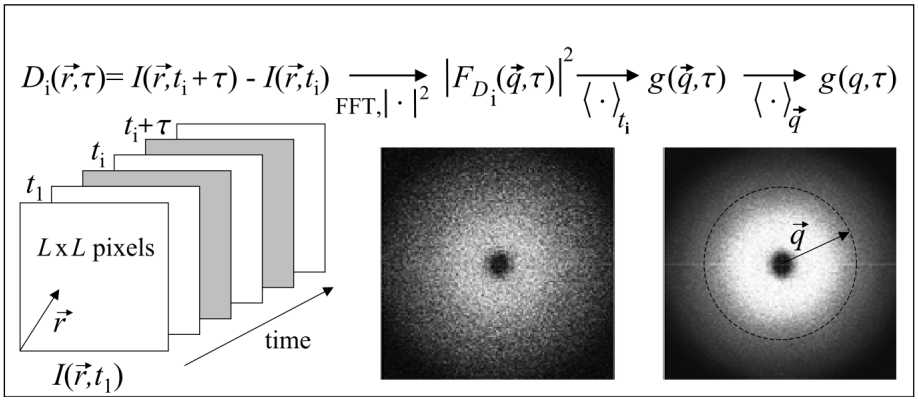

Figure 2.6: *Schematic of the image processing to obtain the DICFs, $g(\vec{q},\tau)$. Left image depicts how the intensity is tracked as images are collected to form videos, middle image is a non-averaged image collected from an experiment, $\langle|F_{D_i}(\vec{q},t)|\rangle^2$ and (right) averaged image, $g(\vec{q},\tau)$. Taken from [98].*

It can be shown that $g(\vec{q},\tau)$ is related to the intermediate scattering function (ISF), $f(q,\tau)$, by assuming the intensity fluctuations are proportional to the fluctuations in the number density of colloids [98]. This results in,

$$g(\vec{q},\tau) = A(q)[1 - f(q,\tau)] + B(q) \tag{2.9}$$

where $A(q)$ depends on the optics, particle shape, and mutual arrangement, and $B(q)$ represents the camera noise. For non-interacting colloids undergoing

Brownian motion,

$$f(q,\tau) = \langle e^{i\vec{q}\cdot\Delta\vec{r_j}(\tau)}\rangle_j, \tag{2.10}$$

where $\Delta\vec{r_j}(\tau)$ is the j^{th}-particle displacement and $\langle ...\rangle_j$ is the average over all particles. Equation 2.6 shows that $f(q,0) = 1$ and $f(q,\infty) = 0$, which reflects that as τ tends to infinity the colloid's correlation decays due to Brownian motion. For identical diffusing spherical colloids, $f(q,\tau) = e^{-\tau/\tau_R}$, where $\tau_R = 1/Dq^2$ is the relaxation time of the system and D is the diffusion coefficient of colloids. For more concentrated suspensions, like gels or glasses, a stretched exponential function of the form $f(q,\tau) = e^{(\tau/\tau_R)^\beta}$ where β is the stretch exponent. For Brownian diffusing spheres $\beta = 1$ and when $\beta < 1$ this indicates that the diffusivity is being be influenced by particle-particle interactions. DDM was used to characterise the size of SZ microgels and their mobility for a range of concentrations. Then the microgels response to salt and osmotic pressure was investigated with all the results detailed in Chapter 4.

2.3.2 Experimental Protocol

2.3.3 Sample Preparation

The stock solution of microgels was diluted down with Milli-Q water to a range of concentrations, 0.0001 wt% - 0.35 wt%.

Microgel and Salt Suspensions

To test how the microgels reacted in the presence of salt, the suspensions were combined with various concentrations of NaCl solution. The NaCl stock was made dissolving a known amount of NaCl salt in Milli-Q water which was then diluted to various concentrations varying from 0.001 mM - 2000 mM. A dilute suspension of microgels 0.000 25 wt% was combined with the various concentrations of NaCl solution just before measuring to minimise any time effects.

Microgel and Ficoll-400 Suspensions

For osmotic pressure measurements Ficoll-400 (Sigma Aldrich), an inert non-excluding polymer, was introduced to the microgel suspensions, allowing the osmotic pressure of the solutions to be tuned. Ficoll-400 is most commonly used as a density gradient medium for the separation and isolation of eukaryotic cells, organelles and bacterial cells. Furthermore, it has been shown that Ficoll-400 can be used to tune the osmotic pressure of microgel suspensions [100]. A stock solution was made by dissolving the Ficoll-400 in Milli-Q water and diluting to a range of concentrations, 0.01 mg/mL - 300 mg/mL. The Ficoll-400 solutions were combined with a dilute suspensions of microgels (0.0025 wt%) just before imaging. A higher concentration of SZ was needed due to the Ficoll-400 altering the refractive index of the microgel suspensions.

2.3.4 Imaging Setup

An inverted microscope (Nikon Eclipse TE2000) equipped with a high acquisition speed camera (Hamamatsu Orca-Flash 4.0 V3, Japan) was used for the acquisition of videos of microgel suspensions. Videos were recorded using phase-contrast imaging using $\times 20$ magnification (Olympus Plan, NA = 0.4 (Ph1)), with a frame rate of 50 frames per seconds, and an image binning 2×2 within a region of interest of 512×512 pixels. These parameters were adjusted to optimize the signal amplitude and to access particle dynamics over an adequate q-range and time-scale for the microgels. Images were recorded in glass capillaries (Vitrocom, UK) of thickness 0.4 mm filled with microgel suspension ($\approx 200\,\mu$L) and sealed using petroleum jelly. Videos were recorded for 5 minutes per sample at least three times. The videos were then analysed using an in house LabView program, a generalized exponential model was used to the dynamics of the microgel suspensions,

$$g(q,\tau) = A(q)\left(1 - e^{-(\frac{\tau}{\tau_R})^{\beta}}\right) + B(q), \tag{2.11}$$

where g is the differential correlation function, q is the wave vector, $A(q)$ is the signal amplitude, τ is the delay time, τ_R is the relaxation time, β is the stretch exponent and $B(q)$ is the instrumental noise. The relaxation time τ_R can be expressed as $\tau_R = 1/Dq^2$ where D is diffusion coefficient. From this fitting

procedure the dynamics of the microgel suspensions could be determined for the a range of SZ concentrations, at different osmotic pressures and salt concentrations.

2.4 Pendent Drop Tensiometry

2.4.1 Background of Pendant Drop Tensiometry

Pendant drop tensiometry (PDT) is a technique for measuring the interfacial tension γ of a pair of fluids such as water and air or water and oil. PDT can determines γ based upon the geometry of the drop shape, this is obtained by imaging the outline of an evenly backlit fluid drop attached to a vertical needle. The drops outline is fitted with the Young-Laplace equation, which relates the pressure difference ΔP across an interface to its curvature in terms of the principal radii of curvature $R_{c,1}$ and $R_{c,2}$ by

$$\Delta P = \gamma \left(\frac{1}{R_{c,1}} + \frac{1}{R_{c,2}} \right). \tag{2.12}$$

A single image provides γ, the surface area of the drop A, the drop volume and the quality of the the fit (which is based upon the profile of the residuals). In fitting the following is assumed: the interfacial tension is isotropic, the interface has a negligible bending modulus and that the pressure difference is due only to the hydrostatic pressure. Given these assumptions the drop shape can be described by the following set of axisymmetric equations [101]:

$$\frac{d\psi}{d\bar{s}} = 2 - \beta\bar{z} - \frac{sin\psi}{\bar{r}} \tag{2.13}$$

$$\frac{d\bar{r}}{d\bar{s}} = cos\psi \tag{2.14}$$

$$\frac{d\bar{z}}{d\bar{s}} = sin\psi. \tag{2.15}$$

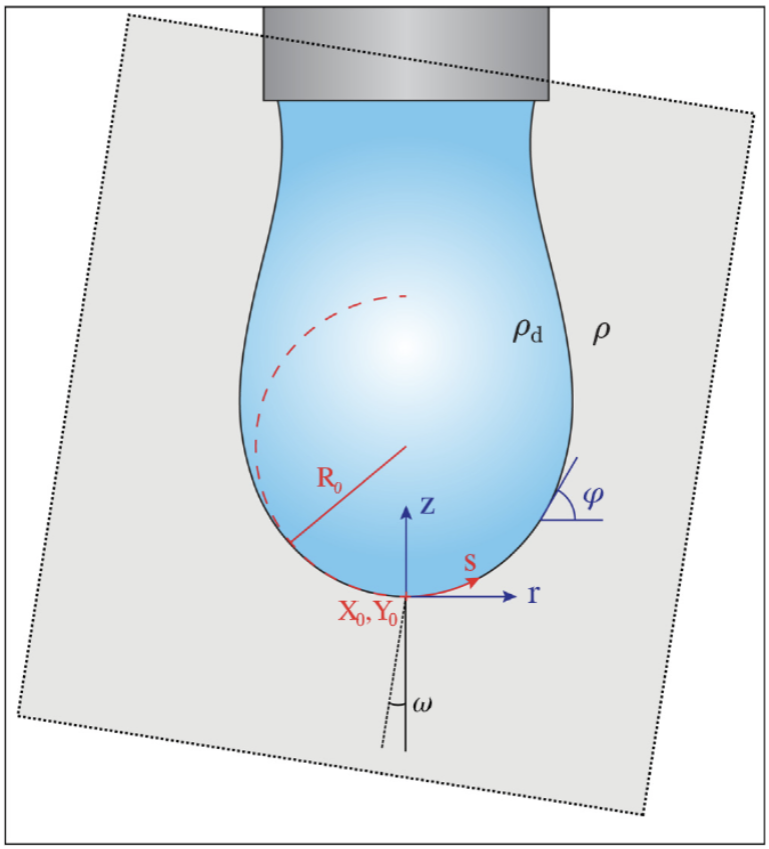

Figure 2.7: *Schematic of a pendant drop with labelled a co-ordinate systems (described in the text) which describes how the Young-Laplace equation is fitted to the drop profile. Taken from [101].*

In these equations z is the height above the drop apex, r is the radial distance from the axis of symmetry, s denotes the arclength along the drop profile from the apex and ψ is the tangent angle to the drop profile. The over bar denotes dimensionless quantities scaled R_0, the radius of curvature at the drop apex. From these approximations the shape is dependent upon the Bond Number β, a dimensionless quantity determined by the ratio gravitational forces compared to surface tension forces, which is given as,

$$\beta = \frac{\Delta\rho g R_0^2}{\gamma}, \tag{2.16}$$

where $\Delta\rho = \rho_d - \rho$ is the density difference between the droplet phase ρ_d and the continuous phase ρ and g is the local gravitational acceleration. Essentially gravity acts to elongate the drop in preference to the surface tension. Therefore, the drop needs to be of an adequate size to ensure that gravitational effects are

non-negligible. If the gravitational effects are too small, then β is close to zero, which will lead to fitting problems. Given $\beta \approx R_0^2$, bigger drops result in larger β decreasing the chance of fitting errors.

Once imaged the drop profile is found, and the edge of pendent drop can be clearly identified, solutions to equations 2.13-2.15 are fit to it by minimising the square of the residuals. To ensure the most effective fitting the drop must be in equilibrium, free of air currents and temperature fluctuations. Furthermore, spurious light sources must be eliminated to avoid unwanted reflections appearing on the drops interface. The best fit solution returns β as well as the drop volume and area which are calculated by assuming an axisymmetric drop. Then by measuring R_0 from the image the interfacial tension γ can be calculated using equation 2.12 since the density difference and local strength of gravity are known.

2.4.2 Oscillatory Tensiometry

By analysing the behaviour of oscillating drops the dilational rheology of the interface can be probed. This is done by measuring how the dynamic interfacial tension γ_t responds as the drop area A_t is varied (by varying the drop volume V_t): from this a stress-strain relationship can be measured by controlling the strain.

The dilational stress of a adsorbed layer can be determined by measuring the difference of interfacial tension γ from its initial value γ_0 to a generic value at the time t, $\Delta\gamma = \gamma(t) - \gamma_0$ while the related surface deformation is the expansion/contraction of the surface area A. For purely elastic dilational behaviour, the surface stress is proportional to the relative area variation, $\alpha = \Delta A/A_0$ where $\Delta A = A(t) - A_0$. However, the interfacial layer may introduce a viscous component, due to relaxation effects. In general the dilational stress can be written as the sum of two terms: one purely elastic, proportional to α and the second one, a viscous term, proportional to the rate of surface deformation that is the rate of the area variation, $\dot{\alpha} = \frac{d\alpha}{dt}$ [102]. A general expression for the dilational viscoelasticity is,

$$\Delta\gamma = E\alpha + \eta\dot{\alpha}, \tag{2.17}$$

where E_0 and η are the dilational elasticity and viscosity, respectively. For a low amplitude perturbation of frequency ω the corresponding area of perturbation can

be expressed as $\Delta A = \tilde{A}e^{i2\pi\omega t}$. Using this expression the dilational viscoelastcity E can be expressed, using equation 2.17, as,

$$E = \frac{\Delta\gamma}{\Delta A/A_0} = E_0 + i2\pi\omega\eta = \frac{d\gamma/dt}{dlnA/dt}. \tag{2.18}$$

E is a frequency dependent complex quantity, where the real part $E_R = E_0$ is the dilational elasticity and the imaginary part $E_I = 2\pi\omega\eta$ is directly related to the dilational viscosity. Furthermore, provided that the applied perturbation is of a low amplitude it can be expressed, according to the Fourier formalism for linear systems, as a superposition of harmonic components in the domain of frequency [102].

Through recording image sequences of pendent drops subjected to a low amplitude harmonic perturbation and fitting the subsequent profiles allowing E to be determined. E can be tracked by recording several videos, each one providing a value of E, allowing the evolution of dilational viscoelastcity of an interface to be recorded as a function of time. Assuming that a perturbed drop oscillates sinusoidally with amplitudes ΔE and $\Delta\gamma$, around mean values A_m and γ_m, as a function time t,

$$A(t) = A_m + \Delta A e^{i\omega t}, \tag{2.19}$$

$$\gamma(t) = \gamma_m + \Delta\gamma e^{i\omega t}, \tag{2.20}$$

Using equation 2.18 E can be expressed as,

$$E = \frac{\Delta\gamma}{\Delta A/A(t)}, \tag{2.21}$$

which to first order in $\Delta A/A_m$ is,

$$E = \frac{\Delta\gamma}{\Delta A/A_m}. \tag{2.22}$$

Now by taking the Fourier transform of both numerator and denominator allows

the frequency spectrum to be discretised, consider,

$$E = \frac{FT[\delta\gamma]}{FT[\delta ln(A)]} = \frac{FT[\gamma_{i+1} - \gamma_i]}{FT[ln(A_{i+1}) - ln(A_i)]}, \tag{2.23}$$

now by substituting in for A and γ using equations 2.19 and 2.20,

$$E = \frac{FT[\Delta\gamma e^{i\omega t_i}(e^{i\omega(t_{i+1}-ti)} - 1]}{FT[ln(A_m + \Delta A e^{i\omega t_{i+1}}) - ln(A_m + \Delta A e^{i\omega t_i})]}. \tag{2.24}$$

Given that this perturbation is small the logarithm terms can be expanded to give,

$$E = \frac{FT[\Delta\gamma e^{i\omega t_i}(e^{i\omega(t_{i+1}-ti)} - 1]}{FT\left[\frac{\Delta A}{A_m} e^{i\omega t_i}(e^{i\omega(t_{i+1}-t_i)} - 1) + \mathcal{O}\left(\left(\frac{\Delta A}{A_m}^2\right)\right)\right]}. \tag{2.25}$$

Considering this equation to only first order reduces to,

$$E = \frac{\Delta\gamma}{\Delta A/A_m} \tag{2.26}$$

which is the result of equation 2.22 which proves E can be extracted by considering the ratio of Fourier transforms. E can be tracked as a function of time by capturing several videos each giving a snapshot of E. This allows other variables such as frequency or ageing to be explored, the results of which are contained in Chapter 5.

2.5 Experimental Protocol

2.5.1 Material Preparation

Microgel suspensions were prepared by weighing out SZ in and dissolving in Milli-Q water. The suspension was then mixed using a Fisons WhirliMixer at 30.000 RPM for 30 seconds. After resting for at least 2 hours the samples were centrifuged in a Thermo Scientific Sorvall ST40 at 1200g to remove any impurities. The n-dodecane was purified before use by filtration of a 1 L batch through a

25 cm×4 cm alumina (Honeywell, Aluminium Oxide, activated, basic, Brockmann I) column three times [103].

2.5.2 Imaging Set Up

To capture images or videos of the drop and to extract the interfacial tension from those images a Krüss DSA100 drop tensiometer (which uses a 780 × 580 pixel CCD camera) controlled by a PC was used. A Krüss DS3265 surface rheology module (a PC-controlled piezoelectric pump) and a separate syringe pump (New Era, model NE-1000) were used to control the drop volume. A schematic of the instrument is shown in Figure 2.8.

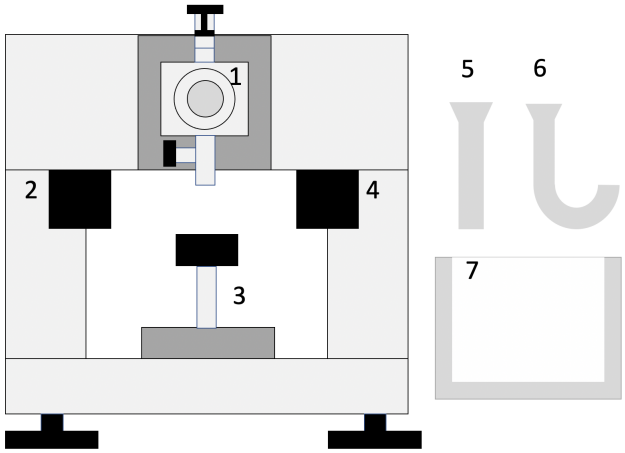

Figure 2.8: *Schematic of Krüss DSA100 drop tensiometer. 1. Computer-controlled piezoelectic pump for volume oscillations, 2. CCD camera and prism to reflect drop image into camera, 3. Moveable z-stage, 4. Diffuse light source, 5. Straight needle, 6. J-needle and 7. Cuvette.*

To clean the system the glassware was rinsed thoroughly with distilled water and ethanol, then dried and put to use. To test for surface active contaminants the interfacial tension of the water-air interface was measured and compared to the expected value of 72.75 ± 0.36 mN/m at 20 °C [104]. A 35 μL drop of n-dodecane in water is prepared and compare its interfacial tension to the reported value of 52.55 ± 0.04 mN/m at 20 °C [105]. Having calibrated the interfacial tension measurement, the dilational measurements were calibrated by oscillating the drop at 10 Hz with a 4% amplitude area strain. For a pure interface, the interfacial tension should be independent of area, and thus the

dilational modulus should be zero. We found a storage modulus of $E' = 2.07 \pm 0.14\,\mathrm{mN/m}$ and a loss modulus of $E" = 0.08 \pm 0.08\,\mathrm{mN/m}$. This is attributed this to variation in apparent interfacial tension with area due to measurement errors, associated with the limitations of the set up. To prepare the microgel-laden interface microgels spontaneously adsorb from aqueous phase, with various SZ concentrations. Purified n-dodecane drops were suspended from a J-shaped needle in a cuvette filled with the SZ microgel suspensions. The interfacial tension of the n-dodecane drop was recorded for approximately 11 hours for static experiments and for 20 hours for dynamic measurements. Once the interface is prepared the dynamic interfacial tension and dilational modulus are measured as described earlier. The interfacial tension of the n-dodecane drop was recorded for approximately 11 hours for static experiments and for 20 hours for dynamic measurements. Finally, the frequency was varied to a number of different values to test the response of the interface.

2.6 Cryo-SEM

Cryo-scanning electron microscopy (cryo-SEM) is is an advanced form of electron microscopy where a sample is cryogenically frozen and then imaged on a scanning electron microscope in a cryogenic chamber. Cryo-SEM of hydrated samples, like emulsions or aqueous particle dispersions, with a high moisture content can be done more effectively than traditional SEM. This is due to the dehydration processes needed to prepare samples for a conventional SEM chamber can disrupt or compromise the structure and composition of the hydrated sample [106]. Therefore, by quickly freezing samples prior to imaging the structure of the sample *in-situ* can be determined. However, in order to be imaged samples must be made conductive. Samples must be conductive as the core principle of SEM is that electrons are fired at the surface of the sample, which interact with surface atoms which results in secondary electrons being ejected, and by collecting them an image of the surface can be constructed (see Figure 2.9) [107].

If the surface is non-conductive electrons may build up on the surface and 'charge' the interface, which leads to a degradation in image quality. Furthermore, SEM and cryo-SEM operates under a vacuum to avoid interactions of electrons with molecules in the environment to obtain high resolution. The primary electrons are typically produced and emitted from an electron gun and are accelerated by heating or applying high energy in the range of 1 keV -40 keV [107].

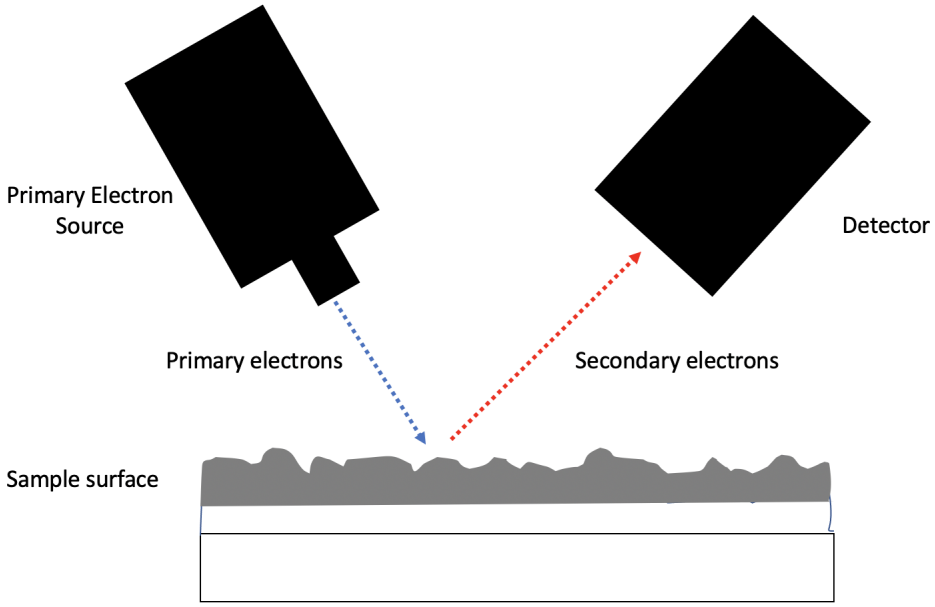

Figure 2.9: *Schematic demonstrating the basic principle of SEM.*

2.6.1 Experimental Protocol

Cryo-SEM observations were carried out using a Zeiss Crossbeam 550 FIB-SEM electron microscope equipped with liquid nitrogen-cooled sample preparation and transfer units with cryogenic attachment from Quorum Technologies. Small samples of model emulsions were deposited into a aluminium specimen holder. The sample was frozen in the slushing station with liquid nitrogen. The specimen was transferred under vacuum from the slushing station to the preparation chamber. The latter was held at a temperature of $-150°C$ and a pressure of $\approx 10^{-7}$mbar and is equipped with a blade used to fracture the sample. Once fractured, the sample was coated by a thin layer of platinum and was then inserted into the observation chamber equipped with a SEM stage cold module held at $-150°C$. Images were taken and analysed using ImageJ.

2.7 Confocal Microscopy

Confocal microscopy is a more advanced optical technique and can be used to build up a 3D images of materials. The principle of confocal microscopy is shown in Figure 2.10. The sample is illuminated by a laser beam which excites fluorescent dye molecules which have been incorporated prior the measurement.

The emitted light is then collected in the objective lens and passed to a dichroic mirror. A pin hole selects light from a particular depth from within the sample, which is then passed onto a photomultiplier tube. By imaging the sample at multiple depths the 3D microstructure can be constructed from a stack of confocal images.

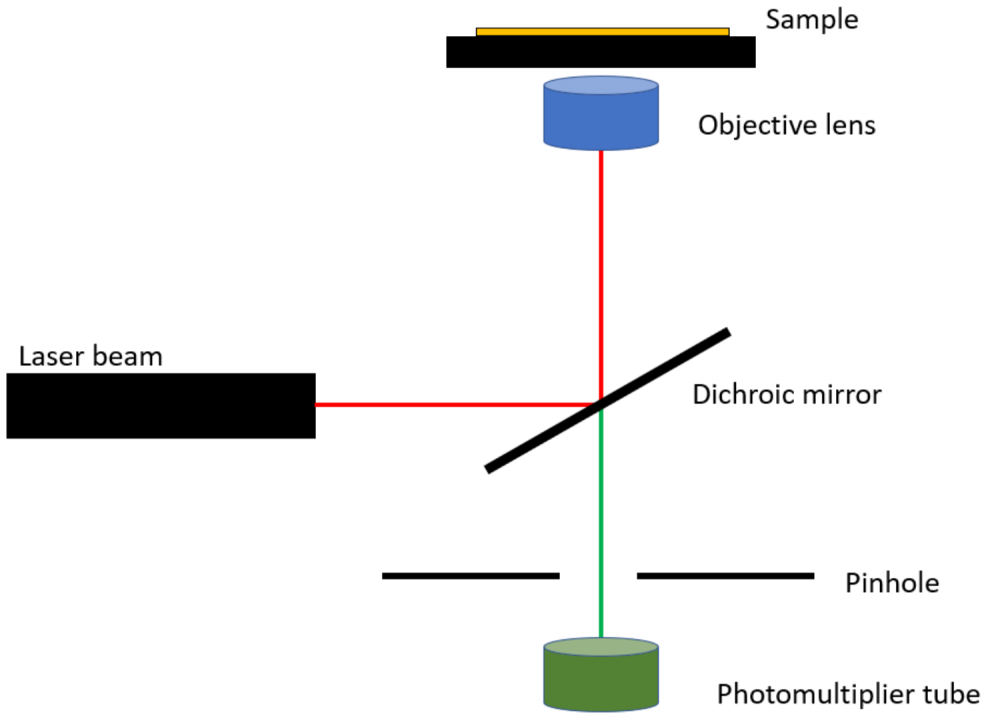

Figure 2.10: *Schematic diagram of the principle of confocal microscopy.*

2.7.1 Experimental Protocol

In order to test emulsion stability in thin films two set ups were used: one in house using a confocal microscopy the other, located at the University of Bordeaux in the lab of Dr. Hamid Kellay, using a high-speed camera attached to an inverted microscope.

2.7.2 Confocal Microscopy Set-Up

Emulsions were sheared down onto coverslips using an aluminium block with a 20 μm gap etched on the side. Once sheared the coverslip was mounted onto a Zeiss LSM700 laser scanning microscope. The oil phase of the emulsions was dyed

using Nile red, excited by a 488 nm laser source the microstructure of the films could be determined. The film was imaged at different heights from the substrate as a function of time, allowing the microstructure of the whole film to be imaged (see Figure 2.11).

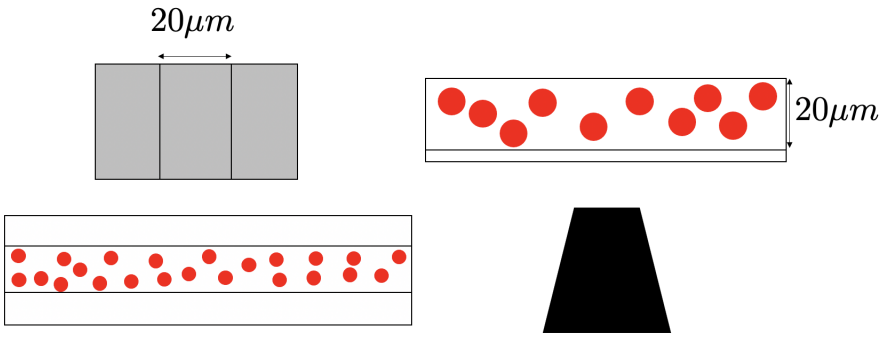

Figure 2.11: *Left: Schematic of the aluminium block with a* 20 μm *gap etched on the side and the resultant coverslip with the emulsion spread on it, the red parts are the dispersed oil phase. Right: Schematic of the of the coverslip being imaged with a* 20 μm *film deposited.*

2.7.3 Bordeaux Set-Up

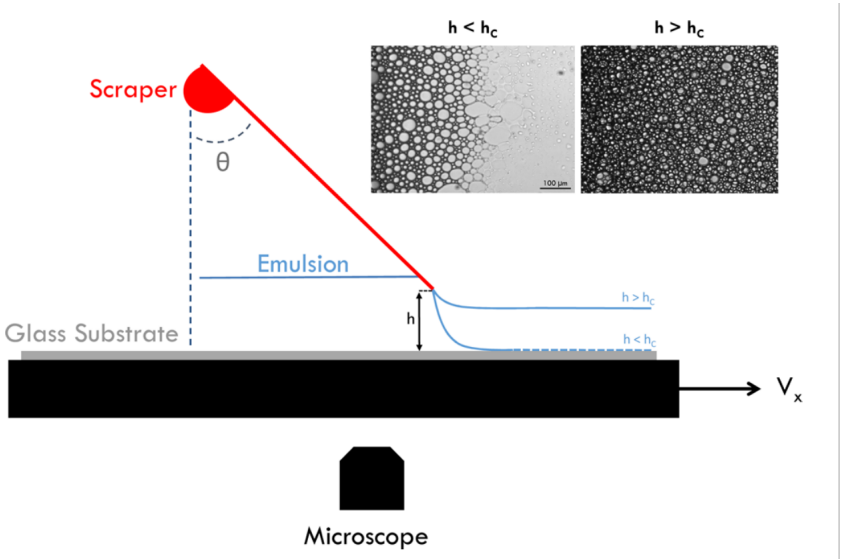

Figure 2.12: *Schematic of the microscopy set-up used while in Bordeaux. Taken from [92].*

Figure 2.12 shows a schematic of the alternative Bordeaux set up. To spread the emulsions on a glass substrate a homemade mechanical tool was used, consisting of a rigid blade and a thin rectangular microscope glass slide of 170 μm thickness, (2.4 cm width and 4 cm in length). The bottom of the blade is held at the desired distance h from the glass substrate on which the emulsion is to be deposited. The distance h, between the bottom end of the blade and the glass substrate, can be set using a precision translation stage and was varied from about 500 μm down to 20 μm. The angle of the blade with respect to the vertical direction θ can also be adjusted between $15 - 90°$. The experiments presented here are for $\theta = 45°$. A microscope (Zeiss Axio observer A1) and a fast camera (Hamamatsu Orca flash 2.8) was used to record the spreading of the emulsions either in transmission, bright-field imaging or by reflection using fluorescent molecules, fluorescein (from Exciton) in the continuous water phase. Fluorescein is excited at 525 nm and emits at 550 nm and allows the dispersed phase to be distinguished from the continuous phase. Using this set up emulsions with 20 wt% of CCT were sheared at a velocity of 10 mm/s at gaps from 40 μm to 10 μm.

2.7.4 Stability Measurements

In order to test emulsion stability various oil-in-water emulsions were made a subjected to centrifugation in order to calculate the critical disjoining pressure as discussed in Chapter 1

2.8 Experimental Protocol

Dilute emulsions (<0.1 wt%) were made by combining SZ with CCT in water using a Fisons WhirliMixer, at 30 000 RPM for 30 seconds. All dilute emulsions were made with 10 wt% CCT present. The dilute emulsions were centrifuged in a Thermo Scientific Sorvall ST40, for 15 minutes, at different acceleration values from 100g to 1200g. SZ concentrations ranged from 2.5×10^{-3} wt% to 0.08 wt%.

More concentrated homogenised emulsions were centrifuged in a Du Pont Sorvall RC-5B centrifuge at 20,000g. These samples were at a concentration of 0.5 wt% of SZ and 20 wt% of CCT.

The supernatant was imaged using a Zeiss LSM700 laser scanning microscope to

determine if the emulsion structure was intact after centrifuging.

Chapter 3

Rheology of SZ Microgels

3.1 Steady-Shear Rheology

3.1.1 Flow Behaviour

Using steady-shear rheology the flow behaviour of the SZ microgel suspensions was determined for a wide range of concentrations. Figure 3.1 shows how the shear stress σ depends on the applied shear rate $\dot{\gamma}$ for concentrated microgel suspensions (>0.1 wt%). For concentrations >0.1 wt% the suspensions developed a measurable yield stress σ_y, hence this is described as the concentrated regime. The dilute regime (<0.1 wt%) will be discussed later in this chapter. As the concentration of SZ increases the flow index converged towards 0.4 which is typical for other microgel systems [108] [109]. The σ_y, which becomes more prominent at the highest concentrations, rose two orders of magnitude from the lowest (0.1 Pa) to the highest (63.1 Pa) concentration of microgels (see Table 3.1). This result is comparable to other microgel systems and is usually indicative of interactions between microgels [109] [110]

Figure 3.2 shows how the relative viscosity η_{rel} depends on the SZ concentration for different applied shear rates $\dot{\gamma}$. From Figure 3.2 two critical concentrations can be identified, 0.025 wt% and 0.1 wt%. The latter critical concentration coincides with the development of a yield stress (σ_y), however, 0.025 wt% remains unclear. In order to ascertain the volume fraction of the microgels the swelling factor k needs to be determined [2]. In order to investigate this further the dilute regime

(<0.1 wt%) was investigated separately.

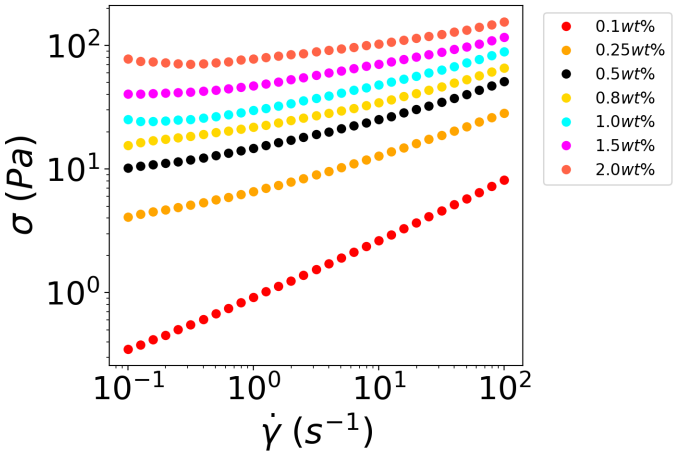

Figure 3.1: *Variations in shear stress σ plotted as a function of applied shear rate $\dot{\gamma}$ for various suspensions at different SZ concentrations.*

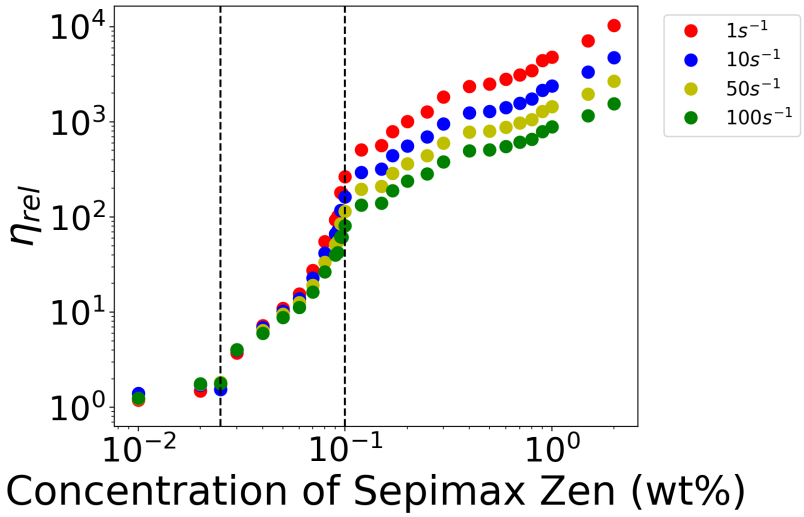

Figure 3.2: *Variations in relative viscosity η_{rel} plotted as a function of SZ concentration measured at specific shear rates. The dotted line highlight critical SZ concentrations:* 0.025 wt% *and* 0.1 wt%.

3.1.2 Dilute Regime

The volume fraction of the microgels was estimated using the Einstein relation, $\eta_{sys} = \eta_s(1 + 2.5\phi_{eff} + 5.9\phi_{eff}^2)$, where η_{sys} is the viscosity of the system, η_s

is the solvent viscosity and ϕ_{eff} is the effective volume fraction of the colloid. Einstein's relation holds for dilute ($\phi_{eff} < 0.2$) suspensions of hard spheres, however, there is an alternative for microgels [111]. In this case the effective phase volume can also be written in terms of a swelling ratio (k ml/g) and concentration (C g/ml), $\phi_{eff} = kC$. The modified Einstein relation takes the form, $\eta_{rel} = 1 + 2.5kC + 5.9(kC)^2)$, where η_{rel} is the relative viscosity. The variations in viscosity of suspensions in the Newtonian regime (C <0.025 wt%) were fitted to the modified Einstein relation and are shown in Figure 3.3.

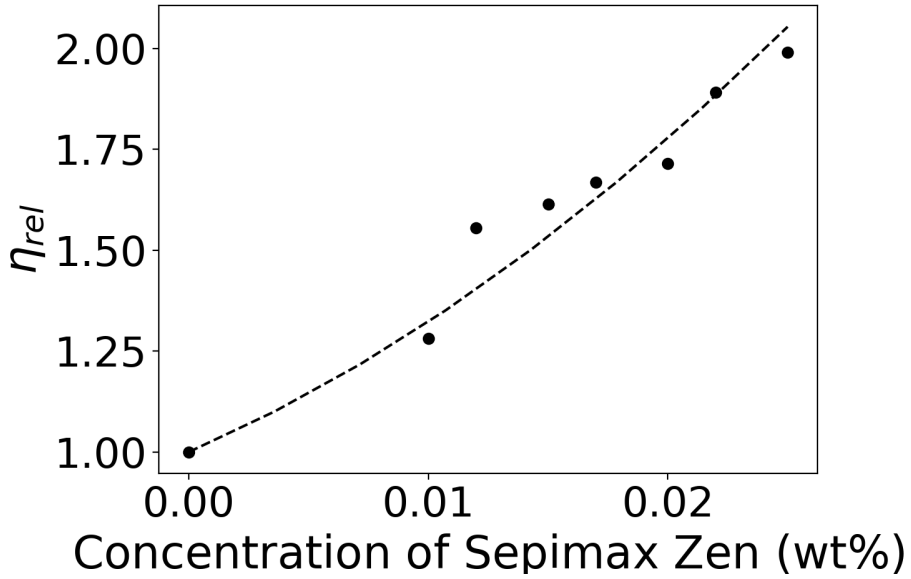

Figure 3.3: *Variations of the relative viscosity η_{rel} plotted as a function of SZ concentration. The dashed line represents the fit to the modified Einstein relation $\eta_{rel} = 1 + 2.5kC + 5.9(kC)^2)$.*

The fit yields $k = 0.10 \pm 0.3$, which is comparable to other microgel systems [111]. Furthermore, using the results of the modified Einstein fit concentration further packing concentrations can be predicted, close-packing ($\phi_{cp} = 0.64$) is predicted at 0.061 wt% and the fully packed concentration ($\phi_{eff} = 1$) is 0.097 wt%. It is important to note that the modified Einstein fit is insufficient to determine the rheology above $\phi_{eff} < 0.2$, however, the fully packed concentration does coincide with the critical concentration of 0.1 wt% identified in Figure 3.2.

In order to identify the concentration at which the suspension becomes fully packed, where $\phi_{eff} = 1$, more concentrated samples beyond the Einstein approximation ($\phi_{eff} > 0.2$) were analysed. The 'jamming' transition is identified

as the concentration where a free-flowing material begins to develop solid-like qualities i.e. a measurable yield stress. An alternative way to identify the critical 'jamming' concentration is to investigate the variations in the inverse viscosity η^{-1} as function of shear stress σ [112]. In Figure 3.4 a transition can be seen at 0.095 wt%, where the curvature of the data changes. This change occurs due to the suspension reaching the critical 'jamming' concentration, where the suspensions develop a yield stress. The work here was compared to Nordstrom *et al.* who performed similar studies on PNIPAM particles. Nordstrom *et al.* found the critical jamming volume fraction was 0.635, the same as with random close packing of spheres. Furthermore, it was found that PNIPAM microgels could deform under compression without deswelling, meaning approximations of packing fractions from dilute suspensions could reliably predict the concentrated rheology. Considering this work there is a inconsistency between the Einstein fits prediction, in Figure3.3, and the concentrated rheology shown in Figure 3.4. This may be due to the architecture of SZ microgels. These deviations from hard-sphere behaviour are often attributed to soft repulsion interactions between microgels [113]. For example the interaction potential between sterically stabilised colloids is mediated by the repulsion between the stabiliser layers, which are considered as soft interacting brushes. This is similar to neutral microgels, where the repulsion coming from the interaction between dangling chains. However, as SZ is a polyelectrolyte, there are charged units present within the system as well as the dangling surface chains, which will influence microgel-microgel interactions. In order to determine the the true ϕ the concentrated regime must be analysed.

The flow behaviour in the dilute regime was determined by considering the suspensions as power-law fluids, and fitting the data to $\sigma = k\dot{\gamma}^n$ [114] [15]. From this analysis the flow index n was determined to ascertain the flow behaviour of the microgel suspensions. Figure 3.5 shows that until a concentration of 0.03 wt% has been reached the suspensions behave as Newtonian fluids. Shear-thinning behaviour is then observed for concentrations above 0.03 wt%. The onset of shear-thinning is indicative of a percolating-network forming [15]. This result coincides with the previous findings shown in Figure 3.2, where 0.025 wt% was identified as a critical concentration. This effect suggests that a percolating network is formed before the ϕ_{cp} is reached meaning this interaction may be down to the composition of the microgels (discussed in Chapter 4). Above 0.1 wt% a definitive yield stress was detected and will be analysed in the following section.

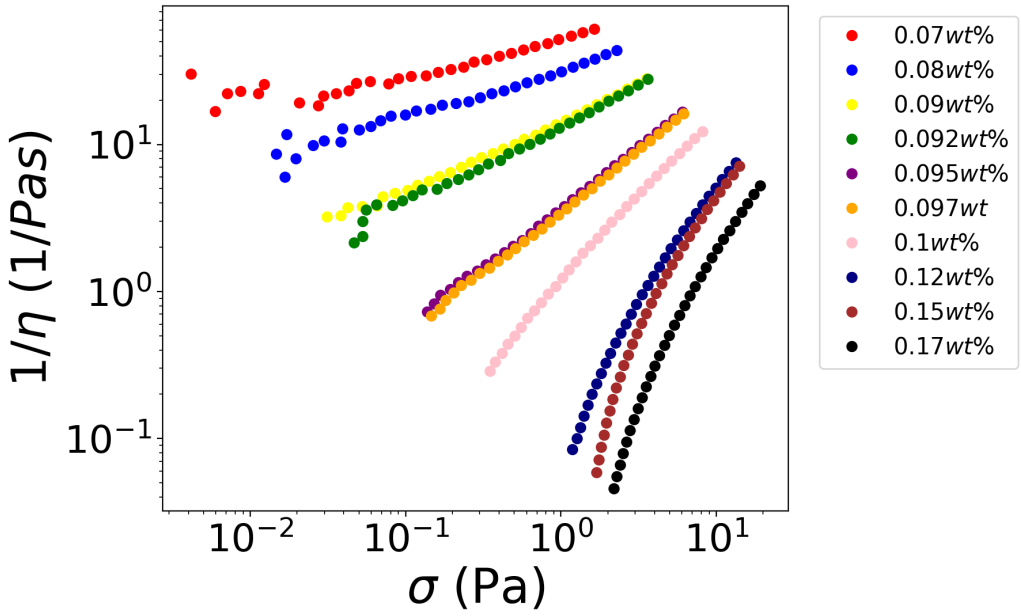

Figure 3.4: *Variations of the inverse viscosity η^{-1} as a function of shear stress σ for different concentrations of SZ.*

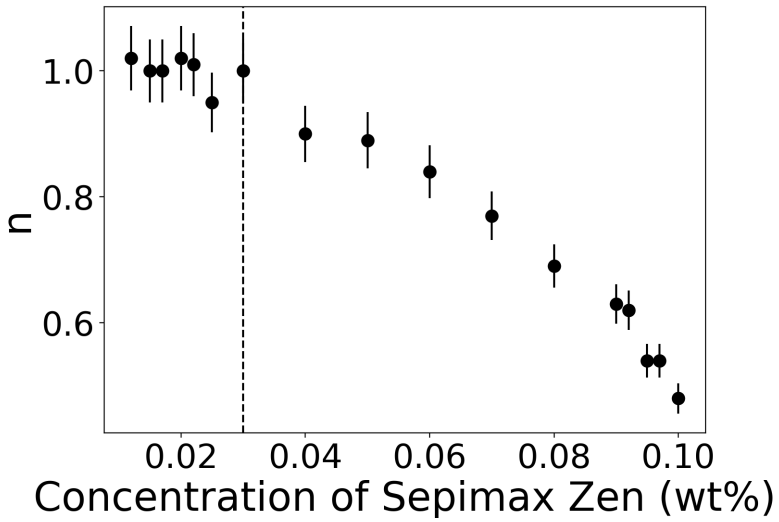

Figure 3.5: *Variations of the flow index n plotted as function of SZ concentration. n was determined by fitting stress-shear rate data to the power-law fluid equation, $\sigma = k\dot{\gamma}^n$. The dotted line at 0.03 wt% represents when the microgel suspensions go from Newtonian ($n = 1$) materials to shear thinning ($n < 1$).*

3.1.3 Concentrated Regime

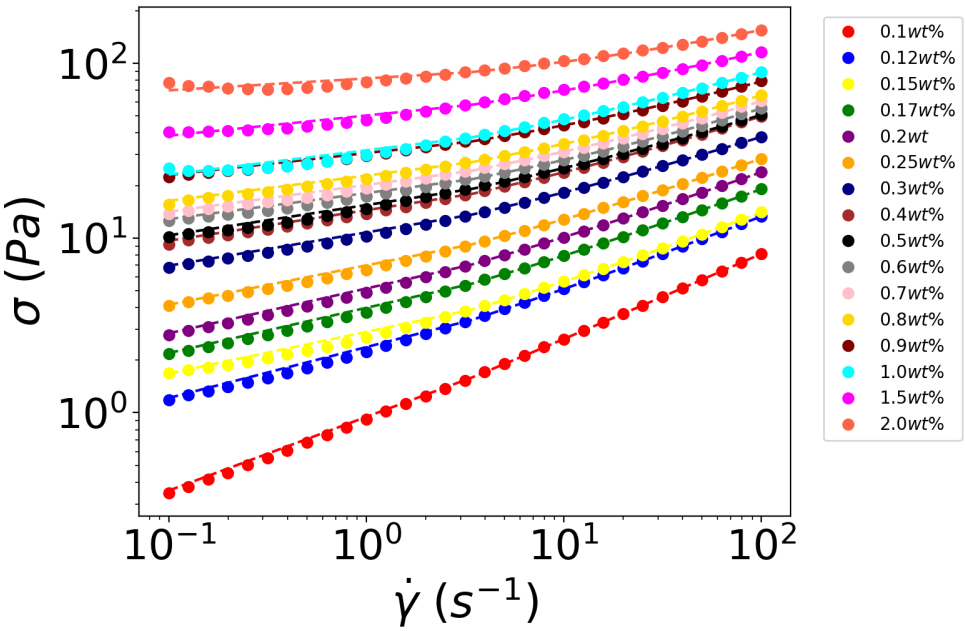

Figure 3.6: *Variations in the shear stress σ plotted as a function of applied shear rate $\dot{\gamma}$. Dashed lines are the fits of the data to $\sigma = \sigma_y(1 + (\tau\dot{\gamma}^{\beta})) = \sigma_y + k\dot{\gamma}^{\beta}$.*

Figure 3.6 shows the flow curves at high concentrations, which do not extrapolate to zero stress at a low shear rate, supporting the existence of a σ_y. These curves were analysed by fitting a generalised Herschel-Bulkley relation of the form:

$$\sigma = \sigma_y(1 + (\tau\dot{\gamma})^{\beta}) = \sigma_y + k\dot{\gamma}^{\beta}, \tag{3.1}$$

where β is the shear thinning exponent, τ is a time constant and k is the consistency index. The flow curves are characterised by a flat plateau, which is more prominent at higher concentrations, at low shear rates and a single power law variation at high shear rates. The values of σ_y, τ and β are reported in Table 3.1. σ_y increases by two order of magnitudes while β decreases from the lowest to the highest concentration. The average β over the concentrated regime is 0.40 ± 0.04 which proved similar to other soft colloids [13] [109]. Furthermore, theoretical studies indicate that a β value of 0.5 is indicative of jammed viscously-interacting athermal particles [115]. τ sharply decreases as concentration is

increased, indicating that the more concentrated the suspension the longer the relaxation time will be, this data is plotted in Figure 3.8. In Figure 3.8 τ begins to diverge as the concentration of SZ is decreased a trend which has been seen in other systems indicating when the critical volume fraction where the first σ_y is detected [109].

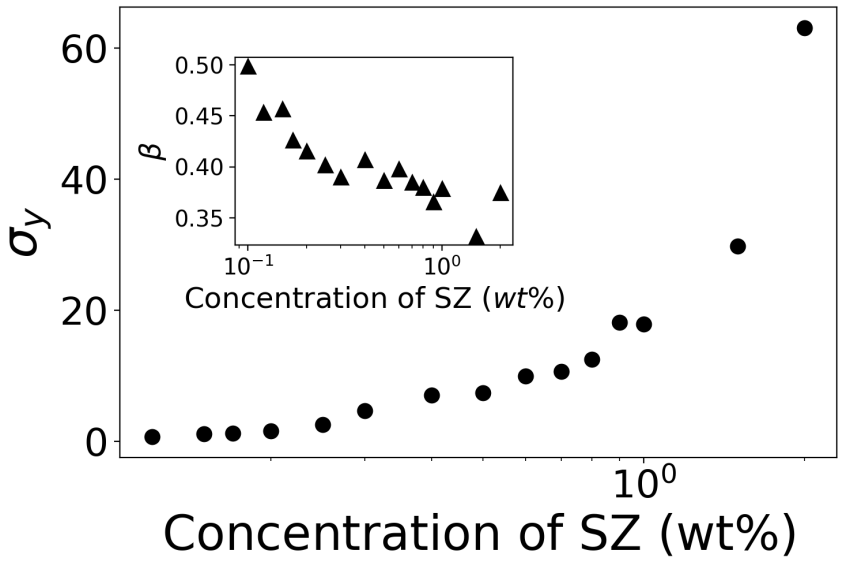

Figure 3.7: *Variations of the yield stress σ_y plotted as a function of concentration of SZ for the concentrated microgel suspensions. Inset shows how the shear thinning exponent β changes with concentration of SZ.*

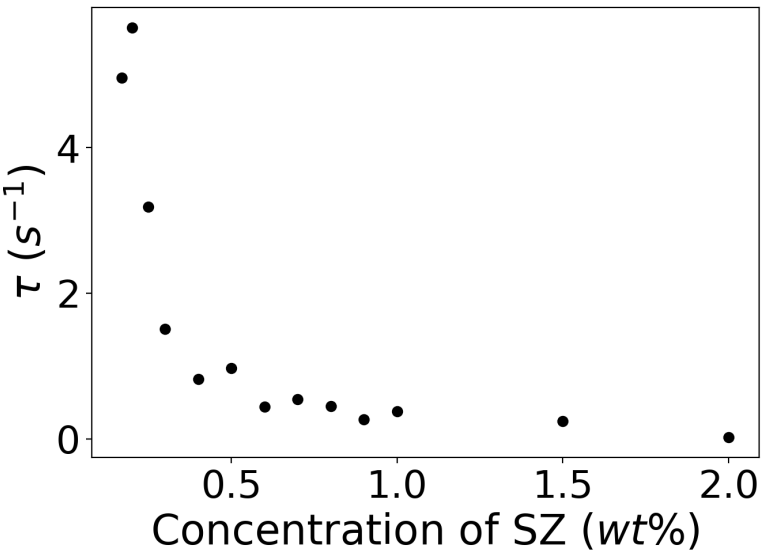

Figure 3.8: *Variations of the time constant τ plotted as a function of concentration of SZ for the concentrated microgel suspensions.*

C (wt%)	σ_y (Pa)	τ (s^{-1})	β
0.1	0.10	60	0.50
0.12	0.66	6.6	0.45
0.15	1.1	2	0.46
0.17	1.3	4.9	0.43
0.2	1.6	5.6	0.41
0.25	2.5	3.2	0.40
0.3	4.7	1.5	0.39
0.4	7.1	0.82	0.41
0.5	7.4	0.97	0.39
0.6	9.9	0.44	0.38
0.7	10.7	0.54	0.38
0.8	12.5	0.45	0.38
0.9	18.1	0.27	0.37
1.0	17.9	0.38	0.38
1.5	29.8	0.24	0.33
2.0	63.1	0.03	0.38

Table 3.1: *Values of experimental parameters determined from fitting the rheology experiments of concentrated microgel suspensions (data shown in Figure 3.6) in the concentrated regime with* $\sigma = \sigma_y(1 + (\tau\dot{\gamma}^{\beta})) = \sigma_y + k\dot{\gamma}^{\beta}$.

3.2 Oscillatory Rheology

3.2.1 Large Amplitude Rheology

Large amplitude oscillatory rheology was used to probe the mechanical nature of the concentrated microgel suspensions. In Figure 3.10 , the variations of G' and G'' are plotted as a function of strain amplitude γ for various concentrations of microgels. The lowest concentration tested was 0.07 wt% and highest being 2 wt%. The results are qualitatively the same as the other yield stress materials like hard sphere and soft particle glasses and emulsions [116] [117]. At low γ , the suspensions exhibit solid-like behaviour with $G' > G''$; both moduli are independent of γ, this is the linear viscoelastic regime (LVR). At larger amplitudes G' decreases whereas G'' goes through a maximum before declining and crossing

the G': the onset of non-linearity which is associated with yielding [118].

Theoretical models have attributed the peak in the G'' to be the γ where the local yielding occurs for attractive systems, and is a characteristic of other soft matter systems such as emulsions [119]. For colloidal systems the peak in G'' typically is found at $\gamma = 10\,\%$ wheras for SZ the peak is always $\gamma \approx 100\,\%$ which is similar to polymer systems [116]. However, the decrease in G' begins at strains as low $\gamma < 10\,\%$, particularly for the lower concentrations indicating with colloid-colloid interactions rather than polymeric behaviour. This again demonstrates the polymer-colloid duality of SZ microgels. However, in contrast to hard spheres where the yielding amplitude has been found to occur at approximately 13 %, which was attributed to the particles rearrangement as the glass begins to yield [116]. For SZ microgels the yield strain γ_y increases as concentration was increased resulting in γ_y above 200 % for the highest concentration which has been observed for polymeric systems such as xanthan gum [120]. The increasing γ_y suggests that as concentration increases the network becomes more compressed, therefore, yielding becomes more difficult. Furthermore, this is consistent with interpenetrating microgel networks where, when concentrated enough, microgel 'fuse' together forming a continuous gel network [121] [122].

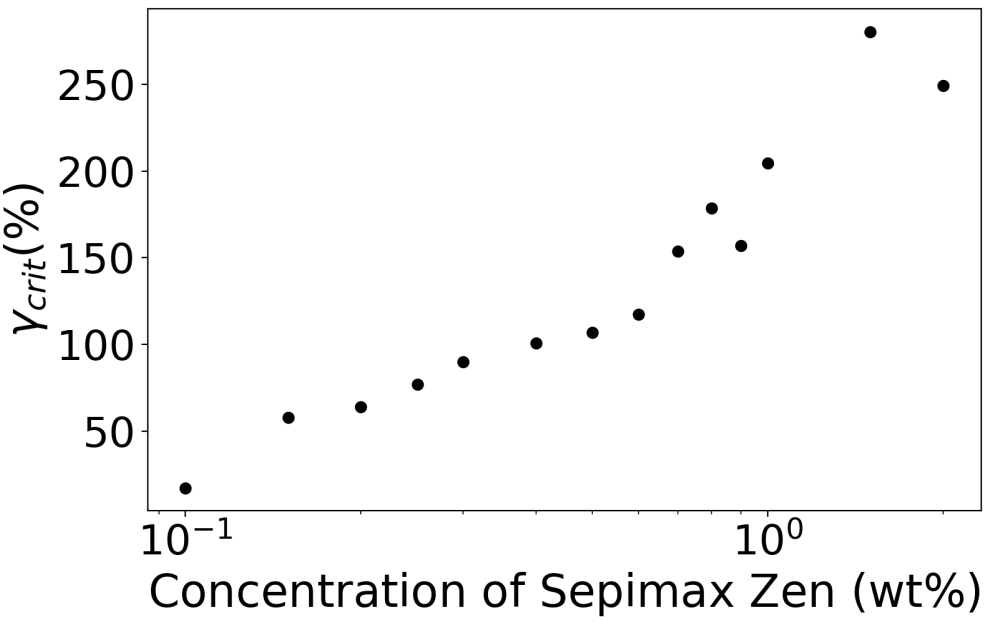

Figure 3.9: *Variations of the critical strain γ_{crit} plotted as a function SZ concentration. γ_{crit} is the strain where G' crosses G'' in the oscillatory rheology plots shown in Figure 3.10.*

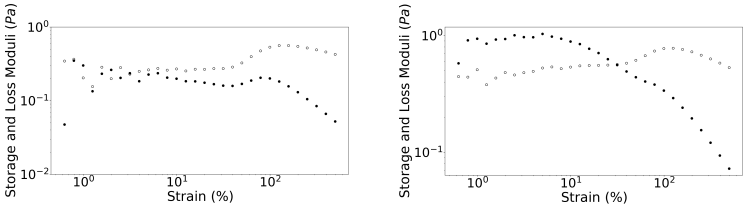

(a) 0.07 wt%

(b) 0.08 wt%

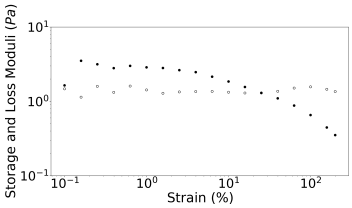

(c) 0.1 wt%

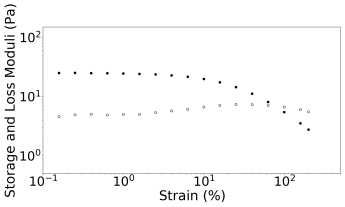

(d) 0.2 wt%

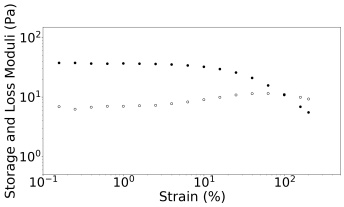

(e) 0.3 wt%

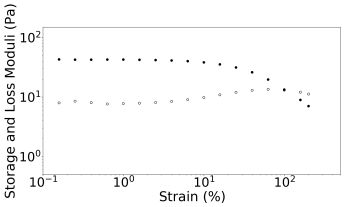

(f) 0.4 wt%

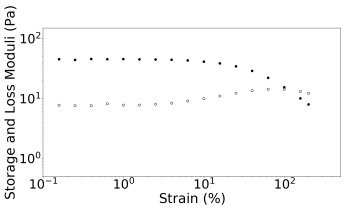

(g) 0.5 wt%

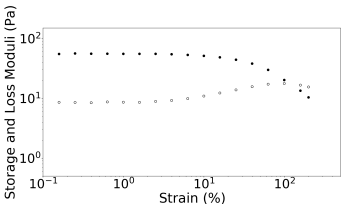

(h) 0.6 wt%

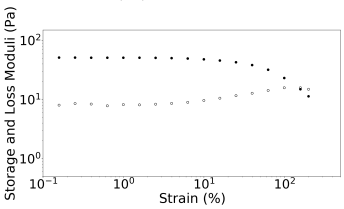

(i) 0.7 wt%

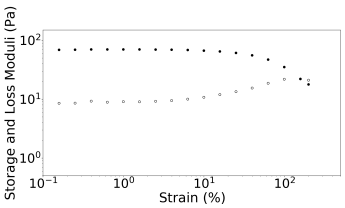

(j) 0.8 wt%

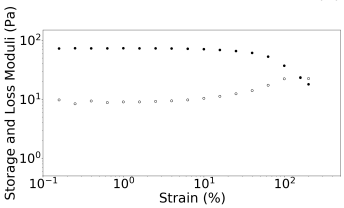

(k) 0.9 wt%

Figure 3.10: *Variations in the storage and the loss moduli plotted as a function of strain of the SZ microgel suspensions at various concentrations. Filled symbols represent the storage modulus and unfilled is the loss modulus.*

3.2.2 Shear Elasticity of the Microgel Network

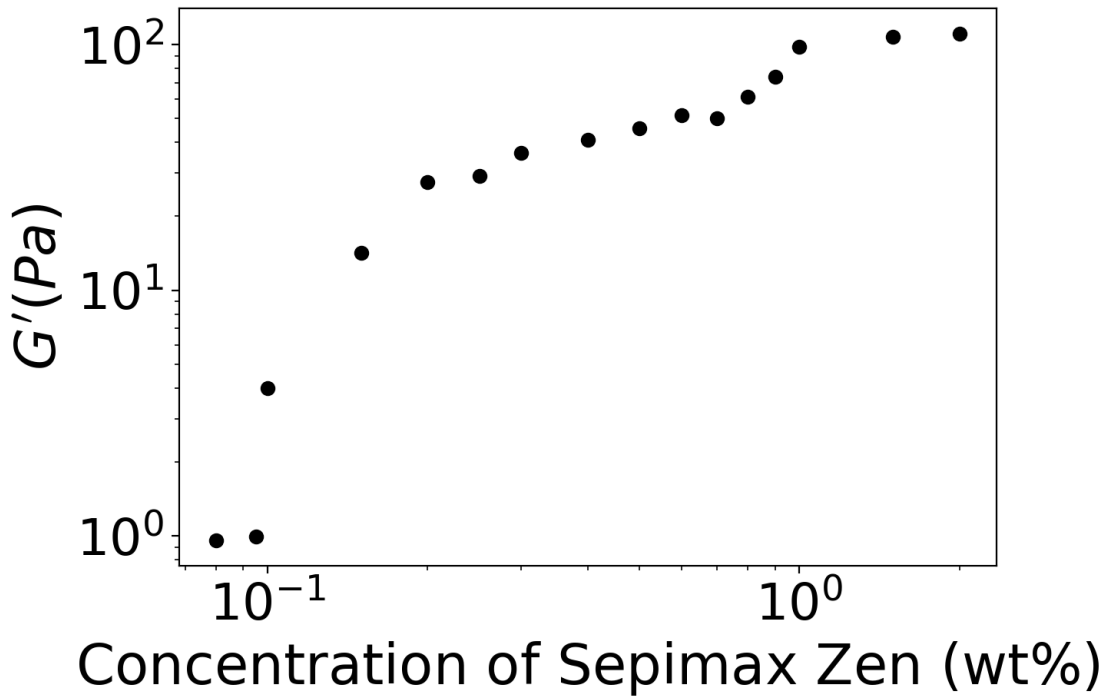

Figure 3.11: *Variations of the plateau modulus G_0 plotted as a function SZ concentration. G_0 is determined by averaging G' is the LVR.*

Figure 3.11 shows how the plateau shear modulus G_0 of the microgel suspensions depends on SZ concentration. G_0 was determined by taking the average value of G' in the LVR. G_0 was found to follow a power law of the form, $G_0 \propto C^{\mu}$ but the value of μ varied depending upon the concentration. G_0 is found to begin increasing from 0.095 wt% till to 0.2 wt%, with a μ value of 3.88, then, μ decreases to 0.67. This trend has been observed for other microgel systems and the change in gradient is attributed to the formation of a compressed-jammed network is formed [33] [38] [117]. In this regime it is theorised that microgels interpenetrate forming a gel which behaves as a connected macroscopic network of flexible elastic strands, like rubbers. From classical rubber theory the elasticity, which is entropic in origin, is from a single strand that spans the whole network in which $G' = c_p[N_a/M_mN]k_bT$, where c_p is the polymer concentration, N_a is Avogadro's number, M_m is the molecular weight of the monomer and N is the number of monomer units per cross link [123]. Using the highly concentrated G' data (>0.2 wt%), where $m = [N_a/M_mN]k_bT$ and M_m is approx 200 g/mol,

the average N was found to be 1300. When comparing to similar studies a $N = 1300$ indicates that SZ forms a soft set gel at high concentrations. The early concentration data (0.095 wt%) is indicative of gel-like material, where full jamming has not yet occurred. It should be noted that these early concentrations, shown in Figure 3.11, show little separation of G' and G'' indicating that this is the onset of 'solid' formation. This is supported by the previous result of random-close packing occurring at 0.061 wt%, as this results in solid character being detected.

3.3 Linking the Shear and Oscillatory Rheology

In an attempt to connect the findings of the oscillatory and shear rheology, the flow curves obtained for the concentrated regime were rescaled using σ_y and G_0, a procedure which has done been with similar systems [13] [38]. In a steady state, elastic restoring forces can be approximated by the plateau modulus, G_0, while interparticle friction can be estimated by considering the viscous drag flow that occurs in the thin film of solvent η_s between the particles which scales with the solvent viscosity [13]. Hence, it is possible to rescale the concentrated flow curves using independently measured values of the G_0 and the yield stress σ_y. Figure 3.12 shows the rescaled flow curves of the most concentrated microgel suspensions. The collapse of the various data sets is resonable to approximate a master curve which is well represented by an equation of the Herschel-Bulkley form. At low shear rates microgels can rearrange retaining the network structure, hence a σ_y is measurable. As the shear rate increases, and flow is induced, microgels begin to constantly rearrange. Given the increased interactions, the stress also increases which is mediated by the inter-microgel friction. The collapse seen with this data is comparable to other colloidal scale microgel suspensions [38].

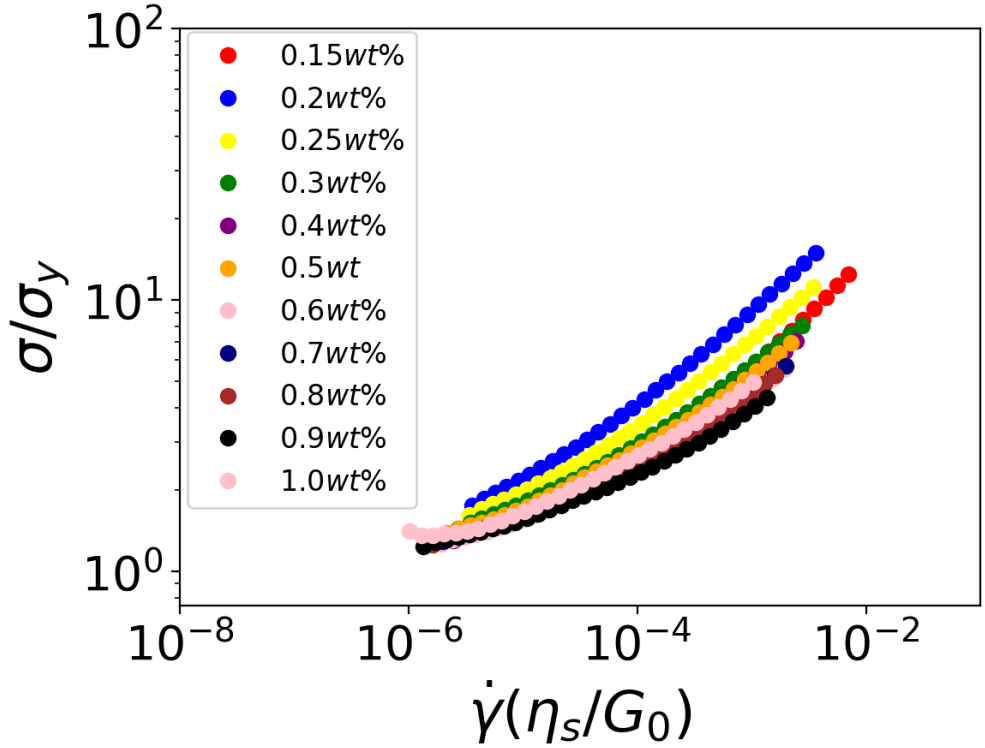

Figure 3.12: *Variations in the shear stress σ, which has been rescaled by the yield stress σ_y, plotted as a function of the shear rate $\dot{\gamma}$, which is rescaled by the solvent viscosity η_s by the plateau modulus G_0.*

The σ_y calculated from the Hershel-Bulkley fits were compared to the σ_y measured in the oscillatory tests (crossover point in Figure 3.10). Figure 3.13 shows that both methods yield the same trend however, there are differences in magnitude between the data sets. This is attributed to the different methods used, for the static case (oscillatory) yielding refers to the separation of the interpenetrated polymer brushes on the surfaces of the microgels, In a dynamic situation, where the microgels are flowing (steady shear), the polymer brushes could be compromised e.g. damaged meaning the determined yield stress will be lower. Hence the yield stress on a flowing material is significantly lower on than that determined by increasing the stress on the same material at rest.

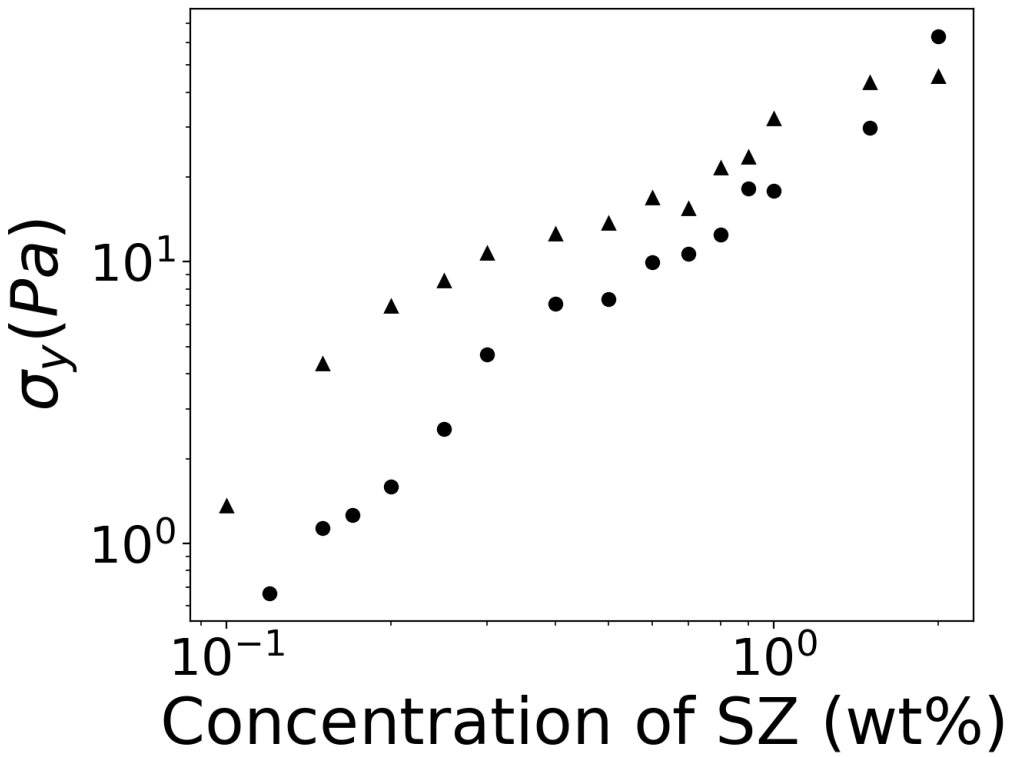

Figure 3.13: *Variations in the yield stress σ_{yield} plotted as a function of SZ concentration, triangles represent σ_{yield} extracted from the oscillatory rheology in Figure 3.10 and circles represent the σ_{yield} obtained by fitting the to steady state shear rheology $\sigma = \sigma_y(1 + (\tau\dot{\gamma}^\beta)) = \sigma_y + k\dot{\gamma}^\beta$.*

3.4 Summary

In this chapter the rheological profile of the SZ microgels was explored using both steady shear and oscillatory rheology. Using steady shear rheology the flow behaviour of the suspensions was determined. Microgel suspensions behave as Newtonian fluids when dilute but as the concentration is increased a percolating network forms with a measurable yield stress. The yield stress increases by two orders of magnitude over the concentration range studied here. The most concentrated regime shows a similar rheological profile of gel-like materials composed of other microgels.

Once significantly concentrated microgels form an elastic compressed gel network. When compared to other microgel systems SZ is a loosely cross-linked network

which forms a soft set gel. The rheological profile of SZ is similar to other colloidal microgels, where at low shear microgels rearrange to retain the network structure but begin to flow as higher shear rates are imposed. In summary the main points from this chapter are as follows:

- Below 0.03 wt% the SZ suspensions behave as Newtonian materials
- Above 0.03 wt% suspensions become shear thinning brought on by microgel interactions
- 0.061 wt% is the predicted close-packing concentration, determined by the modified Einstein relation
- 0.07 wt% is the first detection of $G' \approx G''$ through oscillatory rheology, showing suspensions becoming elastic
- 0.1 wt% is the onset of the yield stress in shear rheology which coincides with predicted fully packed concentration 0.097 wt% again determined by the modified Einstein fit.

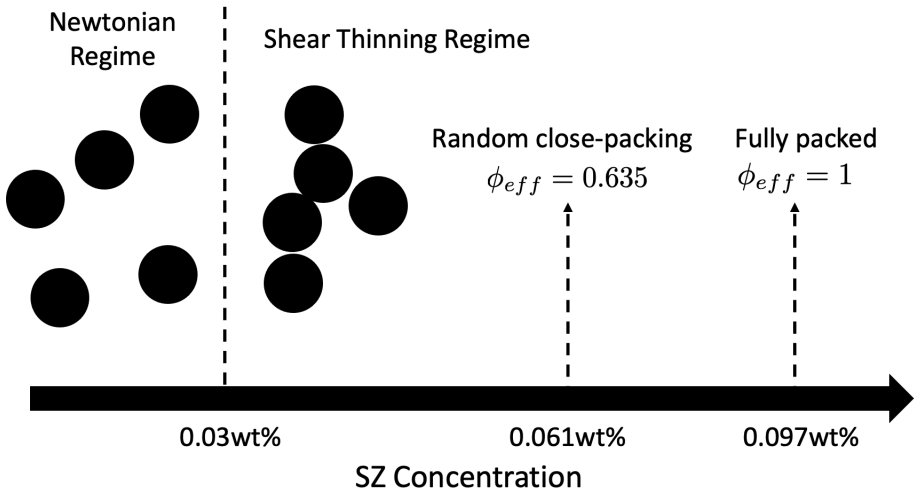

Figure 3.14: *Phase diagram of the SZ microgels, showing the key features uncovered from the rheological measurements detailed throughout this chapter.*

In the next chapter the dynamics of SZ microgels is analysed in order to ascertain the size of particles. This will reveal how the motion of the particles changes as packing is increased.

Chapter 4

Dynamics of SZ Microgels

The characterisation of the dynamics of the SZ microgels is essential in order to understand the gel formation mechanism. By studying the dynamics, using DDM (see Chapter 2 for details), the mobility of the microgels can be determined and compared to the results from the previous chapter. The combination of the mobility and rheology measurements will result in a much more detailed picture of how the SZ microgels interact to eventually form 'soft' gel networks.

4.1 SZ Microgels Diffusivity in Water

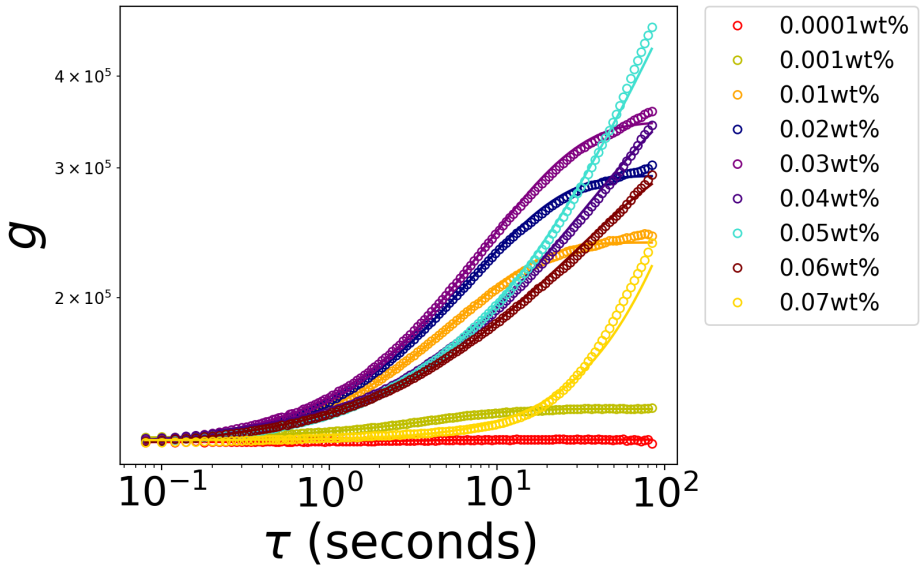

Figure 4.1: *Variation of the differential image correlation function g plotted as a function of the delay time τ, at fixed q value of $1.66\,\mu\mathrm{m}^{-1}$, for a variety of SZ concentrations.*

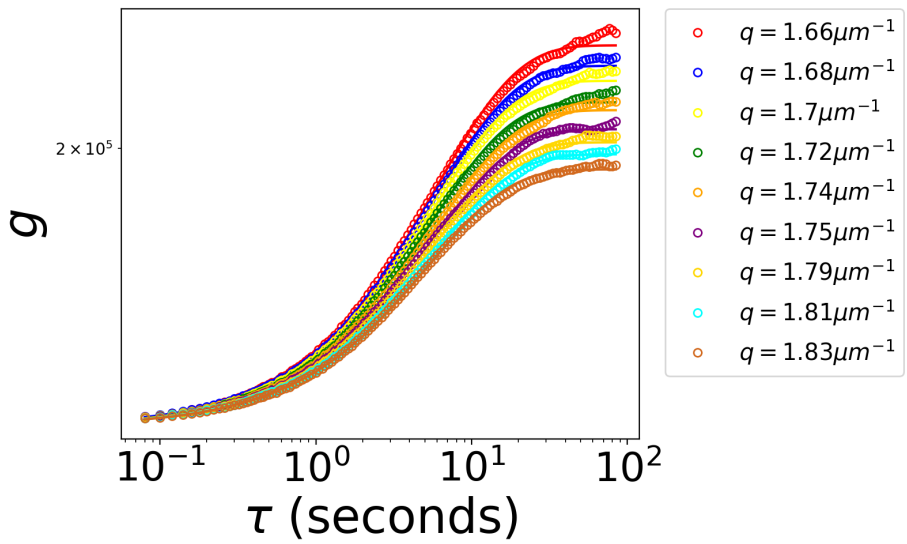

Figure 4.2: *Variation of the differential image corrlation function g plotted as a function of the delay time τ, for a fixed concentration of SZ of $0.01\,\mathrm{wt}\%$, at a variety of q values.*

Figure 4.1 shows how g the differential image correlation function (see Chapter 2) varies as function of the delay time τ, for a specific q value ($q = 1.66\,\mu\mathrm{m}^{-1}$). It can be seen that g reaches a steady plateau for concentrations under 0.04 wt%. Beyond 0.04 wt% the g functions do not reach a steady plateau, therefore, it is more difficult to extract the dynamics, in this situation an effective diffusion coefficient is determined. Using the fits to g, the stretch exponent β and relaxation time τ_R from which a diffusion coefficient D (or an effective diffusion coefficient) can be determined from $\tau_R = 1/Dq^2$. A selection of fits can be seen in Figure 4.2.

Figure 4.3 shows the of variation of τ_R as a function of q. The data follows a power law of the form $\tau_R \approx q^{-n}$, the average n-value across the concentrations shown (0.0001 wt% - 0.03 wt%) is 2.4 ± 0.5. The inset shown in Figure 4.3 shows how n behaves as a function of SZ concentratation. From the results it can be seen that n decreases as the concentration of SZ increases. If $n = 2$ the colloid particles undergo simple diffusive Brownian motion [124]. However, in the case of SZ $n > 2$ until 0.03 wt% where $n = 1.7$. A value of $n > 2$ has been observed for polymer systems where motion is influenced by the composition of the polymers or hydrodynamic interactions [125]. As microgels are not hard spheres, there will be fluctuations in density associated with the internal degrees of freedom of the microgel particles, as well as due to any diffusive motion, and also collective motion of the concentrated polymer solution. Such exponents have been seen in polymeric systems where collective and internal motions and degrees of freedom can result in values of $n > 2$ [125]. Given that this is the dilute limit (< 0.005 wt%), where hydrodynamic interactions are minimised, this effect is likely due to structure of the microgels. As the microgels are dispersed in an aqueous environment the hydrophobic sections will act to avoid the water where the hydrophilic parts will be in contact with the water, thereby influencing the diffusivity of the particles. However, as the concentration of SZ is increased n decreases below 2 at 0.03 wt%. This effect is likely due to the increase in hydrodynamic interactions of the microgels, which would act to overtake the influence of the hydrophobic parts. The decrease in the exponent n has been been observed in other studies for concentrated systems, where the diffusivity is dominated interaction of particles [126] [127] [128]. This is reflected in the data shown in Figure 4.4 which shows the variation of β as a function of SZ concentration. Below a SZ concentration of 0.03 wt% β remains at a consistent value of ≈ 1, however, beyond this it decreases to 0.52 at 0.07 wt%. The decrease of β typically signals the onset of the colloids forming cages, where colloids become

trapped by neighbours slowing down the dynamics of the system [129] [130] [131]. This behaviour is also signalled by the onset of a yield stress, which was measured at 0.07 wt%, which is just above the predicted close-packed concentration of 0.061 wt% in Chapter 3, which further reinforces the fact that SZ microgels form packed networks similar to soft colloidal gels [132].

The average diffusion coefficient D is plotted as a function of concentration of SZ is shown in Figure 4.5. Below a SZ concentration of $c \approx 0.005$ wt%, we find an approximate constant diffusivity of $D \approx 0.08\,\mu\text{m}^2\text{s}^{-1}$, consistent with spherical particles of hydrodynamic radius $R = 2.7\,\mu\text{m} \pm 0.3\,\mu\text{m}$, which is much larger compared with other microgel systems [2] [133] [134]. Between $c \approx 0.005$ wt% and 0.04 wt% , D decreases by an order of magnitude, reaching a minimum at $c \approx 0.04$ wt%. For suspensions with a concentration of 0.04 wt% or higher D was due to drift of the collective suspension, and proved difficult to eliminate. However, in some samples it was shown that impurities such as dust were still free to diffuse throughout. This result coincides with the shear rheology measurements highlighted in Chapter 3, where a transition between Newtonian and non-Newtonian motion occurs at 0.04 wt%. The non-Newtonian or shear thinning observed in the rheology suggest a microgel network forming leading to a reduction in particle motion, this has been observed form both hard colloids and microgels [135] [136] [137]. However, as impurities could still diffuse at this concentration it indicates that 0.03 wt% is the start of network formation.

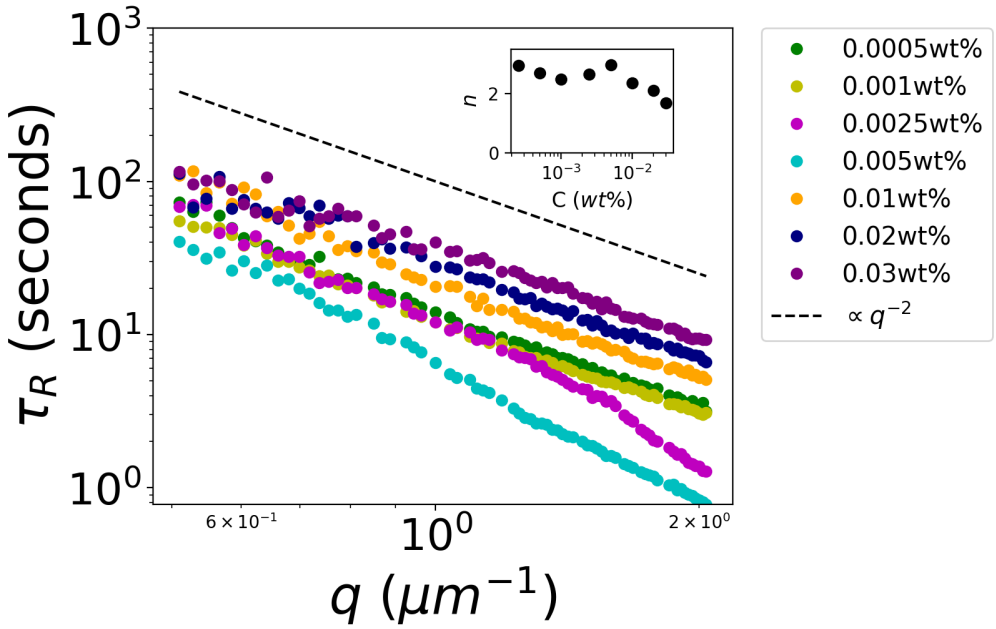

Figure 4.3: *Variation of the relaxation time τ_R plotted as a function of the wave vector magnitude q. τ_R was determined from the fits shown in Figure 4.1. Inset graph shows how the exponent n depends on the SZ concentration (C).*

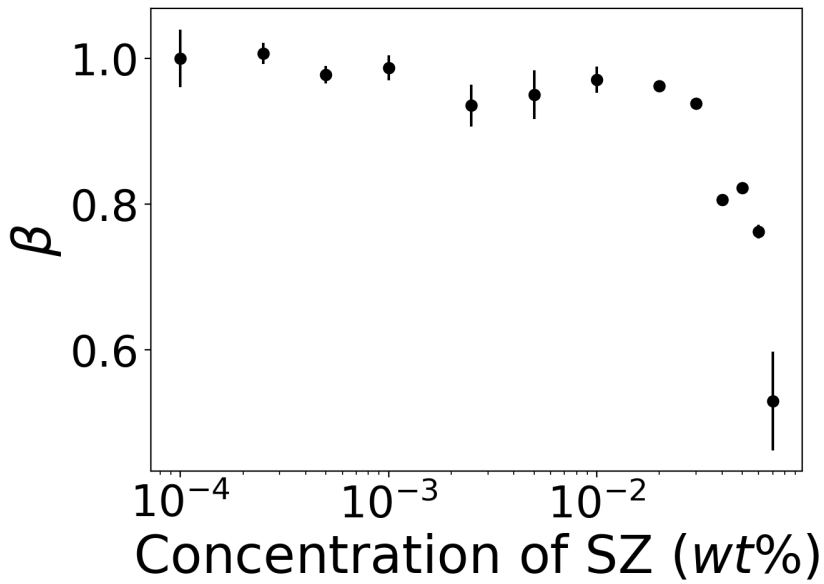

Figure 4.4: *Variation of the average stretch exponent β plotted as a function of the SZ concentration. β was determined from the fits shown in Figure 4.1.*

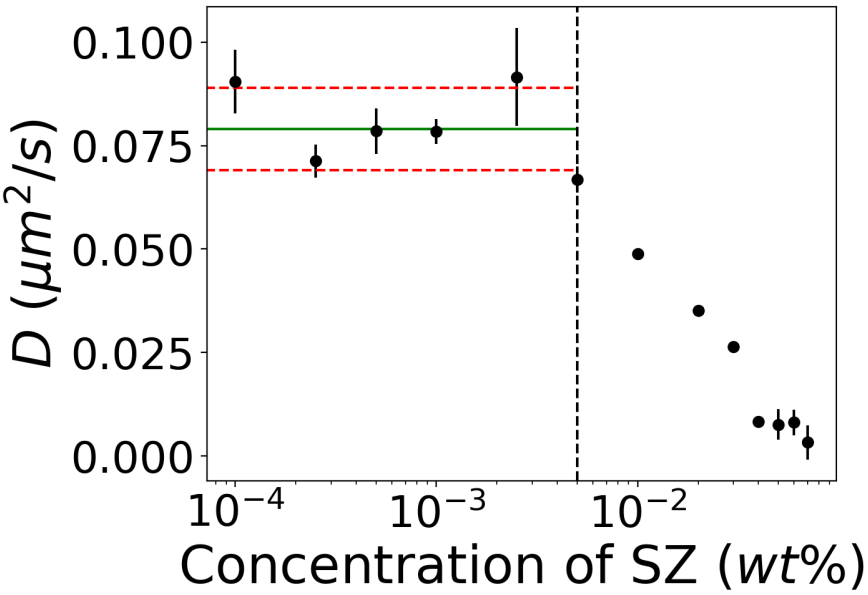

Figure 4.5: *Variation of the average diffusion coefficient D plotted as a function of the SZ concentration. D was determined from the fits shown in Figure 4.1. The dotted black indicates where the dilute regime ends (*0.005 wt%*) and the green line represents the average D for dilute regime while the red lines represents the standard deviation.*

4.2 Effect of Salt on SZ microgels

In order to investigate the swelling of the microgel a dilute concentration of 0.000 25 wt% was mixed with various NaCl solutions. The concentration of 0.000 25 wt% was chosen as this was in the dilute regime, where microgel-microgel interactions are minimised (to reflect this $\beta \approx 1$ for all measuremtents in Figure 4.6). Figure 4.6 shows the dependence of D for dilute microgels exposed to different concentrations of saline solution. Below 200 mM of NaCl, D remains at a constant value of $\approx 0.09\,\mu\text{m}^2/\text{s}$, which corresponds to a hydrodynamic radius $R_h \approx 2.3\,\mu\text{m} \pm 0.2\,\mu\text{m}$. Once 200 mM NaCl has been reached the diffusivity increases to an average value of $\approx 1.6\,\mu\text{m}^2/\text{s}$, which corresponds to $R_h \approx 1.3\,\mu\text{m} \pm 0.04\,\mu\text{m}$. This decrease in size is due to microgels deswelling in response to the added NaCl. This effect occurs as the salt changes the osmotic pressure balance between the inside and outside of the microgels [138] [139]. Additionally, the ions are capable of penetrating the lightly cross-linked corona of the microgel, which

allows them to interact with the charged monomer units. A similar result has been observed for nanoparticles with electrolytes grafted to the surface, with the shrinkage in this case due to the neutralisation of the grafted chains [140].

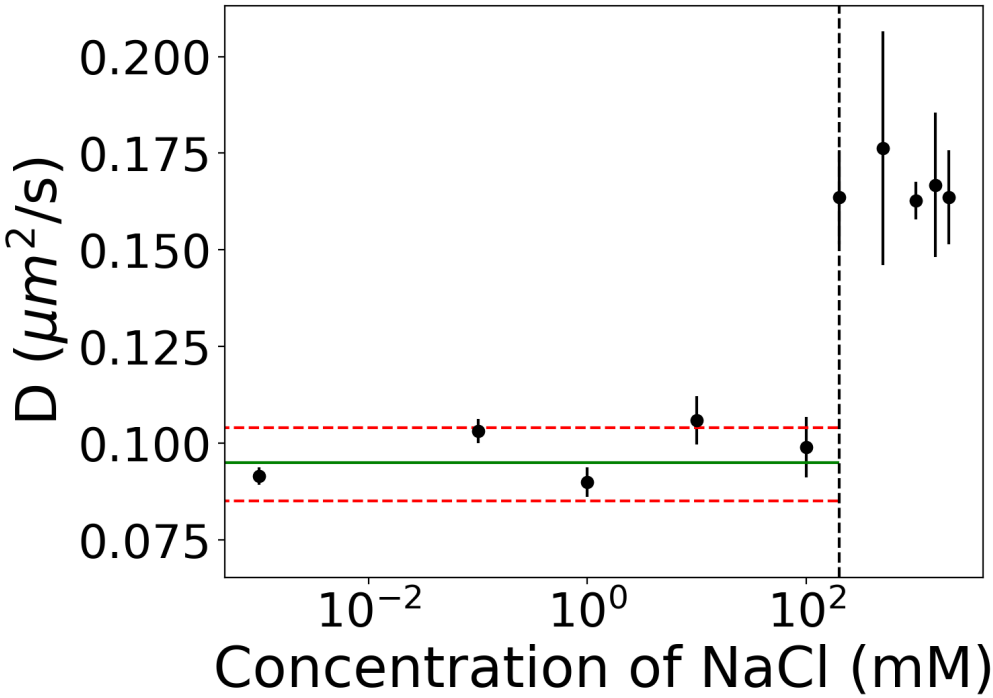

Figure 4.6: *Variation of the average diffusion coefficient D plotted as a function of the NaCl concentration, at a fixed SZ concentration of* 0.000 25 wt%. *The dotted black indicates where the shrinkage occurs (*200 mM*) and the green line represents the average D for dilute regime while the red lines represents the standard deviation.*

Figure 4.7 shows how g varies as a function of τ for various SZ concentrations with 200 mM of NaCl added. The diffusivity and β was extracted using the same procedure in the previous section. Similar to the swollen case, $D \approx 0.19\,\mu\text{m}^2/\text{s}$ up to 0.02 wt% where it continued to decrease up to 0.35 wt%. This behaviour is reflected in Figure 4.9, where the variations of β are plotted against SZ concentration, as β drops to 0.8 at 0.35 wt%, indicating at the highest concentration measured particle interactions become prominent. The q-dependence of τ_R is shown in Figure 4.8, where again similar to the swollen case n is above 2 for all measurements. However, the variation in this case is not as drastic as observed in Figure 4.3, this is likely due to the shrinkage of the

microgels. As the microgels have shrunk the particles will be pack more tightly meaning the particles motion is dominated by Brownian diffusion.

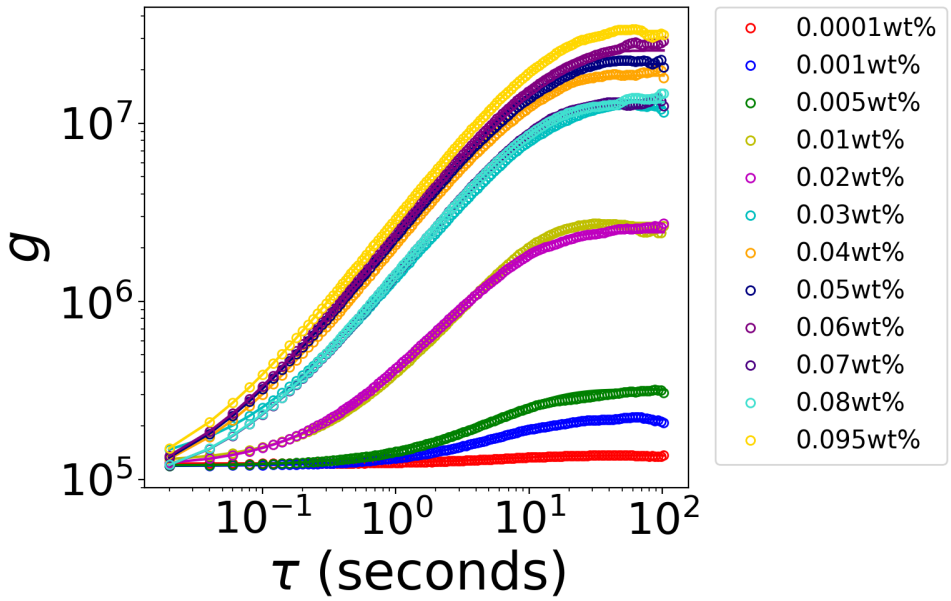

Figure 4.7: *Variation of the differential image corrlation function g plotted as a function of the delay time τ, at fixed q value of* $1.5\,\mu\mathrm{m}^{-1}$*, for a variety of SZ concentrations with* 200 mM *NaCl added.*

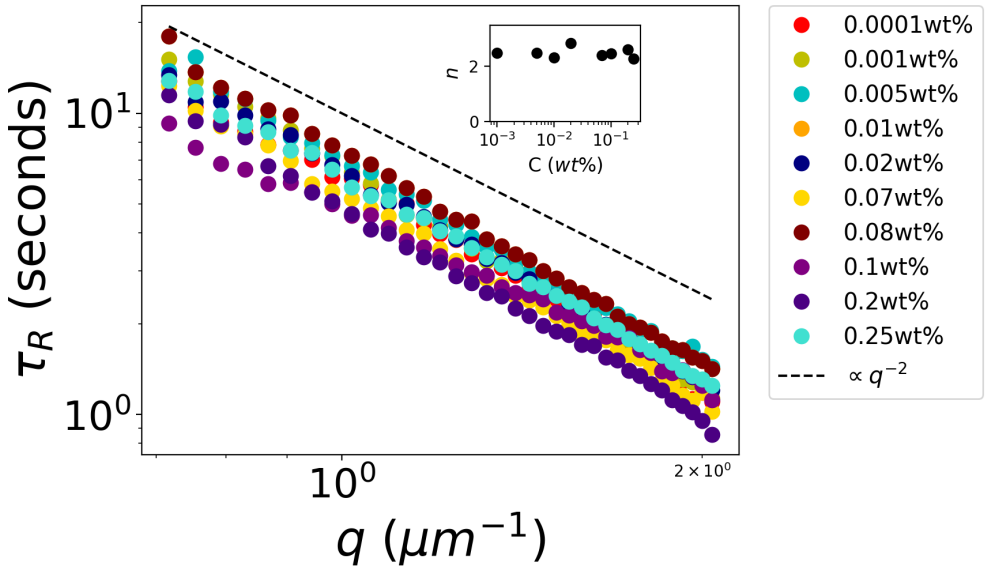

Figure 4.8: *Variation of the relaxation time τ_R plotted as a function of the wave vector magnitude q concentration for a variety of SZ concentrations with* 200 mM *NaCl added. β was determined from the fits shown in Figure 4.7, where the data was fitted to equation 4.1*

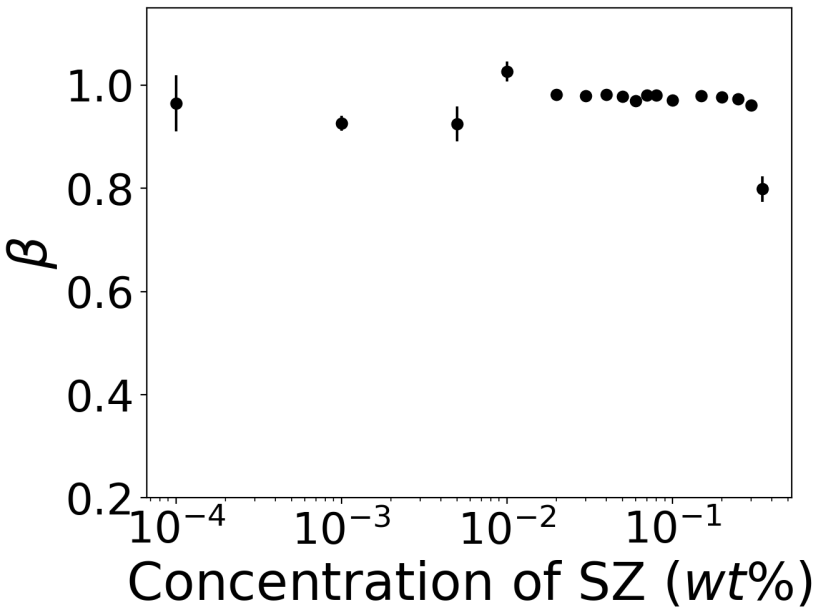

Figure 4.9: *Variation of the average stretch exponent β plotted as a function of the SZ concentration at a fixed salt concentration of* 200 mM. *β was determined from the fits shown in Figure 4.1, where the data was fitted to equation 4.1.*

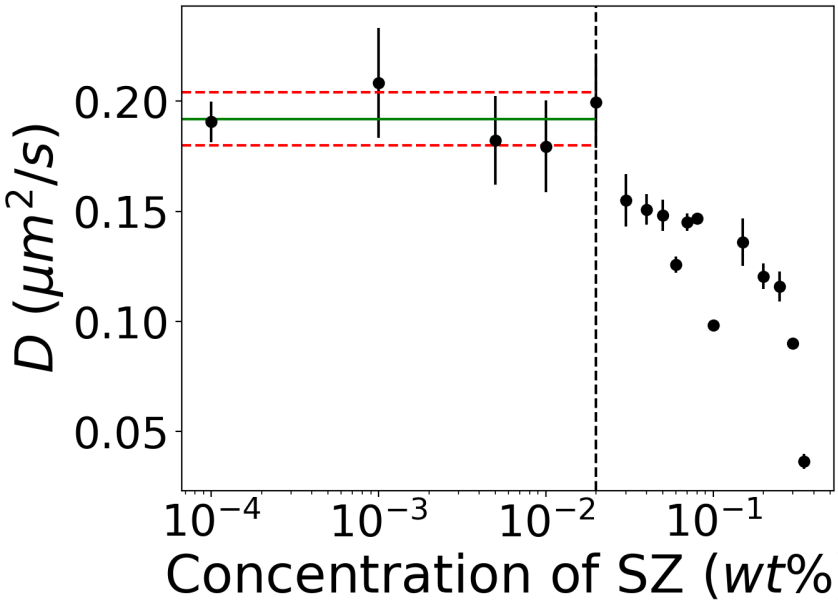

Figure 4.10: *Variation of the average diffusion coefficient D plotted as a function of the SZ concentration, at a fixed salt concentration of* 200 mM. *D was determined from the fits shown in Figure 4.7, where the data was fitted to equation 4.1.*

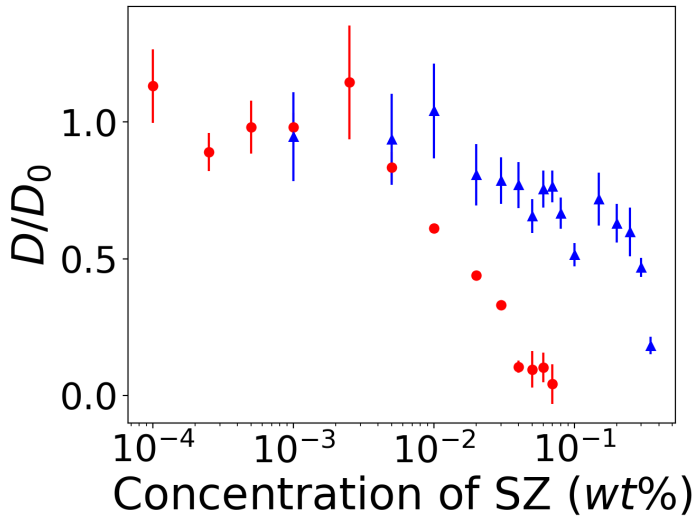

Figure 4.11: *Variation of the rescaled diffusivity D/D_0 plotted as a function of the SZ concentration for both swollen and deswollen microgels. Red points represent the swollen microgels and blue points represent the deswollen case.*

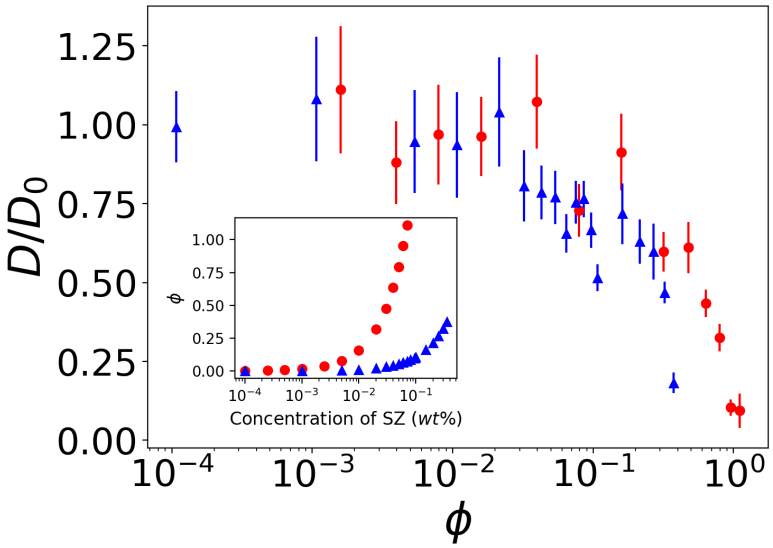

Figure 4.12: *Variation of the rescaled diffusivity plotted D/D_0 as a function of the volume fraction of microgels ϕ. Inset: ϕ plotted as a function of the SZ concentration. Red points represent the swollen microgels and blue points represent the deswollen case.*

In order to compare the diffusivity of the swollen and deswollen microgels, D was rescaled by the initial constant diffusivity D_0 (for swollen microgels $D_0 \approx 0.08\,\mu\text{m}^2/\text{s}$ and $D_0 \approx 0.19\,\mu\text{m}^2/\text{s}$ for deswollen microgels) and plotted as a function of SZ concentration, which is shown in Figure 4.11. If the SZ microgels are taken as hard colloids the minimisation of diffusivity signals the onset of close-packing ($\phi_{cp} = 0.63$) i.e. where crowding reduces mobility of individual particles [141]. The decrease of D/D_0 occurs at 0.005 wt% for swollen microgels and 0.2 wt% for deswollen microgels. Assuming the microgels are hard colloids for 0.005 wt% of swollen microgels corresponds to $\phi = 0.08$ and 0.2 wt% of deswollen microgels corresponds to $\phi = 0.02$ (see Figure 4.12). This result indicates that diffusivity begins to decrease far below the onset of close-packing, therefore, this effect may be due to the dangling polymers chains on the microgels surface. As the concentration of microgels increases the potential of microgels interacting increases which will be mediated by the dangling polymer chains. When brought closer together grafted-polymer chains are known to interact with each other [142]. This result is comparable with studies into attractive sphere where effects can be seen as low as $\phi \approx 0.1$ [143] [144] [145]. In such systems motion is effected as the attraction between spheres causes clusters to form thereby reducing the diffusivity, similar results have been seen in polymer-colloid

systems where depletion occurs. Furthermore, as mentioned earlier impurities could freely diffuse within the network despite the diffusivity of the microgel matrix minimising. Therefore, this supports the previous results from Chapter 3 where close-packing was predicted at 0.061 wt%. As the concentration of microgels increases, and interactions occur, diffusivity decreases until a sufficient network forms (0.03 wt%). However, this network is fragile as close-packing has not been reached yet (evidenced by impurities being able to freely diffuse in the matrix) which occurs at 0.061 wt%, predicted by shear rheology and confirmed by oscillatory measurements. The trend occurs in both the deswollen and swollen cases but at different concentrations due to the size difference between the two cases.

4.3 Effect of Osmotic Pressure on SZ Microgels

In order to test how the compressibility of SZ microgel, Ficoll-400 was used to tune the osmotic pressure of the suspensions. Figure 4.13 shows how diffusivity of the SZ microgels, at a fixed concentration of 0.0025 wt%, varies as a function of the Ficoll-400 concentration. From the data shown in Figure 4.13 the diffusivity remains constant until the a concentration of 50 mg/ml where it begins to decrease. By comparing to previous work done by Martinez *et al* and Latreille *et al* , a relation can be made between the concentration of Ficoll with both the osmotic pressure (Π_{osmo}) and the viscosity of resultant solutions [99] [100].

Figure 4.14 shows how the Π_{osmo} and viscosity depend upon the concentration of Ficoll-400. From the data shown in Figure 4.14 the Π_{osmo} can be determined for each concentration. Given that both Π_{osmo} and viscosity increase with Ficoll concentration the measured diffusivity needs to be corrected for by dividing through by the viscosity of the suspension. The shrinkage can be approximated considering the ratio of the diffusivities between microgels with no Ficoll-400 D_0 and microgels with a specific concentration of Ficoll-400 D. The approximation between the radius of the SZ microgels with no Ficoll-400 added, R_0, and the radius of the SZ microgels with an amount of Ficoll-400 added, R,

$$\frac{D_0}{D} = \frac{k_b T}{6\pi\eta_0 R_0}\frac{6\pi\eta R}{k_b T} = \eta_{rel}\frac{R}{R_0} \tag{4.1}$$

where k_b is the Boltzmann constant, T is the temperature, η is the viscosity

of the microgel + Ficoll-400 mix, η_0 is the viscosity of the microgel suspension and η_{rel} is the relative viscosity of the microgel + Ficoll-400 solution. R/R_0 is plotted as a function of Π_{osmo} in Figure 4.15, where it is shown to decrease as Π_{osmo} increases. The last point of Figure 4.15 corresponds to a hydrodynamic radius of $\approx$ 520 nm, showing that the SZ microgels are capable of deswelling significantly. Given that shrinkage occurs at a specific Π_{osmo} it can be assumed that there is minimal interactions with the microgels, and this effect is due to increased osmotic compression [146]. Other studies have shown the deswelling ability of other microgel systems using a similar approach, however, the degree of deswelling with SZ is more extreme [33] [147] [148]. This most likely due to the low cross-linking density of the SZ microgels, as other studies have shown that stiffer, more cross-linked, microgels resist shrinkage [146]. From Chapter 3 the SZ microgels are considered 'soft' when compared to other systems which means they are more susceptible to compression forces, which is an important consideration when analysing the crowding at high concentrations. These findings also suggest that a hard colloid model is insuffient to completely analyse the packing of the microgels given their intrinsic compressiabilty, as close-packing may not signal loss of mobility due to the microgels deswelling ability. Furthermore, the surface structure of the microgels will affect the swelling/deswelling behaviour in crowded environments, the dangling polymer chains will affect the compression by the creation or suppression of lubrication layers or by establishment of a significant disjoining pressure to break these layers during compression [146]. This shrinkage also suggests that the hydrophobic chains are contained within the core, as the microgels are in an aqueous environment. As the osmotic pressure is increased shrinkage may occur due to the hydrophobic units 'rejecting' the water, leading to deswelling. Overall these results indicate that during crowding SZ microgels are capable of significant shrinkage, which will occur when suspensions develop a yield stress (0.07 wt%), which directly contrasts hard colloids. This observation will have consequences for the microgels when at the interface between liquids which will be explored in Chapter 5 and 6.

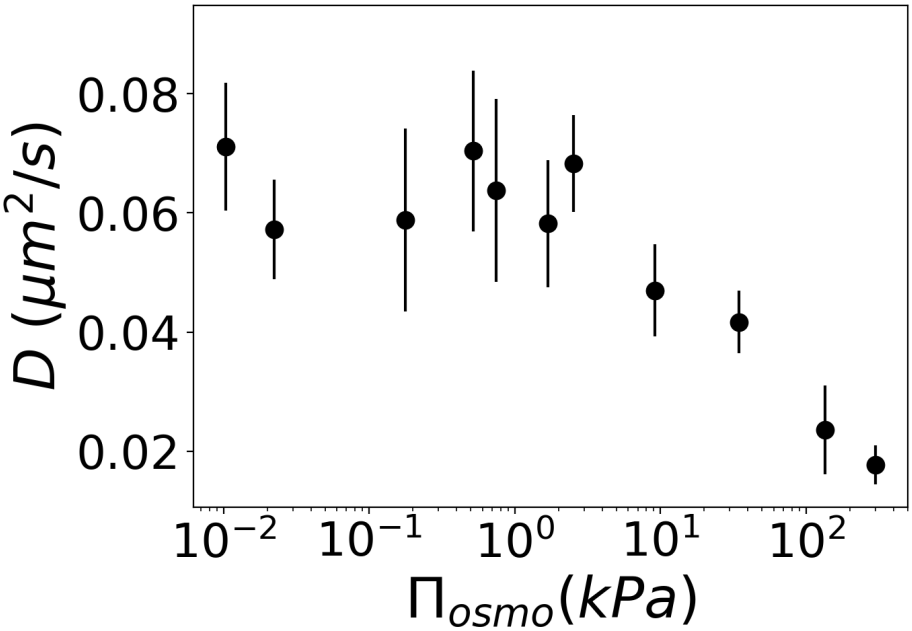

Figure 4.13: *Variation of the average diffusion coefficient D plotted as a function of the osmotic pressure Π_{osmo}, at a fixed concentration of SZ* 0.0025 wt%.

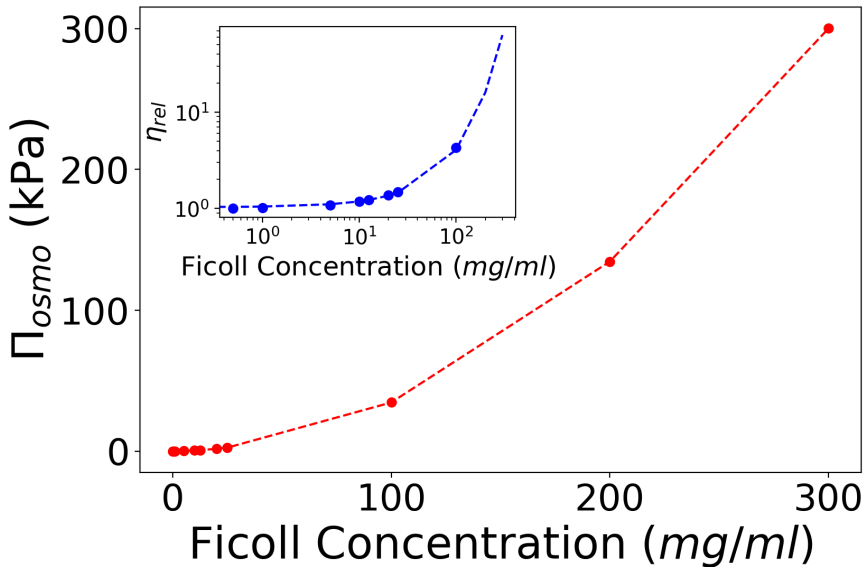

Figure 4.14: *Variations in osmotic pressure Π_{osmo} as a function of Ficoll-400 concentration, taken from work done in [100]. Inset: Variations of the relative viscosity η_{rel} as a function of Ficoll 400 concentration, taken from work done in [99].*

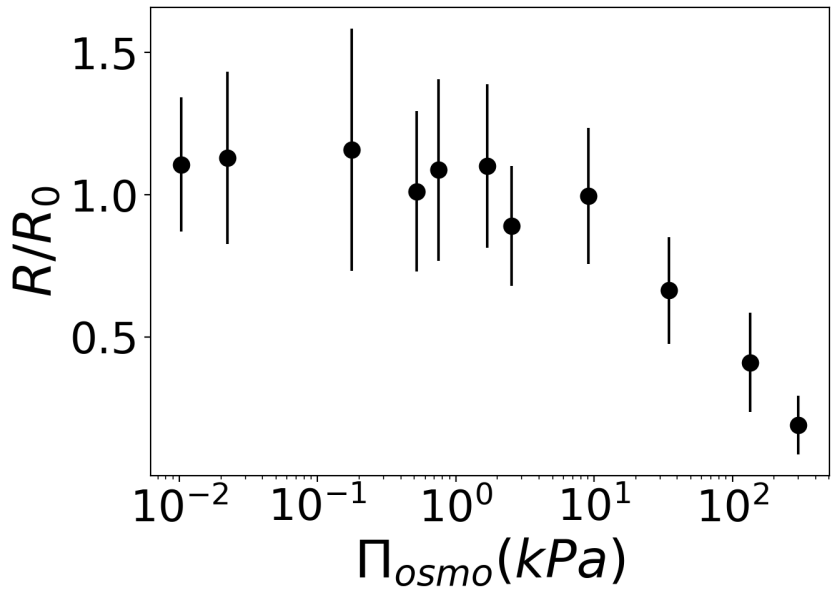

Figure 4.15: *Variation of the rescaled hydrodynamic radius R/R_0 plotted as a function of the osmotic pressure Π_{osmo}, exerted by Ficoll-400, for a fixed concentration of SZ* 0.0025 wt%.

4.4 Summary

In summary in this chapter the dynamics of SZ microgels were probed using Differential Dynamic Microscopy with respect to polymer concentration, added salt and osmotic pressure. DDM revealed that as the concentration of SZ is increased the dynamics transition from a freely diffusing colloids to a gel network. While salt measurements revealed that SZ microgels shrink at a critical salt concentration. The dynamics of the swollen and deswollen microgels were compared and showed similarities to results seen with attractive spheres, indicating how the surface chains influence the mobility. Finally SZ microgels have shown to deswell significantly at sufficiently high osmotic pressures which has consequences for understanding the crowding behaviour of SZ. In summary the main points from this chapter are as follows:

- SZ microgels have a hydrodynamic radius of 2.7 μm $\pm$ 0.3 μm significantly larger than other microgels
- At 0.03 wt% mobility is minimised which is also the concentration where

microgel suspensions begin shear thinning

- When 200 mM is added microgels shrink by a factor 2
- The dynamics of the shrunken microgels were compared to the swollen case (2.7 μm) and it was found the the mobility of both showed the same trend. The trend was consistent with the attractive sphere systems where mobility is effected at $\phi < 0.1$
- By comparing to the steady shear and oscillatory rheology measurements it is evident that at 0.03 wt% percolating networks form but the lack of yield stress indicates that these networks are 'fragile'. Once more concentrated above 0.061 wt% the network develops a yield stress
- Under high osmotic compression SZ microgels have been shown to deswell from 2.7 μm down to 520 nm which is likely due to the low cross-linking density of the gels

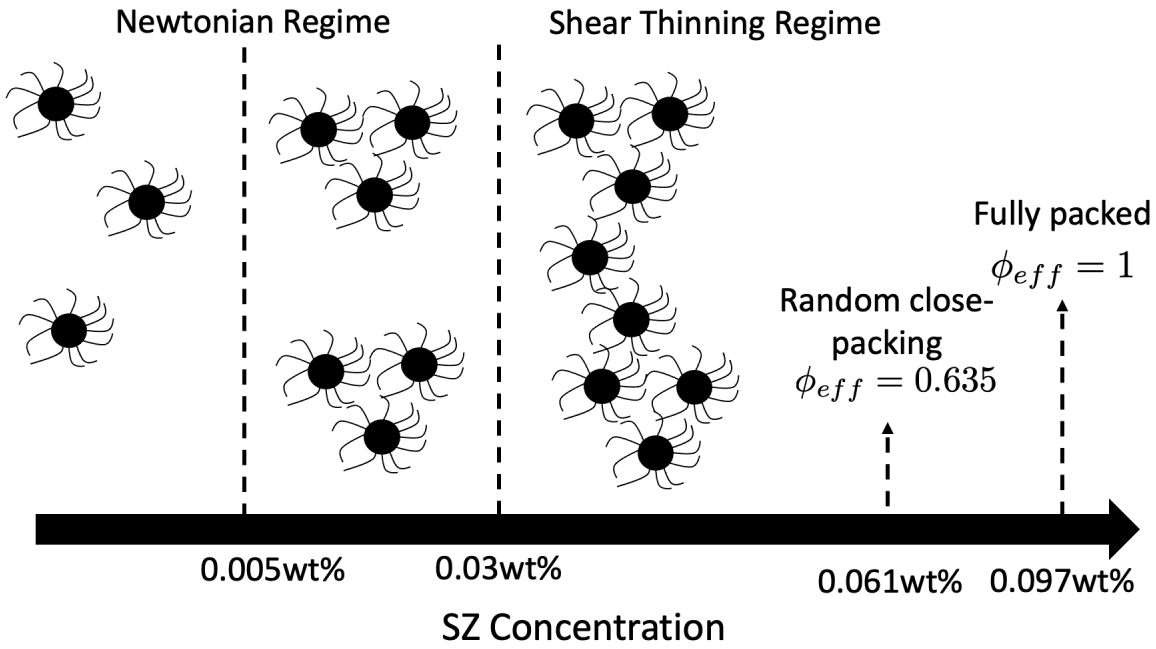

Figure 4.16: *Phase diagram of the SZ microgels, showing the key features uncovered from the DDM and rheology measurements detailed in Chapter 3 and Chapter 4.*

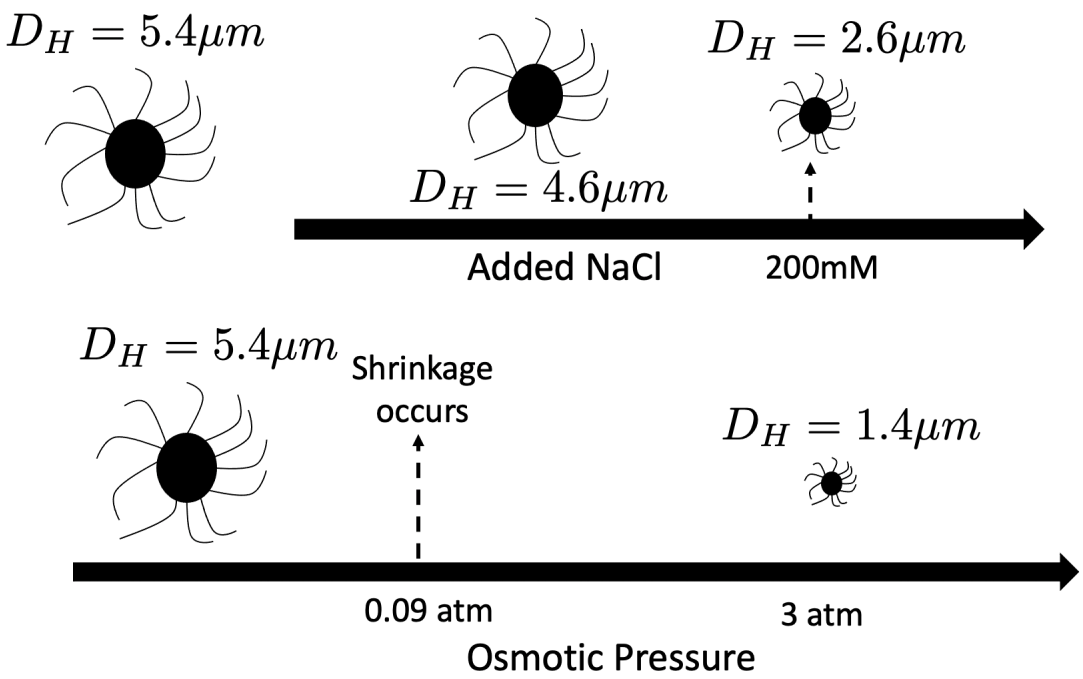

Figure 4.17: *Schematics diagrams showing how SZ microgels act in response to increasing salt concentration (top) and increasing osmotic pressure (bottom).*

The results of this chapter and the previous has provided a solid understanding of the size and interactions of the SZ microgels and how it relates to the rheology. In the next chapter the interfacial nature of the SZ microgels is investigated.

Chapter 5

SZ Microgels at the Oil-Water Interface

5.1 Effect on Interfacial Tension

5.1.1 Variations of IFT with different SZ Concentrations

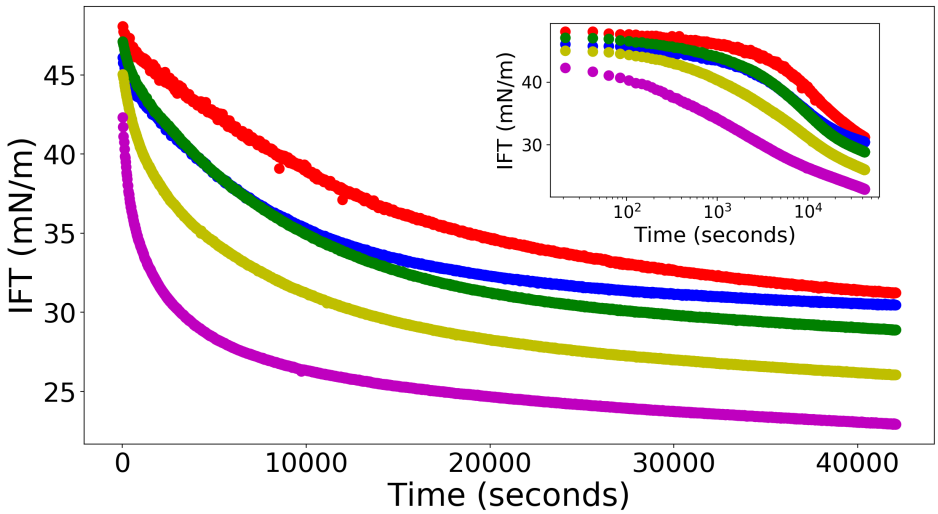

Figure 5.1: *Variations of interfacial tension IFT as a function of drop age of a dodecane drop in an aqueous background with various concentrations of SZ microgels present. SZ concentrations are as follows:* 0.000 25 wt% *(red),* 0.005 wt% *(blue),* 0.01 wt% *(green),* 0.05 wt% *(yellow) and* 0.08 wt% *(purple). The inset shows the same data but the the natural logarithm of x-axis has been taken.*

Figure 5.1 shows the effect of SZ concentration on the dynamic surface tension γ. The general trend shows γ decreasing as the n-dodecane drop ages, and as the SZ concentration increased this effect becomes more apparent. Intuitively this result is expected since increasing the SZ concentration results in more particles available to go to the interface. The data displayed in Figure 5.1 can also be used to provide details on the microgels adsorption to the interface. The inset graph in Figure 5.1 shows the time plotted on a log scale, and shows that γ decreases at different rates at different times. At low times ($t < 100\,s$) there is a distinct plateau stage, at intermediate times ($100\,s < t < 10\,000\,s$) γ decreases at an initial rate rate until approx. $10\,000\,s$ where the rate changes. These results have been seen in other studies on similar systems and have been attributed to the build up of microgels on the interface.

The evolution of γ of an oil-water interface laden with protein molecules was found to follow similar dynamics as the SZ, a schematic of the process is shown in Figure 5.2. Three distinct regimes were identified: Regime I an incubation phase where proteins diffuse to the interface and initiate confirmation changes in order to adsorb to the interface (Figure 5.3), Regime II where the interface is filled with protein molecules which relax into less compact structures causing a decline in γ (Figure 5.4) and Regime III where continued conformational changes of initial adsorbed layers and aggregation promote gradual reduction in tension over extended periods of time (Figure 5.5) [149]. The inset in Figure 5.1 shows the IFT plotted as a function of the time, where the time axis has been logged, this data clearly shows the three distinct regimes. As the SZ concentration is increased the incubation time, Regime I, shortens due to the increase of microgels in the environment. Similarly the timescales for all transitions between regimes are shortened as the microgel concentration increases. Given that proteins change confirmation at the interface this is analogous to the microgels possibility flattening out at the interface (Regime I), then as more microgels crowd to the interface the hydrophobic chains will all try and reach the oil causing further adsorption and crowding (Regime II) and then once the interface is saturated changes in IFT are mediated by changes in the adsorbed microgel layer.

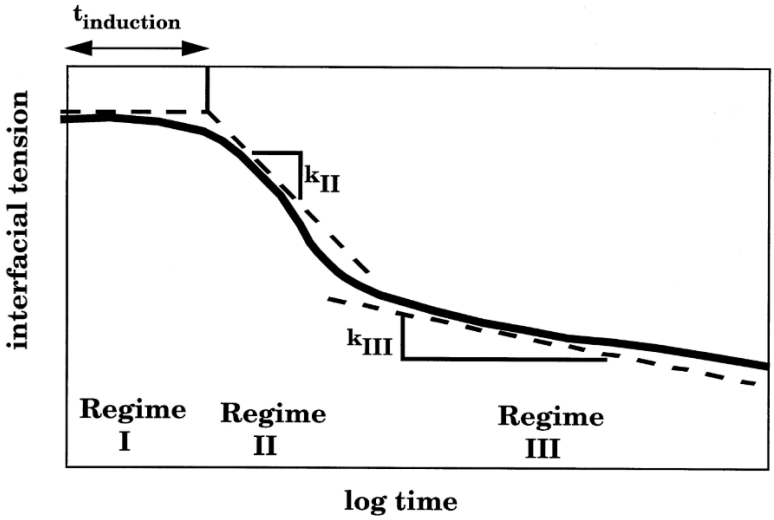

Figure 5.2: *Typical interfacial tension dynamics of protein adsorption at the oil-water interface showing methods of quantifying each regime. Induction time of Regime I determined by extrapolating slope from Regime II to zero surface pressure. Slopes of Regimes II and III show logarithmic dependence of tension on time. Taken from [149].*

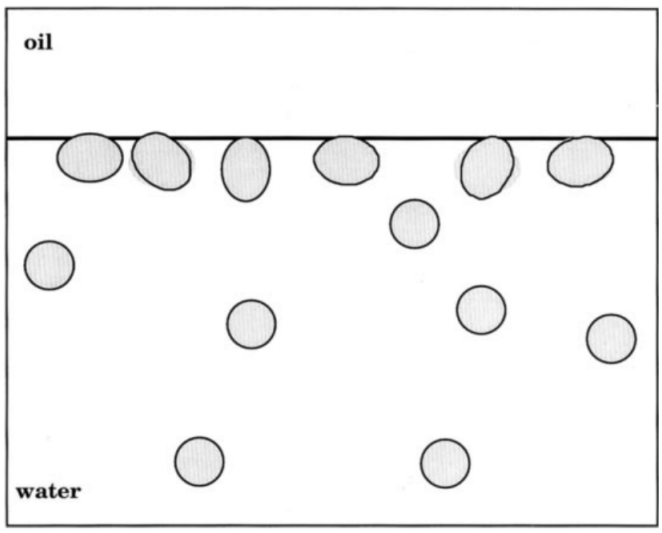

Figure 5.3: *Schematic of protein adsorption at the oil-water interface in the early stages of adsorption, named Regime I . Regime I where the interface is filled with protein molecules which relax into less compact structures causing declines in IFT at the oil-water interface. Taken from [149].*

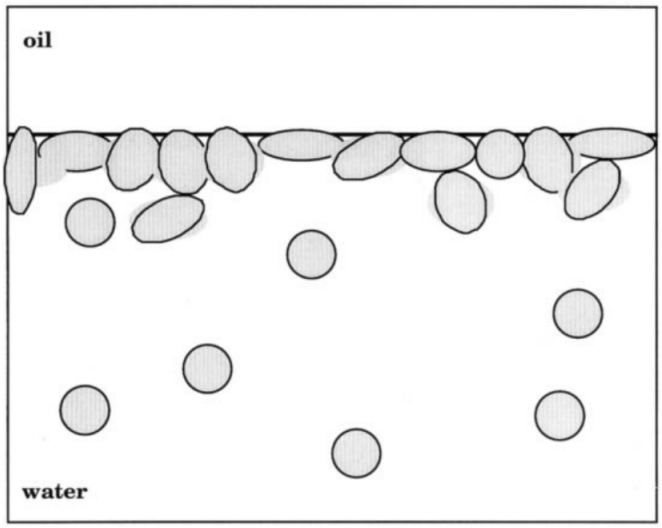

Figure 5.4: *Schematic of protein adsorption at the oil-water interface in the mid stages of adsorption, named Regime II . Regime II where an incubation phase where proteins diffuse to the interface and initiate confirmation changes in order to adsorb to the oil-water interface. Taken from [149].*

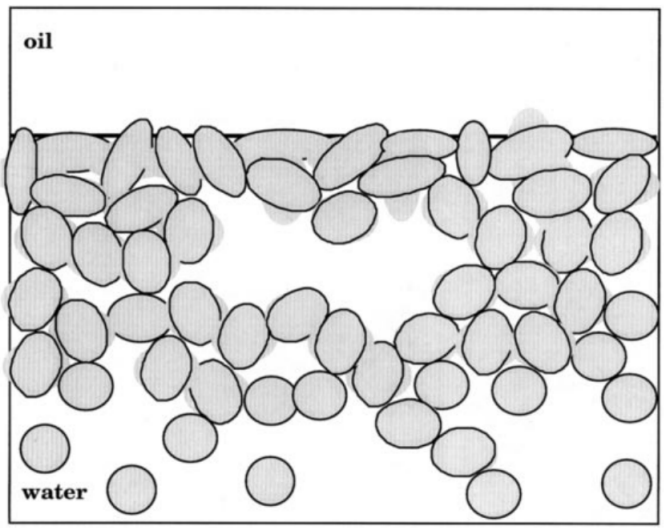

Figure 5.5: *Schematic of protein adsorption at the oil-water interface in the late stages of adsorption, named Regime III. Regime III where continued conformational changes of initial adsorbed layers and aggregation promote slow declines in tension over extended periods of time. Taken from [149].*

In order to understand the kinetics of microgel absorption a recent model developed by Bizmark *et al.* was applied to the data in Figure 5.1 [150] (a revised

version of Tordai work explained in Chapter 1). Bizmark *et al.* constructed a model for nanoparticle absorption which builds on previous work conducted on surfactants and nanoparticles, however, their model takes into account that nanoparticles can irreversibly bind at interfaces [151] [152]. Specifically the authors found that there were two limiting adsorption regimes exist, at short and long times. At short times, t $\rightarrow$ 0, an individual NP adsorbs to the interface finding no other particles there. Therefore, assuming that there is no barrier to stop adsorption the rate of diffusion of the particles through the bulk is the limiting factor. In this regime, γ obeys the following equation,

$$t \rightarrow 0 : \gamma = \gamma_0 - 2N_A \Delta E C_0 \sqrt{\frac{Dt}{\pi}}, \tag{5.1}$$

where where t is drop age, γ_0 is the initial dynamic surface tension, N_A is Avogadro's number, ΔE is the energy cost of adsorption, D is the diffusion coefficient and C_0 the initial bulk concentration. However, as t $\rightarrow \infty$ nanoparticles experience a crowded interface therefore, for additional particles to adsorb those already on the interface must rearrange. The rate of adsorption is determined by the mobility of particles attached at the interface, in order to account for this a blocking function is introduced and combined with model of Bizmark *et al.* [153]. The long-time behaviour of γ can be described as,

$$t \rightarrow \infty : \gamma = \gamma_\infty + \frac{K_1 \Delta E}{C_0 N_A (\pi R^2)^2} \sqrt{\frac{\pi}{Dt}}, \tag{5.2}$$

where γ_∞ is the dynamic surface tension at long-time saturation and K is a dimensionless reaction coefficient. K can be related to the surface coverage Θ and $\bar{k_a}$, a the dimensionless adsorption constant, by,

$$K_1 = \sqrt{\frac{\theta^3}{4.64\bar{k_a}}}. \tag{5.3}$$

Using this approach the data shown in Figure 5.1 was separated into short-time (plateau region) and long-time (beyond plateau region) and γ was plotted as a function of $\sqrt{t}$ and $1/\sqrt{t}$ respectively. A linear regression fit was performed to extract the key parameters γ_0, γ_∞ and ΔE. Figure 5.6 shows the rescaled data for both long and short timescales along with the fits to each concentration. Table 5.1 shows the calculated values of γ_0, γ_∞ and ΔE. γ_0 and γ_∞ are the simply

the y-intercepts from the linear fits while ΔE and K_1 can be calculated from the slopes as follows,

$$t \to 0 : \Delta E = \frac{m_{short}}{2N_A C_0}\sqrt{\frac{\pi}{D}}, \tag{5.4}$$

$$t \to \infty : K_1 = \frac{m_{late} C_0 N_A (\pi R^2)^2}{\Delta E}\sqrt{\frac{D}{\pi}}, \tag{5.5}$$

where m_{short} and m_{late} are the gradients of the short and late-time fits respectively. The calculated value of C_0 and the diffusivity D, from Chapter 4, are shown in Table 5.1, and R is taken to be 2.7 μm.

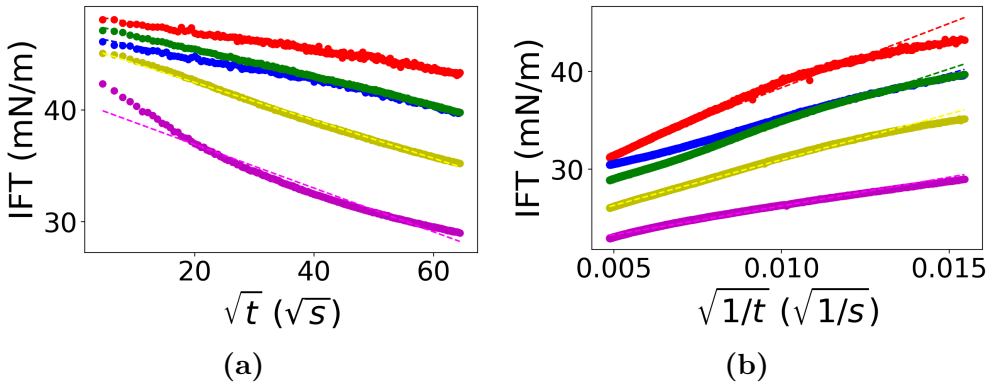

Figure 5.6: *(a) Short-time and (b) long-time adsorption curves fitted with equations 5.1 and 5.2 respectively. SZ concentrations are as follows:* 0.000 25 wt% *(red),* 0.005 wt% *(blue),* 0.01 wt% *(green),* 0.05 wt% *(yellow) and* 0.08 wt% *(purple) along with respective dashed fit lines.*

C (wt%)	C_0 (mol/m^3)	D (m^2/s)
2.5×10^{-3}	7.93×10^{-11}	$7.6 \times 10^{-14} \pm 0.3 \times 10^{-14}$
0.005	1.59×10^{-9}	$7.5 \times 10^{-14} \pm 0.5 \times 10^{-14}$
0.01	3.17×10^{-9}	$5.0 \times 10^{-14} \pm 0.4 \times 10^{-14}$
0.05	1.59×10^{-8}	$1.2 \times 10^{-14} \pm 0.1 \times 10^{-14}$
0.08	2.54×10^{-8}	-

Table 5.1: *Bulk concentration of microgels, in wt% C and mol/m^3 C_0, and the Stokes-Einstein Diffusion Coefficient D. D values were taken from previous DDM results in Chapter 4.*

C (wt%)	Short-time		Long-time	
	m_{short} ($\mathrm{mNm^{-1}s^{0.5}}$)	R^2	m_{late} ($\mathrm{mNm^{-1}s^{-0.5}}$)	R^2
2.5×10^{-3}	-0.081 ± 0.001	0.998	1316 ± 4	0.991
0.005	-0.106 ± 0.001	0.990	932 ± 1	0.996
0.01	-0.125 ± 3×10^{-4}	0.998	1125 ± 2	0.998
0.05	-0.170 ± 0.001	0.997	935 ± 1	0.996
0.08	-0.195 ± 0.002	0.974	590 ± 1	0.989

Table 5.2: *Slopes and R^2 of the linear fits to the short and long time IFT data.*

C (wt%)	γ_0 (mN/m)	γ_∞ (mN/m)	ΔE (k_bT)
2.5×10^{-3}	48.58 ± 0.03	25.18 ± 0.03	$1.32 \times 10^9 \pm 3.06 \times 10^7$
0.005	46.76 ± 0.03	25.81 ± 0.01	$8.70 \times 10^7 \pm 8.71 \times 10^5$
0.01	47.91 ± 0.02	23.38 ± 0.01	$6.27 \times 10^7 \pm 2.25 \times 10^6$
0.05	45.82 ± 0.03	21.64 ± 0.01	$3.42 \times 10^7 \pm 1.40 \times 10^6$
0.08	40.90 ± 0.12	20.35 ± 0.01	-

Table 5.3: *Values of γ_0, γ_∞ and ΔE determined from fitting the short and long time IFT data using 5.1 and 5.2.*

The interfacial tension of a bare dodecane-water interface was measured to be 51.1 ± 0.2 mN/m, which is higher than any of the γ_0 values. This is most likely due to individual polymers and/or impurities being present in the raw SZ polymer. The mass spectroscopy results, shown in Chapter 2, have shown that the molecular mass of SZ is wide spread being as high as 150 000 Da or as low as 50 000 Da. Therefore, given the polydispersity it is plausible that there may be small amounts of individual polymers may be present which will get to the interface much faster than micron-sized microgels. Furthermore, each measurement was calibrated by measuring a bare dodecane-water interface first in order to check for contaminants. Once a value of approx. 51 mN/m was reached the microgel suspension was tested. All suspensions were made using the same Milli-Q treated water that was used to calibrate the tensiometer. Therefore, any impurities would have been introduced with the addition of SZ.

The adsorption kinetics are concentration dependent, however, this has been widely observed on both surfactants and colloids alike [154] [155] [156]. The evolution of the kinetics demonstrates the spontaneous microgel adsorption,

which increases as the concentration increases due to the increased presence of microgels i.e. the flux of microgels approaching the surface will increase with concentration.

The γ_∞ values are comparable to colloidal systems such as nanoparticles, other microgels and even large polymeric surfactants [156] [157] [158]. γ_∞ values are approximately 50 % of the γ_0, which is comparable to colloids but not for surfactants. The γ_∞ values decrease as the SZ concentration is increased which differs from PNIPAM, the most widely studied microgel. Several studies have shown that the γ_∞ is not concentration dependent, all concentrations result in the same γ_∞ value [159] [160]. This is thought to be due to the cooperative behaviour between microgels resulting in attraction to the interface. However, for SZ γ_∞ decreases with increasing concentration. For the lowest two concentrations γ_∞ is the most similar, these concentrations are also dilute enough to not experience crowding effects (see DDM results Chapter 3). Therefore, it is plausible that as the concentration increases crowding becomes a factor as interactions between neighbouring microgel particles will increase. As the concentration of microgels increases deviations in the short-time kinetics is expected as crowding effects will become more apparent. Polymer restructuring at the interface due to the amphiphilic nature of the polymer building blocks will become more apparent due to the increased presence of microgels. This is reflected as the most concentrated data (0.08 wt%) is shown to deviate from Bizmarks model. From the results of Chapter 3 and 4, at 0.08 wt% of SZ a yield stress has been developed from the formation of a network, therefore, collective effects such as polymeric rearrangement/segregation are very likely. Furthermore, the DDM measurements also revealed that above 0.005 wt% distinct clusters of microgels were observed. This clustering effect could happen at the interface resulting in more microgels being adsorbed onto the interface leading to reductions in γ_∞. Whereas the effect has not been seen in microgel systems it has been observed for particles [161]. However, the swelling capability of the SZ microgels could also influence this effect, this will be addressed later in the Chapter.

5.2 Effect on Interfacial Elasticity

5.2.1 Variations of Elasticity with SZ Concentration

Table 5.4 contains the average dilational storage E' and loss E'')moduli measured for a n-dodecane/water interface after microgel adsorption. All measurements were conducted after the pendant drop experiments, discussed earlier, were completed ($\tau_{drop} > 11$ hours). Even at the lowest concentration, 2.5×10^{-3} wt%, the interface becomes more elastic over time, with E' increasing by a factor of 10. At 0.08 wt% E' reaches a value of 27 mN/m and E'' has increased by two orders of magnitude to 6.9 mN/m. These values are comparable to other microgel systems such as PNIPAM and protein microgels [156] [162].

Similar to these other studies it was found that E' becomes more frequency dependent as the SZ concentration was increased. Figure 5.7 shows the variations in E' with frequency f for the all the SZ concentration. Figure 5.7 shows on increasing the applied frequency the value of E' increases, while as the SZ concentration increases the variance in E' also increases. For the lowest concentrations there is almost no variation of E', however, at 0.08 wt% E' increases from 22 mN/m up to 32 mN/m.

This trend is indicative of a viscoelastic film forming on the interface of the drop. Previous work by Kobayashi *et al.* demonstrated that latex-laden interfaces are viscoelastic by measuring E' and E'' and finding a cross-over region occurring a small frequencies (< 20 mHz) [163]. This result is analogous to bulk rheological measurements, where the crossover behavior is often observed in measurements of the rheological responses of linear polymer materials under solution and melt conditions [164]. E' is comparable to Kobayashi *et al.* work but E'' of SZ-laden interfaces is much lower. The lower E'' is most likely due to the difference in size as the latex particles have a radius of 400 nm, meaning they will have lower adhesion energies and therefore, more mobility on the interface. For all measured frequencies E'' <10 mN/m unlike latex stabilised interfaces. This may be due to the difference in measured frequencies or even due to bulk effects. For SZ concentrations > 0.005 wt%, diffusion decreases and the rheology of suspensions is influenced and for 0.061 wt% a yield stress is formed. Therefore, bulk effects become more apparent as the SZ concentration is increased which will influence E' and E'' [165].

C (wt%)	E' (mN/m)	E'' (mN/m)
0	2.1 ± 0.2	0.06 ± 0.08
2.5×10^{-3}	21 ± 0.2	1.3 ± 0.5
0.005	26 ± 1	3.0 ± 1.7
0.01	24 ± 0.4	2.8 ± 0.1
0.05	21 ± 2	3.4 ± 1.3
0.08	27 ± 4	6.9 ± 0.5

Table 5.4: *Average values of the dilational storage E' and loss E'' moduli for aged (> 11 hours) n-dodecane drop surrounded by microgel suspensions at multiple concentrations.*

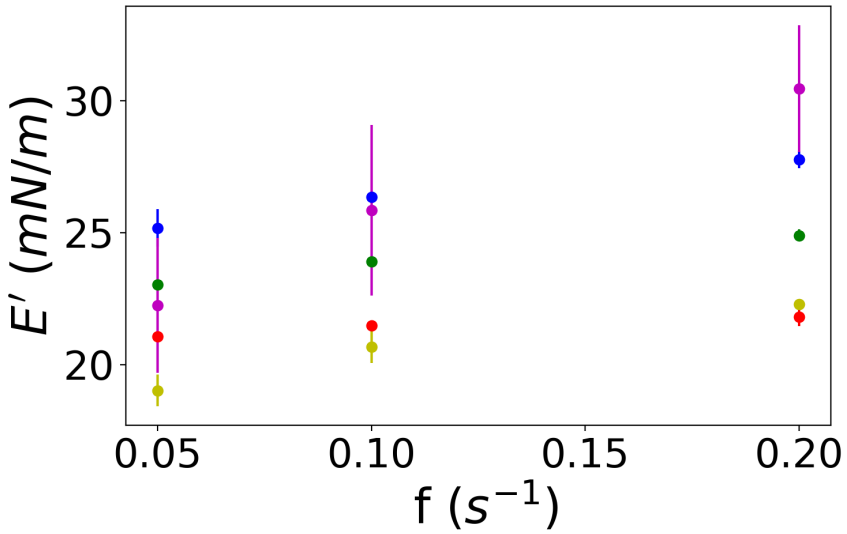

Figure 5.7: *Variations in dilational storage modulus E', plotted as a function applied frequency f, of the microgel laden dodecane-water interface. SZ concentrations are as follows:* 0.000 25 wt% *(red),* 0.005 wt% *(blue),* 0.01 wt% *(green),* 0.05 wt% *(yellow) and* 0.08 wt% *(purple).*

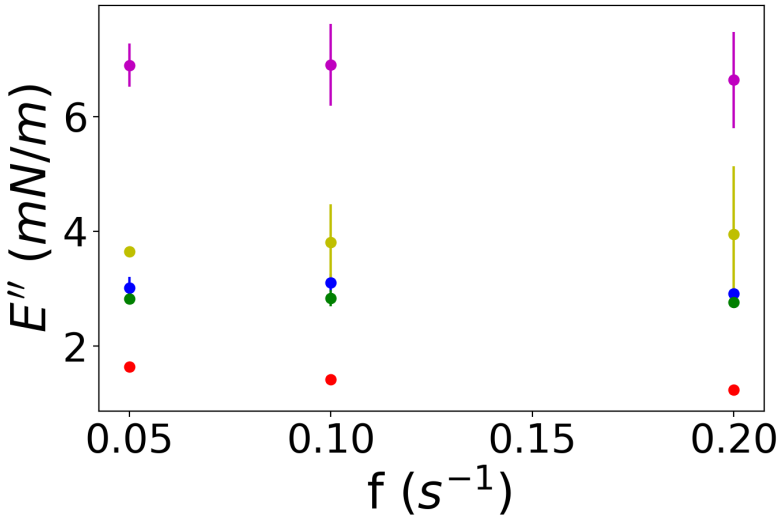

Figure 5.8: *Variations in dilational loss modulus E'', plotted as a function applied frequency f, of the microgel laden dodecane-water interface. SZ concentrations are as follows:* 0.000 25 wt% *(red),* 0.005 wt% *(blue),* 0.01 wt% *(green),* 0.05 wt% *(yellow) and* 0.08 wt% *(purple).*

5.2.2 Variations of Elasticity and Surface Pressure with Time

The variations in E', E'' and γ were measured over several hours with both swollen and deswollen microgels to understand the key differences between the two states.

Over several hours the E' increases while E'' remains low, as shown in Figure 5.9 for both cases. The dominance of E' is typical for colloids at interfaces, as well as other microgel systems [166] [156] [167]. The first measurement at $t =$ 1072 s, gave a value of 10.3 mN/m which is relatively high for colloidal particles, however, these values of typical of polymeric surfactants [168]. This effect may be due to the interactions between microgel particles, from the Chapter 3 and 4 interactions start to occur as low as 0.005 wt% with networks forming at 0.03 wt%. Furthermore, as the concentration increases oscillatory rheology indicated that they can interpenetrate, both effects could result in higher E' values.

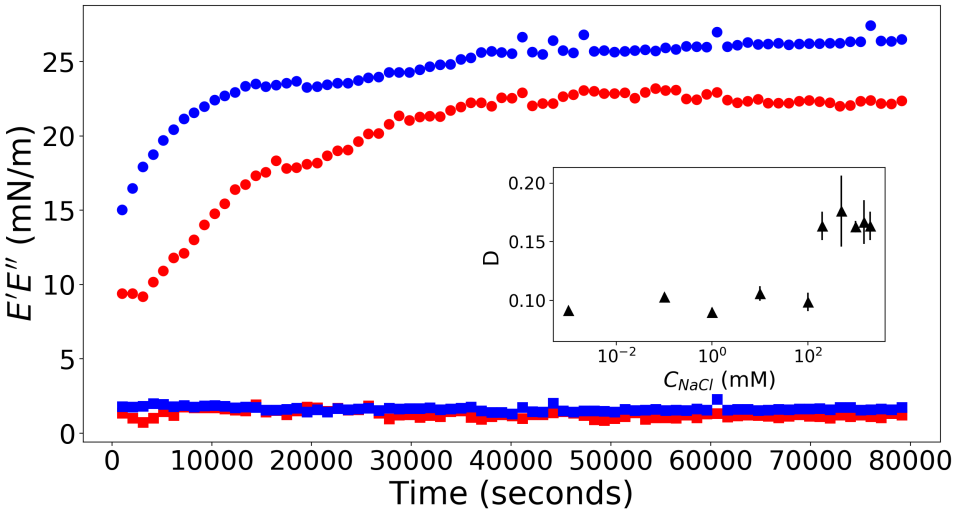

Figure 5.9: *Variations of the dilational storage E', dots and loss moduli E'', squares plotted as a function of time as SZ microgels adsorb to a n-dodecane/water interface. The red curve denotes swollen microgels sized at* $2.7\,\mu$m *and the blue curve denotes the deswollen case, with* 200 mM *of NaCl was added to osmotically shrink the microgels to* $1.3\,\mu$m.

The surface pressure Π, which is the difference between the interfacial tension of the bare interface γ_0 and the interfacial tension at time t, γ_t, was also calculated to compare to the elasticity results. Both surface pressure ($\Pi = \gamma_0 - \gamma_t$) and E' show a clear transition from a fast regime to a slower regime. Figure 5.9 E' increases readily until $t \approx 20\,000$ s for the deswollen microgels (blue curve) while for the swollen case it occurs at $t \approx 30\,000$ s (red curve), after which E' plateaus. This transition is also reflected in the Π data shown in Figure 5.10. These result suggests that as the drop ages microgels build up on the interface imparting elasticity, however, eventually the interface becomes saturated. Once saturated microgels continue adsorbing but at lower rate. This result was also seen in the Section 5.1. From the data in Figures 5.9 and 5.10 smaller microgels reach the interface quicker to produce more elastic interfaces. Smaller microgels can adsorb faster due to their enhanced diffusivity and can produce more elastic interfaces due to their packing efficiency.

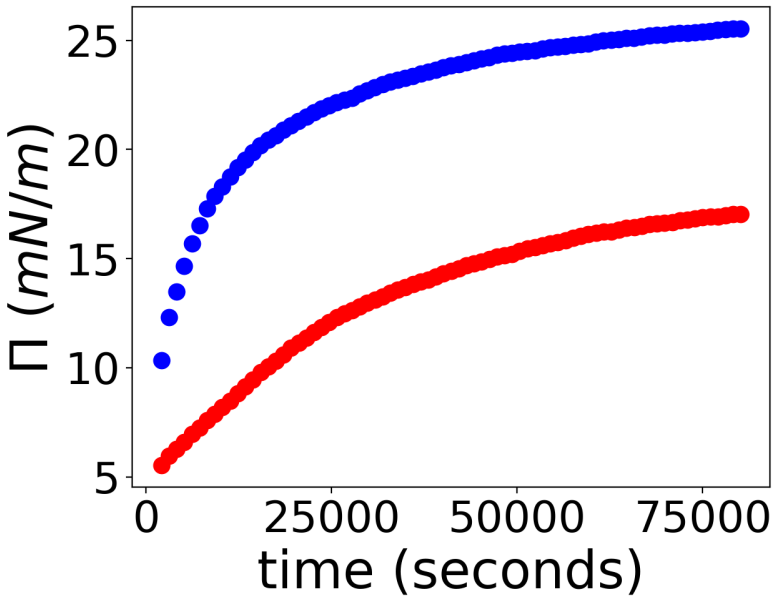

Figure 5.10: *Variations of the surface pressure* Π *and plotted as a function of time as SZ microgels adsorb to a n-dodecane/water interface. The red curve denotes swollen microgels sized at* $2.7\,\mu$m *and the blue curve denotes the deswollen case, were* 200 mM *of NaCl was added to osmotically shrink the microgels to* $1.3\,\mu$m.

5.2.3 Variations of Elasticity with Surface Pressure

Figures 5.11 and 5.12 show the variations of E' as a function of Π. The data form an approximately linear relationship, in both swollen and deswollen states, with a gradients of 1.42 ± 0.01 and 1.08 ± 0.01. However there is a small but visible change around $\Pi = 12\,\mathrm{mN/m}$ for the swollen microgels and $\Pi = 20\,\mathrm{mN/m}$ for the deswollen case, the point in time in which transitions in both E' and Π occurs. A plausible explanation is that particle adsorption has been slowed by the interface becoming saturated. Similar trends have been observed other microgels and generally Π increases as an interface becomes more crowded [167] [169] [170]. This has been attributed to more regular structures forming as the microgels are pushed together. The formation or ordered polycrystalline structures results in the intrinsic elasticity of such films. The gradients of the E' versus Π plots in Figures 5.11 and 5.11 also give details of particle-particle interactions.

There have been numerous studies which have tried to qualitatively relate the

variations in E' and Π to particle-particle interactions. Aveyard *et al.* modelled the interaction of charged particles and their image charges to explain the initial increase in surface pressure at larger area per particle, predicting that $\Pi \propto \phi^{5/2}$, ϕ being the area fraction $\phi = A_P/A$ [171]. However, Kralchevsky *et al.* found that their surface pressure scaled as $\Pi \propto \phi^{3/2}$ [172]. This difference was explained by expanding the model used by Aveyard *et al.* to include collective effects, such as electrostatics and aggregation.

In contrast, other studies simply modelled the surface pressure changes as a result of by adsorption alone, and this model was found to agree with data for a range of different colloid systems [173] [174]. In the adsorption only model, a scaling of $\Pi \propto \phi$ is expected.

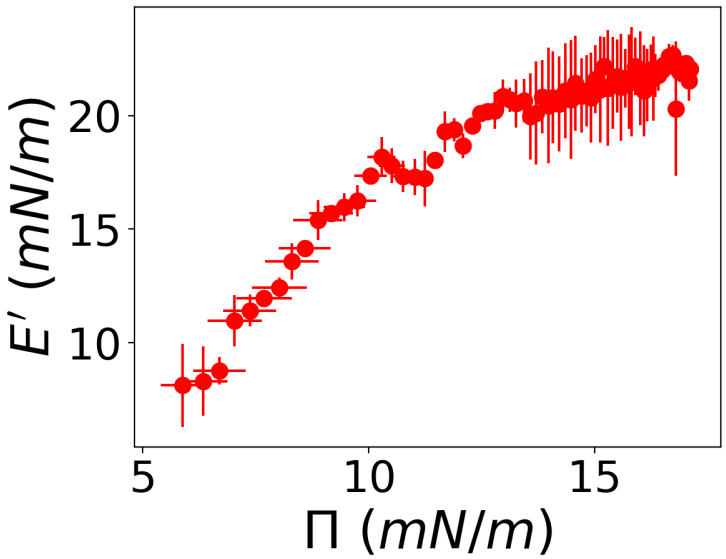

Figure 5.11: *Variations of the dilational storage modulus E' plotted as a function of surface pressure Π as SZ microgels adsorb to a n-dodecane/water interface.* 0.000 25 wt% *of SZ was used and microgels had a radius of* 2.7 μm.

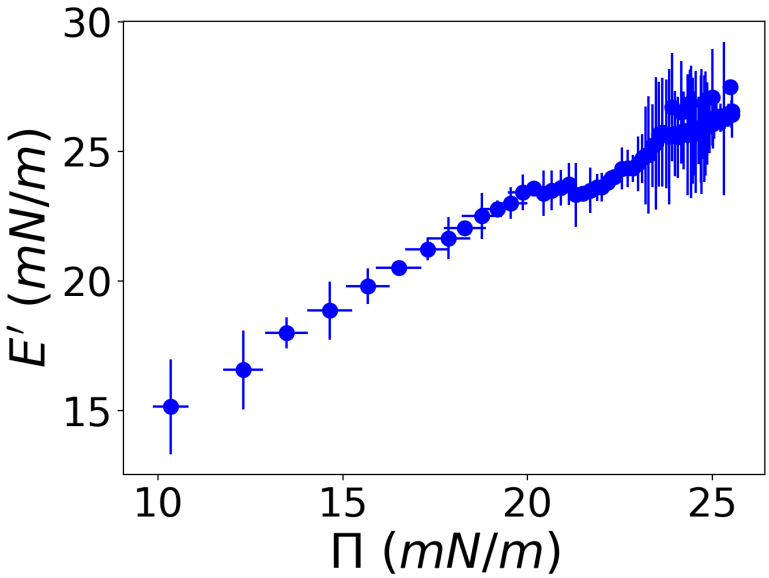

Figure 5.12: *Variations of the dilational storage modulus E' plotted as a function of surface pressure Π as SZ microgels adsorb to a n-dodecane/water interface.* 0.000 25 wt% *of SZ was used with* 200 mM *salt, in order to shrink the microgels, giving an average radius of* 1.3 μm.

To test how the SZ results compares to the various models the relationship between Π and ϕ, the area fraction of the microgels, must be considered. From Chapter 2, $E^* = E' + iE''$, where E^* is the complex dilational modulus. Assuming E' and for sufficiently small sinusoidal oscillations,

$$E' = \frac{d\gamma}{d(ln(A))}. \tag{5.6}$$

Now considering that desorption does not occur during measurements and therefore, $dln(A) = -dln(\phi)$ and using the definition $\Pi = \gamma_0 - \gamma$ gives,

$$E' = \frac{d\Pi}{d(ln(\phi))}. \tag{5.7}$$

	m
Figure 5.13	1.61 ± 0.02
Figure 5.14	1.23 ± 0.02

Table 5.5: *Gradients obtained for the linear fits in Figures 5.13 and 5.14.*

Now considering the simplest model, the adsorption model, $\Pi \propto \phi$ is substituted into equation results in $E' = \Pi$, which results in a gradient of 1. The data in Figures 5.11 and 5.11 was fitted with a linear relation up to the plateau of both plots (where the interface has been saturated) with the gradients shown in Table 5.5 and the fits are shown in Figure 5.13 and Figure 5.14. Interestingly, for both m is higher than 1 especially the swollen case. These gradients are closer to Kralchevsky *et al.* result of $\Pi \propto \phi^{3/2}$ which indicates that interactions occur between adsorbing microgels, which is expected given the size of the particles. This seems reasonable as m is lower for the deswollen case where microgels can pack more efficiently due their shrunken size.

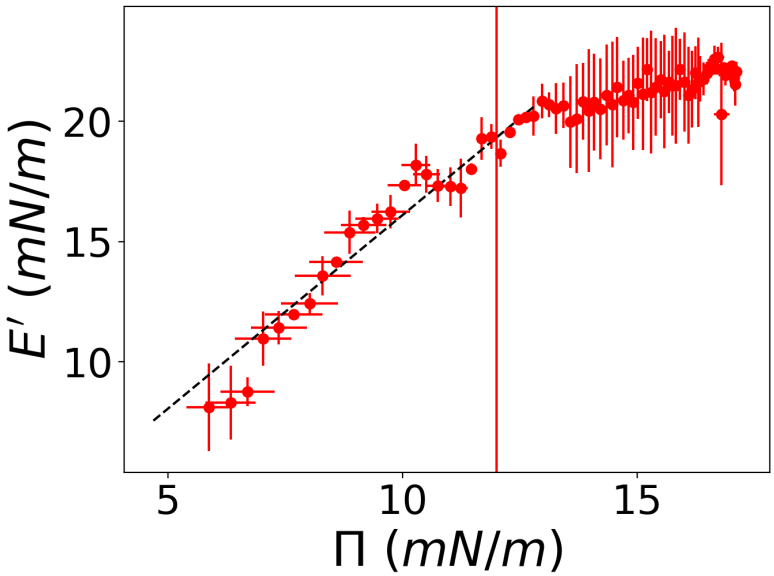

Figure 5.13: *Variations of the dilational storage modulus E' plotted as a function of surface pressure Π as SZ microgels adsorb to a n-dodecane/water interface.* 0.000 25 wt% *of SZ was used and microgels had a radius of* 2.7 µm. *The black line is the linear fit to the data and the solid red line marks where the interface has been saturated with microgels.*

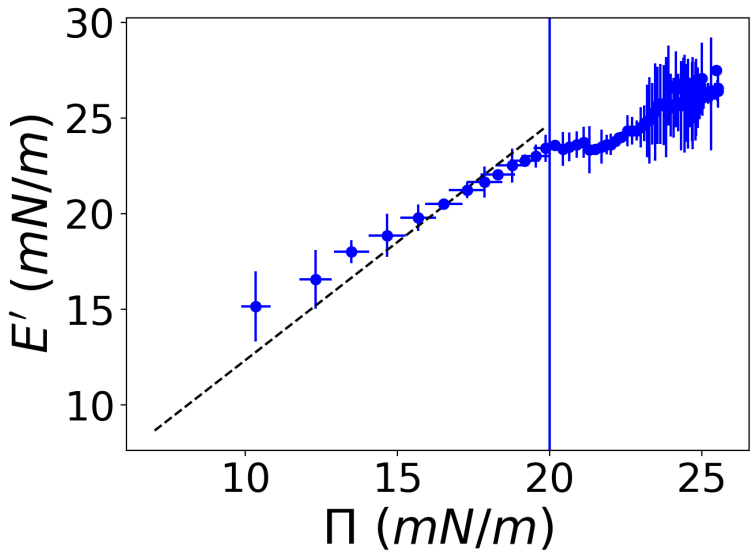

Figure 5.14: *Variations of the dilational storage modulus E' plotted as a function of surface pressure* Π *as SZ microgels adsorb to a n-dodecane/water interface.* 0.000 25 wt% *of SZ was used with* 200 mM *salt, in order to shrink the microgels, giving an average radius of* 1.3 μm. *The black line is the linear fit to the data and the solid blue line marks where the interface has been saturated with microgels.*

At late times and high Π, E' plateaus which is due to the interface being saturated. Once the interface is saturated, microgels may deform given their intrinsic viscoelasticity and from previous results SZ microgels are shown to interpenetrate. The deformation of microgels has been widely observed in other studies [175] [156] [176]. As microgels are compressed the soft corona begins to spread out over the interface, surrounding the more cross-linked cores [176]. Furthermore, as SZ is polyelectrolyte there are charged monomers incorporated of the microgel (demonstrated In Chapter 4). As the interface becomes more crowded interactions will become stronger, which is taken into account in Kralchevsky *et al.* model which predicts $\Pi \propto \phi^{3/2}$, which fits the results obtained for the swollen and deswollen microgels at interfaces.

5.3 Absence of Interfacial Buckling

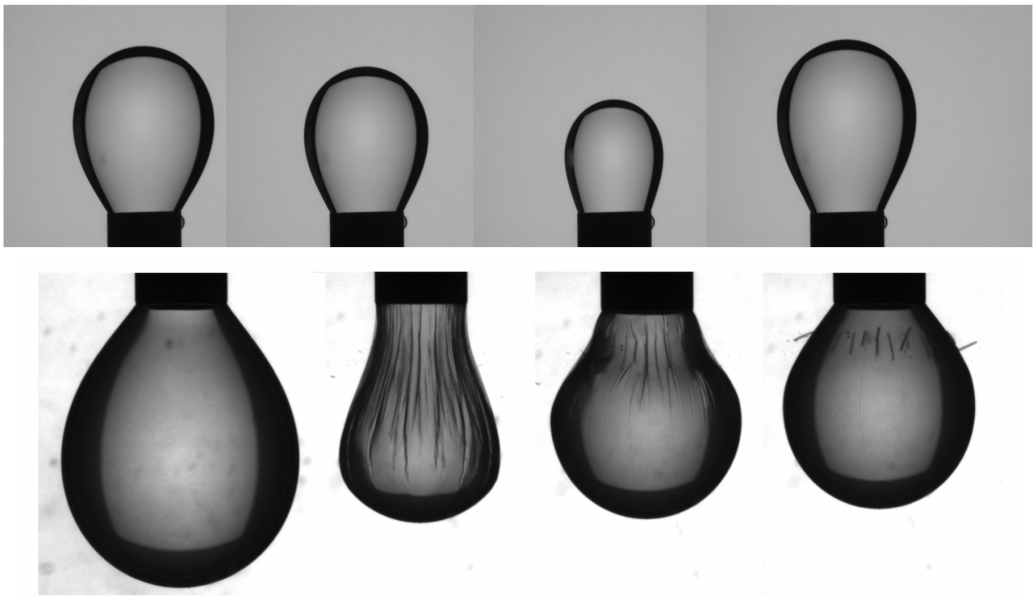

Figure 5.15: *Top: A SZ-stabilised dodecane drop undergoing a compression-expansion (*$30\,\mu$L *compressed to* $5\,\mu$L *and expanded back to* $30\,\mu$L*) cycle in an aqueous background, the droplet has been shrunk with no buckling occurring on the surface. Bottom: A particle-stabilised water drop in oil buckling during a compression-expansion cycle, taken from [177].*

A surprising observation which was consistent through all the measurements was that none of the SZ-stabilised interfaces showed any signs of buckling. Buckling occurs when an interface is compressed because the packing density increases and eventually reaches a maximum where particles can no longer rearrange on the interface [178]. Because the particles cannot rearrange, further compression of the interface leads to compressive deformation of the particles themselves or out-of-plane deformation evidenced by the surface wrinkling. Figure 5.15 shows how the the compression and expansion of SZ-laden interfaces compared particle-stabilised ones. Figure 5.15 shows that even under compression SZ-laden interfaces show no sign of buckling which directly contrasts the particle-stabilised droplet. The absense of buckling shows that unlike particles microgels are able to rearrange and compensate for the decrease in surface area. This may be due to the fact that the parts of the microgels may have the ability to detach from the interface, as some parts of the microgels are hydrophobic and some are hydrophilic. However, it also

may be due to the swelling ability of the microgels. If the interface shrinks and the microgels are forced closer together, deswelling may occur to counteract this. From Chapter 4 the microgels deswell in the presence of salt by approximately a factor 2. Consider a spherical droplet of radius R with an initial surface area S_0 as $S_0 \propto R^2$, if the SZ microgels were to deswell they could stabalise an interface 4 times smaller, as $R_{swollen} \approx 2R_{unswollen}$. Furthermore, given that oscillatory rheology in Chapter 3 indicates SZ microgels form interpentrating networks it is possible that they build up continuous gels on interfaces. Then given the soft nature of the SZ gels it may be possible to suppress buckling given the gels viscoelastic nature. This result is also unusual in comparison to other microgel systems which have been shown to buckle when compressed [14] [167]. The non-buckling property of SZ seems to be unique and is most likely the result of the chemical composition of microgel.

However, instead of restructuring or deswelling on interfaces microgels may detach if perturbed like during an compression expansion cycle. Figure 5.1 shows γ after approx. 11 hours ($\approx 40\,000$ seconds), comparing to Figure 5.9 at this time the elasticity of the interface has plateaued. For the former these measurements were performed for a fixed SZ concentration for a static drop while the the data in Figure 5.9 was taken from while the drop was oscillating. In order to determine any differences the γ data for both the oscillating and static drops need to be compared. The γ vs. drop age data for both the oscillating droplet, for both swollen (red) and unswollen (blue) microgels, and the static drop (black) for swollen microgels is shown in Figure 5.16 (SZ concentration of 0.000 25 wt%). Figure 5.16 shows a clear differences between all three curves, even the swollen static drop (black curve) and the swollen oscillating drop (red curve) case. In order to make a comparison the γ_∞ values were calculated for the oscillating drop curves using same approach detailed in Section 5.1. The γ_∞ of the curves in Figure 5.16 are shown in Table 5.6. In the case of the oscillating swollen drop the projected γ_∞ value is smaller when compared to the static case. This suggests that the oscillations of the drop may be disrupting the adsorption process. Furthermore, for the oscillating drop the γ value does not drop below the static drop curve, despite the final drop age being much higher. Given the results detailed in Section 5.1, which inferred that even after the interface is saturated adsorption still occurs, meaning oscillations may suppress adsorption.

The γ curve for oscillating drop, stabilised by unswollen microgels (blue), shows even lower than values than the other curves. This result is expected as these

microgels are smaller and therefore can pack more efficiently on the interface. However, when comparing to the data in Table 5.3 the γ_∞ value is most comparable to the highest concentration static result (0.08 wt%). This infers that unswollen microgels affect the interface in a similar way to more concentrated suspensions. This suggests that in concentrated suspensions microgel interactions can act to lower the interfacial tension further,

Curve	γ_∞ (mN/m)
Black	25.18 ± 0.03
Red	27.19 ± 0.04
Blue	21.58 ± 0.04

Table 5.6: *γ_∞ values for each of the curves displayed in Figure 5.16.*

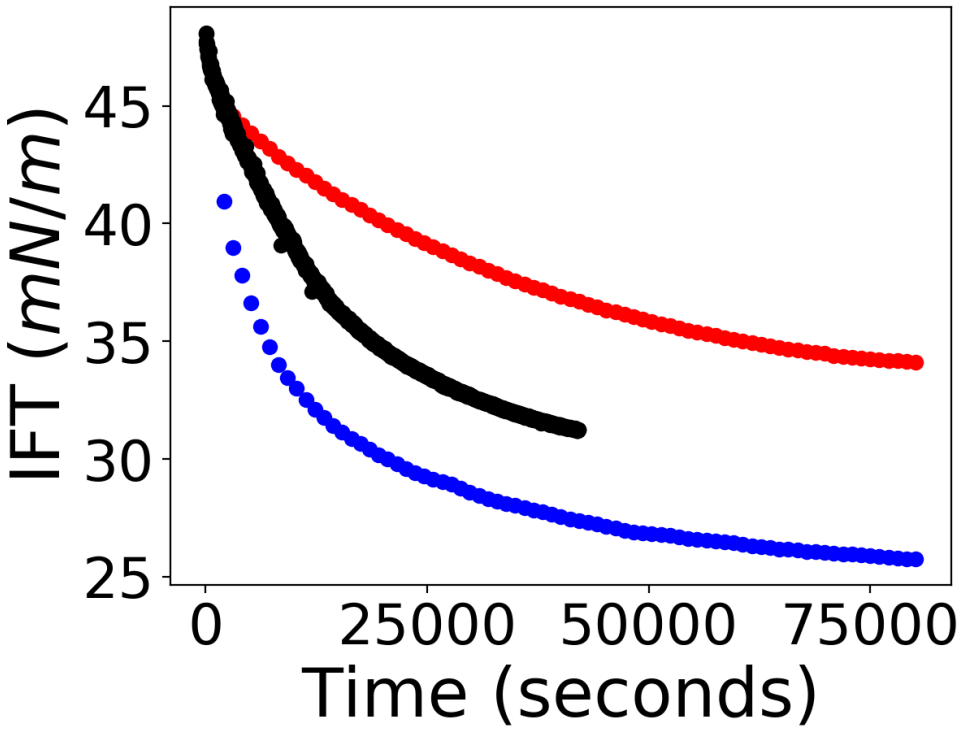

Figure 5.16: *Variations of interfacial tension γ as a function of drop age of a dodecane drop in an aqueous background with* 0.000 25 wt% *SZ microgels present. The red curve represents swollen SZ microgels ($R = 2.7\,\mu$m), the blue curve is for deswollen microgels ($R = 1.3\,\mu$m) adsorbing to an oscillating drop. The black curve is for swollen microgels ($R = 2.7\,\mu$m) adsorbing to a static drop.*

5.4 Cryo-SEM Measurements of SZ-stabilised Interfaces

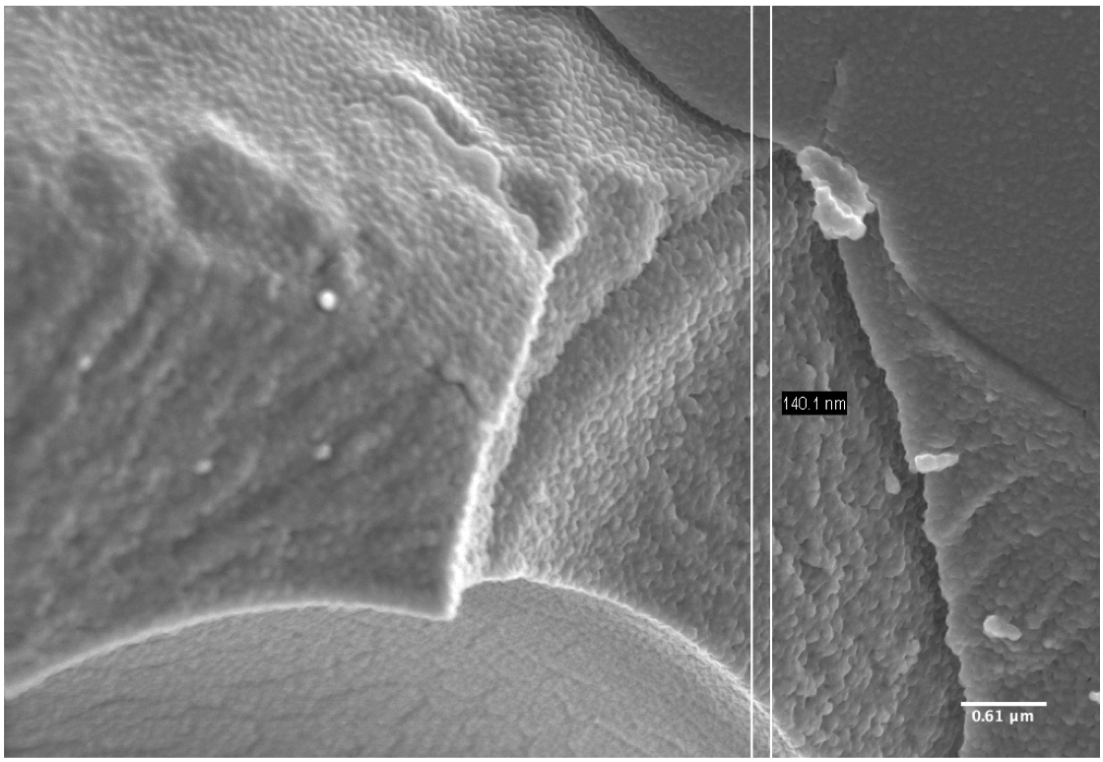

Figure 5.17: *A Cryo-SEM image of an caprylic/capric triglyceride oil drop stabilised by a highly compressed layer of microgels. This image was taken of an oil-in-water emulsion stabilised by* 0.5 wt% *which has been sublimed for 30 minutes to remove any ice crystals on the surface.*

Figure 5.17 shows an oil drop (Caprylic/Capric Triglyceride) being stabilised by layers of microgels (0.5 wt% of SZ was used in the emulsion). It should be noted that this image was taken after the drop was sublimed, meaning some of the water had been removed to improve the image quality. On the interfacial 'shell' surrounding the oil drop 'bumps' were found on the surface. However, the bumps were approximately 100 nm-200 nm in size which is much smaller than the lowest microgel size (520 nm measured by DDM with increased osmotic pressure). These artefacts may be a result of the sublimation process. Therefore the procedure was repeated with no sublimation at the same concentration of microgels and lower concentrations. Figure 5.18 shows a SZ-stabilised oil drop (same concentration as Figure 5.17) which has not been subjected to sublimation, and the bumps are

not present on the surface. This shows that the presence of the bumps is likely an artefact of sublimation process, where the microgel layer has been partially dehydrated.

Figure 5.19 shows a SZ-stabilised oil drop with only 0.01 wt% of SZ used and shows a much thinner and incomplete microgel layer. Figure 5.20 shows a zoomed of the oil droplets surface shown in Figure 5.19. The surface of the oil drop shown in Figure 5.20 shows distinct craters which shows evidence of microgels being adsorbed to the interface. The lace structure was probed using the cryo-SEM microscope and responded to partially sublimation indicating it contained water, most likely trapped when the microgels were adsorbed at the interface and frozen during the measurements. In order to estimate an effective contact angle of the microgels, the microgels were assumed to be perfect spheres as shown in Figure 5.21 and Figure 5.22. The average crater size D_c was measured using image analysis and then by comparing to the hydrodynamic radius of the microgels the wettability can be determined. The average crater size was calculated as $D_c = 1.3\,\mu\text{m} \pm 0.3\,\mu\text{m}$ which is much lower than the hydrodynamic diameter of the SZ microgels, $5.4\,\mu$m, indicating that the particles have are only partial adsorbed onto the interface. By considering the microgels as spherical particles the protrusion depth D_p can be calculated by knowing the contact diameter D_c (the average crater diameter) and the microgels hydrodynamic diameter $D_h = 5.4\,\mu$m. Figure 5.21 shows how the D_p can be calculated geometrically, $D_p = D_h - S$ where S is the distance between the D_h and D_c. D_p was determined as $0.09\,\mu$m which corresponds to an approximate contact angle 20°. Given the low wettability of the SZ microgels it is plausible that when they are perturbed on an interface that parts of the microgel could detach, meaning no buckling would be observed. This observation also contrasts the adhesion energies calculated from the fits to the IFT data in shown in Table 5.2. For a contact angle of 90° the subsequent adhesion energy for SZ microgels is $2.2 \times 10^8\ k_bT$, which is lower than the value for 0.000 25 wt%, $1.4 \times 10^9\ k_bT$. This is likely due to overestimated as the microgels will associate with the interface rather than adhere like a solid particle (Figure 5.22). Then as the drop is perturbed some of the hydrophobic polymers could be deposited on the surface of the oil drop. Bizmark's approach also assumes that the bulk diffusion drives the adhesion, however, given that SZ is more soluble in water and will be readily interact in bulk which could provide an effective adsorption barrier. DDM measurements confirm the microgels are associative and readily interact with each other, therefore, microgels will be more likely to interact in bulk which may interfere with adsorption to an interface. Furthermore,

there is also evidence of microgels interpenetrating, given the irregular shapes of the craters on the oil drops surface shown in Figure 5.20. The interpenetration also indicates that as microgels concentrate up they form'soft' gel layers on the surface, which explains why at higher concentrations there is little evidence of individual particles at the interface.

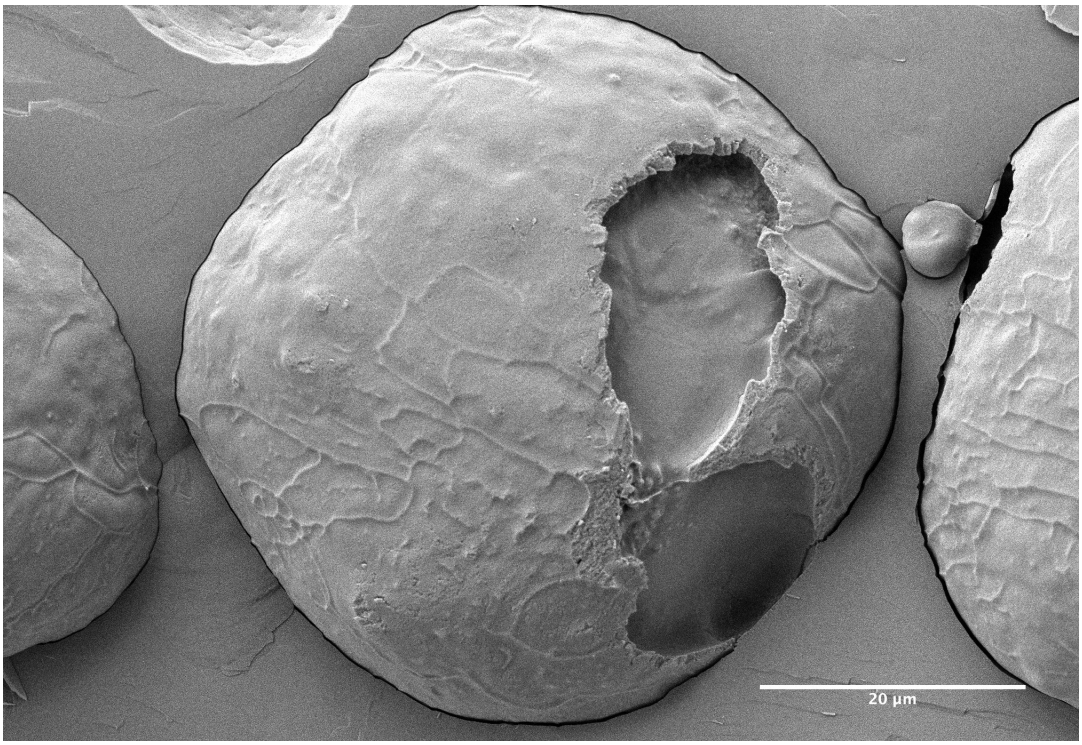

Figure 5.18: *A cryo-SEM image of an caprylic/capric triglyceride oil drop stabilised by a highly compressed layer of microgels. This image was taken of an oil-in-water emulsion stabilised by* 0.5 wt% *which had not been sublimed.*

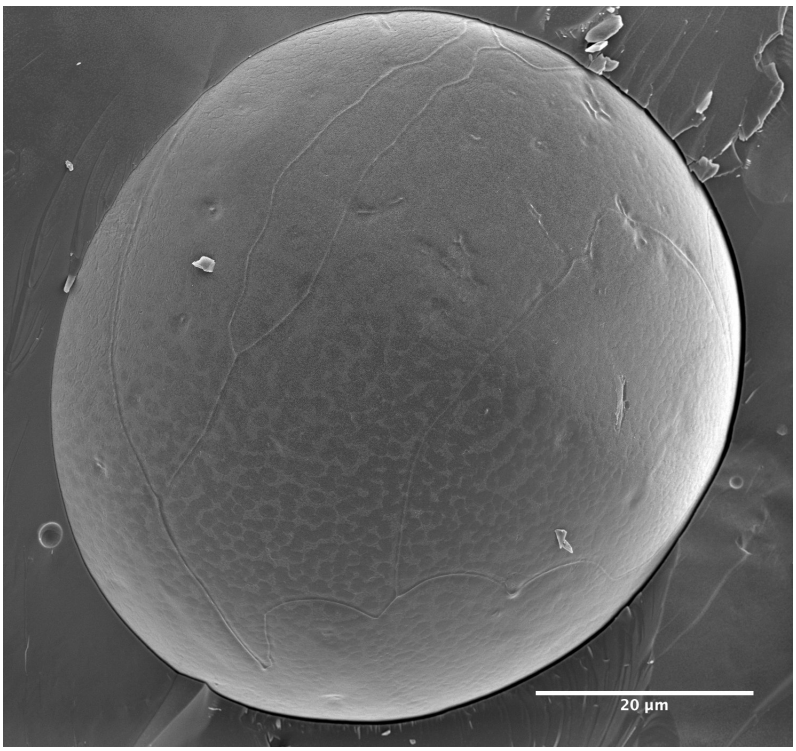

Figure 5.19: *A cryo-SEM image of an caprylic/capric triglyceride oil drop stabilised by a highly compressed layer of microgels. This image was taken of an oil-in-water emulsion stabilised by* 0.01 wt% *which has not been sublimed.*

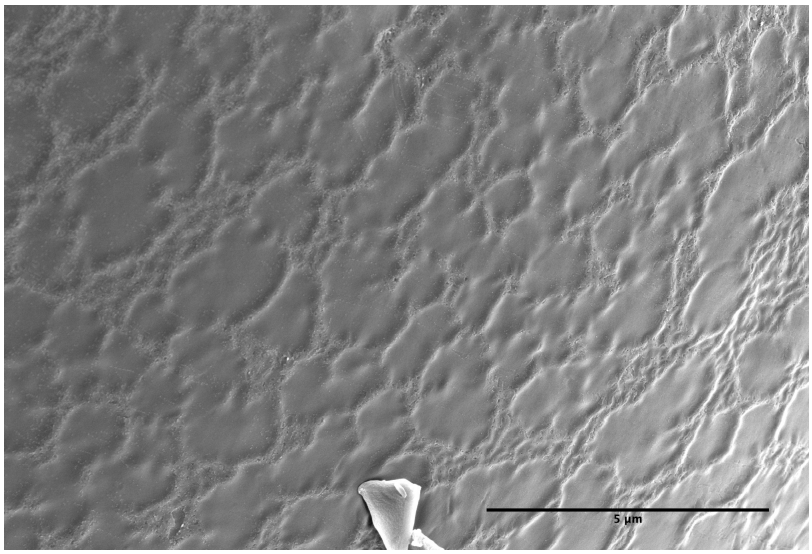

Figure 5.20: *A cryo-SEM image of the surface of a partially stabilised caprylic/capric triglyceride oil drop, showing the imprints of microgels on the surface. This image was taken of an oil-in-water emulsion stabilised by* 0.01 wt% *which has not been sublimed.*

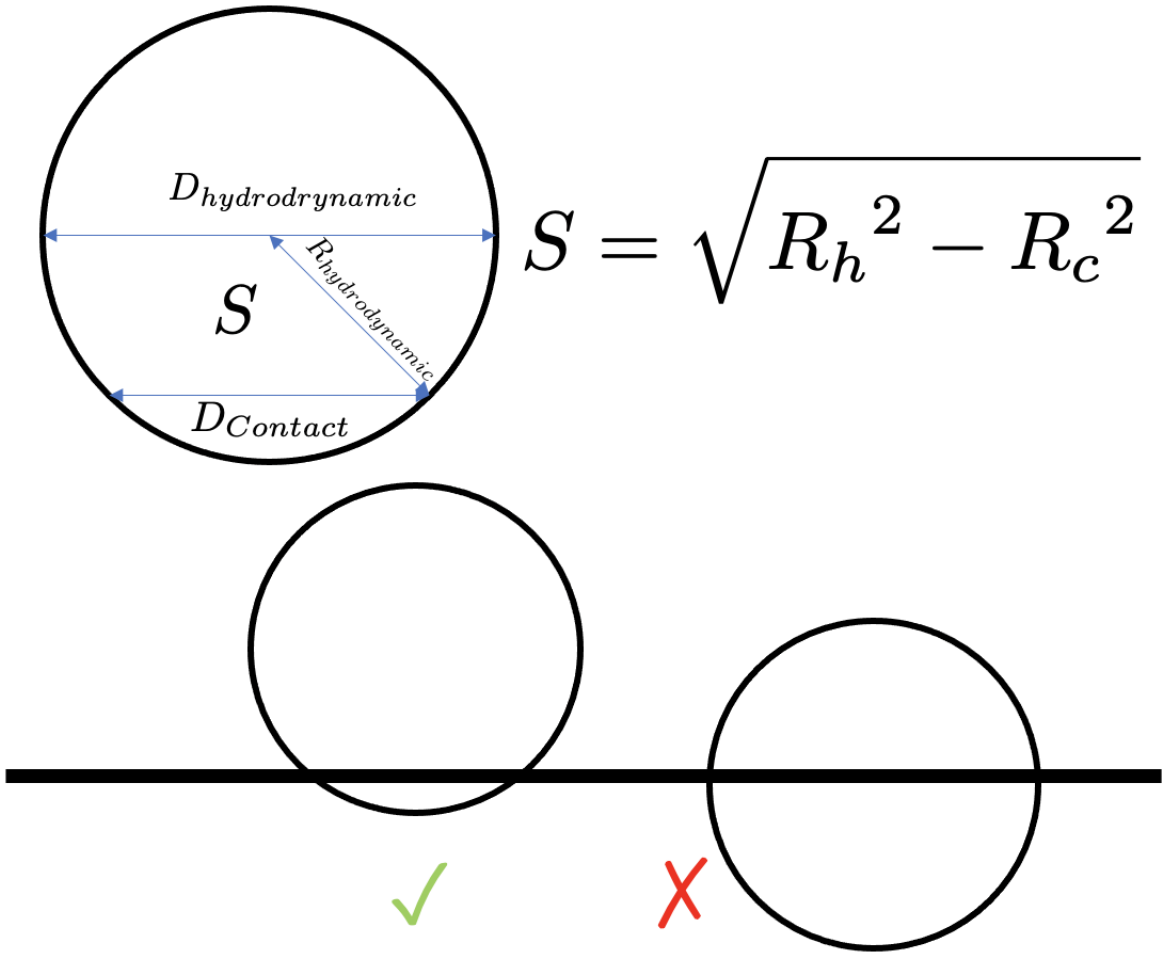

Figure 5.21: *Schematic of the geometry used to measure the protrusion depth of the SZ microgel. In the diagram $D_{hydrodynamic}$ is the hydrodynamic diameter of the microgel,$R_{hydrodynamic}$ is the hydrodynamic radius of the microgel, $D_{contact}$ is the diameter of the microgel in contact with the interface, R_c is the radius of the microgel in contact with the interface and S is the distance from the center of the microgel to the $D_{contact}$. The bottom image shows how the microgel is attached at the interface. The microgel on the bottom left is indicative of SZ with an approximate contact angle of* 20° *whereas on the right is particle with contact angle of* 90°.

Figure 5.22: *Schematic of the SZ adsorption mechanism showing the comparison to a spherical particle (right) and microgel (left). For the microgel the blue represents the hydrophilic sections and the red being the hydrophobic chains which mediate adsorption to the interface.*

5.5 Summary

In this chapter the interfacial properties of SZ microgels were investigated at a water-dodecane interface. SZ microgels were shown to lower the interfacial tension considerably and shows evidence of additional adsorption occurring even after the interface has been saturated. Further adsorption is likely to due to interactions between microgels at the interface and in bulk.

The elasticity of the SZ-laden interfaces was probed to determine how it compared to other colloids and surfactants. The elasticity and surface pressure was found to increase gradually before plateau as the interface became saturated. From plotting elasticity as a function of surface pressure it was determined that adsorption was more dominant for unswollen microgels. This was attributed to the larger size of swollen microgels which lead to interactions occur at the interface such as spreading and rearrangement. The frequency response of SZ-stabilised interface was also tested and confirmed that microgels form viscoelastic films.

SZ-stabilised interfaces also show no buckling upon compression which is different to particles and other microgel systems. This unique property is likely due to the chemical composition of the microgels as well as its ability to swell and interpenetrate. In summary the main points from this chapter are as follows:

- The mechanism at which SZ microgels stabalise interfaces is comparable to proteins, where interactions play a key role

- SZ-stabilised interfaces are very elastic with $E' > 20\,\mathrm{mN/m}$ which is similar to hard colloids
- Deswollen microgels produce more elastic interfaces with an $E' \approx 27\,\mathrm{mNm}$ whereas swollen microgels $E' \approx 22\,\mathrm{mNm}$ most likely due to more efficient packing
- From analysing how E' depends on ϕ it was found that SZ microgels interact at the interface
- SZ-stabilised interfaces were shown to be immune to buckling
- SZ microgels are shown to be lightly attached at interfaces, with a contact angle of $\approx 160°$, but concentrate up to form continuous gels

From the results of this chapter, along with previous chapter, the rheological and interfacial properties of SZ microgels have been determined. In the following chapter the role of SZ in emulsions is investigated.

Chapter 6

SZ Microgels in Emulsions

6.1 Rheology of SZ-stabilised emulsions

The results of the steady shear rheology of the emulsions is shown in Figure 6.1 and Figure 6.2 (for the composition of the emulsions please refer to Section 2.1.2). Figure 6.1 and Figure 6.2 show how the shear stress σ and viscosity η depend on the applied shear rate $\dot{\gamma}$ respectively. The data in Figure 6.1 shows that there is evidence of a yield stress at low $\dot{\gamma}$, which becomes more prominent at higher oil fractions, then as $\dot{\gamma}$ increases the emulsions shear thin. The shear thinning behaviour is also shown in Figure 6.2, where η decreases as $\dot{\gamma}$ increases.

The data in Figure 6.1 was fitted with a standard Hershel-Bulkley relation of the form, $\sigma = \sigma_y + k\dot{\gamma}^n$, where σ_y is the yield stress, k is the consistency index and n is the shear index. The results of the Hershel-Bulkley fit can be found in Table 6.1.

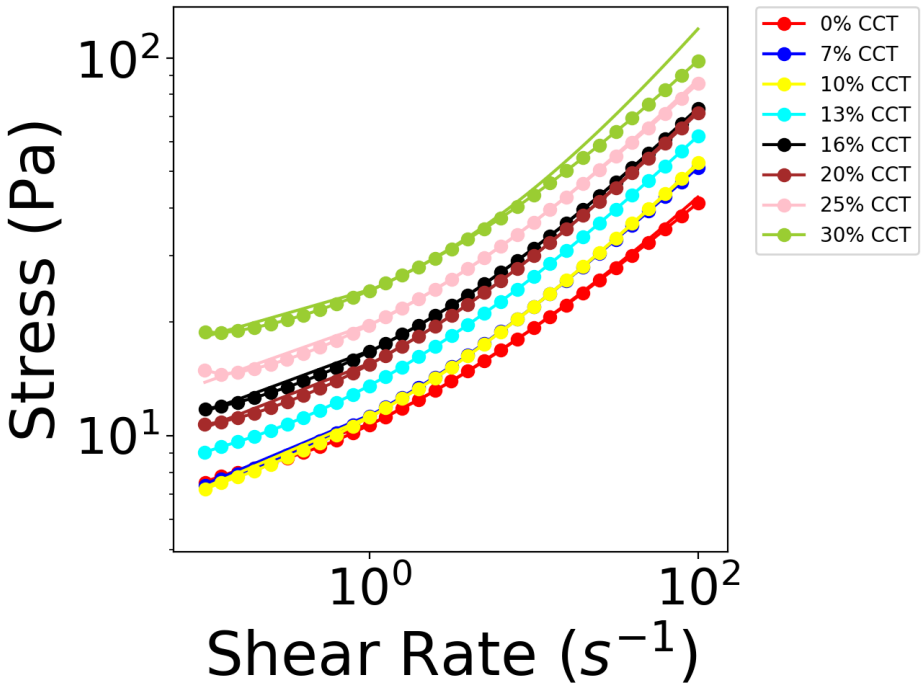

Figure 6.1: *Variations in shear stress σ plotted as a function of applied shear rate $\dot{\gamma}$ for the a range of SZ-stabilised emulsions. The SZ concentrations is* 0.5 wt% *is each case. Solid lines indicate the fits to the Hershel-Bulkley equation.*

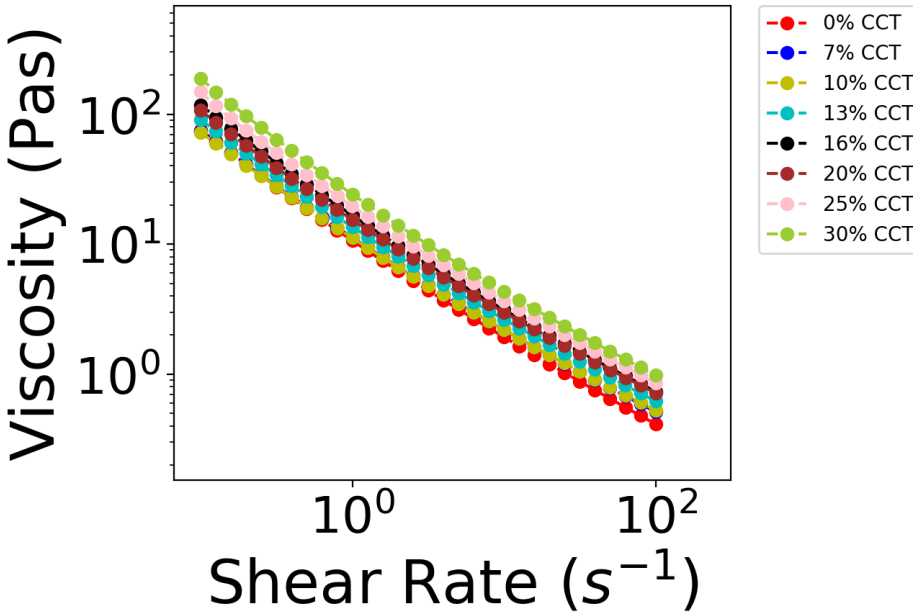

Figure 6.2: *Variations in viscosity η plotted as a function of applied shear rate $\dot{\gamma}$ for the a range of SZ-stabilised emulsions. The SZ concentrations is* 0.5 wt% *is each case.*

CCT (wt%)	σ_y (Pa)	k	n
0	7.4	7.3	0.39
7	5.2	6.1	0.44
10	5.2	5.9	0.45
13	6.5	7.1	0.45
16	8.9	7.7	0.46
20	7.8	7.6	0.46
25	11	8.9	0.46
30	15	9.7	0.47

Table 6.1: *Values of experimental parameters determined from fitting the rheology data of SZ-stabilised emulsions with the Herschel-Bulkley relation.*

The average shear thinning index across all the emulsion sample is 0.45 ± 0.02 which is comparable to similar studies done on soft particle pastes and concentrated emulsions [179] [180]. The σ_y is found to decrease slightly from 0 wt% - 13 wt% , however, above this the yield stress starts to increase above the initial value of 7.4 Pa. This initial decrease in σ_y is indicative of adsorption of

microgels from the continuous phase to stabilise the dispersed oil drops [86]. In order to test this the elastic modulus G' (averaged in the LVR) was measured for as function of oil content which is shown Figure 6.3.

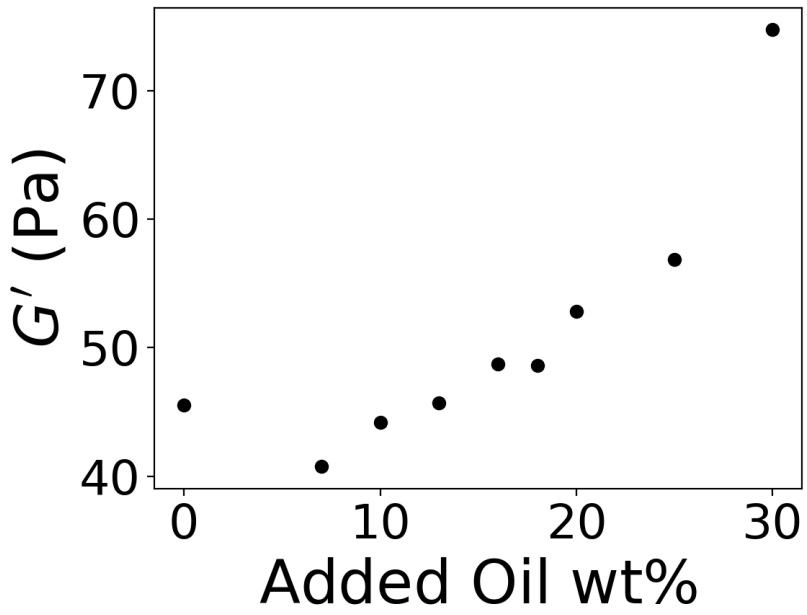

Figure 6.3: *Variations in the storage modulus G' of SZ-stabilised emulsions, with a fixed SZ concentration of* 0.5 wt%*, as a function of oil content.*

Figure 6.3 shows again a decrease in G' up to 13 wt% however, beyond this an increase in gel strength is observed. This behaviour suggests that the oil droplets go from being an 'inactive' to an 'active' filler. An active filler has a strong interaction with the gel matrix, resulting in a strong mechanical reinforcement of the network and an increase in gel strength. In contrast, an inactive filler has little chemical affinity for the the matrix and hence does not strengthen the gel. Protein-stabilised emulsion drops have been shown to behave as active fillers while surfactant-stabilised drops behave as inactive fillers [84] [83] [85]. The elastic modulus of the emulsion G'_E was normalised by dividing the modulus of the gel matrix G'_M which represents the storage modulus of the gel matrix, i.e., the modulus of the equivalent oil-free gel. Figure 6.4 shows the how the ratio of G'_E to G'_M changes as the more filler/oil is added. It is observed that initially the CCT droplets act as inactive fillers upto 20 wt%, after which they become active and strengthen the gel. Microgel-stabilised emulsion gels with have been studied before, however, in these cases the oil always acts to strengthen the gel [83] [181].

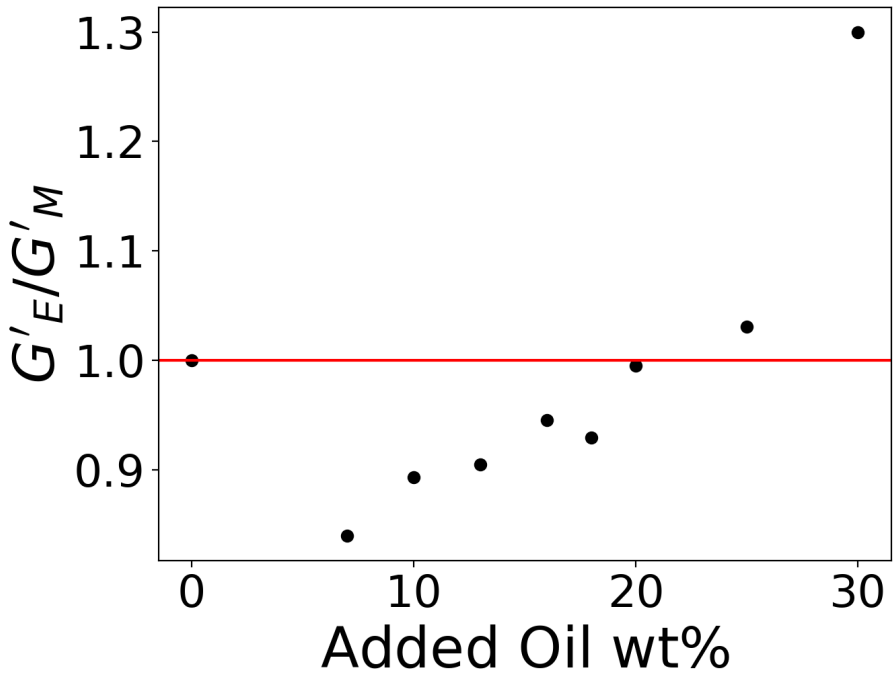

Figure 6.4: *Effects of oil content on the elasticity of SZ-stabilised emulsions. The logarithm of G'_E/G'_M, where G'_E is the storage modulus of the emulsion gel and G'_M is the storage modulus of the gel matrix, is plotted against the oil content.*

This effect is likely due to the SZ microgels stabilising the oil drops. As microgels adsorb onto the droplets surface, given their size, they will effectively enlarge the droplet as seen in the cryo-SEM images in Chapter 5. Therefore, this increase needs to be accounted for when considering the effective volume fraction of the system. If the microgels can pack on the surfaces then the limiting volume fraction needs to be determined by considering the packing of emulsion drops with an adsorbed layer of microgels. The limiting volume fraction can be calculated by considering the particle separation between droplets and accounting for an adsorbed layer of microgels as shown in Figure 6.5. In the emulsions prepared droplets were measured as small as $5\,\mu$m and considering swollen SZ microgels have a hydrodynamic diameter of $5.4\,\mu$m, adsorption will have a significant effect on droplet packing. Considering the case shown in Figure 6.5, droplets coming into contact, if there are no microgels adsorbed onto the droplets surface, the ratio of the separation of the emulsion centres r and the droplet diameter d is $r/d = 1$. However, in the case an adsorbed layer of 1 microgel thickness $r/d = 1.27$, which predicts the emulsion drops will close pack at $\phi_{cp} = 0.3$

($\phi_{cp} = 0.635/(r/d)^3$). Given that the results of the previous chapters indicate that it is likely that layers of microgels act to stabilise the interface a multilayer must be considered. If it is assumed that neighbouring emulsion interfaces are each stabilised by a layer 1 microgel thick ($r/d = 1.27$), as seen in Figure 6.5, close packing occurs at $\phi = 0.31$ which becomes $\phi = 0.17$ for a layer 2 microgels thick ($r/d = 1.54$). These volume fractions correlate with the droplets become active fillers, $\phi = 0.2$, and the limiting volume fraction, $\phi = 0.3$. This indicates that the 'active' response of the emulsions seen in the rheology is due to adsorbed microgels causing emulsion drops to rub together. In this case it means there is no 'free' microgel between the droplets to lubricate and separate them, thereby this interaction gives rise to an enhanced elastic response when probed. It should be noted that this estimation does not take into account polydispersity of the drops or an shrinkage effects, however, it does predict the extent the microgels could affect the packing properties of the emulsions.

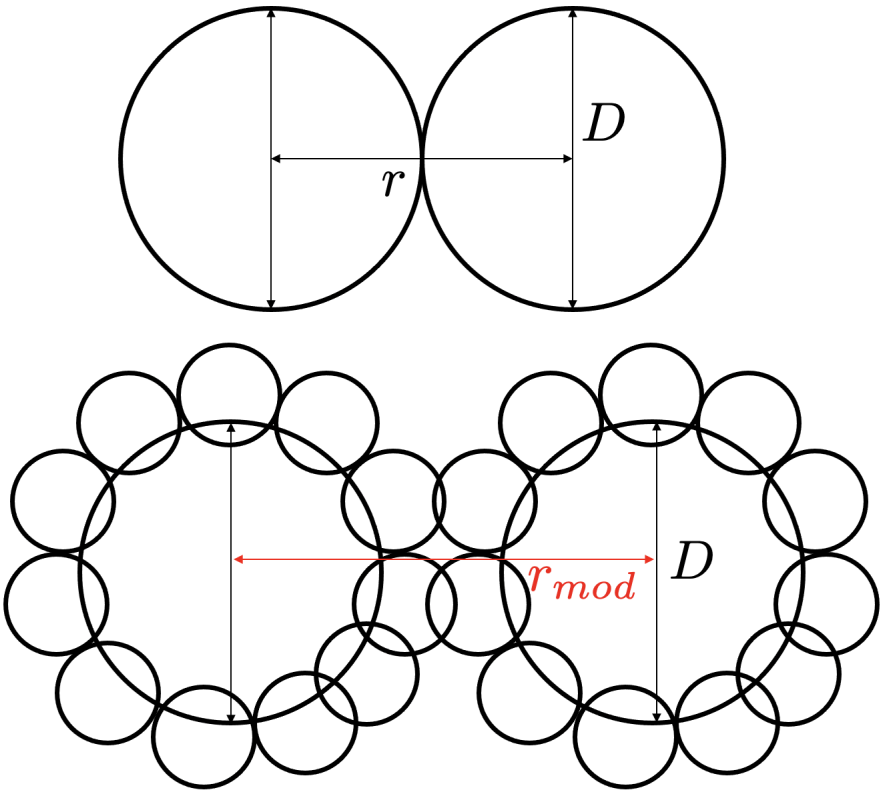

Figure 6.5: *Schematic of emulsion drops coming together without a microgel layer (top) and with a microgel layer (bottom). D represents the diameter of the emulsion drop, r is the separation between the emulsion centres and r_{mod} is the separation with a microgel layer added.*

6.2 Centrifugation of SZ-stabilised emulsions

Figure 6.6 shows the emulsions after they were centrifuged, the oil phase was dyed using Nile Red to give better contrast to the continuous phase. Each emulsion was centrifuged until the cream layer at the top of the sample was a continuous layer i.e. containing no emulsion drops.

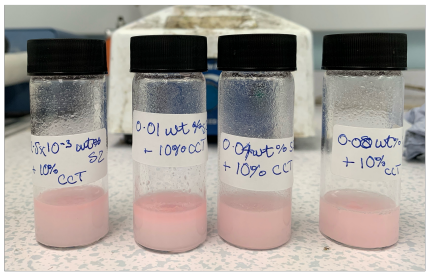

(a) *Emulsions after vortexing*

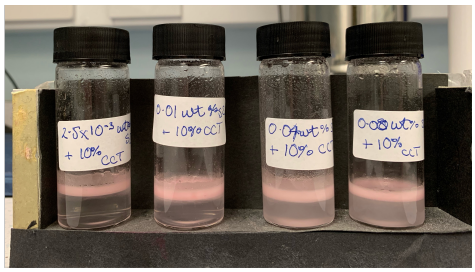

(b) *Vortexed emulsions after 24 hours*

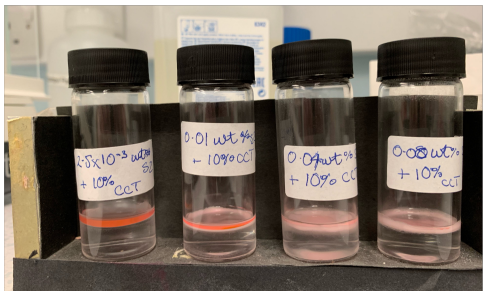

(c) *Emulsions after centrifuging*

Figure 6.6: *Vortexed emulsions each containing* 10 wt% *of oil with various concentrations of SZ: left to right* 2.5×10^{-3} wt%, 0.01 wt%, 0.04 wt% *and* 0.08 wt%. *(a) Emulsions after vortexing, (b) Vortexed emulsions after 24 hours and (c) Centrifuged emulsions.*

As expected as the concentration of microgels was increased the greater centrifugal acceleration was needed to destabilise the oil drops. In order to get a quantitative measure of coalescence stability the critical osmotic pressure, P_{OSM}^{CR}, at which this continuous oil layer is released from the emulsion was calculated for each emulsion [87]. P_{OSM}^{CR} is calculated from the experimental data through the

relation,

$$P_{OSM}^{CR} = \Delta\rho g_k (V_{OIL} - V_{REL})/A_{TT}, \tag{6.1}$$

where $\Delta\rho$ is the difference in mass densities of the oil and water phases, g_k is the centrifugal acceleration, V_{OIL} is the the total volume of oil in the emulsion and V_{REL} is the volume of oil released on top of the cream and A_{TT} is the cross sectional area of the vial [87]. Droplet size R of each emulsion was estimated using confocal microscopy. Table 6.2 shows the calculated values of P_{OSM}^{CR} and g_{kcrit}, the g-value at which the oil had been completely removed.

C (wt%)	g_{kcrit} (g)	P_{OSM}^{CR} (Pa)
0.00025	100	68
0.01	500	343
0.04	1200	824
0.08	1200	824

Table 6.2: *Values of the critical g-value critical g_{kcrit} and critical osmotic pressure P_{OSM}^{CR} for the various emulsions. Each emulsion contained* 10 wt% *of oil with various concentrations of SZ.*

From the results shown in Table 6.2 it can be seen that the P_{OSM}^{CR} increases by a factor 10 from 0.000 25 wt% to 0.04 wt%. This increase is due to the build up of microgels on the surface of droplets and this is before a yield stress has been devolped in the continous phase. From Cryo-SEM measurements at 0.01 wt% the microgel layers stabilising the oil droplets did not sufficiently cover the entire interface. However, above 0.01 wt% droplets were completed coated, staggering coalescence. In order to test the effect of microgel compression, emulsions containing 20 wt% of oil and 0.5 wt% of SZ were centrifuged. Given that these emulsions have a considerable σ_y a much larger centrifuging acceleration was needed to separate the oil. These concentrated emulsions were centrifuged at 20 000 g overnight and P_{OSM}^{CR} was calculated to be 5×10^4 Pa. 20.000 g was selected as lower g values did not destablise the emulsions most likely due to the significant yield stress developed in the continous phase. This value is comparable to other protein and surfactant stabilised emulsion systems [87] [88]. This result indicates that the the microgels behave is a similar way to surfactants directly influencing the emulsion stability.

6.3 Analysis of Thin-films of SZ-stabilised emulsions

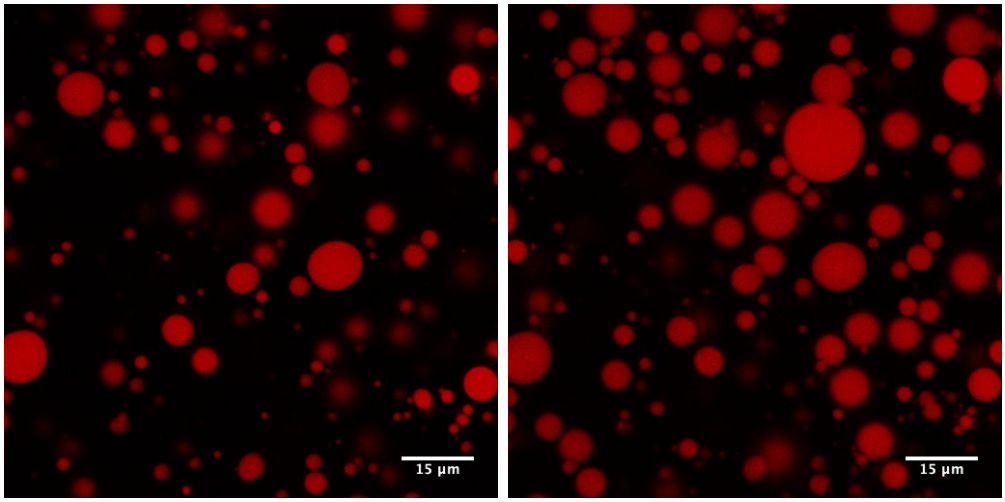

(a) *0 minutes* **(b)** *10 minutes*

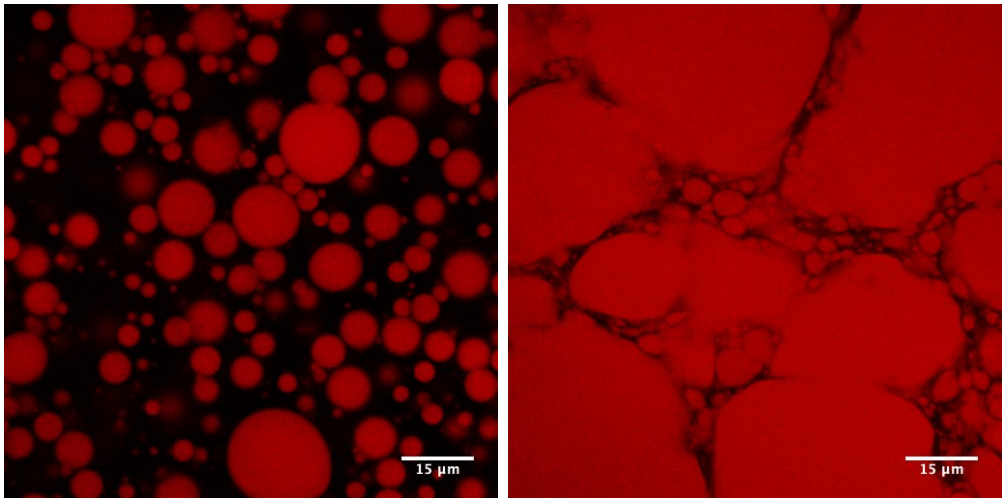

(c) *15 minutes* **(d)** *20 minutes*

Figure 6.7: *Confocal microscopy images of drying model emulsions containing* 20 wt% *of CCT and* 0.5 wt% *of SZ. The CCT has been dyed with Nile red while the dark areas represent the gel matrix. Each panel is taken at different time points of the the drying process.*

Figure 6.8 shows the evolution of a a thin film of SZ-stabilised emulsion as a function of time, for the procedure please refer to Section 2.7. As time progresses the water begins to evaporate and the oil drops begin to coalesce before halting after approximately 20 minutes. Films eventually dried down to where minimal

water remains, due to evaporation, however some water remained trapped down at the substrates surface i.e. the bottom of the film. Using the previous data on the rheology of the SZ gels (Chapter 3) and the emulsion gels (Chapter 6), the bulk properties of the films can be estimated. To do this ImageJ was used to measure the area fraction of the oil at various depths of the 20 μm film, which allowed the area of fraction of continuous gel phase (A) to tracked. This procedure was repeated at each time point along the drying process. Figure 6.8(a) shows how A varies as a function of time for different depths of the emulsion film. Figure 6.8(b) shows how A_{Norm} ($A_{Norm} = A/A_{initial}$) where $A_{initial}$ is the initial area fraction recorded at the beginning of the measurement) varies as a function of time. From the results shown in Figure 6.8 (a) and (b) the water is mostly evaporated by the end of the measurement with lower depths taking longer since water from the bottom of the film needs to travel through the rest of the film to evaporate. Figure 6.8(b) shows two decay rates: a slower initial rate (< 500 seconds) and a second faster rate > 500 seconds).

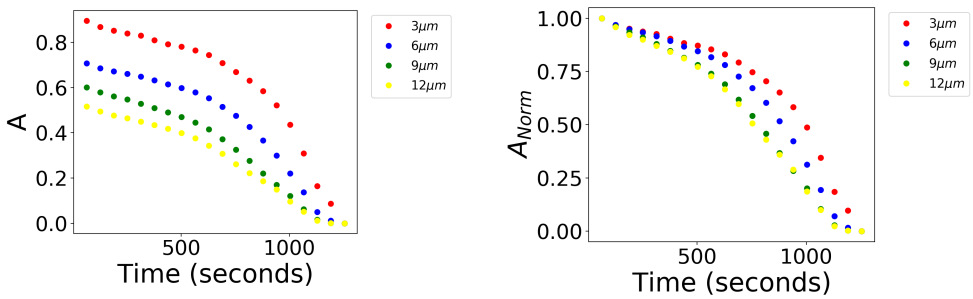

Figure 6.8: *(a) Variations of the area of aqueous phase A, at different heights of the SZ-stabilised emulsion film, plotted as a function of time. (b) Variations of the normalised area of aqueous phase A_{norm}, at different heights of the SZ-stabilised emulsion film, plotted as a function of time.*

Figure 6.9 shows the A averaged over the four depths ($< A_{norm} >$) as a function of time. From Figure 6.9 at 500 seconds the oil fraction can be estimated at approx. 0.34. From the emulsion rheology mixtures remain stable up until 30 wt% of oil, at higher oil content coalescence is observed. Through evaporation the water phase will be depleted leading to oil drops coming together further compressing the surrounding microgels. Adsorption will halt when the energy gain per new adsorbed particle is surpassed by the energy penalty required to compress the microgels already at the interface. In the case of the core-shell nanoparticles,

although it is reasonable to consider Pickering stabilisers with $\approx 10^3\ k_BT$ to be irreversibly adsorbed, sufficiently compression of an interface can change this. Under significant compression these core-shell nanoparticle can desorb once a critical surface pressure is reached, which can occur between coalescing droplets [182]. It should also be noted that during other studies where similar drying experiments were conducted that coalescence signalled the reaching of the critical osmotic pressure. From knowing the initial SZ concentration and by tracking the subsequent water loss the the polymer concentration of the mixture can be plotted as a function of time, shown in Figure 6.10. At 500 seconds the SZ concentration is 0.6 wt%, and the oil fraction is predicted to be 0.34 %, which is above the threshold of stability for samples, 0.3 %, however this is for quiescent samples but gives an indication of stability. Figure6.8(d) shows the final state of the emulsion film on the substrate which shows that the dispersed oil phase has heavily coalesced with some thin polymer layers (dark areas) separating them.

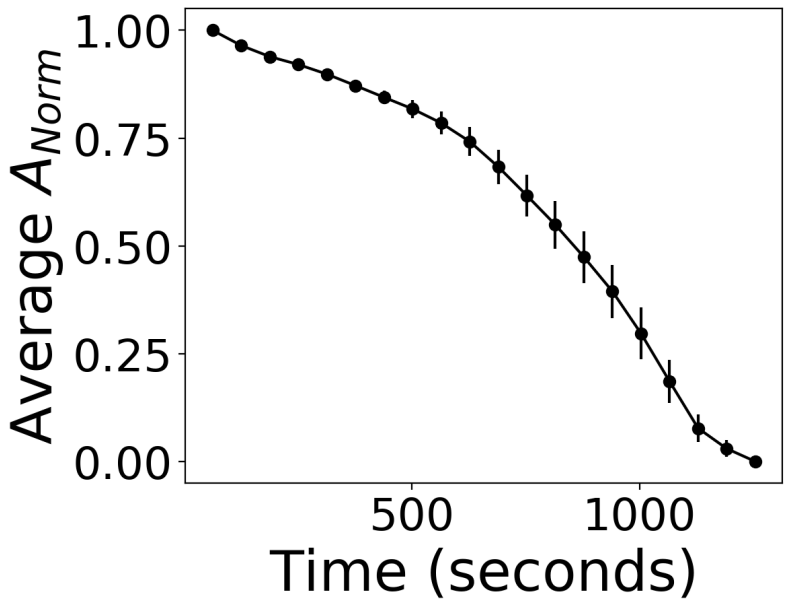

Figure 6.9: *Variations of the normalised area of aqueous phase averaged over all depths of the film* $< A_{norm} >$ *plotted as a function of time.*

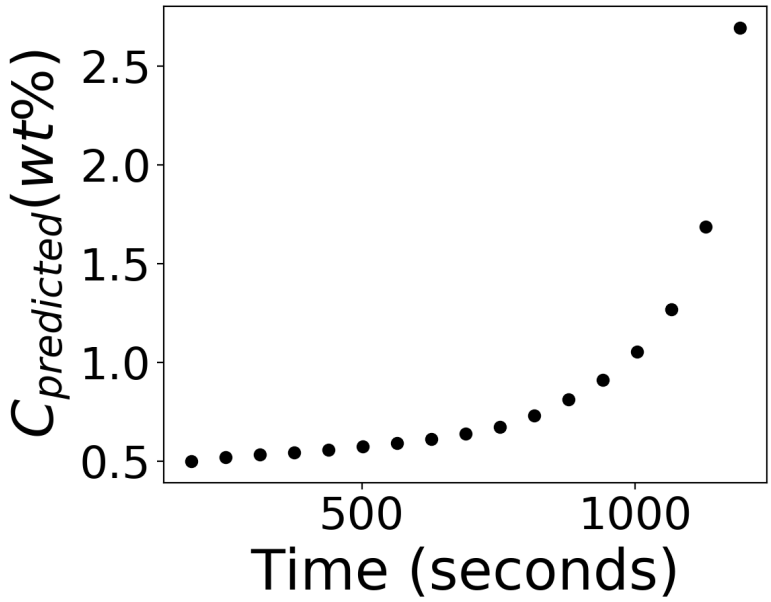

Figure 6.10: *Variations of the predicted SZ concentration $C_{predicted}(wt\%)$ plotted as a function of time.*

In order to confirm this some subsequent thin measurements are shown in Figure 6.13 done with microscopy setup in Bordeaux. Figures 6.13 and 6.12 show images of dried down thin films of SZ-stabalised emulsions. Both Figures show artefacts similar to the structures seen in Figure 6.8 where the initial emulsions had undergone partial coalescence, resulting in a network of oil drops separated by thin polymeric films. This indicates that microgel-stabilised emulsions could be used to create thin films with specific microstructures, a result which has been seen for other emulsions and polymer solutions [92] [93].

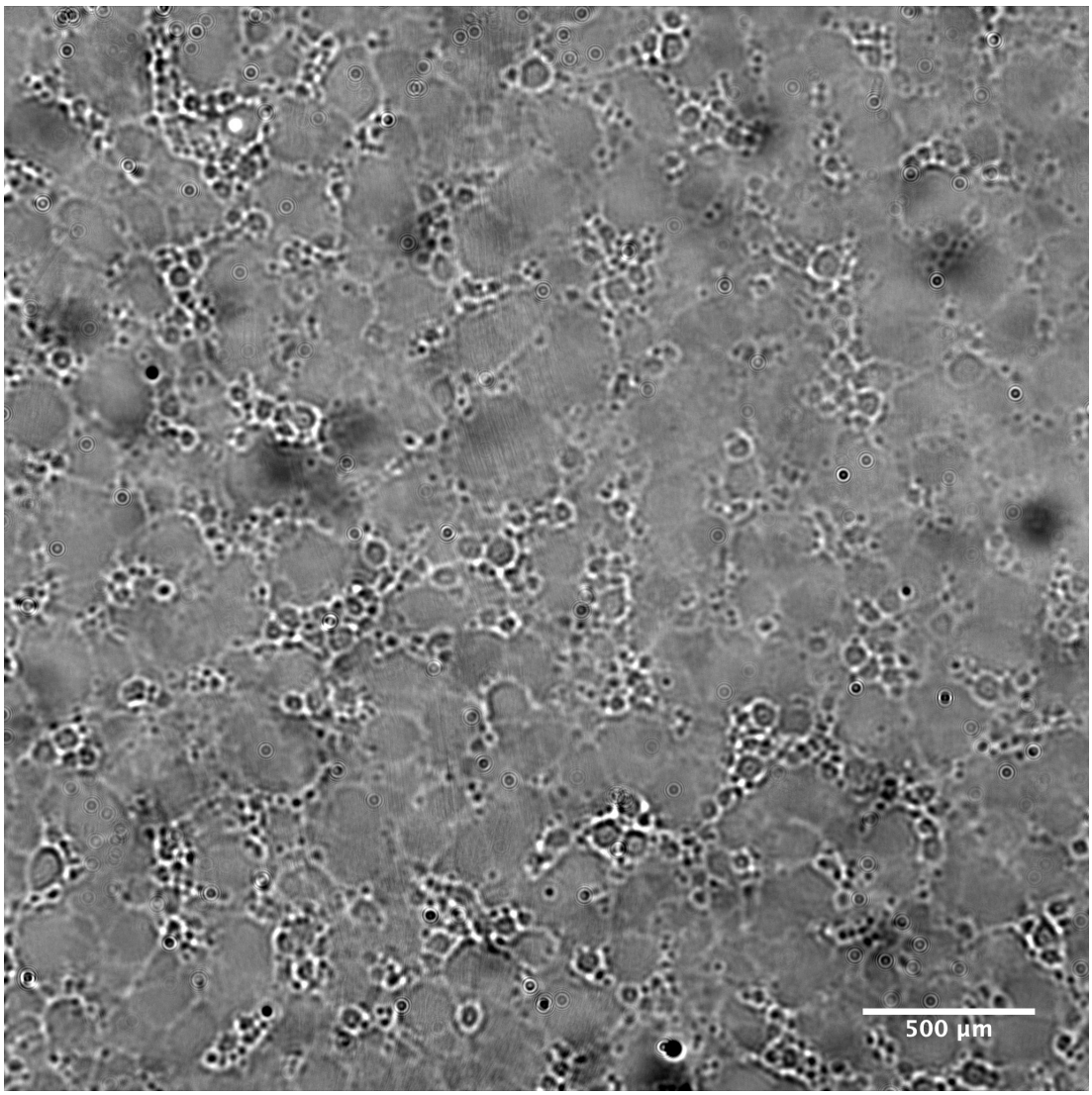

Figure 6.11: *Image of the base of a dried sheared thin film of a SZ-stabilised (*0.5 wt%*) emulsion with* 20 wt% *of Caprylic/Capric Triglyceride. The film had been dried, in the open atmosphere, for approximately 30 minutes. The resulting structure shows partially coalesced droplets of oil separated by thin polymer films resulting in web-like structure.*

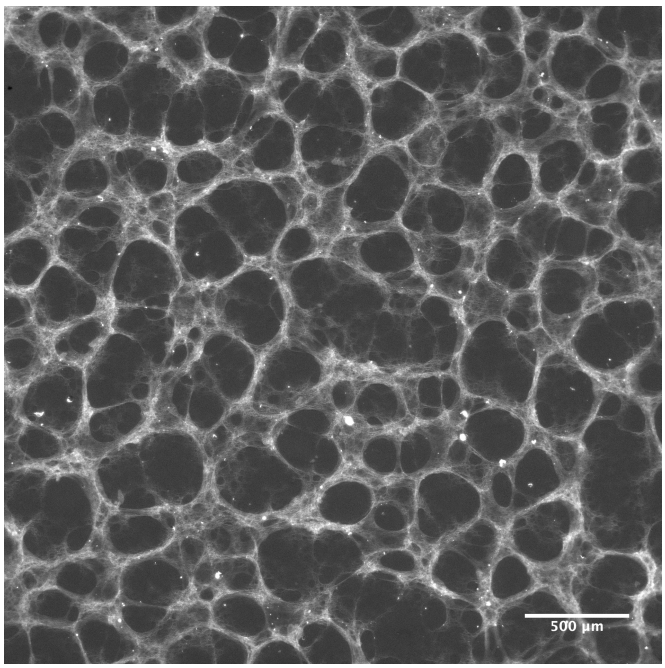

(a)

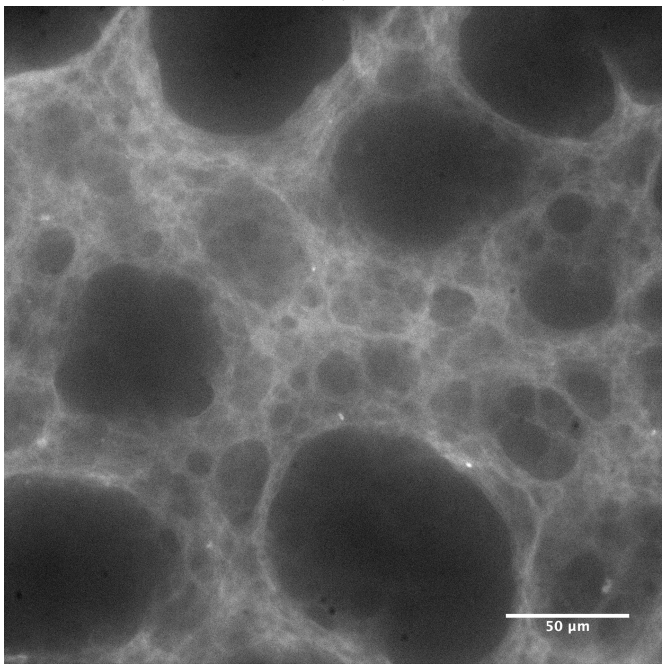

(b)

Figure 6.12: *Image of the base of a dried sheared thin film of a SZ-stabilised (*0.5 wt%*) emulsion with* 20 wt% *of Caprylic/Capric Triglyceride. The film had been dried, in the open atmosphere, for approximately 30 minutes. The resulting structure shows partial coalescenced pools of oil separated by thin polymer films resulting in web-like structure.Images show base of thin films of a SZ-stabilised (*0.5 wt%*) emulsion with* 20 wt% *of Caprylic/Capric Triglyceride, where the aqueous phase has been dyed with fluorescein, darker regions indicate where the Caprylic/Capric Triglyceride oil is.*

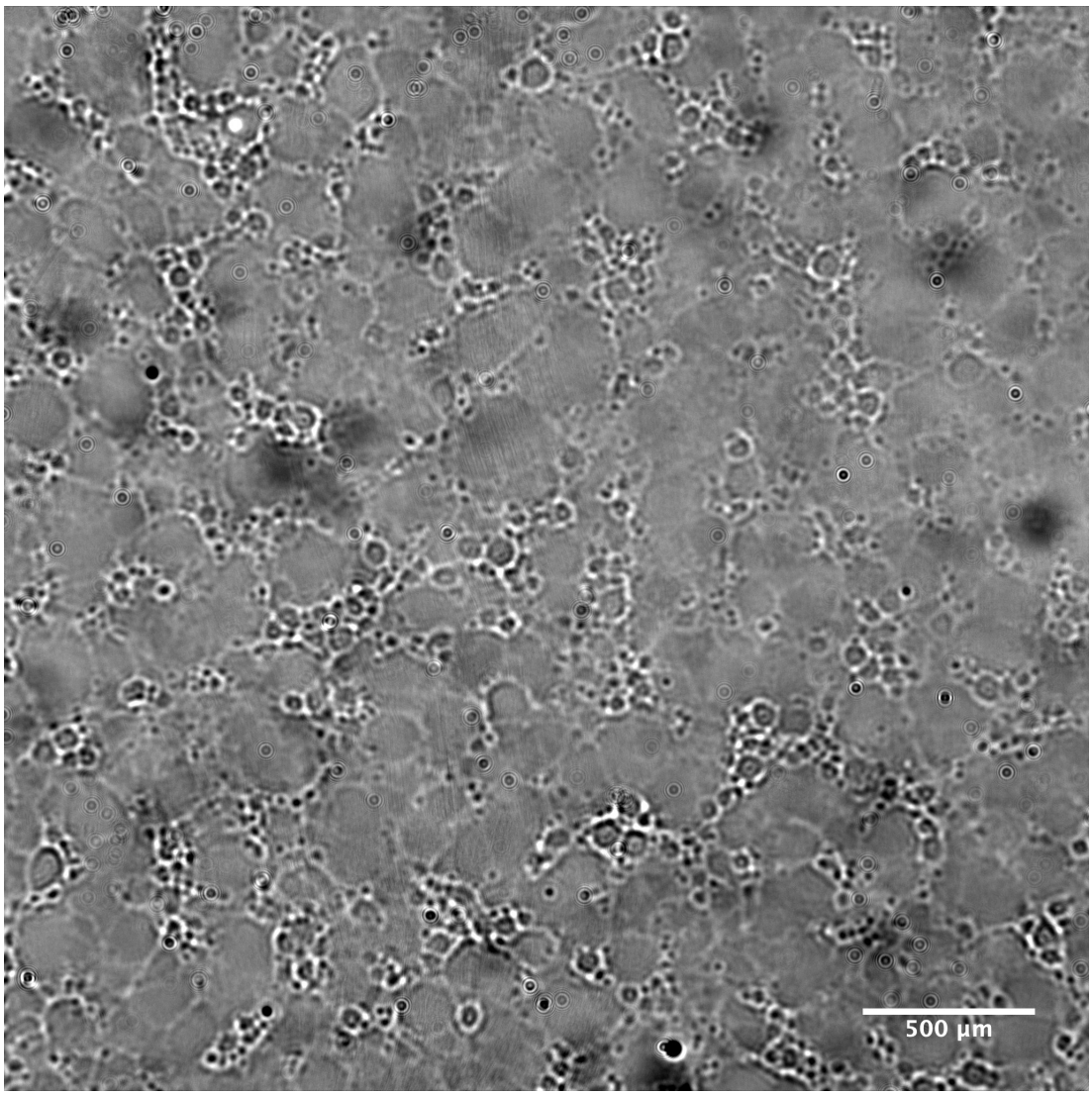

Figure 6.13: *Images show base of thin films of a SZ-stabilised (*0.5 wt%*) emulsion with* 20 wt% *of Caprylic/Capric Triglyceride, where the aqueous phase has been dyed with fluorescein, darker regions indicate where the Caprylic/Capric Triglyceride oil is..*

6.4 Summary

In conclusion in this chapter explores the behaviour of SZ when used in emulsion systems. The rheology of such emulsions shows that SZ thickens emulsions by gels around the oil droplets. However, the oil content becomes an important factor at high filler fractions (>20 wt%) where droplets interact more strongly with the network resulting in emulsions with higher elastic character. Furthermore, this effect also influences when emulsions become unstable, and begin to coalesce. This

result was seen in thin films of SZ-stabilised emulsions where the compression of microgels resulting in partially coalesced films with distinct networks of oil drops. This effect means microgel-stabilised emulsions can be used to engineer thin films with distinct microstructures, which needs to be considered when using SZ to formulate emulsions. In summary the main points from this chapter are as follows:

- SZ-stabilised emulsions are shown to produce active emulsion-filled gels above a critical oil volume fraction of 0.2
- The active network arises from microgels adsorbing onto the surface of oil drops causing droplets to rub together acting to strengthen the mechanical nature of the gels
- SZ-stabilised emulsions were shown to have a limit on the amount of oil that could be stabilised $\phi = 0.3$ which is due to microgel adsorption at the interface
- The critical disjoining pressure of SZ microgels was found to be comparable to other surfactant based systems
- SZ-stabilised emulsions eventually dried down to partially coalesced emulsion films similar to those produced by surfactant stabilised films

The results of this chapter build upon previous chapters by trying to understand the role of SZ in emulsions. The findings provide a basis to understanding how microgels act to thicken and stabilise emulsions by building on the results of the previous chapter which consider both processes separately.

Chapter 7

Conclusions and Outlook

This thesis provides the first study of a widely used commercial microgel system called Sepimax Zen. The aims of thesis was to quantify how the polymer-colloidal duality of SZ determines bulk characteristics of microgel suspensions and contrast those results with model, more established, microgels. This thesis concludes with a summary of the findings of each chapter's results. Chapters 1 explores the wide literature on microgels focussing on their structure, bulk characteristics and emulsifying capabilities. Specifically, the literature review identified the key results and measurements needed to best characterise SZ and provided candidates, such as PNIPAM, to compare to. The rational, protocols and background of the experimental techniques that were employed are detailed in Chapter 2.

Chapter 3 is first results section of this thesis. In Chapter 3 the main findings of the rheological measurements are outlined. The rheological profile of the SZ microgels was tested using a combination of steady shear and oscillatory rheology. Steady state measurements revealed that at sufficiently dilute concentrations the suspensions behave as Newtonian liquids, however, once a critical concentration (0.03 wt%) has been reached they become shear thinning. Furthermore, at higher concentrations (0.08 wt%) a yield stress develops indicating the formation of network structure. Oscillatory measurements revealed the nature of these networks. Strain measurements show that microgels form networks by interpenetrating with each other similar to polymers. The resultant networks were found to be 'soft' gels when compared to other microgel systems. Furthermore, the results showed a distinct difference of to other microgel

systems, as most other examples (including PNIPAM) only develop a yield stress at close-packing ($\phi_{cp} = 0.63$) which is not the case for SZ.

Chapter 4 reports on the Differential Dynamic Microscopy data. From these measurements SZ microgels were found to be 2.7 μm (approximately a factor 3 larger than PNIPAM) in radius and the mobility is greatly reduced at 0.03 wt%, the shear thinning concentration. After further investigation the reduced mobility is likely due to the interactions between the polymer chains at the surface of SZ, as similar results are predicted for adhesive spheres. The response to salt was also investigated by exposing the microgel to a range of NaCl concentrations from 0.001 mM to 2000 mM. Unexpectedly, a high critical concentration of 200mM of NaCl is required to reduce the size of the microgel, by a factor of 2; an important observation when considering them in commercial formulations. In order to simulate the effect crowding has on this microgel a non-excluding polymer called Ficoll-400 was used to tune the osmotic pressure of suspensions. At the highest Ficoll-400 concentration SZ microgels were found to deswell from a radius of 2.7 μm down to 520 nm, a much larger decrease than other microgel systems. As one of the first studies to analyse microgel particles using DDM these results demonstrate how valuable DDM is to provide insight into the rheology of these soft particle systems.

Once the bulk interactions of the SZ microgels were determined, SZ microgels were introduced to the oil-water interface and using both static and oscillatory pendant drop tensiometry was used to determine the particles interfacial properties. SZ microgels were found to significantly reduce the interfacial tension by building up layers of microgels on the surface of the interface. These SZ-stabilised interfaces are highly elastic, $E' > 20$ mN/m, $E'' < 5$ mN/m, similar to colloid-laden interfaces. The interfacial elasticity was dependent on size of the microgel, as deswollen microgels resulted in more effectively packed interfaces resulting in more elastic interfaces, E' increases from 22 mN/m to 27 mN/m. A surprising observation was that SZ-stabilised interfaces appeared to be immune to buckling, a phenomenon observed when particle-laden interfaces are destabilised. This is effect is thought to be due to low wettability of the SZ which have a contact angle $\approx 20^\circ$ whereas for other systems the contact angle is typically around 90°. However, despite this SZ is capable of making emulsions which are stable for several months. This effect is likely due adhesive nature of SZ, as previous results indicates it forms gels at low concentrations and these gels interpenetrate as concentration is increased. This findings will have important consequences for

the use SZ emulsion stabilisation.

To test our findings the final chapter looks at how SZ affects the rheology and stability of model emulsion systems. SZ-stabilised oil-in-water emulsions were found to make emulsion-filled gels where oil drops behave as active fillers increasing the elasticity of the resultant gels. This increased mechanical stability was found to be due to the microgels at the interface causing droplets to come into contact at oil volume fractions above 0.2. However, it was also found that there was an upper limit on the total oil fraction which could be incorporated in the emulsions, $\phi = 0.3$. A oil fraction of 0.2 was found to correspond to the close-packing concentration of emulsion drops stabilised by a double microgel layer, whereas $\phi = 0.3$ was close-packing for a single microgel layer on oil drops. The stability of emulsions was tested by combining the results of centrifugation and drying experiments. The centrifugation experiments determined the critical disjoining pressure, the pressure at which the oil is dispelled from the matrix, which was found to be similar to traditional surfactant systems. While drying experiments revealed that emulsion dried down to partially coalesced emulsion film, separated by a thin polymeric film which is similar to studies on surfactant-stabilised systems.

In conclusion by choosing a commercial microgel, previously unstudied, a new system has been introduced to the field and can be used to bridge the gap between academic and industrial studies. Going forward to enhance the results gathered in this thesis further work should focus on single microgel events. Single microgel studies would provide more precise details on the deformation and interactions between microgels, which could further explain results such as the absence of buckling. Alternatively, one can test different oils such as more polar oils to determine how microgels stabilise different interfaces.

Bibliography

[1] W. Baker, "Microgel, a new macromolecule," *Industrial & Engineering Chemistry*, vol. 41, no. 3, pp. 511–520, 1949.

[2] J. R. Stokes, "Rheology of Industrially Relevant Microgels," *Microgel Suspensions: Fundamentals and Applications*, pp. 327–353, 2011.

[3] M. Heskins and J. E. Guillet, "Solution properties of poly (n-isopropylacrylamide)," *Journal of Macromolecular Science—Chemistry*, vol. 2, no. 8, pp. 1441–1455, 1968.

[4] J. O. Carnali and M. S. Naser, "The use of dilute solution viscometry to characterize the network properties of carbopol microgels," *Colloid & Polymer Science*, vol. 270, no. 2, pp. 183–193, 1992.

[5] E. Dickinson and Y. Yamamoto, "Rheology of milk protein gels and protein-stabilized emulsion gels cross-linked with transglutaminase," *Journal of Agricultural and Food Chemistry*, vol. 44, no. 6, pp. 1371–1377, 1996.

[6] M. Heskins and J. E. Guillet, "Solution properties of poly(n-isopropylacrylamide)," *Journal of Macromolecular Science: Part A - Chemistry*, vol. 2, no. 8, pp. 1441–1455, 1968.

[7] B. R. Saunders and B. Vincent, "Microgel particles as model colloids: Theory, properties and applications," *Advances in Colloid and Interface Science*, vol. 80, no. 1, pp. 1–25, 1999.

[8] P. A. Lovell and M. S. El-Aasser, *Emulsion polymerization and emulsion polymers*. Wiley, 1997.

[9] K. Landfester, M. Willert, and M. Antonietti, "Preparation of polymer particles in nonaqueous direct and inverse miniemulsions," *Macromolecules*, vol. 33, no. 7, pp. 2370–2376, 2000.

[10] J. A. Bonham, M. A. Faers, and J. S. Van Duijneveldt, "Non-aqueous microgel particles: Synthesis, properties and applications," *Soft Matter*, vol. 10, no. 47, pp. 9384–9398, 2014.

[11] M. S. Wolfe, "Rheology of swellable microgel dispersions," *Polymeric Materials Science and Engineering, Proceedings of the ACS Division of*

Polymeric Materials Science and Engineering, vol. 61, no. 1, pp. 398–402, 1989.

[12] S. Tsuji and H. Kawaguchi, "Temperature-sensitive hairy particles prepared by living radical graft polymerization," *Langmuir*, vol. 20, no. 6, pp. 2449–2455, 2004.

[13] M. Cloitre, R. Borrega, F. Monti, and L. Leibler, "Structure and flow of polyelectrolyte microgels: From suspensions to glasses," *Comptes Rendus Physique*, vol. 4, no. 2, pp. 221–230, 2003.

[14] W. Richtering and A. Pich, "The special behaviours of responsive core-shell nanogels," *Soft Matter*, vol. 8, no. 45, pp. 11423–11430, 2012.

[15] R. G. Larson, *The structure and rheology of complex fluids*, vol. 150. Oxford university press New York, 1999.

[16] I. Teraoka, *Polymer solutions*. John Wiley & Sons, Inc, 2002.

[17] I. Vukovic, G. T. Brinke, and K. Loos, "Block copolymer template-directed synthesis of well-ordered metallic nanostructures," *Polymer (United Kingdom)*, vol. 54, no. 11, pp. 2591–2605, 2013.

[18] N. S. Nikouei, N. Ghasemi, and A. Lavasanifar, "Temperature/ph responsive hydrogels based on poly (ethylene glycol) and functionalized poly (e-caprolactone) block copolymers for controlled delivery of macromolecules," *Pharmaceutical research*, vol. 33, no. 2, pp. 358–366, 2016.

[19] S. Parida, C. Maiti, Y. Rajesh, K. K. Dey, I. Pal, A. Parekh, R. Patra, D. Dhara, P. K. Dutta, and M. Mandal, "Gold nanorod embedded reduction responsive block copolymer micelle-triggered drug delivery combined with photothermal ablation for targeted cancer therapy," *Biochimica et Biophysica Acta (BBA)-General Subjects*, vol. 1861, no. 1, pp. 3039–3052, 2017.

[20] J. A. Hanson, C. B. Chang, S. M. Graves, Z. Li, T. G. Mason, and T. J. Deming, "Nanoscale double emulsions stabilized by single-component block copolypeptides," *Nature*, vol. 455, no. 7209, pp. 85–88, 2008.

[21] J. Mewis and N. J. Wagner, *Colloidal suspension rheology*. Cambridge University Press, 2012.

[22] G. Cuvelier and B. Launay, "Concentration regimes in xanthan gum solutions deduced from flow and viscoelastic properties," *Carbohydrate Polymers*, vol. 6, no. 5, pp. 321–333, 1986.

[23] E. R. Morris, D. A. Rees, and G. Robinson, "Cation-specific aggregation of carrageenan helices: Domain model of polymer gel structure," *Journal of Molecular Biology*, vol. 138, no. 2, pp. 349–362, 1980.

[24] C. Michon, G. Cuvelier, P. Relkin, and B. Launay, "Influence of thermal history on the stability of gelatin gels," *International Journal of Biological Macromolecules*, vol. 20, no. 4, pp. 259–264, 1997.

[25] M. F. Law and P. B. Deasy, "Use of hydrophilic polymers with microcrystalline cellulose to improve extrusion-spheronization," *European Journal of Pharmaceutics and Biopharmaceutics*, vol. 45, no. 1, pp. 57–65, 1998.

[26] A. P. Nowak, V. Breedveld, L. Pakstis, B. Ozbas, D. J. Pine, and T. J. Deming, "Rapidly recovering hydrogel scaffolds from self-assembling diblock copolypeptide amphiphiles," *Nature*, vol. 417, no. 6887, pp. 424–428, 2002.

[27] I. M. Krieger and T. J. Dougherty, "A mechanism for non-newtonian flow in suspensions of rigid spheres," *Transactions of the Society of Rheology*, vol. 3, no. 1, pp. 137–152, 1959.

[28] J. R. Stokes and W. J. Frith, "Rheology of gelling and yielding soft matter systems," *Soft Matter*, vol. 4, no. 6, pp. 1133–1140, 2008.

[29] B. H. Tan, K. C. Tam, Y. C. Lam, and C. B. Tan, "A semi-empirical approach for modeling charged soft microgel particles," *Journal of Rheology*, vol. 48, no. 4, pp. 915–926, 2004.

[30] B. H. Tan and K. C. Tam, "Review on the dynamics and micro-structure of pH-responsive nano-colloidal systems," *Advances in Colloid and Interface Science*, vol. 136, no. 1-2, pp. 25–44, 2008.

[31] H. Senff, W. Richtering, C. Norhausen, A. Weiss, and M. Ballauff, "Rheology of a temperature sensitive core-shell latex," *Langmuir*, vol. 15, no. 1, pp. 102–106, 1999.

[32] J. Mewis, W. J. Frith, T. A. Strivens, and W. B. Russel, "The rheology of suspensions containing polymerically stabilized particles," *AIChE Journal*, vol. 35, no. 3, pp. 415–422, 1989.

[33] I. D. Evans and A. Lips, "Concentration dependence of the linear elastic behaviour of model microgel dispersions," *Journal of the Chemical Society, Faraday Transactions*, vol. 86, no. 20, pp. 3413–3417, 1990.

[34] B. W. Barry, "Viscoelastic properties of concentrated emulsions," *Advances in Colloid and Interface Science*, vol. 5, no. 1, pp. 37–75, 1975.

[35] H. Senff and W. Richtering, "Temperature sensitive microgel suspensions: Colloidal phase behavior and rheology of soft spheres," *Journal of Chemical Physics*, vol. 111, no. 4, pp. 1705–1711, 1999.

[36] H. Senff and W. Richtering, "Temperature sensitive microgel suspensions: Colloidal phase behavior and rheology of soft spheres," *Journal of Chemical Physics*, vol. 111, no. 4, pp. 1705–1711, 1999.

[37] H. Hertz, *The constitution of matter: a lecture "u on the fundamentals of physics from 1884*. Springer-Verlag, 2013.

[38] P. Menut, S. Seiffert, J. Sprakel, and D. A. Weitz, "Does size matter? Elasticity of compressed suspensions of colloidal- and granular-scale microgels," *Soft Matter*, vol. 8, no. 1, pp. 156–164, 2012.

[39] J. Israelachvili, "The science and applications of emulsions - an overview," *Colloids and Surfaces A: Physicochemical and Engineering Aspects*, vol. 91, no. C, pp. 1–8, 1994.

[40] S. Pautot, B. J. Frisken, and D. A. Weitz, "Production of Unilamellar Vesicles Using an Inverted Emulsion," no. 10, pp. 2870–2879, 2003.

[41] A. Kumar, S. Li, C.-m. Cheng, and D. Lee, "Recent Developments in Phase Inversion Emulsi fi cation," 2015.

[42] H. Kunieda, Y. Fukui, H. Uchiyama, and C. Solans, "Spontaneous Formation of Highly Concentrated Water-in-Oil Emulsions (Gel-Emulsions)," *Langmuir*, vol. 12, no. 9, pp. 2136–2140, 1996.

[43] D. S. Masson, G. G. Morais, J. M. de Morais, F. F. de Andrade, O. D. H. Dos Santos, W. P. de Oliveira, and P. a. Rocha Filho, "Polyhydroxy Alcohols and Peach Oil Addition Influence on Liquid Crystal Formation and Rheological Behavior of O/W Emulsions," *Journal of Dispersion Science and Technology*, vol. 26, no. 4, pp. 463–468, 2005.

[44] A. Kogan and N. Garti, "Microemulsions as transdermal drug delivery vehicles," vol. 126, pp. 369–385, 2006.

[45] S. U. Pickering, "Cxcvi.—emulsions," *J. Chem. Soc., Trans.*, vol. 91, pp. 2001–2021, 1907.

[46] B. P. Binks and T. S. Horozov, *Colloidal particles at liquid interfaces*. Cambridge University Press, 2006.

[47] T. Zhang, A. Davidson, S. L. Bryant, and C. Huh, "Nanoparticle-stabilized emulsions for applications in enhanced oil recovery," *Proceedings - SPE Symposium on Improved Oil Recovery*, vol. 2, no. January 2014, pp. 1009–1026, 2010.

[48] F. Husband, M. Ridout, P. Clegg, M. Hermes, J. Forth, W. Poon, and P. Wilde, "The impact of the interfacial behaviour on emulsion rheology: A potential approach to reducing fat content in emulsified foods," in *Gums and Stabilisers for the Food Industry 17*, pp. 230–237, 2014.

[49] H. Xu, S. Melle, K. Golemanov, and G. Fuller, "Shape and buckling transitions in solid-stabilized drops," *Langmuir*, vol. 21, no. 22, pp. 10016–10020, 2005.

[50] N. Tsapis, E. R. Dufresne, S. S. Sinha, C. S. Riera, J. W. Hutchinson, L. Mahadevan, and D. A. Weitz, "Onset of buckling in drying droplets of colloidal suspensions," *Physical Review Letters*, vol. 94, no. 1, pp. 1–4, 2005.

[51] N. Hijnen and P. S. Clegg, "Assembling cellular networks of colloids via emulsions of partially miscible liquids: A compositional approach," *Materials Horizons*, vol. 1, no. 3, pp. 360–364, 2014.

[52] S. Razavi, K. D. Cao, B. Lin, K. Y. C. Lee, R. S. Tu, and I. Kretzschmar, "Collapse of Particle-Laden Interfaces under Compression: Buckling vs Particle Expulsion," *Langmuir*, vol. 31, no. 28, pp. 7764–7775, 2015.

[53] E. Dickinson, "Food Hydrocolloids Biopolymer-based particles as stabilizing agents for emulsions and foams," *Food hydrocolloids*, vol. 68, pp. 219–231, 2017.

[54] B. Li, Y. P. Cao, X. Q. Feng, and H. Gao, "Mechanics of morphological instabilities and surface wrinkling in soft materials: A review," *Soft Matter*, vol. 8, no. 21, pp. 5728–5745, 2012.

[55] S. Knoche, D. Vella, E. Aumaitre, P. Degen, H. Rehage, P. Cicuta, and J. Kierfeld, "Elastometry of deflated capsules: Elastic moduli from shape and wrinkle analysis," *Langmuir*, vol. 29, no. 40, pp. 12463–12471, 2013.

[56] R. V. Hooghten, V. E. Blair, A. Vananroye, A. B. Schofield, J. Vermant, and J. H. Thijssen, "Interfacial Rheology of Sterically Stabilized Colloids at Liquid Interfaces and Its Effect on the Stability of Pickering Emulsions," *Langmuir*, vol. 33, no. 17, pp. 4107–4118, 2017.

[57] J. H. Thijssen and J. Vermant, "Interfacial rheology of model particles at liquid interfaces and its relation to (bicontinuous) Pickering emulsions," *Journal of Physics Condensed Matter*, vol. 30, no. 2, 2018.

[58] O. S. Deshmukh, D. Van Den Ende, M. C. Stuart, F. Mugele, and M. H. Duits, "Hard and soft colloids at fluid interfaces: Adsorption, interactions, assembly & rheology," *Advances in Colloid and Interface Science*, vol. 222, pp. 215–217, 2015.

[59] Z. Li, K. Geisel, W. Richtering, and T. Ngai, "Poly(N-isopropylacrylamide) microgels at the oil-water interface: Adsorption kinetics," *Soft Matter*, vol. 9, no. 41, pp. 9939–9946, 2013.

[60] K. Roger and B. Cabane, "Why are hydrophobic/water interfaces negatively charged?," *Angewandte Chemie - International Edition*, vol. 51, no. 23, pp. 5625–5628, 2012.

[61] H. Ma, M. Luo, and L. L. Dai, "Influences of surfactant and nanoparticle assembly on effective interfacial tensions," *Physical Chemistry Chemical Physics*, vol. 10, no. 16, pp. 2207–2213, 2008.

[62] A. F. Ward and L. Tordai, "Time-dependence of boundary tensions of solutions I. The role of diffusion in time-effects," *The Journal of Chemical Physics*, vol. 14, no. 7, pp. 453–461, 1946.

[63] H. Ritacco, D. Langevin, H. Diamant, and D. Andelman, "Dynamic surface tension of aqueous solutions of ionic surfactants: Role of electrostatics," *Langmuir*, vol. 27, no. 3, pp. 1009–1014, 2011.

[64] Z. Adamczyk and P. Warszyński, "Role of electrostatic interactions in particle adsorption," *Advances in Colloid and Interface Science*, vol. 63, pp. 41–149, 1996.

[65] Z. Adamczyk, "Particle adsorption and deposition: Role of electrostatic interactions," *Advances in Colloid and Interface Science*, vol. 100-102, no. SUPPL., pp. 267–347, 2003.

[66] B. Wang, M. Wang, H. Zhang, N. S. Sobal, W. Tong, C. Gao, Y. Wang, M. Giersig, D. Wang, and H. Möhwald, "Stepwise interfacial self-assembly of nanoparticles via specific DNA pairing," *Physical Chemistry Chemical Physics*, vol. 9, no. 48, pp. 6313–6318, 2007.

[67] N. Bizmark, M. A. Ioannidis, and D. E. Henneke, "Irreversible adsorption-driven assembly of nanoparticles at fluid interfaces revealed by a dynamic surface tension probe," *Langmuir*, vol. 30, no. 3, pp. 710–717, 2014.

[68] M. Stieger, W. Richtering, J. S. Pedersen, and P. Lindner, "Small-angle neutron scattering study of structural changes in temperature sensitive microgel colloids," *Journal of Chemical Physics*, vol. 120, no. 13, pp. 6197–6206, 2004.

[69] M. Karg and T. Hellweg, "New "smart" poly(NIPAM) microgels and nanoparticle microgel hybrids: Properties and advances in characterisation," *Current Opinion in Colloid and Interface Science*, vol. 14, no. 6, pp. 438–450, 2009.

[70] D. M. Heyes and A. C. Brańka, "Interactions between microgel particles," *Soft Matter*, vol. 5, no. 14, pp. 2681–2685, 2009.

[71] M. Destribats, V. Lapeyre, M. Wolfs, E. Sellier, F. Leal-Calderon, V. Ravaine, and V. Schmitt, "Soft microgels as Pickering emulsion stabilisers: Role of particle deformability," *Soft Matter*, vol. 7, no. 17, pp. 7689–7698, 2011.

[72] W. Richtering, "Responsive emulsions stabilized by stimuli-sensitive microgels: Emulsions with special non-pickering properties," *Langmuir*, vol. 28, no. 50, pp. 17218–17229, 2012.

[73] B. Brugger and W. Richtering, "Emulsions stabilized by stimuli-sensitive poly(N-isopropylacrylamide)-co- methacrylic acid polymers: Microgels versus low molecular weight polymers," *Langmuir*, vol. 24, no. 15, pp. 7769–7777, 2008.

[74] Y. Cohin, M. Fisson, K. Jourde, G. G. Fuller, N. Sanson, L. Talini, and C. Monteux, "Tracking the interfacial dynamics of PNiPAM soft microgels particles adsorbed at the air-water interface and in thin liquid films," *Rheologica Acta*, vol. 52, no. 5, pp. 445–454, 2013.

[75] L. A. Lyon and A. Fernandez-Nieves, "The Polymer/Colloid Duality of Microgel Suspensions," *Annual Review of Physical Chemistry*, vol. 63, no. 1, pp. 25–43, 2012.

[76] S. Schmidt, T. Liu, S. Rütten, K. H. Phan, M. Möller, and W. Richtering, "Influence of microgel architecture and oil polarity on stabilization of emulsions by stimuli-sensitive core-shell poly(N -isopropylacrylamide- co -methacrylic acid) microgels: Mickering versus pickering behavior?," *Langmuir*, vol. 27, no. 16, pp. 9801–9806, 2011.

[77] M. Destribats, V. Lapeyre, M. Wolfs, E. Sellier, F. Leal-Calderon, V. Ravaine, and V. Schmitt, "Soft microgels as Pickering emulsion stabilisers: Role of particle deformability," *Soft Matter*, vol. 7, no. 17, pp. 7689–7698, 2011.

[78] M. Destribats, V. Lapeyre, E. Sellier, F. Leal-Calderon, V. Schmitt, and V. Ravaine, "Water-in-oil emulsions stabilized by water-dispersible poly(N-isopropylacrylamide) microgels: Understanding anti-Finkle behavior," *Langmuir*, vol. 27, no. 23, pp. 14096–14107, 2011.

[79] K. Geisel, L. Isa, and W. Richtering, "Unraveling the 3D localization and deformation of responsive microgels at oil/water interfaces: A step forward in understanding soft emulsion stabilizers," *Langmuir*, vol. 28, no. 45, pp. 15770–15776, 2012.

[80] H. Karbstein and H. Schubert, "Developments in the continuous mechanical production of oil-in-water macro-emulsions," *Chemical Engineering and Processing: Process Intensification*, vol. 34, no. 3, pp. 205–211, 1995.

[81] J. Bibette, F. L. Calderon, and P. Poulin, "Emulsions: basic principles," *Reports on Progress in Physics*, vol. 62, no. 6, p. 969, 1999.

[82] E. Dickinson, "Emulsion gels: The structuring of soft solids with protein-stabilized oil droplets," *Food hydrocolloids*, vol. 28, no. 1, pp. 224–241, 2012.

[83] E. Dickinson and J. Chen, "Heat-Set Whey Protein Emulsion Gels: Role of Active and Inactive Filler Particles," *Journal of Dispersion Science and Technology*, vol. 20, no. 1-2, pp. 197–213, 1999.

[84] J. Chen and E. Dickinson, "Viscoelastic Properties of Protein-Stabilized Emulsions: Effect of Protein-Surfactant Interactions," vol. 8561, no. 97, pp. 91–97, 1998.

[85] S. Weir, K. M. Bromley, A. Lips, and W. C. K. Poon, "Celebrating Soft Matter's 10th Anniversary: Simplicity in complexity – towards a soft matter physics of caramel," *Soft Matter*, vol. 12, no. 10, pp. 2757–2765, 2016.

[86] S. Tcholakova, N. Denkov, and A. Lips, "Comparison of solid particles, globular proteins and surfactants as emulsifiers," *Physical Chemistry Chemical Physics*, vol. 10, no. 12, pp. 1608–1627, 2008.

[87] S. Tcholakova, N. D. Denkov, I. B. Ivanov, and B. Campbell, "Coalescence stability of emulsions containing globular milk proteins," *Advances in Colloid and Interface Science*, vol. 123-126, no. SPEC. ISS., pp. 259–293, 2006.

[88] H. Feng, J. Sprakel, D. Ershov, T. Krebs, M. A. Cohen Stuart, and J. Van Der Gucht, "Two modes of phase inversion in a drying emulsion," *Soft Matter*, vol. 9, no. 10, pp. 2810–2815, 2013.

[89] A. F. Routh and W. B. Russel, "Horizontal drying fronts during solvent evaporation from latex films," *AIChE Journal*, vol. 44, no. 9, pp. 2088–2098, 1998.

[90] B. P. Binks, P. D. Fletcher, A. J. Johnson, I. Marinopoulos, J. M. Crowther, and M. A. Thompson, "Evaporation of Particle-Stabilized Emulsion Sunscreen Films," *ACS Applied Materials and Interfaces*, vol. 8, no. 33, pp. 21201–21213, 2016.

[91] J. L. Salager, A. Forgiarini, L. Márquez, A. Peña, A. Pizzino, M. P. Rodriguez, and M. Rondón-González, "Using emulsion inversion in industrial processes," *Advances in Colloid and Interface Science*, vol. 108-109, pp. 259–272, 2004.

[92] A. Deblais, R. Harich, D. Bonn, A. Colin, and H. Kellay, "Spreading of an Oil-in-Water Emulsion on a Glass Plate: Phase Inversion and Pattern Formation," *Langmuir*, vol. 31, no. 22, pp. 5971–5981, 2015.

[93] A. Deblais, R. Harich, A. Colin, and H. Kellay, "Taming contact line instability for pattern formation," *Nature Communications*, vol. 7, no. Umr 5798, pp. 1–7, 2016.

[94] "Differential dynamic microscopy: A high-throughput method for characterizing the motility of microorganisms," 2011.

[95] H. A. Barnes, J. F. Hutton, and K. Walters, *An introduction to rheology*, vol. 3. Elsevier, 1989.

[96] M. Instruments, "A basic introduction to rheology," *Ref: BIR-V1*, vol. 1, pp. 1–30, 2016.

[97] M. Instruments, "Understanding yield stress measurements," 2012.

[98] V. A. Martinez, R. Besseling, O. A. Croze, J. Tailleur, M. Reufer, J. Schwarz-Linek, L. G. Wilson, M. A. Bees, and W. C. Poon, "Differential dynamic microscopy: A high-throughput method for characterizing the motility of microorganisms," *Biophysical Journal*, vol. 103, no. 8, pp. 1637–1647, 2012.

[99] V. A. Martinez, J. Schwarz-Linek, M. Reufer, L. G. Wilson, A. N. Morozov, and W. C. Poon, "Flagellated bacterial motility in polymer solutions," *Proceedings of the National Academy of Sciences of the United States of America*, vol. 111, no. 50, pp. 17771–17776, 2014.

[100] P.-L. Latreille, V. Adibnia, A. Nour, J.-M. Rabanel, A. Lalloz, J. Arlt, W. C. K. Poon, P. Hildgen, V. A. Martinez, and X. Banquy, "Spontaneous shrinking of soft nanoparticles boosts their diffusion in confined media," *Nature Communications*, vol. 10, no. 1, p. 4294, 2019.

[101] J. D. Berry, M. J. Neeson, R. R. Dagastine, D. Y. Chan, and R. F. Tabor, "Measurement of surface and interfacial tension using pendant drop tensiometry," *Journal of Colloid and Interface Science*, vol. 454, pp. 226–237, 2015.

[102] F. Ravera, G. Loglio, and V. I. Kovalchuk, "Interfacial dilational rheology by oscillating bubble/drop methods," *Current Opinion in Colloid and Interface Science*, vol. 15, no. 4, pp. 217–228, 2010.

[103] A. Goebel and K. Lunkenheimer, "Interfacial tension of the water/n-alkane interface," *Langmuir*, vol. 13, no. 2, pp. 369–372, 1997.

[104] N. B. Vargaftik, B. N. Volkov, and L. D. Voljak, "International Tables of the Surface Tension of Water," *Journal of Physical and Chemical Reference Data*, vol. 12, no. 3, pp. 817–820, 1983.

[105] S. Zeppieri, J. Rodríguez, and A. L. López De Ramos, "Interfacial tension of alkane + water systems," *Journal of Chemical and Engineering Data*, vol. 46, no. 5, pp. 1086–1088, 2001.

[106] R. Aston, K. Sewell, T. Klein, G. Lawrie, and L. Grøndahl, "Evaluation of the impact of freezing preparation techniques on the characterisation of alginate hydrogels by cryo-SEM," *European Polymer Journal*, vol. 82, pp. 1–15, 2016.

[107] K. Akhtar, S. A. Khan, S. B. Khan, and A. M. Asiri, "Scanning electron microscopy: Principle and applications in nanomaterials characterization," in *Handbook of materials characterization*, pp. 113–145, Springer, 2018.

[108] J. M. Piau, "Carbopol gels: Elastoviscoplastic and slippery glasses made of individual swollen sponges. Meso- and macroscopic properties, constitutive equations and scaling laws," *Journal of Non-Newtonian Fluid Mechanics*, vol. 144, no. 1, pp. 1–29, 2007.

[109] K. N. Nordstrom, E. Verneuil, P. E. Arratia, A. Basu, Z. Zhang, A. G. Yodh, J. P. Gollub, and D. J. Durian, "Microfluidic rheology of soft colloids above and below jamming," *Physical Review Letters*, vol. 105, no. 17, pp. 1–4, 2010.

[110] C. Pellet and M. Cloitre, "The glass and jamming transitions of soft polyelectrolyte microgel suspensions," *Soft Matter*, vol. 12, no. 16, pp. 3710–3720, 2016.

[111] R. Borrega, M. Cloitre, I. Betremieux, B. Ernst, and L. Leibler, "Concentration dependence of the low-shear viscosity of polyelectrolyte micro-networks: From hard spheres to soft microgels," *Europhysics Letters*, vol. 47, no. 6, pp. 729–735, 1999.

[112] P. Olsson and S. Teitel, "Critical scaling of shear viscosity at the jamming transition," *Physical Review Letters*, vol. 99, no. 17, pp. 1–4, 2007.

[113] J. Mewis, W. J. Frith, T. A. Strivens, and W. B. Russel, "The rheology of suspensions containing polymerically stabilized particles," *AIChE Journal*, vol. 35, no. 3, pp. 415–422, 1989.

[114] G. W. Blair, J. C. Hening, and A. Wagstaff, "The flow of cream through narrow glass tubes," *Journal of Physical Chemistry*, vol. 43, no. 7, pp. 853–864, 1939.

[115] B. P. Tighe, E. Woldhuis, J. J. Remmers, W. Van Saarloos, and M. Van Hecke, "Model for the scaling of stresses and fluctuations in flows near jamming," *Physical Review Letters*, vol. 105, no. 8, pp. 1–4, 2010.

[116] K. N. Pham, G. Petekidis, D. Vlassopoulos, S. U. Egelhaaf, P. N. Pusey, and W. C. K. Poon, "Yielding of colloidal glasses," *Europhysics Letters*, vol. 75, no. 4, pp. 624–630, 2006.

[117] A. Ghosh, G. Chaudhary, J. G. Kang, P. V. Braun, R. H. Ewoldt, and K. S. Schweizer, "Linear and nonlinear rheology and structural relaxation in dense glassy and jammed soft repulsive pNIPAM microgel suspensions," *Soft Matter*, vol. 15, no. 5, pp. 1038–1052, 2019.

[118] M. Dinkgreve, J. Paredes, M. M. Denn, and D. Bonn, "On different ways of measuring "the" yield stress," *Journal of Non-Newtonian Fluid Mechanics*, vol. 238, pp. 233–241, 2016.

[119] T. G. Mason and D. A. Weitz, "Linear viscoelasticity of colloidal hard sphere suspensions near the glass transition," *Physical Review Letters*, vol. 75, no. 14, pp. 2770–2773, 1995.

[120] J. Carmona, P. Ramírez, N. Calero, and J. Muñoz, "Large amplitude oscillatory shear of xanthan gum solutions. effect of sodium chloride (nacl) concentration," *Journal of Food Engineering*, vol. 126, pp. 165–172, 2014.

[121] S. E. Bakarich, G. C. Pidcock, P. Balding, L. Stevens, P. Calvert, and M. In Het Panhuis, "Recovery from applied strain in interpenetrating polymer network hydrogels with ionic and covalent cross-links," *Soft Matter*, vol. 8, no. 39, pp. 9985–9988, 2012.

[122] E. S. Dragan, "Design and applications of interpenetrating polymer network hydrogels. A review," *Chemical Engineering Journal*, vol. 243, pp. 572–590, 2014.

[123] P. J. Flory, *Principles of polymer chemistry*. Cornell University Press, 1953.

[124] B. Abou, D. Bonn, and J. Meunier, "Aging dynamics in a colloidal glass," *Physical Review E - Statistical Physics, Plasmas, Fluids, and Related Interdisciplinary Topics*, vol. 64, no. 2, p. 6, 2001.

[125] B. Nystrom, H. Walderhaug, and F. K. Hansen, "Hydrophobically Associating Water-Soluble," pp. 7743–7752, 1993.

[126] L. Cipelletti, S. Manley, R. C. Ball, and D. A. Weitz, "Universal aging features in the restructuring of fractal colloidal gels," *Physical Review Letters*, vol. 84, no. 10, pp. 2275–2278, 2000.

[127] L. Ramos and L. Cipelletti, "Ultraslow dynamics and stress relaxation in the aging of a soft glassy system," *Physical Review Letters*, vol. 87, no. 24, pp. 245503–1–245503–4, 2001.

[128] L. Cipelletti and L. Ramos, "Slow dynamics in glassy soft matter," *Journal of Physics Condensed Matter*, vol. 17, no. 6, 2005.

[129] D. Pontoni, T. Narayanan, J. M. Petit, G. Grübel, and D. Beysens, "Microstructure and Dynamics near an Attractive Colloidal Glass Transition," *Physical Review Letters*, vol. 90, no. 18, p. 4, 2003.

[130] N. Greinert, T. Wood, and P. Bartlett, "Measurement of effective temperatures in an aging colloidal glass," *Physical Review Letters*, vol. 97, no. 26, pp. 1–4, 2006.

[131] J. Mattsson, H. M. Wyss, A. Fernandez-Nieves, K. Miyazaki, Z. Hu, D. R. Reichman, and D. A. Weitz, "Soft colloids make strong glasses," *Nature*, vol. 462, no. 7269, pp. 83–86, 2009.

[132] A. M. Philippe, D. Truzzolillo, J. Galvan-Myoshi, P. Dieudonné-George, V. Trappe, L. Berthier, and L. Cipelletti, "Glass transition of soft colloids," *Physical Review E*, vol. 97, no. 4, pp. 1–5, 2018.

[133] R. Graziano, V. Preziosi, D. Uva, G. Tomaiuolo, B. Mohebbi, J. Claussen, and S. Guido, "The microstructure of carbopol in water under static and flow conditions and its effect on the yield stress," *Journal of Colloid and Interface Science*, vol. 582, pp. 1067–1074, 2021.

[134] T. Farjami, A. Madadlou, and M. Labbafi, "Characteristics of the bulk hydrogels made of the citric acid cross-linked whey protein microgels," *Food Hydrocolloids*, vol. 50, pp. 159–165, 2015.

[135] I. M. De Schepper, E. D. Cohen, and R. Verberg, "Comment on "Viscosity and structural relaxation in suspensions of hard-sphere colloids"," *Physical Review Letters*, vol. 77, no. 3, p. 584, 1996.

[136] E. Zaccarelli, C. Valeriani, E. Sanz, W. C. Poon, M. E. Cates, and P. N. Pusey, "Crystallization of hard-sphere glasses," *Physical Review Letters*, vol. 103, no. 13, pp. 1–4, 2009.

[137] T. Kureha, H. Minato, D. Suzuki, K. Urayama, and M. Shibayama, "Concentration dependence of the dynamics of microgel suspensions investigated by dynamic light scattering," *Soft Matter*, vol. 15, no. 27, pp. 5390–5399, 2019.

[138] A. Fernández-Nieves, A. Fernández-Barbero, B. Vincent, and F. J. De Las Nieves, "Charge controlled swelling of microgel particles," *Macromolecules*, vol. 33, no. 6, pp. 2114–2118, 2000.

[139] Y. Huang and Y. Lapitsky, "Monovalent salt enhances colloidal stability during the formation of chitosan/tripolyphosphate microgels," *Langmuir*, vol. 27, no. 17, pp. 10392–10399, 2011.

[140] H. Jia, I. Grillo, and S. Titmuss, "Small angle neutron scattering study of polyelectrolyte brushes grafted to well-defined gold nanoparticle interfaces," *Langmuir*, vol. 26, no. 10, pp. 7482–7488, 2010.

[141] W. Van Megen and P. N. Pusey, "Dynamic light-scattering study of the glass transition in a colloidal suspension," *Physical Review A*, vol. 43, no. 10, pp. 5429–5441, 1991.

[142] S. Minko, "Responsive polymer brushes," *Journal of Macromolecular Science, Part C: Polymer Reviews*, vol. 46, no. 4, pp. 397–420, 2006.

[143] K. N. Pham, A. M. Puertas, J. Bergenholtz, S. U. Egelhaaf, A. Moussaïd, P. N. Pusey, A. B. Schofield, M. E. Cates, H. Fuchs, and W. C. Poon, "Multiple glassy states in a simple model system," *Science*, vol. 296, no. 5565, pp. 104–106, 2002.

[144] E. Zaccarelli, G. Foffi, K. A. Dawson, S. V. Buldyrev, F. Sciortino, and P. Tartaglia, "Confirmation of anomalous dynamical arrest in attractive colloids: A molecular dynamics study," *Physical Review E - Statistical Physics, Plasmas, Fluids, and Related Interdisciplinary Topics*, vol. 66, no. 4, p. 14, 2002.

[145] C. P. Royall, S. R. Williams, and H. Tanaka, "The nature of the glass and gel transitions in sticky spheres," pp. 1–12, 2014.

[146] I. Bouhid De Aguiar, T. Van De Laar, M. Meireles, A. Bouchoux, J. Sprakel, and K. Schroën, "Deswelling and deformation of microgels in concentrated packings," *Scientific Reports*, vol. 7, no. 1, pp. 1–11, 2017.

[147] J. J. Lietor-Santos, B. Sierra-Martin, R. Vavrin, Z. Hu, U. Gasser, and A. Fernandez-Nieves, "Deswelling microgel particles using hydrostatic pressure," *Macromolecules*, vol. 42, no. 16, pp. 6225–6230, 2009.

[148] B. Sierra-Martin, J. A. Frederick, Y. Laporte, G. Markou, J. J. Lietor-Santos, and A. Fernandez-Nieves, "Determination of the bulk modulus of microgel particles," *Colloid and Polymer Science*, vol. 289, no. 5-6, pp. 721–728, 2011.

[149] C. J. Beverung, C. J. Radke, and H. W. Blanch, "Protein adsorption at the oil/water interface: Characterization of adsorption kinetics by dynamic interfacial tension measurements," *Biophysical Chemistry*, vol. 81, no. 1, pp. 59–80, 1999.

[150] N. Bizmark, M. A. Ioannidis, and D. E. Henneke, "Irreversible adsorption-driven assembly of nanoparticles at fluid interfaces revealed by a dynamic surface tension probe," *Langmuir*, vol. 30, no. 3, pp. 710–717, 2014.

[151] A. Ward and L. Tordai, "Time-dependence of boundary tensions of solutions i. the role of diffusion in time-effects," *The Journal of Chemical Physics*, vol. 14, no. 7, pp. 453–461, 1946.

[152] S. Kutuzov, J. He, R. Tangirala, T. Emrick, T. Russell, and A. Böker, "On the kinetics of nanoparticle self-assembly at liquid/liquid interfaces," *Physical Chemistry Chemical Physics*, vol. 9, no. 48, pp. 6351–6358, 2007.

[153] Z. Adamczyk, "Kinetics of diffusion-controlled adsorption of colloid particles and proteins," *Journal of colloid and interface science*, vol. 229, no. 2, pp. 477–489, 2000.

[154] C. Kotsmar, V. Pradines, V. S. Alahverdjieva, E. V. Aksenenko, V. B. Fainerman, V. I. Kovalchuk, J. Krägel, M. E. Leser, B. A. Noskov, and R. Miller, "Thermodynamics, adsorption kinetics and rheology of mixed protein-surfactant interfacial layers," *Advances in Colloid and Interface Science*, vol. 150, no. 1, pp. 41–54, 2009.

[155] Z. Li, K. Geisel, W. Richtering, and T. Ngai, "Poly(N-isopropylacrylamide) microgels at the oil-water interface: Adsorption kinetics," *Soft Matter*, vol. 9, no. 41, pp. 9939–9946, 2013.

[156] F. Pinaud, K. Geisel, P. Massé, B. Catargi, L. Isa, W. Richtering, V. Ravaine, and V. Schmitt, "Adsorption of microgels at an oil-water interface: Correlation between packing and 2D elasticity," *Soft Matter*, vol. 10, no. 36, pp. 6963–6974, 2014.

[157] J. Zhang and R. Pelton, "The dynamic behavior of poly(N-isopropylacrylamide) at the air/water interface," *Colloids and Surfaces A: Physicochemical and Engineering Aspects*, vol. 156, no. 1-3, pp. 111–122, 1999.

[158] N. Bizmark, M. A. Ioannidis, and D. E. Henneke, "Irreversible adsorption-driven assembly of nanoparticles at fluid interfaces revealed by a dynamic surface tension probe," *Langmuir*, vol. 30, no. 3, pp. 710–717, 2014.

[159] J. Zhang and R. Pelton, "Poly (n-isopropylacrylamide) microgels at the air-water interface," *Langmuir*, vol. 15, no. 23, pp. 8032–8036, 1999.

[160] L. Lee, B. Jean, and A. Menelle, "Effect of temperature on the adsorption of poly (n-isopropylacrylamide) at the air- solution interface," *Langmuir*, vol. 15, no. 9, pp. 3267–3272, 1999.

[161] A. M. Atta, "Surface-active amphiphilic poly [(2-acrylamido-2-methylpropanesulfonic acid)-co-(n-isopropylacrylamide)] nanoparticles as stabilizer in aqueous emulsion polymerization," *Polymer international*, vol. 63, no. 4, pp. 607–615, 2014.

[162] P. Erni, "Deformation modes of complex fluid interfaces," *Soft Matter*, vol. 7, no. 17, pp. 7586–7600, 2011.

[163] T. Kobayashi and M. Kawaguchi, "Surface dilational moduli of latex-particle monolayers spread at air-water interface," *Journal of Colloid and Interface Science*, vol. 390, no. 1, pp. 147–150, 2013.

[164] R. G. Larson, *Constitutive Equations for Polymer Melts and Solutions: Butterworths Series in Chemical Engineering*. Butterworth-Heinemann, 2013.

[165] E. M. Freer, K. S. Yim, G. G. Fuller, and C. J. Radke, "Shear and dilatational relaxation mechanisms of globular and flexible proteins at the hexadecane/water interface," *Langmuir*, vol. 20, no. 23, pp. 10159–10167, 2004.

[166] V. Garbin, J. C. Crocker, and K. J. Stebe, "Nanoparticles at fluid interfaces: Exploiting capping ligands to control adsorption, stability and dynamics," *Journal of Colloid and Interface Science*, vol. 387, no. 1, pp. 1–11, 2012.

[167] R. W. Murphy, B. E. Farkas, and O. G. Jones, "Dynamic and viscoelastic interfacial behavior of β-lactoglobulin microgels of varying sizes at fluid interfaces," *Journal of Colloid and Interface Science*, vol. 466, pp. 12–19, 2016.

[168] D. Georgieva, V. Schmitt, F. Leal-Calderon, and D. Langevin, "On the possible role of surface elasticity in emulsion stability," *Langmuir*, vol. 25, no. 10, pp. 5565–5573, 2009.

[169] M. Rey, M. Á. Fernández-Rodríguez, M. Steinacher, L. Scheidegger, K. Geisel, W. Richtering, T. M. Squires, and L. Isa, "Isostructural solid-solid phase transition in monolayers of soft core-shell particles at fluid interfaces: Structure and mechanics," *Soft Matter*, vol. 12, no. 15, pp. 3545–3557, 2016.

[170] C. Picard, P. Garrigue, M. C. Tatry, V. Lapeyre, S. Ravaine, V. Schmitt, and V. Ravaine, "Organization of Microgels at the Air-Water Interface under Compression: Role of Electrostatics and Cross-Linking Density," *Langmuir*, vol. 33, no. 32, pp. 7968–7981, 2017.

[171] R. Aveyard, J. H. Clint, D. Nees, and V. N. Paunov, "Compression and structure of monolayers of charged latex particles at air/water and octane/water interfaces," *Langmuir*, vol. 16, no. 4, pp. 1969–1979, 2000.

[172] P. A. Kralchevsky, K. D. Danov, and P. V. Petkov, "Soft electrostatic repulsion in particle monolayers at liquid interfaces: Surface pressure and effect of aggregation," *Philosophical Transactions of the Royal Society A: Mathematical, Physical and Engineering Sciences*, vol. 374, no. 2072, 2016.

[173] K. Du, E. Glogowski, T. Emrick, T. P. Russell, and A. D. Dinsmore, "Adsorption energy of nano- and microparticles at liquid-liquid interfaces," *Langmuir*, vol. 26, no. 15, pp. 12518–12522, 2010.

[174] Y. Zhang, S. Wang, J. Zhou, R. Zhao, G. Benz, S. Tcheimou, J. C. Meredith, and S. H. Behrens, "Interfacial Activity of Nonamphiphilic Particles in Fluid-Fluid Interfaces," *Langmuir*, vol. 33, no. 18, pp. 4511–4519, 2017.

[175] K. Geisel, L. Isa, and W. Richtering, "Unraveling the 3D localization and deformation of responsive microgels at oil/water interfaces: A step forward in understanding soft emulsion stabilizers," *Langmuir*, vol. 28, no. 45, pp. 15770–15776, 2012.

[176] O. S. Deshmukh, D. Van Den Ende, M. C. Stuart, F. Mugele, and M. H. Duits, "Hard and soft colloids at fluid interfaces: Adsorption, interactions, assembly & rheology," *Advances in Colloid and Interface Science*, vol. 222, pp. 215–227, 2015.

[177] R. Mears, "Colloids as an experimental model for proteins at liquid interfaces," *PhD thesis, The University of Edinburgh*, 2019.

[178] T. D. Kassuga and J. P. Rothstein, "Buckling of particle-laden interfaces," *Journal of Colloid and Interface Science*, vol. 448, pp. 287–296, 2015.

[179] S. P. Meeker, R. T. Bonnecaze, and M. Cloitre, "Slip and flow in soft particle pastes," *Physical Review Letters*, vol. 92, no. 19, pp. 1–4, 2004.

[180] L. Bécu, S. Manneville, and A. Colin, "Yielding and flow in adhesive and nonadhesive concentrated emulsions," *Physical Review Letters*, vol. 96, no. 13, pp. 7–10, 2006.

[181] O. Torres, N. M. Tena, B. Murray, and A. Sarkar, "Novel starch based emulsion gels and emulsion microgel particles: Design, structure and rheology," *Carbohydrate Polymers*, vol. 178, no. July, pp. 86–94, 2017.

[182] Z. A. Zell, L. Isa, P. Ilg, L. G. Leal, and T. M. Squires, "Adsorption energies of poly(ethylene oxide)-based surfactants and nanoparticles on an air-water surface," *Langmuir*, vol. 30, no. 1, pp. 110–119, 2014.